frontiers | Research Topics

Advances in numerical model, data assimilation, and observations for hazardous weather prediction

Edited by
Feifei Shen, Dongmei Xu, Yunheng Wang
and Yuefei Zeng

Published in
Frontiers in Earth Science
Frontiers in Environmental Science

ISSN 1664-8714
ISBN 978-2-8325-3772-5
DOI 10.3389/978-2-8325-3772-5

About Frontiers

Frontiers is more than just an open access publisher of scholarly articles: it is a pioneering approach to the world of academia, radically improving the way scholarly research is managed. The grand vision of Frontiers is a world where all people have an equal opportunity to seek, share and generate knowledge. Frontiers provides immediate and permanent online open access to all its publications, but this alone is not enough to realize our grand goals.

Frontiers journal series

The Frontiers journal series is a multi-tier and interdisciplinary set of open-access, online journals, promising a paradigm shift from the current review, selection and dissemination processes in academic publishing. All Frontiers journals are driven by researchers for researchers; therefore, they constitute a service to the scholarly community. At the same time, the *Frontiers journal series* operates on a revolutionary invention, the tiered publishing system, initially addressing specific communities of scholars, and gradually climbing up to broader public understanding, thus serving the interests of the lay society, too.

Dedication to quality

Each Frontiers article is a landmark of the highest quality, thanks to genuinely collaborative interactions between authors and review editors, who include some of the world's best academicians. Research must be certified by peers before entering a stream of knowledge that may eventually reach the public - and shape society; therefore, Frontiers only applies the most rigorous and unbiased reviews. Frontiers revolutionizes research publishing by freely delivering the most outstanding research, evaluated with no bias from both the academic and social point of view. By applying the most advanced information technologies, Frontiers is catapulting scholarly publishing into a new generation.

What are Frontiers Research Topics?

Frontiers Research Topics are very popular trademarks of the *Frontiers journals series*: they are collections of at least ten articles, all centered on a particular subject. With their unique mix of varied contributions from Original Research to Review Articles, Frontiers Research Topics unify the most influential researchers, the latest key findings and historical advances in a hot research area.

Find out more on how to host your own Frontiers Research Topic or contribute to one as an author by contacting the Frontiers editorial office: frontiersin.org/about/contact

Advances in numerical model, data assimilation, and observations for hazardous weather prediction

Topic editors

Feifei Shen — Nanjing University of Information Science and Technology, China
Dongmei Xu — Nanjing University of Information Science and Technology, China
Yunheng Wang — University of Oklahoma, United States
Yuefei Zeng — Nanjing University of Information Science and Technology, China

Citation

Shen, F., Xu, D., Wang, Y., Zeng, Y., eds. (2023). *Advances in numerical model, data assimilation, and observations for hazardous weather prediction*.
Lausanne: Frontiers Media SA. doi: 10.3389/978-2-8325-3772-5

Table of contents

04 Effect of precipitation on synthetic aperture radar hurricane wind field retrieval
Chaogang Guo, Weihua Ai, Shensen Hu, Xiaoyong Du and Nan Chen

16 Sea surface temperature retrieval based on simulated space-borne one-dimensional multifrequency synthetic aperture microwave radiometry
Chaogang Guo, Weihua Ai, Maohong Liu, Mengyan Feng, Junqi Qiao and Shensen Hu

28 A high-resolution numerical simulation of the “7.19” extraordinary heavy rainfall in Henan Province under topographic effect
Han Li, Le Xi and Xin-Min Wang

41 A high-resolution soil moisture content analysis product in Jing-Jin-Ji using the successive correction method
Changliang Shao, Yakai Guo, Yunchang Cao and Jiao Wang

51 Effects of vertical shear on intensification of tropical cyclones of different initial sizes
Mingyu Bi, Ruifang Wang, Tim Li and Xuyang Ge

65 The numerical study on the sensitivity of different auto-conversion parameterization to CCN concentration
Yi Li, Xiaoli Liu and Chaoyu Yuan

81 Evolution characteristics of impact weather system and SST signals during years of anomalous Meiyu onset over the Yangtze-Huaihe River Basin
Xiaoxia Jin, Yutong Ma, Mei Liu and Shanshan Zhong

92 Effects of joint assimilation of FY-4A AGRI and ground-based microwave radiometer on heavy rainfall prediction
Yinglong Shi, Zhixian Luo, Xiangguo Chen, Qian Zhang, Yin Liu and Chun Liu

103 Simultaneous assimilation of Fengyun-4A and Himawari-8 aerosol optical depth retrieval to improve air quality simulations during one storm event over East Asia
Xiaoli Xia, Jinzhong Min, Shangpeng Sun and Xu Chen

115 Comparison of different momentum control variables on assimilating radar observations for the forecasts of a dispersive convective event
Wei Song, Erliang Lin, Xiaobin Qiu and Yuting Xue

frontiers | Frontiers in Environmental Science

TYPE Original Research
PUBLISHED 04 October 2022
DOI 10.3389/fenvs.2022.1034045

OPEN ACCESS

EDITED BY
Feifei Shen,
Nanjing University of Information Science and Technology, China

REVIEWED BY
Tao Xie,
Nanjing University of Information Science and Technology, China
Fen Xu,
Chinese Academy of Meteorological Sciences, China

*CORRESPONDENCE
Weihua Ai,
awhzjax@126.com

SPECIALTY SECTION
This article was submitted to Environmental Informatics and Remote Sensing,
a section of the journal
Frontiers in Environmental Science

RECEIVED 01 September 2022
ACCEPTED 16 September 2022
PUBLISHED 04 October 2022

CITATION
Guo C, Ai W, Hu S, Du X and Chen N (2022), Effect of precipitation on synthetic aperture radar hurricane wind field retrieval.
Front. Environ. Sci. 10:1034045.
doi: 10.3389/fenvs.2022.1034045

Effect of precipitation on synthetic aperture radar hurricane wind field retrieval

Chaogang Guo, Weihua Ai*, Shensen Hu, Xiaoyong Du and Nan Chen

College of Meteorology and Oceanography, National University of Defense Technology, Changsha, China

C-band synthetic aperture radar (SAR) with all-weather observation capability is gradually being used for the high-resolution observation of hurricane. The extreme wind speed in hurricanes is retrieved by combining the co- and cross-polarized SAR signals. However, the heavy precipitation associated with hurricanes will seriously affect the retrieval of SAR sea surface wind speed. In this study, the effects of precipitation-related parameters and phenomena on wind speed retrieval under strong hurricane conditions were examined by using the data from co-located global precipitation measurement Dual-frequency Precipitation Radar, SAR on Sentinel-1 and Radarsat-2, and stepped frequency microwave radiometer. The results show that precipitation will increase the retrieval error of wind speed, and the effect of convective precipitation is more obvious than that of stratiform precipitation. When the wind speed is less than 30 m/s and the rain rate is less than 20 mm/h, the distribution of the melting layer has no obvious effect on SAR wind speed retrieval. Rain cells are mainly the product of convective precipitation and can also be produced when the storm top height is very low. An increase in the vertical-horizontal (VH) polarized normalized radar cross section (NRCS) in rain cells is usually greater than that of the vertical-vertical (VV) polarized NRCS because the sensitivity of the VH signal in a hurricane area is usually greater than that of the VV signal. When the rain rate is low, the difference between the retrieved wind speed inside and outside the rain cells is within the error range of hurricane wind speed retrieval. When the rain rate is further increased, the difference will exceed 10 m/s.

KEYWORDS

SAR, rain, global precipitation measurement, stepped frequency microwave radiometer, wind speed, NRCS, rain cells

1 Introduction

The synthetic aperture radar (SAR) is capable of all-day, all-weather, and high-spatial-resolution imaging. It is an important means to monitor the sea surface wind field. To accurately retrieve the wind speed in the middle and low range, several geophysical model functions (GMFs), such as CMOD4, CMOD_IFR2, and CMOD5, have been established based on the analysis of co-located European Remote Sensing (ERS) satellites

scatterometer data, European Centre for Medium-Range Weather Forecasts (ECMWF) reanalysis data, and National Data Buoy Center (NDBC) buoy data and t based on the empirical relationship between co-polarized normalized radar cross section (NRCS) and the sea surface wind speed (Stoffelen and Anderson, 1997; Quilfen et al., 1998; Hersbach et al., 2007). However, when the sea surface wind speed exceeds 20 m/s, the vertical-vertical (VV) polarized NRCS tends to be saturated and will no longer increase monotonically with the wind speed, resulting in a rapid increase in the error of retrieving high wind speed from the VV NRCS (Donnelly et al., 1999; Shen et al., 2009). Meanwhile, the ability of vertical-horizontal (VH) polarized NRCS to retrieve high wind velocity was revealed from the superior performance of the four-polarization low-noise data of Radarsat-2 (Vachon and Wolfe, 2011). Studies have shown that compared to VV NRCS, VH NRCS has higher sensitivity at high wind speeds, making it more suitable for high wind speed retrieval (Hwang et al., 2010). VH NRCS increases monotonically with wind speed, does not depend on the external wind direction, and has little or no dependence on the radar incidence angle. Using the matching data of VH NRCS and NDBC buoys, dropsondes, and ECMWF reanalysis data and based on the empirical relationship between VH polarization NRCS and sea surface wind speed, GMFs such as C-2PO, C-2POD, and C-3PO, were established (Zhang and Perrie, 2012; Zhang and Perrie, 2013; Zhang et al., 2017). As these models do not require wind direction, wind speed can be retrieved directly from radar measurement data without extracting wind direction information from VV NRCS or external data.

A hurricane is an extremely destructive weather phenomenon and is often accompanied by heavy precipitation. Compared with X-band and Ku-band with shorter wavelengths, the C-band SAR is less affected by precipitation, and hence, it is more widely used for retrieving hurricane wind speed (Weissman and Bourassa, 2008; Marzano et al., 2010). Full polarimetric SAR data can provide complementary direction information for wind field retrieval. It can help improve the accuracy of wind field retrieval by comprehensively using multiple polarimetric data (Zhang et al., 2012). Based on the Satellite Hurricane Observation Campaign (SHOC) data of ESA, a new geophysical model function (MS1A) was proposed to interpret cross-polarized NRCS for wind speeds greater than 25 m/s. The extreme wind speed retrieved using co- and cross-polarized SAR data together showed that the maximum value of retrieved wind speed can reach 60 m/s (Mouche et al., 2017). GMF quantifies the relationship between VH NRCS and wind speed. However, the sea surface roughness is also affected by other non-wind-induced external factors, which will increase or decrease the VH NRCS signal. Precipitation is one of the important factors affecting sea surface roughness (Carratelli et al., 2006). However, almost none of the current GMF functions based on empirical relationships contain the precipitation paraments. In particular, for strong winds, reaching the hurricane level, the effect of precipitation can even produce 100% wind speed errors (Moore et al., 1983).

Precipitation generally affects the NRCS of microwave sensors in three ways, namely, the attenuation of the microwave signal in the atmosphere by precipitation, the backscattering caused by the falling precipitation, and the backscattering changes caused by the interaction of the precipitation with the sea surface (Nie and Long, 2008). The interaction between the precipitation and sea surface is a complex process, and it includes the splashing products (ring waves, stalks, and crowns) produced by raindrops striking the water surface, the changes in sea surface roughness caused by the downdraft associated with precipitation, and the turbulence in the upper water layer caused by raindrops, which attenuates the short gravity wave spectrum (Xu et al., 2014). A scatterometer usually has multiple antennas, which can be combined to obtain wind vectors from measurements from different angles. In order to remove the influence of precipitation, a rainfall algorithm is developed, which is used to infer the rainfall rate in the rainfall area and provide a rainfall marker for the wind vector. (Mears et al., 2000). However, the SAR has only one antenna, which cannot measure wind and rain simultaneously. Alpers et al. (Alpers et al., 2016) established the imaging mechanism of the SAR by analyzing the images and signals of SAR rain cells in different frequency bands and polarization modes when the rain rate is less than 50 mm/h. By matching Tropical Precipitation Measuring Mission (TRMM) PR, ERS-1/2, and ECMWF reanalysis data, Nie et al. (Nie and Long, 2008) established a wind–rain backscattering model of the scatterometer and re-evaluated the effect of precipitation on the C-band scatterometer. By analyzing co-located typhoon data observed by SAR and TRMM PR precipitation data, Shi et al. (Shi et al., 2019) found that when the incidence angle is in the range of 15°–30°, precipitation will suppress NRCS, and when the incidence angle is less than 10° and the incidence angle is in the range of 30°–45°, precipitation will enhance NRCS. Based on the difference between the co–and cross-polarization retrieval of the wind speed affected by precipitation, Hui et al. (Hui et al., 2018) proposed the quality index of the retrieval SAR vector wind speed polluted by rain and also proposed a method to rectify the effect of precipitation in the hurricane core area; this method effectively improved the wind speed retrieval in precipitation-contaminated areas.

The rain rate is clearly an intuitive and important parameter to study the effect of precipitation on microwave signals, but few studies explored the effect of other precipitation-related parameters on microwave signals. In this regard, we used the co-located global precipitation measurement (GPM) Dual-frequency Precipitation Radar (DPR) precipitation data, the SAR hurricane data of Sentinel-1 and Radarsat-2, and the stepped frequency microwave radiometer (SFMR) data to analyze the effects of precipitation, melting layer (ML)

distribution, and precipitation type on SAR wind speed retrieval. The rest of this paper is organized as follows. Section 2 presents the data we used and the data-matching method. Section 3 provides an analysis of the effect of wind speed retrieval under different precipitation environments. Section 4 presents an analysis of the effect of rain cells on NRCS and wind speed retrieval. Section 5 provides a discussion and perspectives.

2 Data sets and methods

2.1 Sentinel-1 and Radarsat-2

Sentinel-1 is part of ESA's Copernicus satellite launch program. It consists of polar-orbiting satellites A and B that form a dual constellation system. Satellites A and B were launched in 2014 and 2016, respectively. The SAR sensor on Sentinel-1 has four imaging modes: Stripmap (SM), Interferometric Wide swath (IW), Extra Wide swath, and Wave (WV). The IW mode we used is to image three sub-bands with a swath of 250 km in a progressive scanning mode, and it covers an incidence angle range of 30°–42°. The level-1 ground range detected product has a range resolution of about 20 m and an azimuth resolution of about 22 m (Geudtner et al., 2014). Radarsat-2 is a high-resolution commercial SAR satellite jointly developed by the Canadian Space Agency and MacDonald Dettwiler and Associates Ltd. (MDA). Radarsat-2 was launched in 2007. We used its Scansar Wide mode (SCW), with an incidence angle of 20°–49° and a resolution of about 100 m in both the range and azimuth directions (Makynen et al., 2002).

As found, the sensitivity of the VH NRCS computed at 3-km resolution is reported to be more than 3.5 times larger than in VV(Mouche et al., 2017). Among the parameters used in wind field retrieval, VH NRCS signal is more sensitive than that of VV NRCS, so it has high requirements for the accuracy of NRCS. Before wind field retrieval, it is necessary to minimize the noise contained in the signal. In 2017, from an evaluation of the error of the Sentinel-1 data cross section, it was confirmed that the Sentinel-1 data met the radiation accuracy requirements. Subsequently, ESA improved the noise equivalent sigma zero (NESZ) estimation method. The first-level data processing algorithm of Sentinel-1 was further optimized, and a more accurate NESZ was obtained in the product (Hajduch et al., 2017). The Radarsat-2 dual-polarization measurement signal can reduce or minimize instrument noise through the noise reduction procedure, which is beneficial for the wind field data retrieval (Hui et al., 2014).

2.2 GPM

The GPM satellite was launched on 27 February 2014, and it is the successor of the world's first spaceborne precipitation radar Tropical Precipitation Measuring Mission (TRMM). The payloads carried by the GPM core satellite are a multi-channel GPM Microwave Imager (GMI) and the first spaceborne Ku/Ka-band Dual-frequency Precipitation Radar (DPR). The DPR radar data used in this study includes a Ku-band precipitation radar (KuPR) operating at 13.6 GHz and a Ka-band precipitation radar (KaPR) operating at 35.5 GHz. The KuPR and TRMM PR operate at almost the same frequency, but the KuPR has twice the power of the TRMM *P*R. Hence, KuPR further improves the accuracy of precipitation measurement. With KaPR with the high-sensitivity scanning mode, the minimum detected precipitation intensity of DPR can reach 0.2 mm/h. GPM has four levels of products, and levels 1–3 are publicly available (Tang et al., 2015).

The GPM data are distributed by the NASA Space Flight Center Data Distribution Center. In this study, the dual-frequency retrieval product DPR_NS in the 2A-DPR orbital data product, which is the secondary product in the sixth edition data, was used. The product scans 49 points under the satellite in each measurement, with a resolution of 5 km, a scanning swath width of 245 km, and a vertical resolution of 250 m (Igarashi and Endo, 2014). These data were used in the research on the horizontal and vertical structures of precipitation, the distribution characteristics of the precipitation types, and the three-dimensional structural characteristics of precipitation under hurricane conditions; these researches laid the foundation for studying the effect of precipitation on SAR signals (Hu et al., 2019; Qiao et al., 2021; Hu et al., 2022).

2.3 SFMR wind speed

Since 2007, the National Oceanic and Atmospheric Administration Hurricane Research Division has conducted the Hurricane Field Program, which performs planned observations of hurricanes in the Atlantic and eastern Pacific every year. The data collection methods of the program include the use of airborne SFMR, GPS dropsondes, doppler radar, *etc.*, providing a large amount of effective data for studying hurricane evolution and path prediction. The SFMRs mounted on all hurricane hunter and hurricane research aircraft take measurements during flyovers over the hurricane by relying on six C-band radiometers spanning 4.6–7.2 GHz to estimate wind speed and precipitation during the hurricane. Uhlhorn et al. (Uhlhorn et al., 2007) revised the SFMR algorithm by using dropsonde data collected in 2003, and they further revised the SFMR processing algorithm in 2007, extending the range of the maximum measurable wind speed to 70 m/s and removing the remaining bias of the medium wind speed to a certain extent. SFMR data enable near-real-time intensity forecasts of hurricanes and are an important source of hurricane climatology data. In addition, these data are widely used to

develop GMFs under medium and high wind speed conditions and even under extreme wind speed conditions (Sapp et al., 2019).

2.4 Data matching

The resolution of the satellite footprint of the GPM data is 5 km. To realize data co-location, we adjusted the spatial resolution of the SAR and SFMR data to 5 km by spatial resampling. As shown in Figure 1, the grayscale image is the SAR VV NRCS, and the red track is the route of the SFMR flying over the hurricane during the measurement. When GPM works, the satellite scans the passing sub-satellite points in the flight direction. The left half of the coverage area shown in Figure 1 is the precipitation rate for the near-surface data measured by the GPM.

Because of the vector motion of the hurricane, the SAR coordinates should be corrected before matching. Previous studies validated the ability of the position offset method to improve the correlation between the SAR NRCS and the SFMR wind speed (Mouche et al., 2019; Guan, 2021). The National Hurricane Center can provide the coordinates, maximum wind force, and central pressure data of hurricanes at 6-hourly intervals. By combining the SAR coordinate information and the SFMR observation time difference, the SAR coordinates were translated according to the following formula:

$$M_{Lat} = \frac{Lat1_{TC} - Lat0_{TC}}{T_{L1-L0}}$$

$$M_{Lon} = \frac{Lon1_{TC} - Lon0_{TC}}{T_{L1-L0}}$$

$$Lat1_{SAR} = Lat0_{SAR} + M_{Lat} * \Delta T$$

$$Lon1_{SAR} = Lon0_{SAR} + M_{Lon} * \Delta T$$

where M_{Lat} (or M_{Lon}) represents the moving speed of the hurricane; $Lat0_{TC}$ (or $Lon0_{TC}$) and $Lat1_{TC}$ (or $Lon1_{TC}$) represent two successive positions of the hurricane; T_{L1-L0} represents the time between the two positions (usually 6 h). Some time periods also provide position information less than 6 h. $Lat0_{SAR}$ (or $Lon0_{SAR}$) represents the longitude and latitude of the original SAR, and $Lat1_{SAR}$ (or $Lon1_{SAR}$) represents the longitude and latitude after translation transformation.

Considering the effects of the violent horizontal movement of the hurricane, each co-located region contains overlapping swaths in which the time difference between the SAR time tags and the GPR DPR time tags is less than ±15 min and that between SAR time tags and SFMR time tags is less than ±1 h. As the co-located regions of SAR, DPR, and SFMR are relatively rare, we processed data from 1 July 2014, to 31 December 2021. Only two co-located hurricanes are found in this period. Information on the data is provided in Table 1. Generally, the duration of SAR acquisition is several seconds, while the SFMR observation time over a hurricane lasts up to several hours or even more. Therefore, it can be considered that the acquisition time of SAR is constant with respect to the observation time of SFMR (Mouche et al., 2019). The SAR observation duration as listed in the table is more than 1 min because the SAR may be continuously observed in the hurricane area, and multiple observation data can be spliced. For example,

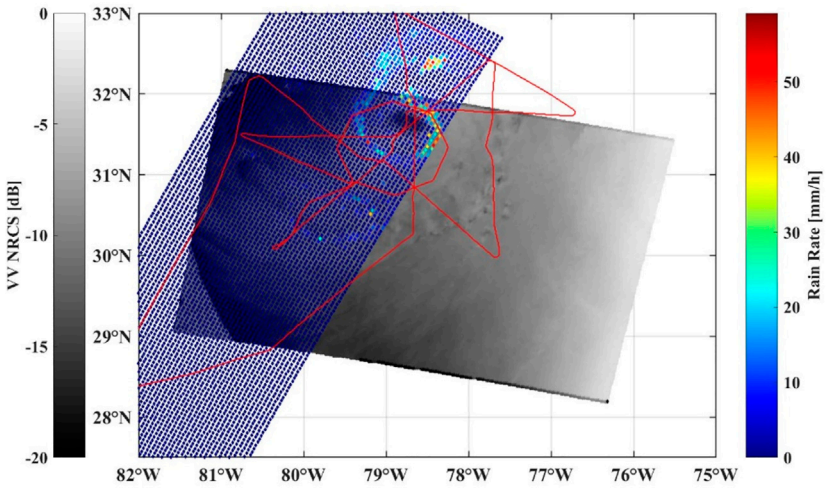

FIGURE 1
Radarsat-2 measured the VV NRCS of Hurricane Arthur during the period 3 July 2014, 11:13:56–3 July 2014, 11:14:50 (UTC). The red line is the SFMR flight route. The area on the left is the GPM scanning area. The scanning time 3 July 2014, 11:08:00–3 July 2014, 11:09:00 (UTC).

TABLE 1 Hurricane Information Collected by the synthetic aperture radar.

TC name	Sensor	Polarization	SAR starting data (UTC)	SAR ending data (UTC)	Matching SFMR
Arthur	Radarsat-2	VV, VH	2014/7/3 11:13	2014/7/3 11:14	2
Nana	Sentinel-1A	VV, VH	2020/9/2 23:58	2020/9/2 23:59	1

the collected data of Hurricane Nana are composed of three adjacent SAR data.

2.5 Wind field retrieval method

Since the discovery of the monotonically increasing relationship between the VH NRCS and wind speed, several GMFs were developed for different loadings and imaging modes. Alexis et al. (Mouche et al., 2017) developed a combined co- and cross-polarization SAR measurement method suitable for extreme wind conditions by using the hurricane data obtained from the SHOC active SAR in 2016, and they preliminarily realized the retrieval of wind speeds below 60 m/s. The method was further optimized in 2019 to retrieve maximum wind speeds of up to 75 m/s, and the deviation and root-mean-square error (RMSE) of the wind speed retrieved by this method compared with SFMR were about 1.5 and 5 m/s, respectively (Mouche et al., 2019). When the wind speed was less than 25 m/s, the VV NRCS, ECMWF wind direction, and CMOD5N GMF were used to retrieve the wind speed. When the wind speed was greater than 25 m/s, the VH NRCS and MS1A GMF were used to retrieve the wind speed. Co-polarization has a stable accuracy in retrieving wind speeds in the middle and low wind speed range, and the sensitivity of cross-polarization in retrieving high wind speeds also compensates for the problem of co-polarization saturation in the high wind speed range. Atlantic and Eastern Pacific hurricane data based on Sentinel-1 and Ra-darsat-2 satellite observations processed by the above methods (spatial resolution of the data: 0.01°) can be obtained from the Cyclobs Archive Center.

3 Effect of precipitation parameters on hurricane wind speed retrieval

3.1 Effects of precipitation

Precipitation is an important factor that affects the transmission of microwave signals. Traditionally, precipitation is considered transparent in the C-band, and its role is more obvious in the Ku band. However, studies revealed that effects of precipitation in the C-band may drastically change the total backscattering cross section and affect the retrieval of sea surface wind speeds (Draper and Long, 2004). The traditional ground-based radar can only observe land and offshore areas but cannot observe the precipitation over the sea. Although GPM satellite is not a polar-orbiting satellite, its observation area covers 90% of the global land and ocean. In addition, DPR data are transmitted to the ground station every 3 h, and hence, the DPR can provide more timely data for forecasting extreme weather events such as floods and hurricanes.

Figure 2 shows the scatter plot of the SAR-retrieved wind speed and the SFMR estimated wind speed. The data in Figure 2 1) shows no effect of precipitation. The RMSE of the two wind speeds is 4.82 m/s, which is almost the same as the RMSE of the combined co- and cross-polarization retrieval of extreme wind speed in the previous study [35]. Figure 2 2) shows the distribution of the SAR-retrieved wind speed and SFMR wind speed during precipitation, and the color map shows the near-surface rain rate measured by the DPR. The RMSE of the two wind speeds is 7.41 m/s. Similar to the conclusions of the previous research, this study showed that the existence of precipitation will lead to an increase in wind speed retrieval error. However, from the distribution of wind speed scatter plot, it is seen that the wind speed error is not clear only in the areas with strong wind or heavy precipitation intensity, indicating that the wind speed retrieval error does not simply increase monotonically with the rain rate but is also related to other factors.

3.2 Effects of different precipitation types

DPR classifies rain into three major categories, namely, stratiform, convective, and other. In single-frequency modules, rain-type classification is made by a vertical profiling method (V-method). First, the bright band (BB) in the zero layer is one of the characteristics of continuous precipitation. A BB is detected by examining the profile of the radar reflective factor (Z). When a BB is detected, the rain type is classified as stratiform. When no BB is detected and the Z exceeds 40 dBZ, the rain type is convective (Awaka, 1998). In the dual-frequency module, a new method called the dual-frequency ratio method was developed by using the difference between the measured Ku-band Z in dB and the measured Ka-band Z in dB. This method was used for detecting the ML and for rain-type classification. The concept of ML has a wider meaning than BB. In other words,

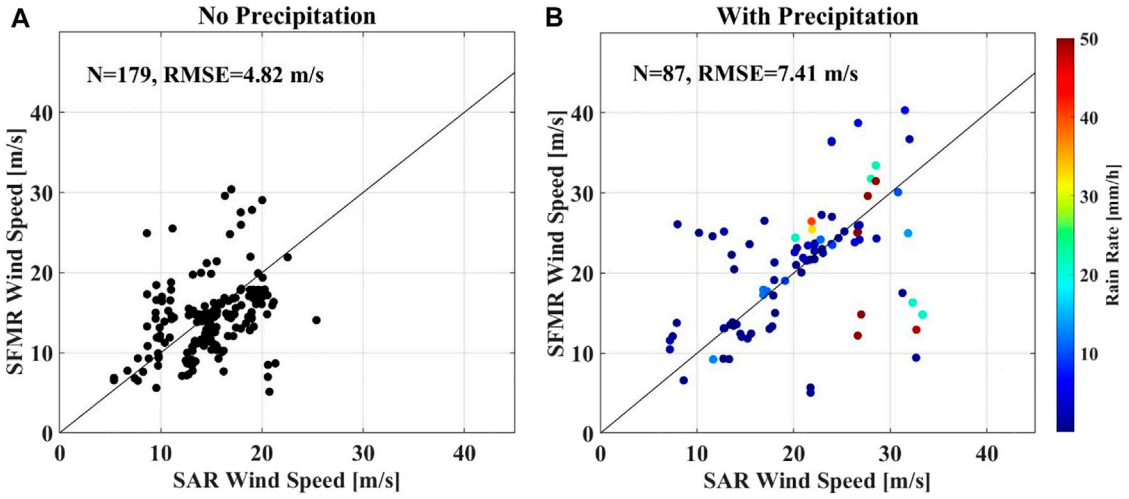

FIGURE 2
Effect of precipitation on SAR wind speed retrieval: **(A)** no precipitation, **(B)** precipitation accompanying the DPR measurement, and the colors represents the DPR near-surface rain rate.

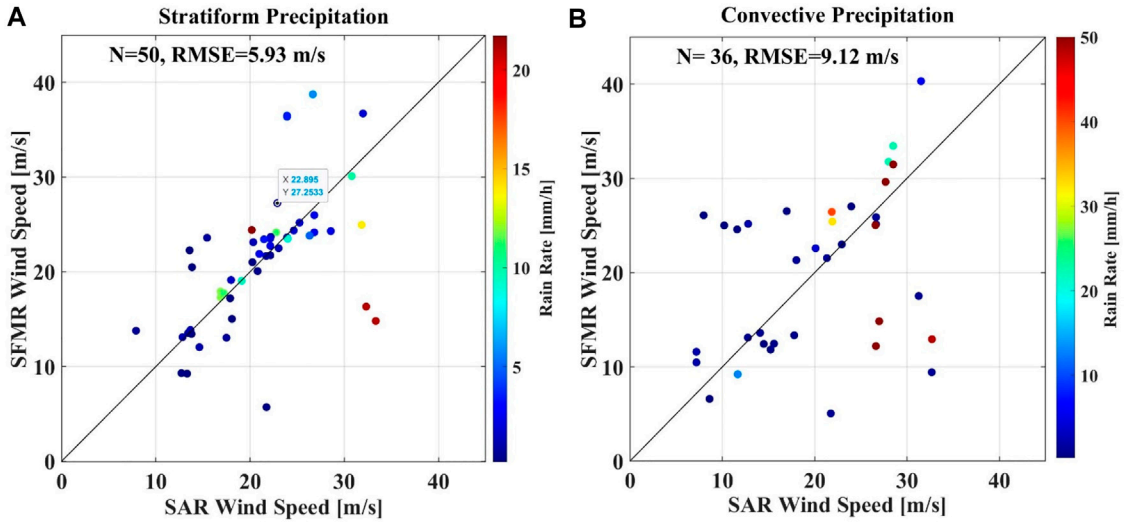

FIGURE 3
Comparison of the SAR-retrieved wind speed and SFMR wind speed for different precipitation types. The color represents the rain rate. **(A)** Stratiform precipitation and **(B)** is convective precipitation.

BB, which appears in stratiform rain, is a subset of ML (Le and Chandrasekar, 2013).

To analyze the effect of precipitation types on wind speed retrieval, we compared the SAR-retrieved wind speed with SFMR wind speeds for two precipitation types, as shown in Figure 3. Figure 3A shows the scatter plot of wind speed during stratiform precipitation (RMSE is 5.93 m/s). Compared with the wind speed error when there is no precipitation, as shown in Figure 2 (a), the wind speed retrieval error increases in the case of stratiform precipitation, but the impact is small. Figure 3B shows the scatter plot of wind speed during convective precipitation (RMSE: 9.12 m/s); compared with the case of no precipitation, the error is higher by 4.3 m/s, and the effect of precipitation is more obvious. Other precipitation types are areas where only

cloud or noise is found in DPR measurement, so no analysis was conducted. A comparison of the distribution of wind speed scatter plots for the two precipitation types shows that convective precipitation has a greater effect on wind speed retrieval. This is so because the convective rain rate is always greater than the stratiform rain rate. The color change of the scatterplot in Figure 3 also reflects this fact.

Figure 4 1) shows the distribution of different precipitation types (indicated by different colors) on Hurricane Arthur. In Figure 4A, convective precipitation is indicated by the red dots, which are mainly distributed around the hurricane eye and in the spiral rainband at the southwest of the hurricane eye. Stratiform precipitation is indicated by blue dots, which is the main precipitation pattern of hurricane. The coverage area is usually larger than that of convective precipitation. Figure 4 2) shows the VV NRCS during Hurricane Arthur. In the rain belt on the southwest side of the hurricane eye, a series of connected rain cells are observed. However, there are almost no rain cells in the convective rain region in the hurricane eye. This is because of the very intense updraft of the hurricane near the eye wall, offsetting the downdraft caused by the precipitation decline. However, there are almost no rain cells or rainbands in the stratiform precipitation area, indicating that the rain cell phenomenon is mainly a product of convective precipitation.

3.3 Effects of different melting layer distributions

The ML is an area where precipitation morphology changes. Above the ML, precipitation mainly exists in the form of solid ice crystals and snow particles. When passing through the ML, the ice crystals and snow particles melt into liquid water and form large water droplets through collision and polymerization. At this stage, the ML is an area where solid and liquid precipitation coexist. Below the ML, precipitation is mainly in the form of liquid water. For a given precipitation intensity, the attenuation and backscattering of ice crystals and snow particles on the C-band SAR signal are far less than that of liquid water, and the effect of precipitation particles above the ML on SAR signal is usually ignored (Long and Nie, 2017). The volume scattering and attenuation of precipitation are closely related to the distribution of the ML. By analyzing the characteristics and microphysical processes of the ML, Qiao et al. (Qiao et al., 2022a; Qiao et al., 2022b) found that the height of the ML is affected by the combined effect of latitude and hurricane category. Most precipitation types have the ML located at around 5 km (Petty, 2001). Considering the effect of raindrop density, the height of the ML in a real scenario was simulated by the uniform distribution height of 4 km for the precipitation density (Xu and Li, 2017).

DPR can provide the data of the top and bottom height of the ML, and the thickness of ML can be obtained by calculating the difference between them. As shown in Figure 5 (a), the red dot indicates the top height of the ML, and the blue dot indicates the bottom height of the ML. The top height of the ML is about 5 km, and the bottom height of the ML is about 4 km, and thus, most of the MLs are about 1 km thick. Figure 5 2) shows the scatter plot of wind speed bias and ML thickness.

The ML thickness is about 2 km at most. The maximum bias between the SAR-retrieved wind speed and SFMR radiometer estimated wind speed is not more than 5 m/s, and is mostly up to 2 m/s. From data analysis, it is seen that when the rain rate does not exceed 20 mm/h, the maximum wind speed does not exceed 30 m/s, and the resolution is 5 km. The effect of changes in the distribution of the ML on the wind speed retrieval can be

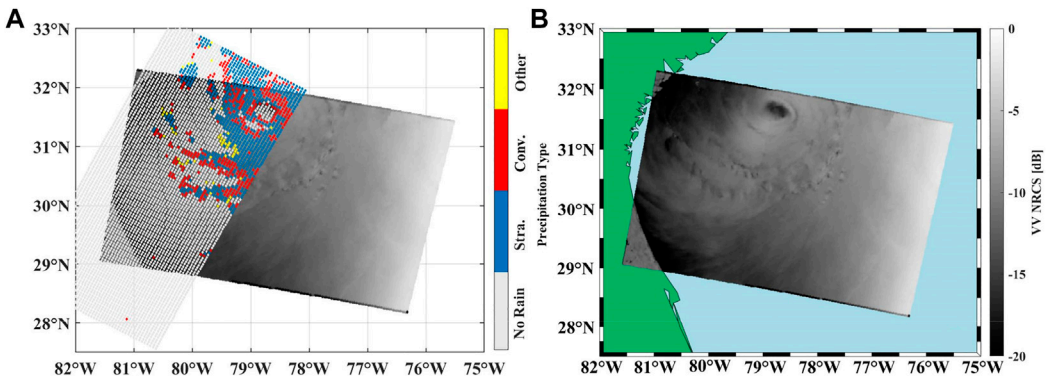

FIGURE 4
(A) Precipitation type classified by DPR during Hurricane Arthur. There is no precipitation in the area covered by white dots; convective precipitation occurs in the area covered by blue dots; layered precipitation occurs in the area covered by red dots; other precipitation types occur in the area covered by yellow dots. **(B)** VV polarization NRCS during Hurricane Arthur.

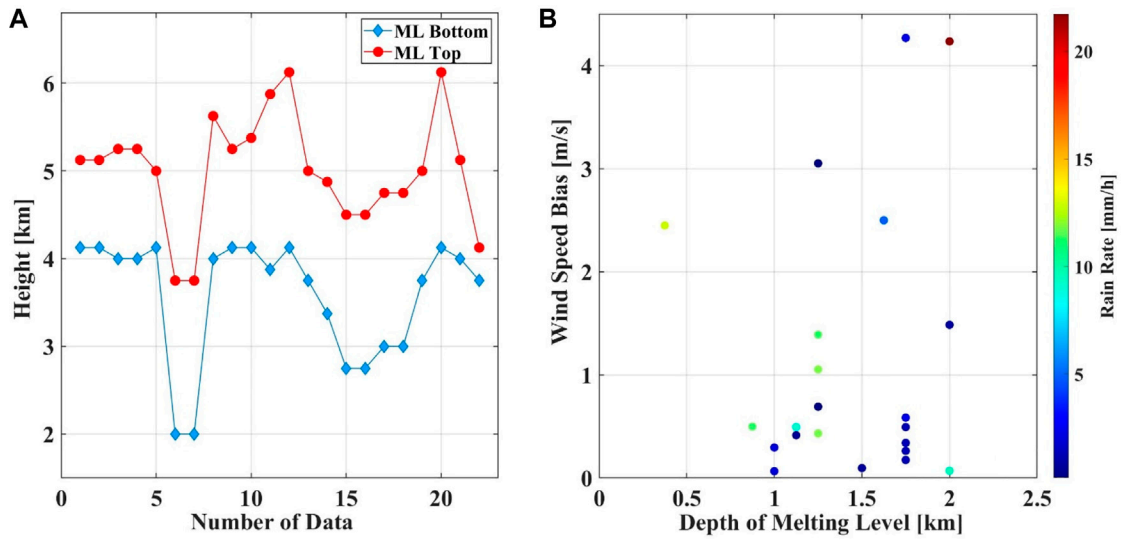

FIGURE 5
Relationship between SAR wind speed and SFMR wind speed difference and ML thickness. **(A)** Height distribution of top and bottom of ML, **(B)** Distribution of wind speed bias with different thickness of ML.

basically ignored. However, note that the current data are insufficient for analyzing the effects of larger rain rates and wind speeds above 30 m/s on the distribution of the ML, and further research is needed for this purpose.

4 SAR rain cells phenomenon

4.1 Effect of rain cells on NRCS

Rain cells are an important indicator of the effect of precipitation on SAR images. This phenomenon has been observed since the first marine satellite was launched in 1978. The footprints of rain cells on SAR images are caused by the interaction between precipitation and signals in the atmosphere and sea surface. When the downdraft reaches the sea surface, it spreads radially outward as a strong local surface wind that increases the sea surface roughness. If the surrounding wind field is too weak to interfere with this downdraft, a nearly circular bright pattern with a sharp edge will appear on the C-band SAR image. This phenomenon is closely related to the frequency band and polarization mode. Alpers et al. (Shi et al., 2019) compared the rain cells in the L-band, X-band, and C-band SAR images and different polarizations and found that there are obvious differences in the manifestations of the rain cell phenomenon.

The gray scale diagram in Figure 6 1) shows Sentinel-1 VV polarimetric SAR NRCS acquired in IW mode over the Gulf of Honduras from 23:58:12 (UTC) on 2 September 2020, to 23:59:27 on 2 September 2020. The area covered by the scatter plot in the southwest to northeast direction is the near-surface rain rate measured by DPR. The time of the DPR covering the hurricane area is from 00:00:23 on 3 September 2020, to 00:01:35 on 3 September 2020 (UTC), which is only 2–3 min away from the SAR observation time. It can almost be considered that the observation time of the two is synchronized. Figure 6B–Figure 6D show the variations in the VV polarization NRCS, VH polarization NRCS, and SAR retrieval wind speed, respectively, along the cross section in the A, B, and C regions during Hurricane Nana. In Figure 6 (b), the SAR incidence angle is about 41°; the DPR near-surface rain rate in the central area is about 3 mm/h, and that in the peripheral area is 0 mm/h. Figure 6 2) shows the VV-polarized NRCS in the center of rain cell about 5–6 dB, and the VH-polarized NRCS increases by about 8 dB and at wind speed, which is an increase of 10 m/s relative to the edge area of rain cell. In Figure 6 (d), the SAR incidence angle is about 37°, the precipitation in the central region is about 91 mm/h, the rain rate in the upper part of the peripheral region is about 17 mm/h, and the rain rate in the lower part of the peripheral region is about 4 mm/h. Figure 6 4) shows that in the region along the C transect, the VV-polarized NRCS in the center of rain cell increases by about 3–4 dB, and the VH-polarized NRCS increases by about 6–7 dB, and the wind speed increases by 10 m/s relative to the edge area of the rain cell.

The changes in NRCS as shown in Figure 6 (b)–(d) show that under different rainfall rates, the increase in VH-polarized NRCS in the rain cell area is greater than that of VV-polarize NRCS, indicating that the sensitivity of VH NRCS is greater than that of VV NRCS. This difference in sensitivity is more pronounced as we approach the eye of the hurricane. Figure 6 2) shows that when the rain rate is small, the increase in NRCS will cause an increase in the retrieved wind speed, though the wind speed is still within the error range of hurricane wind speed retrieval.

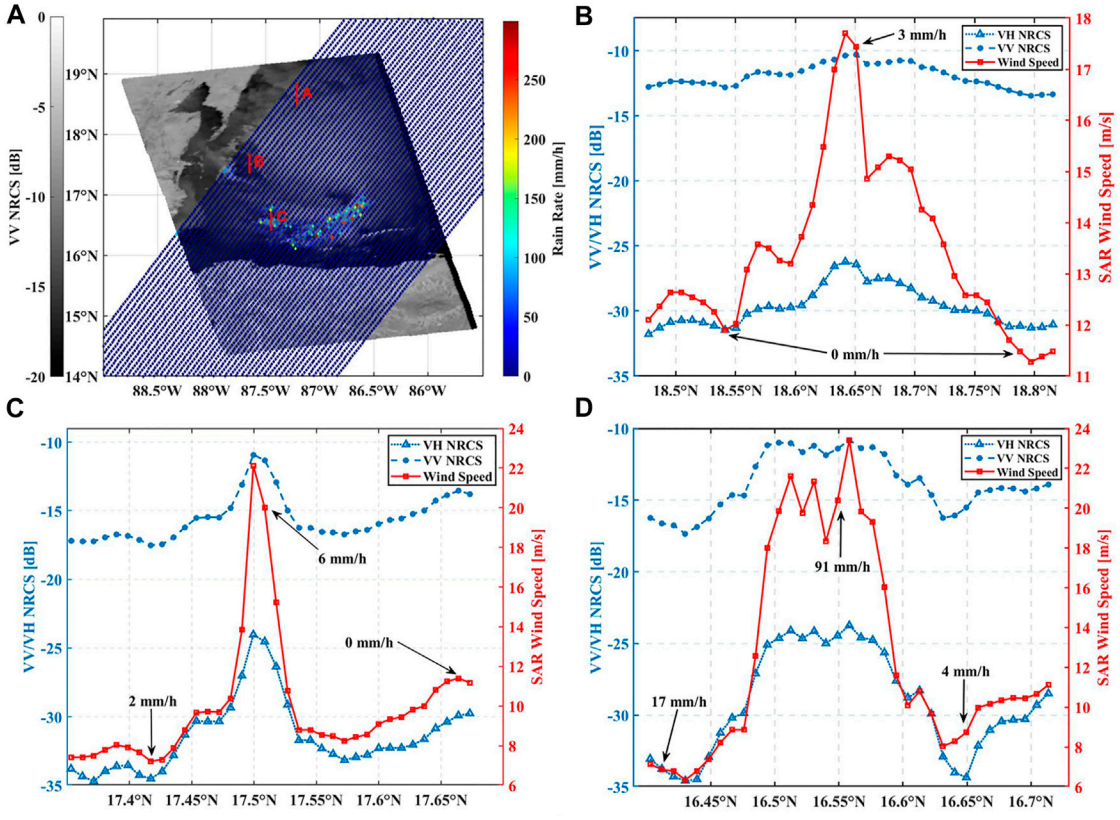

FIGURE 6
(A) VV-polarized NRCS acquired by Sentinel-1 during Hurricane Nana, overlaid with DPR-measured near-surface rain rate, with a color map representing the rain rate. The DPR time tags are in range of 00:00:23–00:01:35 on 3 October 2020 (UTC). Figures **(B)**–**(D)** show the NRCS and SAR-retrieved wind speed changes in regions **(A)**, **(B)**, and **(C)** during Hurricane Nana in Figure **(A)**.

However, the rain rate of the rain cell further increases, and the increase in NRCS will lead to a wind speed retrieval error even exceeding 10 m/s. The comparison of the rain rate and NRCS changes in the peripheral areas in Figure 6 3) and Figure 6 4) shows that the NRCS in the areas with higher rain rates are smaller than those in the areas with lower rain rates. This, it is confirmed that the magnitude of rain rate does not have a simple positive correlation with the change in NRCS.

In Figure 6 (a), we do not observe any obvious dark spots in the center of the rain cell. Meanwhile, dark spots are usually located in a very small range at the center of the rain cell. The data resolution used in this study is too coarse to observe these spots clearly. In Figure 6B and Figure 6D, the NRCS in the central region shows obvious fluctuations, which are most likely caused by the dark spots at the center of the rain cell. On the other hand, because the rain cells in this study are located in the spiral rainbands of hurricanes, the wind speed at the center of the rain cell is usually in the medium–high wind speed range, and even if dark patches appear at the center of the rain cell, they are not as obvious as in the normal area.

4.2 Relationship between storm top height and rain cell

The storm top height is the highest position where precipitation occurs. This height is usually slightly lower than the cloud top height. The analysis of storm top height can indirectly reflect the strength and stability of the updraft in clouds, and the effect of different cloud thickness on SAR NRCS is also different. Figure 7 1) shows the near-surface corrected reflectivity factor of Hurricane Arthur. In the figure, two continuous strong radar echo rainbands are observed at the lower left of the hurricane eye. Figure 7B shows the distribution of storm top heights during Hurricane Arthur. The storm top heights are concentrated in the range of 5–11 km, with a minimum height of less than 2 km and a maximum height of over 15 km. From a comparison of the rain rates during hurricanes, as shown in Figure 1, we can see that the storm top height is not positively correlated with rain rate. For example, the rain rate on the north side of the hurricane eye is as high as 55 mm/h, and the storm top

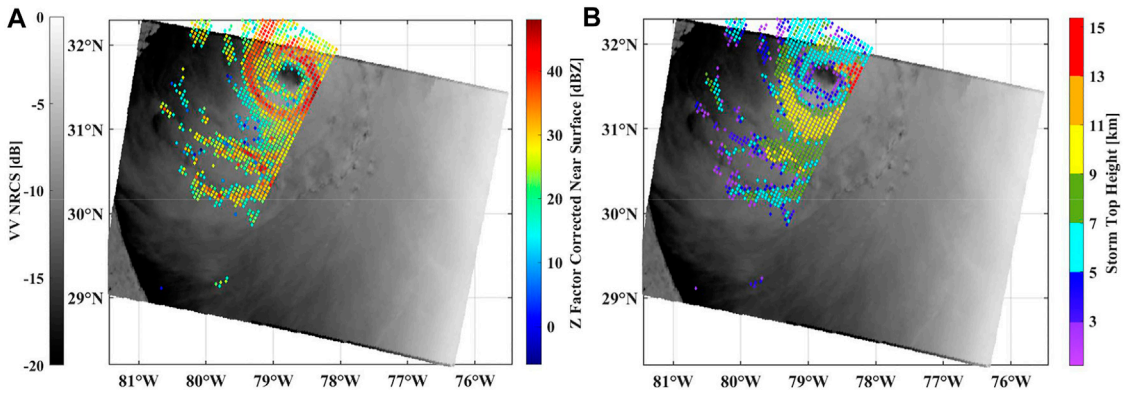

FIGURE 7
(A) Scatter plot of near-surface reflectance factor. **(B)** Storm top height for Hurricane Arthur.

height is about 5.5 km, while the rain rate on the west side of the hurricane eye is about 50 mm/h, and the corresponding storm top height is about 13 km. The precipitation intensity is not entirely determined by the storm top height; instead, it is also closely related to other physical processes occurring in the cloud.

A comparison of the precipitation types during Hurricane Arthur in Figure 4 1) show that the storm top height of convective precipitation is not always greater than that of stratiform precipitation. The storm top height of most stratiform precipitation is concentrated in the range of 5–11 km, while the distribution of convective precipitation is not concentrated but spread across all heights. In the two spiral rain belts in the southwest of the hurricane eye, the storm top height of convective precipitation was distributed between 2 and 9 km. From a comparison of the rain rate during Hurricane Arthur (Figure 1), it is seen that the rain rate in the rain cell area is concentrated at 10–30 mm/h, indicating that the generation of rain cells does not necessarily require very deep convective activities, and it may also occur when the storm top height is very low, but a certain intensity of rain rate is necessary.

5 Discussion and perspective

The development and movement of hurricanes include complex interaction processes between the atmosphere and ocean. To accurately predict the hurricane intensity and track, it is necessary to accurately grasp the physical processes involved in TC production and development. Although a large number of studies explored hurricane, it is difficult to obtain accurate measurement data because of the wide coverage area involved and the intense movement of hurricane. Thus, the prediction of hurricane trajectory and wind intensity still remain a great challenge. The combined C-band SAR co-polarized and cross-polarized NRCS were found to enable the retrieval of hurricane winds. However, since TCs are usually accompanied by large-scale heavy precipitation activities, which will affect the measurement of SAR backscattering cross section, further analysis of the effect of precipitation is required.

In this study, by using co-located C-band SAR data, DPR precipitation data, and SFMR wind field data, we analyzed the effects of precipitation, different precipitation types, and ML distribution on wind speed retrieval. By comparing the RMSEs of the SAR-retrieved wind speeds and SFMR estimated wind speeds under different precipitation parameters, we found that the precipitation causes an increase in the wind speed retrieval error. This increasing trend is not simply positively related to rain rate but is related to other factors. The effect of convective precipitation on the retrieval error of wind speed is obviously greater than that of stratiform precipitation, which is inseparable from the fact that the rain rate of convective precipitation is usually greater than that of stratiform precipitation (M et al., 2019). Rain cells are mainly the product of convective precipitation. In the stratiform precipitation area, there are no rain cells even when the precipitation reaches a certain intensity. The ML height is used to calculate the attenuation and volume scattering parameters of the C-band SAR in the atmosphere. However, when the wind speed is less than 30 m/s and the rain rate is less than 20 mm/h, the distribution of the ML does not have a significant effect on the wind speed retrieval.

Both VV NRCS and VH NRCS increase in the rain cell area. However, because of the different sensitivities of SAR signals with VH polarization and VV polarization, the increase in the VH NRCS in the rain cell area is usually greater than that in the VV NRCS. This sensitivity is closely related to the distance between the rain cell and the hurricane center. When the rain rate is small, the difference between the SAR-retrieved wind speeds inside and outside the rain cell is about 5 m/s. After the rain rate increases, the difference between the two can reach more than 10 m/s, but this change does not follow a simple positive correlation with the rain rate. The storm top height is a parameter that characterizes

the intensity of vertical motion in the cloud and the stability of the cloud; in this study, the storm top height of the convective precipitation during the hurricane was not completely higher than that of the stratiform precipitation. Rain cells can also occur at low storm top heights, but a certain rate of precipitation is necessary. More data are needed to determine this threshold.

When the rain cells are associated with the downdraft pattern, this geophysical phenomenon can be observed in the SAR of all frequency bands. However, the rain cells are not always associated with the downdraft, and precipitation may also occur in other forms, such as stratified rain, rain belt, and squall line. These different forms make it difficult to observe precipitation in SAR images. As the next step, we plan to use the co-located GPM data to mark the rainfall phenomenon in the SAR image and build a data set to train the depth learning model to identify the region containing precipitation from the SAR image. By restoring the NRCS of the precipitation area, the accuracy of the sea surface wind field retrieval can be further improved.

Although the platforms and payloads of hurricane research have increased in recent years, achieving high-resolution hurricane wind speed retrieval still remains a challenge. Precipitation is a continuous process, but the observation time of SAR for a given area is usually less than 1 min. So, it is impossible to fully describe the effect of precipitation. It is necessary to perform continuous observation and analysis of the precipitation process. The SHOC in Europe and the Hurricane Field Program in the United States provide valuable data for studying hurricanes. At present, the data of multiple load matching is not very rich, so it is necessary to carry out multi-platform joint observation. With accumulation of data, it is expected that SAR will become useful for accurately retrieving extreme weather events such as hurricanes.

Data availability statement

The original contributions presented in the study are included in the article/supplementary material, further inquiries can be directed to the corresponding authors.

Author contributions

CG and WA designed the experiments; CG, SH, and XD performed the experiments; CG and NC analyzed the data; CG wrote the paper. All authors have read and agreed to the published version of the manuscript.

Funding

This research received no external funding.

Acknowledgments

We thank the Cyclobs for making the Sentinel-1 and Radarsat-2 products publicly available. We thank the National Oceanic and Atmospheric Administration for SFMR wind measurements and hurricane reports. We thank Earth Observation Research Center, Japan Aerospace Exploration Agency (JAXA/EROC) for providing the tropical cyclone database.

Conflict of interest

The authors declare that the research was conducted in the absence of any commercial or financial relationships that could be construed as a potential conflict of interest.

Publisher's note

All claims expressed in this article are solely those of the authors and do not necessarily represent those of their affiliated organizations, or those of the publisher, the editors and the reviewers. Any product that may be evaluated in this article, or claim that may be made by its manufacturer, is not guaranteed or endorsed by the publisher.

References

Alpers, W., Zhang, B., Mouche, A., Zeng, K., and Chan, P. W. (2016). Rain footprints on C-band synthetic aperture radar images of the ocean - Revisited. *Remote Sens. Environ.* 187, 169–185. doi:10.1016/j.rse.2016.10.015

Awaka, J. (1998). *Early results on rain type classification by the Tropical Rainfall Measuring Mission (TRMM) precipitation radar*. China: CiNii.

Carratelli, E. P., Dentale, F., and Reale, F. (2006). Numerical pseudo-random simulation of SAR sea and wind response. *Adv. SAR Oceanogr. Envisat ERS Missions* 613, 35. https://www.researchgate.net/publication/234248364_Numerical_Pseudo-Random_Simulation_of_SAR_Sea_and_Wind_Response.

Donnelly, W. J., Carswell, J. R., Mcintosh, R. E., Chang, P. S., Wilkerson, J., Marks, F., et al. (1999). Revised ocean backscatter models at C and Ku band under high-wind conditions. *J. Geophys. Res.* 104 (5), 11485–11497. doi:10.1029/1998JC900030

Draper, D. W., and Long, D. G. (2004). Evaluating the effect of rain on SeaWinds scatterometer measurements. *J. Geophys. Res.* 109 (12), C02005. doi:10.1029/2002JC001741

Fang, M., He, J., Fu, Y., Zheng, P., Wang, D., et al. (2019). The precipitation structure for super typhoon Maria (1808) based on GPM satellite rainfall products. *Trans. Atmos. Sci.* 42 (6), 10. doi:10.13878/j.cnki.dqkxxb.20181101001

Geudtner, D., Torres, R., Snoeij, P., Davidson, M., and Rommen, B., (2014) SENTINEL-1 system capabilities and applications", in: IEEE Joint International Geoscience and Remote Sensing Symposium (IGARSS)/35th Canadian Symposium on Remote Sensing), 13-18 July 2014, Quebec City, 1457-1460.

Guan, C., Sun, J., and Zhang, J. (2021). Extreme wind speeds retrieval using sentinel-1 IW mode SAR data. *Remote Sens.* 13, 1867. doi:10.3390/rs13101867

Hajduch, G., Miranda, N., Piantanida, R., Meadows, P., and Franceschi, N. (2017). *Thermal denoising of products generated by the S-1 IPF*. MPC-0392.

Hersbach, H., Stoffelen, A., and de Haan, S. (2007). An improved C-band scatterometer ocean geophysical model function: CMOD5. *J. Geophys. Res.* 112 (3), C03006. doi:10.1029/2006JC003743

Hu, X., Ai, W., Qiao, J., Hu, S., Han, D., and Yan, W. (2022). Microphysics of summer precipitation over yangtze-huai river valley region in China revealed by GPM DPR observation. *Earth Space Sci.* 9 (3), e2021EA002021. doi:10.1029/2021ea002021

Hu, X., Li, G. L., Zhang, C., and Yan, W. (2019). Precipitation and latent heating properties of tropical cyclone in the northwest pacific measured by gpm dpr and himawari-8. *Int. Arch. Photogramm. Remote Sens. Spat. Inf. Sci.* XLII-3/W9, 77–82. doi:10.5194/isprs-archives-XLII-3-W9-77-2019

Hui, S., Perrie, W., He, Y., and Liu, G. (2014). Wind speed retrieval from VH dual-polarization RADARSAT-2 SAR Images. *IEEE Trans. Geosci. Remote Sens.* 52 (9), 5820–5826. doi:10.1109/TGRS.2013.2293143

Hui, S., Seitz, C., Perrie, W., He, Y., and Powell, M. (2018). Developing a quality index associated with rain for hurricane winds from SAR. *Remote Sens.* 10 (11), 1783. doi:10.3390/rs10111783

Hwang, P. A., Zhang, B. A., Toporkov, J. V., and Perrie, W. (2010). Comparison of composite Bragg theory and quad-polarization radar backscatter from RADARSAT-2: With applications to wave breaking and high wind retrieval. *J. Geophys. Res.* 115, C08019. doi:10.1029/2009jc005995

Igarashi, T., and Endo, T. (2014). Status of global precipitation measurement (GPM) mission. *jsprs.* 53 (3), 111–117. doi:10.4287/jsprs.53.111

Le, M., and Chandrasekar, V. (2013). Precipitation type classification method for dual-frequency precipitation radar (DPR) onboard the GPM. *IEEE Trans. Geosci. Remote Sens.* 51 (3), 1784–1790. doi:10.1109/tgrs.2012.2205698

Long, D. G., and Nie, C. (2017). "Hurricane precipitation observed by SAR," in *Hurricane monitoring with spaceborne synthetic aperture radar*. Editor X. Li (Singapore: Springer Singapore), 1–24.

Makynen, M., Manninen, T., Simila, M., Karvonen, J., and Hallikainen, M. (2002). "Incidence angle dependence of the mean C-band HH-polarization backscattering signatures of the Baltic Sea ice", in: IEEE International Geoscience and Remote Sensing Symposium), 24-28 June 2002, Toronto.

Marzano, F. S., Mori, S., and Weinman, J. A. (2010). Evidence of rainfall signatures on X-band synthetic aperture radar imagery over land. *IEEE Trans. Geosci. Remote Sens.* 48 (2), 950–964. doi:10.1109/tgrs.2009.2034843

Mears, C. A., Smith, D., and Wentz, F. J. (2000). "Detecting rain with QuikScat", in: IEEE International Geoscience & Remote Sensing Symposium), 24-28 July 2000, Honolulu.

Moore, R., Chaudhry, A., and Birrer, I. (1983). Errors in scatterometer-radiometer wind measurement due to rain. *IEEE J. Ocean. Eng.* 8 (1), 37–49. doi:10.1109/JOE.1983.1145541

Mouche, A. A., Chapron, B., Zhang, B., and Husson, R. (2017). Combined Co- and cross-polarized SAR measurements under extreme wind conditions. *IEEE Trans. Geosci. Remote Sens.* 55, 6746–6755. doi:10.1109/TGRS.2017.2732508

Mouche, A., Chapron, B., Knaff, J., Zhao, Y., Zhang, B., and Combot, C. (2019). Co- and Cross- polarized SAR measurements for high resolution description of major hurricane wind structures : Application to Irma category-5 Hurricane. *J. Geophys. Res. Oceans* 124 (6), 3905–3922. doi:10.1029/2019JC015056

Nie, C., and Long, D. G. (2008). A C-band scatterometer simultaneous wind/rain retrieval method. *IEEE Trans. Geosci. Remote Sens.* 46 (11), 3618–3631. doi:10.1109/TGRS.2008.922146

Petty, G. W. (2001). Physical and microwave radiative properties of precipitating clouds. Part II: A parametric 1D rain-cloud model for use in microwave radiative transfer simulations. *Am. Meteorological Soc.* 40 (12), 2115–2129. doi:10.1175/1520-0450

Qiao, J., Ai, W., Hu, X., Hu, S., and Du, X. (2022a). Characteristics of melting layer in cyclones over the western north pacific detected by the GPM dual-frequency precipitation radar. *Earth Space Sci.* 9 (3). doi:10.1029/2021ea001967

Qiao, J., Ai, W., Hu, X., Liu, M., and Hu, S. (2022b). An identification method of melting layer using the covariance wavelet transform based on GPM-DPR observations. *Earth Space Sci.* 9 (3). doi:10.1029/2021EA002103

Qiao, J. Q., Ai, W. H., Hu, X., Hu, S. S., and Yan, W. (2021). A recognition method of hydrometeor in tropical cyclones by using the GPM dual-frequency precipitation radar. *J. Trop. Meteorology* 27 (2), 161–168. doi:10.46267/j.1006-8775.2021.015

Quilfen, Y., Chapron, B., Elfouhaily, T., Katsaros, K., and Tournadre, J. (1998). Observation of tropical cyclones by high-resolution scatterometry. *J. Geophys. Res.* 103 (C4), 767. doi:10.1029/97JC01911

Sapp, J., Alsweiss, S., Jelenak, Z., Chang, P., and Carswell, J. (2019). Stepped frequency microwave radiometer wind-speed retrieval improvements. *Remote Sens.* 11 (3), 214. doi:10.3390/rs11030214

Shen, H., He, Y., and Perrie, W. A. (2009). Speed ambiguity in hurricane wind retrieval from SAR imagery. *Int. J. Remote Sens.* 30, 2827–2836. doi:10.1080/01431160802555879

Shi, J., Hu, J., Shao, W., Wang, X., Li, X., Zhao, L., et al. (2019). The impact of rain to observed signal from Chinese Gaofen-3 synthetic aperture radar in typhoons. *Acta Oceanol. Sin.* 38 (11), 121–133. doi:10.1007/s13131-019-1502-7

Stoffelen, A., and Anderson, D. (1997). Scatterometer data interpretation: Estimation and validation of the transfer function CMOD4. *J. Geophys. Res.* 102 (C3), 5767–5780. doi:10.1029/96JC02860

Tang, G., Wei, W., Zeng, Z., Guo, X., Na, L., Di, L., et al. (2015). An overview of the global precipitation measurement (GPM) mission and it's latest development. *Remote Sens. Technol. Appl.*. doi:10.11873/j.issn.1004-0323.2015.4.0607

Uhlhorn, E. W., Black, P. G., Franklin, J. L., Goodberlet, M., Carswell, J., and Goldstein, A. S. (2007). Hurricane surface wind measurements from an operational stepped frequency microwave radiometer. *Mon. Weather Rev.* 135 (9), 3070–3085. doi:10.1175/mwr3454.1

Vachon, P. W., and Wolfe, J. (2011). C-band cross-polarization wind speed retrieval. *IEEE Geosci. Remote Sens. Lett.* 8 (3), 456–459. doi:10.1109/LGRS.2010.2085417

Weissman, D. E., and Bourassa, M. A. (2008). "Measurements of the effect of rain-induced sea surface roughness on the QuikSCAT scatterometer radar cross section and wind stress", in: OCEANS, 15-18 September 2008, Quebec.

Xu, F., and Li, X. (2017). "Electromagnetic scattering of rainfall and tropical cyclones over ocean," in *Hurricane monitoring with spaceborne synthetic aperture radar*. Editor X. Li (Singapore: Springer Singapore), 271–298.

Xu, F., Li, X., Wang, P., Yang, J., Pichel, W. G., and Jin, Y. Q. (2014). A backscattering model of rainfall over rough sea surface for synthetic aperture radar. *IEEE Trans. Geosci. Remote Sens.* 53, 3042–3054. doi:10.1109/TGRS.2014.2367654

Zhang, B., and Perrie, W. (2012). Cross-polarized synthetic aperture radar: A new potential measurement technique for hurricanes. *Bull. Am. Meteorol. Soc.* 93 (4), 531–541. doi:10.1175/BAMS-D-11-00001.1

Zhang, B., and Perrie, W. (2013). "Recent development in SAR-derived winds using polarized RADARSAT-2 data", in: IGARSS 2013 - 2013 IEEE International Geoscience and Remote Sensing Symposium, 21-26 July 2013, Melbourne.

Zhang, B., Perrie, W., Vachon, P. W., Li, X., Pichel, W. G., Guo, J., et al. (2012). Ocean vector winds retrieval from C-band fully polarimetric SAR measurements. *IEEE Trans. Geosci. Remote Sens.* 50 (11), 4252–4261. doi:10.1109/TGRS.2012.2194157

Zhang, G., Li, X., Perrie, W., Hwang, P. A., Zhang, B., and Yang, X. (2017). A hurricane wind speed retrieval model for C-band RADARSAT-2 cross-polarization ScanSAR images. *IEEE Trans. Geosci. Remote Sens.* 55, 4766–4774. doi:10.1109/TGRS.2017.2699622

frontiers | Frontiers in Environmental Science

TYPE Methods
PUBLISHED 28 November 2022
DOI 10.3389/fenvs.2022.1054076

OPEN ACCESS

EDITED BY
Dongmei Xu,
Nanjing University of Information Science and Technology, China

REVIEWED BY
Yinan Li,
China Academy of Space Technology (CAST), China
Mukesh Gupta,
Independent Researcher, Calgary, AB, Canada

*CORRESPONDENCE
Weihua Ai,
awhzjax@126.com

SPECIALTY SECTION
This article was submitted to Environmental Informatics and Remote Sensing, a section of the journal Frontiers in Environmental Science

RECEIVED 26 September 2022
ACCEPTED 03 November 2022
PUBLISHED 28 November 2022

CITATION
Guo C, Ai W, Liu M, Feng M, Qiao J and Hu S (2022), Sea surface temperature retrieval based on simulated space-borne one-dimensional multifrequency synthetic aperture microwave radiometry.
Front. Environ. Sci. 10:1054076.
doi: 10.3389/fenvs.2022.1054076

Sea surface temperature retrieval based on simulated space-borne one-dimensional multifrequency synthetic aperture microwave radiometry

Chaogang Guo, Weihua Ai*, Maohong Liu, Mengyan Feng, Junqi Qiao and Shensen Hu

College of Meteorology and Oceanography, National University of Defense Technology, Changsha, China

The space-borne one-dimensional multifrequency synthetic aperture microwave radiometer (1D-MSAMR) offers new possibilities for detecting high spatial resolution sea surface temperature (SST). To achieve higher SST retrieval accuracy, an SST retrieval algorithm, the two-step retrieval algorithm (TSSR), is proposed based on the multiple linear regression (MLR) algorithm. In this study, we investigated the SST retrieval accuracy of 1D-MSAMR based on simulation experiments. For the study, we assumed that the frequencies of the 1D-MSAMR were 6.9, 10.65, 18.7, 23.8, and 36.5 GHz, and that all frequencies worked in a dual polarization (vertical and horizontal) manner. We used an ocean-atmosphere microwave radiation brightness temperature model and the 1D-MSAMR simulator to simulate the measured brightness temperature based on WindSat data provided by the Remote Sensing Systems (RSS). An MLR algorithm and the TSSR were then developed to retrieve the SST within the incidence angle range of 0°–65°. The results show that the SST retrieval errors of the two SST retrieval algorithms decreased with the increase of incidence angle. The TSSR had higher retrieval accuracy, especially at low incidence angle. The average retrieval accuracy of the TSSR was about 0.3 K higher than that of the MLR algorithm. The retrieval error of the TSSR was also less sensitive to the measurement error of the 6.9 GHz frequency than the MLR algorithm.

KEYWORDS

space-borne one-dimensional multifrequency synthetic aperture microwave radiometer, sea surface temperature retrieval, two-step retrieval algorithm, multiple incidence angles, frequency

1 Introduction

With the development of satellite remote sensing technologies, remote sensing data is now being used to monitor global sea surface temperature (SST). Clouds and aerosols are essentially transparent to microwave radiation at frequencies below about 12 GHz, therefore microwave remote sensing can potentially eliminate the atmospheric

contamination problems that plague infrared measurements and is considered an enabling technology for all-day and all-weather SST measurement (Chelton and Wentz, 2005). Most microwave radiometers in orbit are real-aperture radiometers with conical scanning, such as the TMI, WindSat, AMSR2, and HY-2. Real-aperture microwave radiometers require large and massive antennas for high spatial resolution, such as that of the CIMR (Ulaby, 1981; Lise et al., 2018).

A synthetic aperture microwave radiometer using an interferometric technique is proposed to overcome the barriers that antenna size has placed on passive microwave sensing from space (RYLE, 1962; Vine, 2000). In such systems, the correlation of the output voltage from pairs of antennas with different spacing (baselines) is measured (Le et al., 1994; Jin et al., 2019). The product at each baseline yields a sample point in the Fourier transform of the brightness temperature map of the scene, and the scene itself is reconstructed by inverting the sampled transform (Le and David, 1990; Vine et al., 1992).

Several synthetic aperture microwave radiometers have been developed for Earth observation, such as electronically steered thinned array L-band radiometer (ESTAR) (Vine et al., 2004), MIRAS (Zine et al., 2008), and GeoSTAR (Lambrigtsen et al., 2006). The first space-borne synthetic aperture microwave radiometer, MIRAS, was mounted onboard the SMOS (Soil Moisture and Ocean Salinity) satellite which is a Y-sparse structure having many small receivers evenly distributed along the arms (Zine et al., 2008). The MIRAS provides soil moisture and ocean surface salinity global coverage measurements from space (Jordi et al., 2010). A study called MICROWAT showed that two-dimensional interferometric systems would be very complex (with a 3.9 K sensitivity on each measurement) and would not satisfy the user requirements in terms of SST accuracy. As a practical alternative, a one-dimensional interferometric system has a much lower systematic complexity, with 0.15 K sensitivity at 6.9 GHz and 0.35 K sensitivity at 18.7 GHz (Prigent et al., 2013).

The first one-dimensional synthetic aperture microwave radiometer (1D-MSAMR), ESTAR, was installed on an aircraft and operates at L-band. This system adopts the real-aperture along the track and the synthetic aperture cross-track dimension, and obtains an angular resolution of 7° (Le et al., 1994). The HUST-ASR is a one-dimensional synthetic aperture microwave radiometer developed by Huazhong University of Science and Technology that generates high-quality images of natural scenes (Li et al., 2008). An SST sensitivity and physical retrieval method based on the C-band 1D-MSAMR has been investigated (Ai et al., 2020; Feng et al., 2022).

At present, the SST retrieval algorithms for microwave remote sensing include primarily physical algorithms (Meissner and Wentz, 2012; Koner and Harris, 2015; Wentz, 2000; Bettenhausen et al., 2006; Brown et al., 2006) and empirical algorithms (Goodberlet et al., 1990; Wentz, 2000; Obligis et al., 2005; Krasnopolsky et al., 2000). The multiple linear regression (MLR) algorithm, one of the empirical algorithms, can be used as an on-board SST retrieval algorithm, as it has minimal computational requirements.

We aimed to develop an on-board SST retrieval algorithm suitable for 1D-MSAMR. In this study, a new SST retrieval algorithm based on MLR, the two-step retrieval algorithm (TSSR), for 1D-MSAMR is proposed. We used the ocean-atmosphere microwave radiation brightness temperature model and the 1D-MSAMR simulator to simulate the brightness temperature detected by 1D-MSAMR. TSSR and MLR were used to retrieve SST. Ample research has demonstrated that the C-band is the most sensitive to SST and is an important frequency band for SST retrieval (Wentz and Meissner, 2007; Ai et al., 2020). In addition, Feng et al. (2022) studied the influence of different frequency combinations on SST retrieval accuracy and showed that the 5-frequency combination scheme resulted in the highest SST retrieval accuracy. Therefore, we assumed that the frequencies of the 1D-MSAMR were 6.9, 10.65, 18.7, 23.8, and 36.5 GHz and that all frequencies worked in a dual polarization (vertical and horizontal) manner. Through the simulation model, we investigated the relationship between the retrieval accuracy and the brightness temperature measurement errors EM_b of 1D-MSAMR within the incidence angle range of 0–65°.

This article is organized as follows. Section 2 introduces measured brightness temperature simulation and the SST retrieval algorithms. The results and discussion are provided in Section 3, followed by conclusions in Section 4.

2 Brightness temperature simulation and SST retrieval algorithms

2.1 Ocean-atmosphere microwave radiation brightness temperature model

We built an ocean-atmosphere microwave radiation brightness temperature model to simulate the brightness temperature received by the 1D-MSAMR ($T_{B,p,\theta}$) as follows:

$$\boldsymbol{T_{B,\,p,\theta}} = \boldsymbol{T_{BU,\theta}} + \boldsymbol{\tau_\theta} \cdot \boldsymbol{E_{p,\theta}} \cdot \boldsymbol{T_S} + \boldsymbol{\tau_\theta} \cdot \boldsymbol{T_{B\Omega,\theta}}$$

$$\boldsymbol{T_{B\Omega,\theta}} = \boldsymbol{R_{p,\theta}} \cdot \left[\boldsymbol{T_{BD,\theta}} + \boldsymbol{\tau} \cdot \boldsymbol{T_{cold}}\right] + \boldsymbol{T_{B,scat,p,\theta}}$$

$$\boldsymbol{T_{B,scat,p,\theta}} == \boldsymbol{\Omega_{p,\theta}}(\boldsymbol{\tau}, \boldsymbol{W}) \cdot \left[\boldsymbol{T_{BD,\theta}} + \boldsymbol{\tau_\theta} \cdot \boldsymbol{T_{cold}}\right] \cdot \boldsymbol{R_{p,\theta}}$$

where p denotes the polarization mode, $p = v, h$. τ_θ is the atmospheric transmittance of the entire atmosphere, $R_{p,\theta} = 1 - E_{p,\theta}$ is sea surface reflectance, and $E_{p,\theta}$ is sea surface emissivity. $T_{BU,\theta}$ is upward atmospheric radiation brightness temperature and $T_{BD,\theta}$ is downward atmospheric radiation brightness temperature. Further, T_{cold} is the effective cold space temperature, which is assumed to be a fixed value of 2.7 K, T_s is the SST, $T_{B\Omega,\theta}$ is the upward sky radiation brightness temperature scattered from the ocean surface, and $\tau \cdot T_{B,scat,p,\theta}$ is used to correct atmospheric path in the downwelling scattered sky radiation. $\Omega_{p,\theta}$ is the empirical correction parameter.

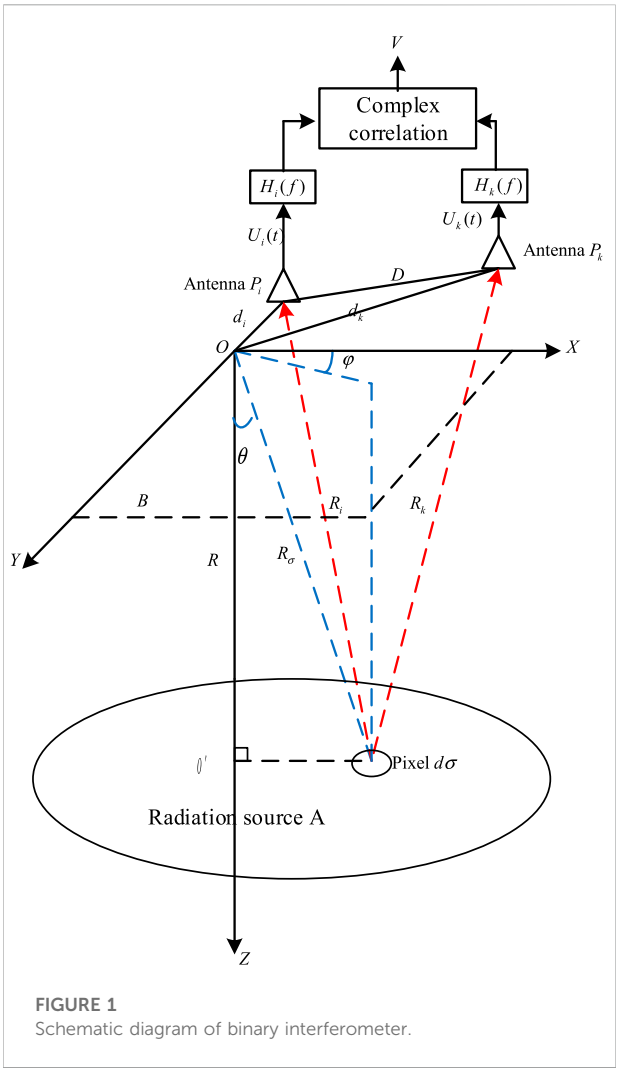

FIGURE 1
Schematic diagram of binary interferometer.

The ocean-atmosphere microwave radiation brightness temperature model is divided into two parts, the atmospheric absorption emission model, and the sea surface emissivity model. The atmospheric absorption emission model used in this study was developed by Wentz (2000) for the AMSR. The sea surface emissivity model used in this study was developed by Meissner and Wentz (2012). The model assumes that the sea surface roughness is only related to the sea surface wind vector, and the specific formula for calculation of sea surface emissivity was not provided.

2.2 The 1D-MSAMR simulator and EMb simulation

The 1D-MSAMR simulator is used to simulate the entire process of 1D-MSAMR detection of bright temperature. The schematic diagram of the detection process is shown in Figure 1.

The 1D-MSAMR uses the principle of binary interference imaging wherein P_i and P_k are two small antennas, $d\sigma$ is a pixel in the radiation source A, and source radiation is received by the small antennas at the same time. The output signals of the two small antennas are processed using complex correlation to obtain the visibility function. The visibility function is then inversely calculated to obtain the brightness temperature image of the observation scene (Schanda, 1979; Ruf et al., 1988). The output voltages are denoted by $U_i(t)$ and $U_k(t)$, where t is a limited period of time, and $H_i(f)$ and $H_k(f)$ are the frequency responses of the receiving channel. Furthermore, D is the distance of the small antenna, D_i and D_k are the distances from each small antenna to the origin o, R_i and R_k are the distances from the pixel to each small antenna, and R_σ is the distance from the pixel to o. The zenith and azimuth angles are denoted by θ and φ, respectively. After correlation calculations, it was concluded that V is only related to the distance between the two antennas (Corbella et al., 2004).

The formula for calculation of the visibility function and image reconstruction of the microwave interferometric radiometer with the 1D-MSAMR simulator is as follows (Wentz and Meissner, 2007; Lise et al., 2018):

$$V_m = \frac{1}{\sqrt{\Omega_m}} \int_{\xi^2 \le 1} \frac{T_B(\xi)}{\sqrt{1-\xi^2}} \cdot F_m(\xi) \cdot \tilde{r}_m\left(-\frac{u_m \xi}{f_c}\right) \cdot exp(-j2\pi u_m \xi) d\xi$$

$$\hat{T}(\xi) = \sum_{m=-N}^{N} V_m \, exp(j2\pi u_m \xi)$$

where Ω_m is the stereo angle of the antenna, $V_m(u_m)$ is the visibility function, $u_m = m \cdot \Delta u$ is the baseline composed of two antennas at different positions, $F_m(\xi)$ is the normalized voltage pattern, $T_B(\xi)$ is the brightness temperature of the observation scene, $\tilde{r}_m$ is the stripe elimination function, $\xi = sin\,\theta$, and f_c is the operating frequency.

We used the brightness temperature received by the 1D-MSAMR to calculate the model brightness temperature $T_{B,mod}$ with the 1D-MSAMR simulator. The antennas and channel of the 1D-MSAMR simulator used in this study were all in an ideal state, so the measured brightness temperature $T_{\theta,p}^{meas}$ was simulated by adding EM_b to the model brightness temperature $T_{B,mod}$. EM_b were assumed to follow a Gaussian distribution; in the absence of satellite observation data, it is a reasonable pre-research method used by many researchers (Bobylev et al., 2010).

2.3 SST retrieval algorithm

Figure 2 shows the schematic diagram of the SST retrieval experiment. First, we established a complete data set describing the background field of the atmosphere and ocean environment.

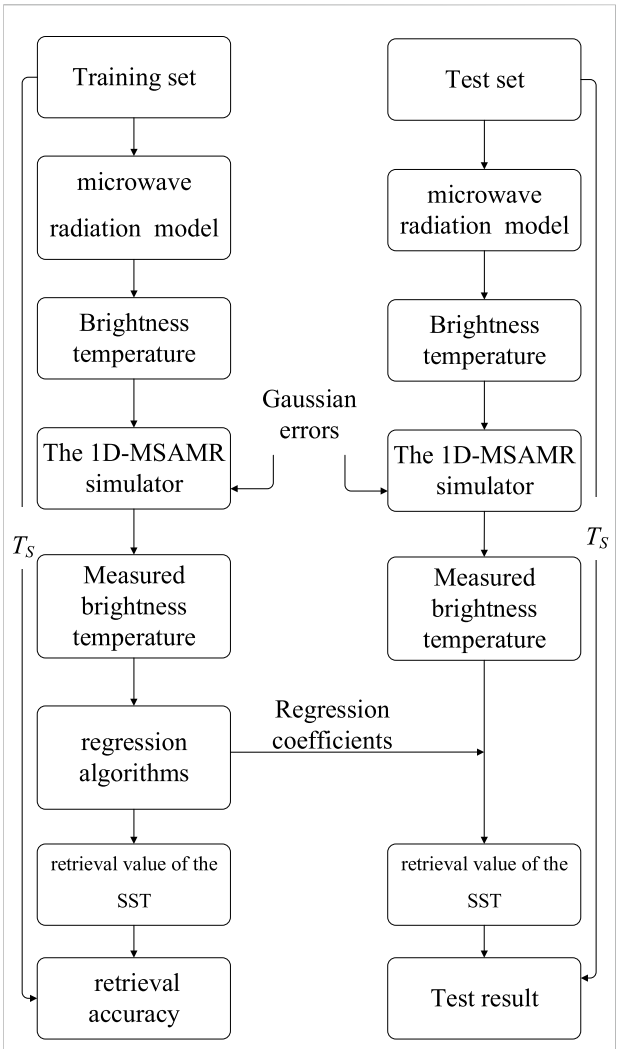

FIGURE 2
Diagram of the process to simulate and retrieve SST.

The data were then divided into training and test sets. The second step was to establish an ocean-atmosphere microwave radiation brightness temperature model to calculate the brightness temperature received by the 1D-MSAMR. The simulator with different Gaussian noises was then used to simulate the measured brightness temperature ($T_{\theta,p}^{meas}$) of the 1D-MSAMR. The last step was to establish a regression relationship between the $T_{\theta,p}^{meas}$ and SST. The obtained regression coefficient was then verified by using the test data set.

The 1D-MSAMR has the characteristics of multiple incidence angles that influence the brightness temperature considerably. Therefore, SST must be retrieved separately from different incidence angles. We used two different SST retrieval algorithms: MLR and TSSR (based on MLR). Calculation of MLR (Wentz and Meissner, 2007) was as follows:

$$T_{s,\theta} = A_{\theta,0} + \sum_{i=1}^{10\,or\,8} a_{\theta,p,i} \cdot t_{\theta,p,i}$$

$$t_{\theta,p,i} = T_{\theta,p,i}^{meas} \quad for\ 6.9,\ 10.65 GHz$$

$$t_{\theta,p,i} = -ln\left(290 - T_{\theta,p,i}^{meas}\right) \quad for\ 18.7,\ 23.8,\ 36.5\ GHz$$

where $A_{\theta,0}$ is a constant term, $a_{\theta,p,i}$ is the regression coefficient, and the subscript i corresponds to different frequencies.

For TSSR, $T_{\theta,p}^{meas}$ and MLR were used first to retrieve the preliminary SST retrieval value ($T_{S,first}$), which was then used as "*a priori*" in a second step to divide $T_{\theta,p}^{meas}$ data. $T_{\theta,p}^{meas}$ data were divided into different data sets in accordance with $T_{S,first}$ for 2 K intervals within 273.15 K–313.15 K. Then we trained the divided data sets to obtain the regression coefficients of each set using MLR. The last step was to use the regression coefficients to retrieve SST ($T_S^{retrieval}$). In the retrieval process, the training set was used to calculate the regression coefficients, and the test set was used to verify the regression coefficients. The specific process is shown in Figure 3.

3 Results and discussion

3.1 Data

This study used the data products of WindSat in Remote Sensing Systems (RSS) to establish the background field data. The data were 7-day average data product worldwide from 2016 to 2018. Specifically, the data included SST (T_s), total atmospheric column water vapor content (V), total atmospheric column cloud liquid water content (L), rainfall rate (R), wind direction at 10 m height (φ), and wind speed at 10 m height (W).

This research focused on the retrieval of SST in the case of non-precipitation; therefore, we excluded data with $R > 0mm/h$. We further excluded data corresponding to $V > 50mm$ and $L > 0.2mm$ due to the limitations of the ocean-atmosphere microwave radiation brightness temperature model. The remaining data contain about 2.1 million sets of data. Our data is randomly divided into training and test sets. Figure 4 shows data histograms. Since seawater salinity is more sensitive to the L-band (1.4 GHz) and has little influence on the frequencies used in this study, we also set the seawater salinity to the value of 35 psu (Feng et al., 2021.).

3.2 Results and discussion

We used the root mean square error (RMSE) to represent the retrieval error:

$$\sigma = \sqrt{\frac{1}{N}\sum_{k=1}^{N}\left(T_{S,k}^{true} - T_{S,k}^{retrieval}\right)^2}$$

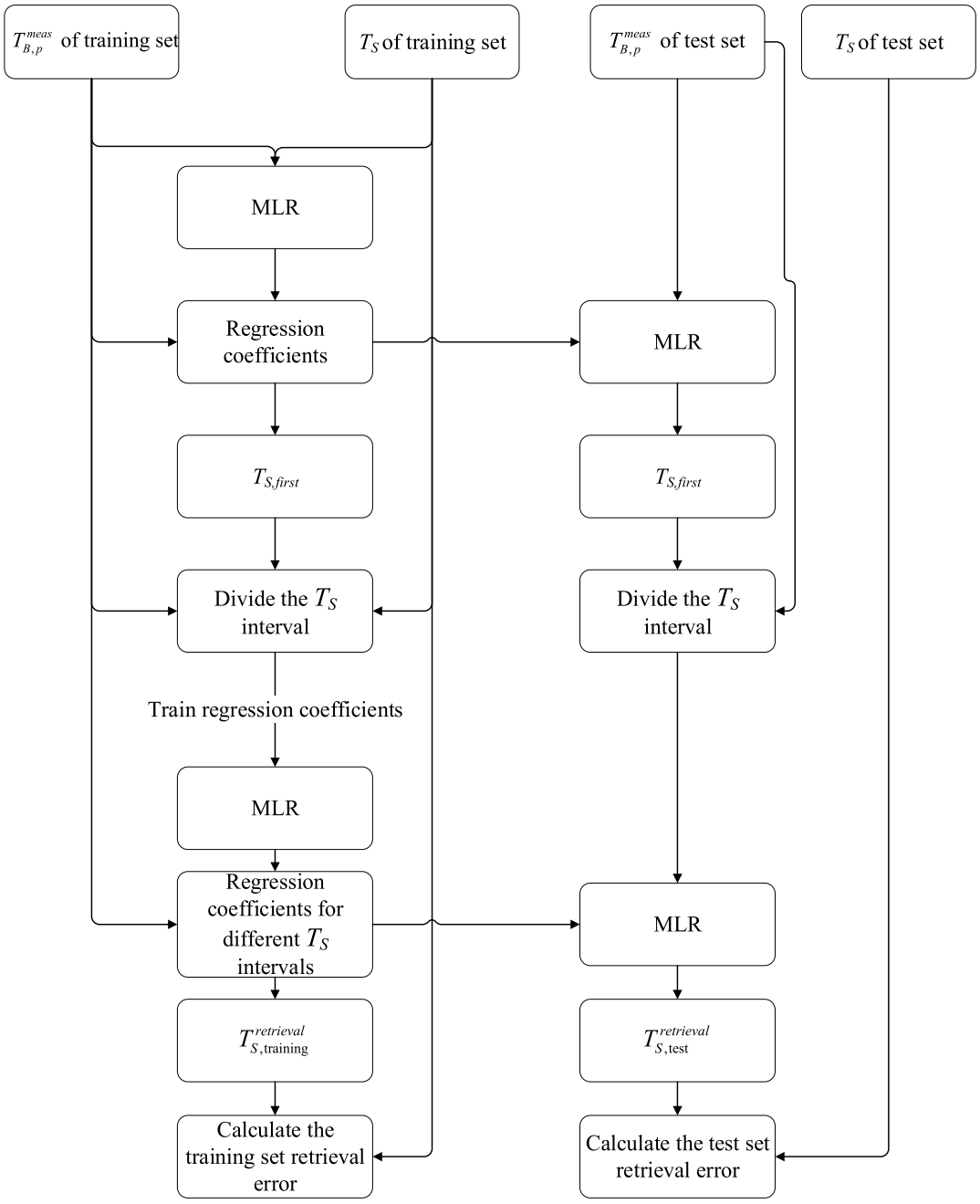

FIGURE 3
Flow chart of two-step algorithms.

where σ represents the RMSE, $T_{S,k}^{true}$ is the true value of the SST, $T_{S,k}^{retrieval}$ denotes the retrieval value of the SST, and N represents the number of $T_{S,k}^{true}$.

Figure 5 shows the relationship between the SST retrieval errors and the incidence angle when all channels of the 1D-MSAMR have the same EM_b (a massif of random Gaussian distribution with a zero mean and σ = 0~1 K). The figure demonstrates that the SST retrieval errors of the training set and the test set were almost the same for the two SST retrieval algorithms. This shows that the two SST retrieval algorithms are generalizable. In addition, the SST retrieval errors of TSSR were less than MLR, especially at low incidence angle and large EM_b. When EM_b of each channel of the 1D-MSAMR was within the range of 0~1 K, the SST retrieval error ranges of the test set and

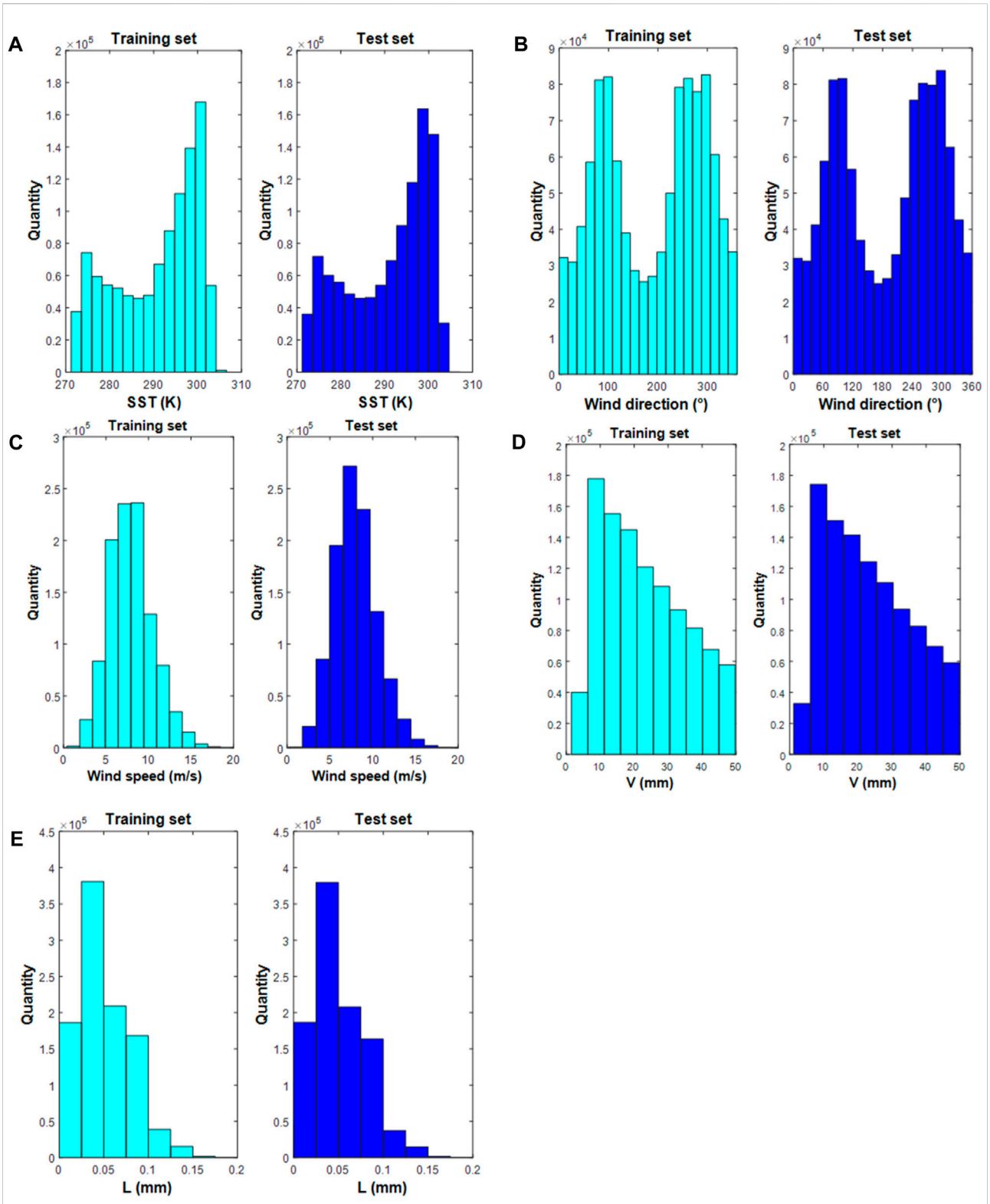

FIGURE 4
Histograms of the atmospheric-ocean background field data. The training set is shown on the left and the test set on the right. **(A)** SST; **(B)** sea surface wind direction; **(C)** sea surface wind speed; **(D)** water vapor content; and **(E)** liquid water content.

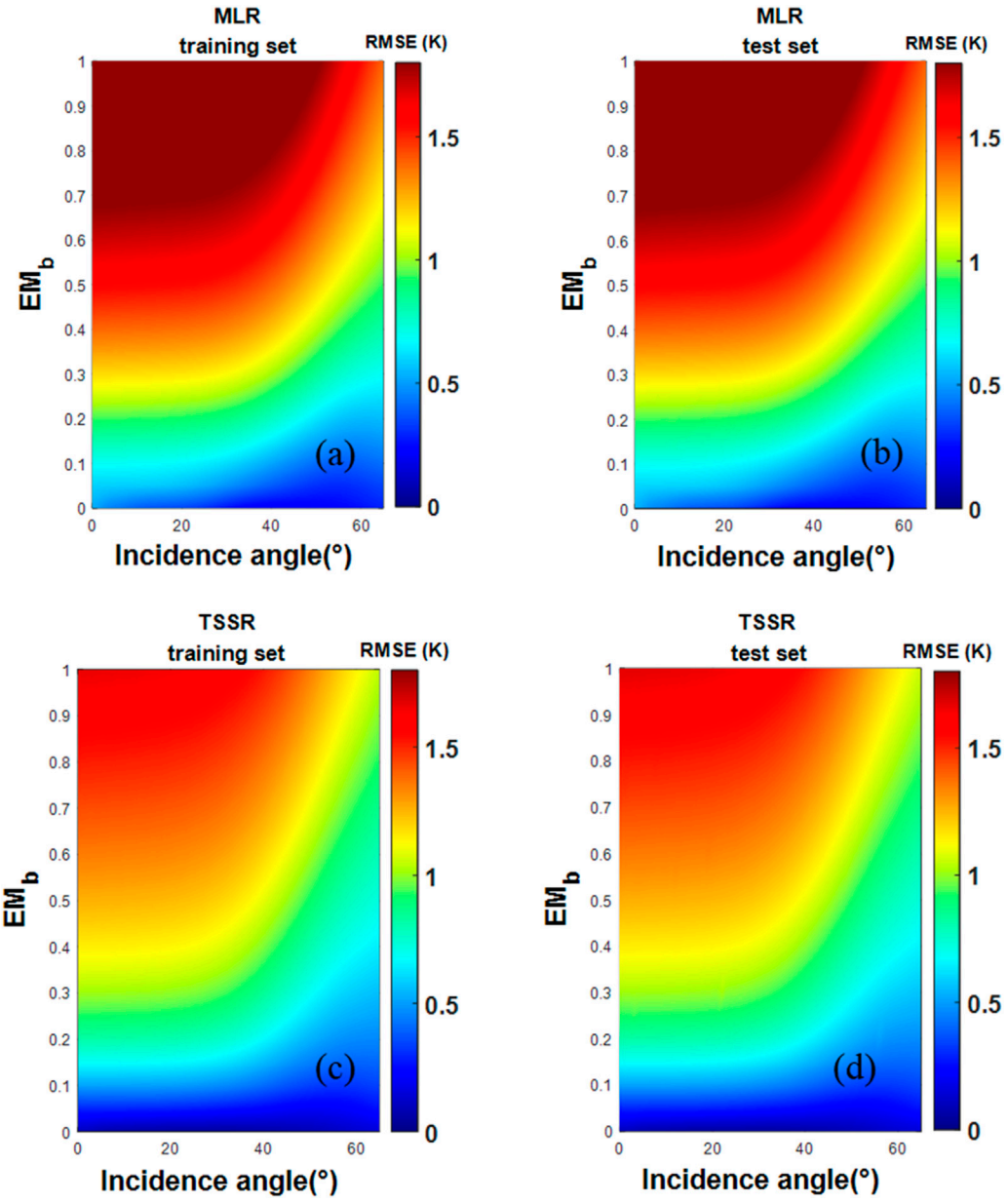

FIGURE 5
Relationship between SST retrieval errors, incidence angle, and EM_b. **(A,B)** MLR train and test; **(C,D)** TSSR train and test.

training set for MLR were 0.21 K–2.14 K and 0.21 K–2.15 K, respectively, and the retrieval error ranges of TSSR were 0.04 K–1.67 K and 0.04 K–1.66 K, respectively. The Gaussian error added by each channel was generated separately.

Figure 6 further illustrates the SST retrieval errors *versus* the incidence angle in the case of different EM_b. The SST retrieval errors of TSSR and MLR decreased with increasing incidence angle. This suggests that larger incidence angles should be set for the 1D-MSAMR to improve SST retrieval accuracy. Feng et al. (2022). reached a similar conclusion when analyzing the influence of frequency combination on the retrieval accuracy of SST and pointed out that an incidence angle set between 30°–60° is most conducive to the retrieval of SST. For different EM_b, the SST retrieval errors of test sets are provided in Table 1. These data indicate that the SST retrieval accuracy decreased with increasing EM_b and the average SST retrieval accuracy of TSSR was about 0.3 K (25%) higher than that of MLR. These results suggest that the 1D-MSAMR system error should be reduced as much as possible with redesign of its hardware system.

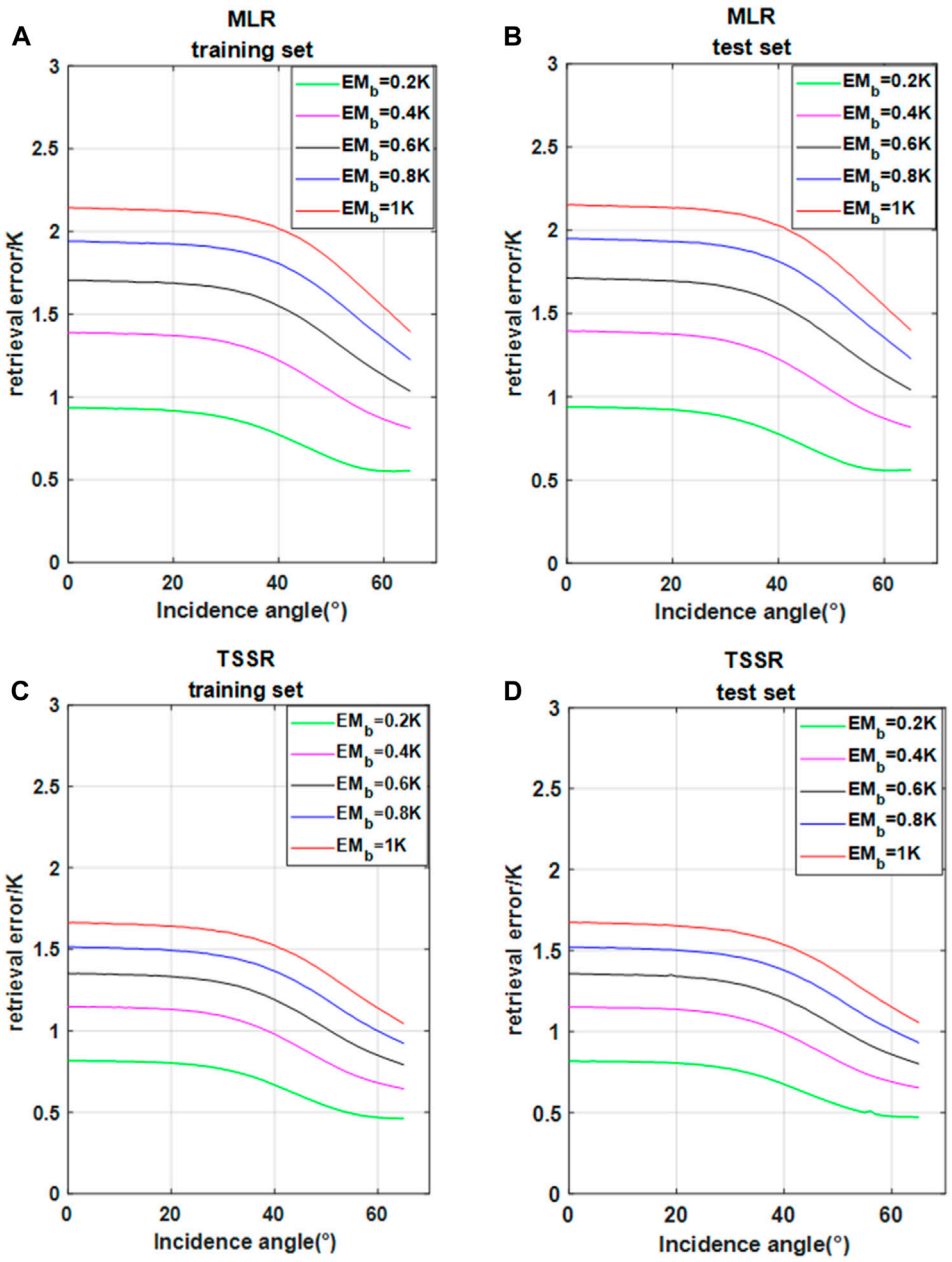

FIGURE 6
Relationship between SST retrieval error and incidence angle for different EM_b. **(A,B)** MLR train and test; **(C,D)** TSSR train and test.

C-band is the band that is most sensitive to SST. Sensitivity to the 6.9 GHz frequency (C_{sens}) is proposed to quantitatively describe the relationship between the EM_b of 6.9 GHz and SST retrieval accuracy. C_{sens} is calculated as follows:

$$C_{sens} = \frac{\partial \sigma}{\partial EM_b}$$

where σ is the RMSE of retrieval error and EM_b is brightness temperature measurement error.

The relationship between C_{sens} of the two SST retrieval algorithms and the EM_b is given in Figure 7. The C_{sens} decreased rapidly with increasing EM_b. This shows that with the increasing EM_b of 6.9 GHz, the C_{sens} curve decreases rapidly and finally trends to zero, which indicates that the retrieval accuracy of SST decreases rapidly when there is a measurement error in the 6.9 GHz channel. However, when the measurement error is greater than a certain value, the retrieval accuracy of SST remains stable. The C_{sens} curve

TABLE 1 SST retrieved with different dilation values.

EM_b (K)	Retrieval accuracy of TSSR (K)	Retrieval accuracy of MLR (K)
0	0.04–0.15	0.21–0.53
0.1	0.33–0.51	0.39–0.69
0.2	0.47–0.82	0.56–0.94
0.3	0.57–1.02	0.69–1.19
0.4	0.65–1.15	0.81–1.40
0.5	0.73–1.26	0.93–1.57
0.6	0.80–1.36	1.04–1.71
0.7	0.87–1.44	1.14–1.84
0.8	0.93–1.52	1.23–1.95
0.9	0.99–1.60	1.32–2.05
1	1.06–1.67	1.40–2.15

(black line) corresponding to TSSR is always below the MLR curve (red line), which shows that the TSSR is less affected by the EM_b of 6.9 GHz. That is, TSSR can reduce the negative impact of 6.9 GHz channel measurement error on the retrieval accuracy of SST, and with an increase in 6.9 GHz channel measurement error, the retrieval accuracy of SST will regain stability faster.

Among future on-board sensors for remote sensing of SST, 1D-MSAMR has excellent potential. This study used the MLR algorithm, which has fast computation speed and small computational memory requirements, to develop an on-board SST retrieval algorithm for 1D-MSAMR. Although the systematic error terms of each channel of 1D-MSAMR cannot be accurately obtained, the maximum error was set at the upper limit of 1 K according to the systematic error published by the on-orbit real-aperture microwave radiometer. Surprisingly, TSSR improved the retrieval accuracy by about 25% on the basis of only one more set of regression coefficients compared to MLR, and TSSR was less affected by the EMb of 6.9 GHz. Therefore, the requirement of 6.9 GHz channel design can be appropriately reduced when TSSR is adopted. One reason for the improved performance of TSSR *versus* MLR is that, with TSSR, the initial retrieval value of SST is divided into intervals and then each interval is retrieved separately. The SST has obvious zonal distribution characteristics (high SST at low latitude), and the sensitivity of each channel to SST is nonlinear (Feng et al., 2021). Therefore, it is more reasonable to adopt different coefficients for different SSTs. TSSR has the capacity for automatic operation without manual intervention. After running for a period of time, the algorithm can automatically update the coefficients of the two-step method and improve the retrieval accuracy by using the temperature data of the sea buoy. However, this study was based on simulation data. Although the Gaussian error we added to each channel was generated separately, the error of each channel has the same distribution (mean value is 0, variance is the same), which is not common in the actual 1D-MSAMR system. Although our simulation model is scientific, it still needs future verification and adjustment based on actual 1D-MSAMR measurement data.

Due to the different baselines of small antennas at different frequencies, it is difficult for the spatiotemporal synchronous observation areas to coincide completely, which leads to the problem of high spatial resolution at high frequencies and low spatial resolution at low frequencies. However, the premise of TSSR algorithm application is that the measured brightness temperature of each channel has spatiotemporal matching. Therefore, before applying TSSR, it is necessary to preprocess the measured brightness temperature so that the measured brightness temperature of each channel corresponds to the same detection area.

There is an advantage to using a microwave radiometer to monitor SST under conditions of weak precipitation. Precipitation will increase the roughness and change the emissivity of the sea surface. Due to limitations of the simulation model, the sea surface emissivity in the presence of precipitation cannot be calculated, so we did not study the retrieval of SST under those conditions; future studies will address measurement of SST *via* the 1D-MSAMR in the presence of precipitation. The 1D-MSAMR used in our study has five frequencies. The detected brightness temperature contains more information about the sea surface and atmospheric environment, and the five frequencies include those that are sensitive to water vapor content and weak precipitation (23.8 GHz and 36.5 GHz, respectively). Therefore, 1D-MSAMR retrieval of SST under conditions of weak precipitation is theoretically feasible, and a direction to be explored in our future research.

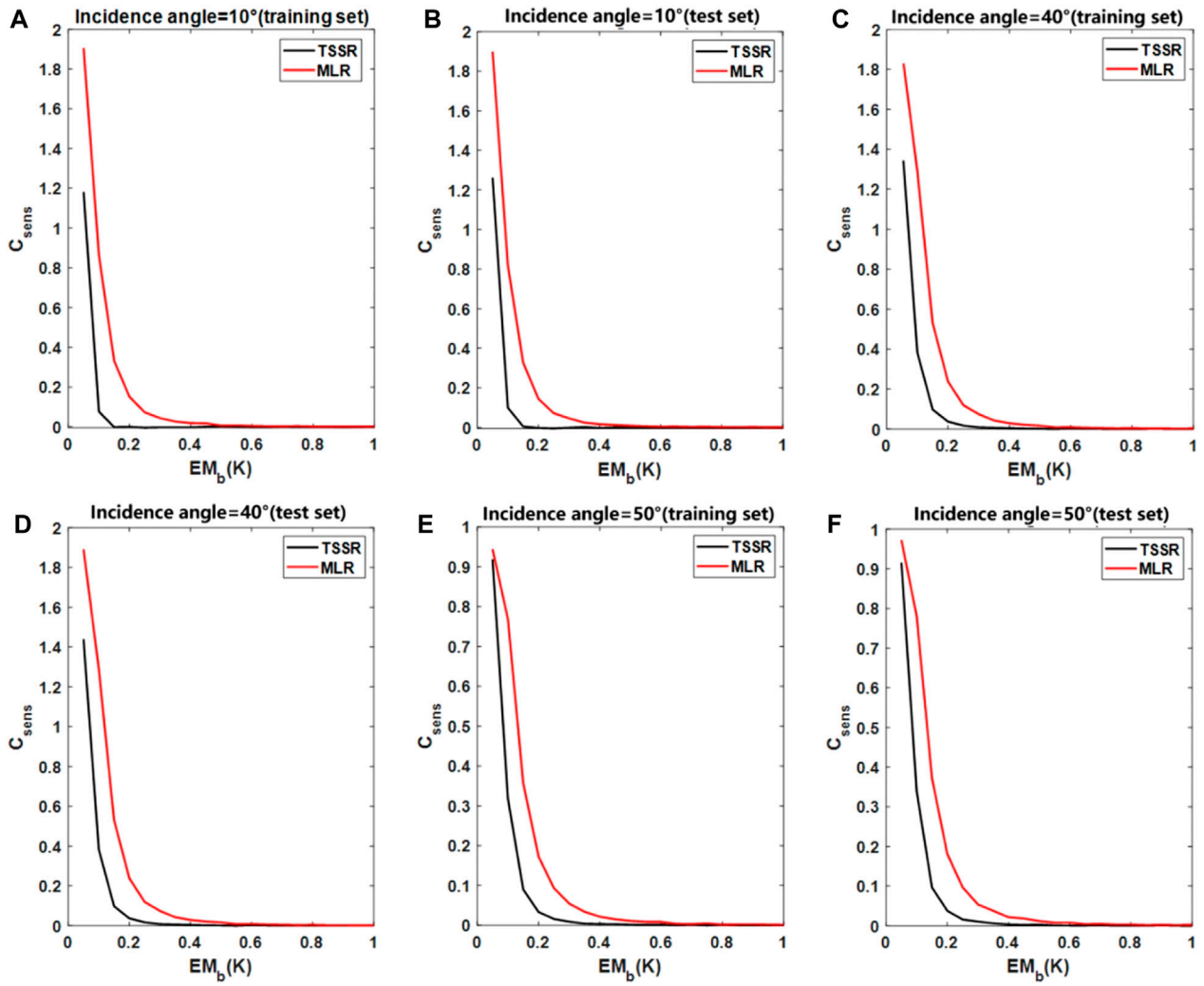

FIGURE 7
Relationship between C_{sens} and EM_b for different antenna angles. **(A,B)** the incidence is 10°, **(C,D)** the incidence is 40°, **(E,F)** the incidence is 60°.

4 Conclusion

MLR requires minimal computation capacity, which makes it a good option for an on-board retrieval algorithm. In this study, an SST retrieval algorithm (TSSR) was proposed to evaluate the SST retrieval error for 1D-MSAMR based on MLR. We investigated the relationship between retrieval errors and brightness temperature measurement errors (EM_b) of the 1D-MSAMR within the incidence angle range of 0–65°. Sensitivity of the SST retrieval algorithms to the 6.9 GHz frequency (C_{sens}) was also assessed. TSSR has higher retrieval accuracy than the MLR algorithm, especially at low incidence angle. The average retrieval accuracy of the TSSR was about 0.3 K higher than that of the MLR algorithm. Moreover, the two-step algorithm had less sensitivity to EM_b of the 6.9 GHz frequency. In summary, TSSR can be used as an on-board retrieval algorithm for 1D-MSAMR. In the design of 1D-MSAMR, the incidence angles should be in as large a range as possible, and the system errors should be reduced as much as possible.

Data availability statement

The original contributions presented in the study are included in the article/Supplementary Material; further inquiries can be directed to the corresponding author.

Author contributions

Conceptualization, CG and WA; methodology, CG and WA; software, SH and MF; validation, JQ, WA, and SH; formal analysis, JQ and WA; investigation, JQ and WA; resources, SH;

data curation, JQ and WA; writing—original draft preparation, JQ and WA; writing—review and editing, JQ and WA; visualization, JQ and WA; supervision, ML; project administration, JQ and WA.

Acknowledgments

We would like to express our gratitude to Professor Frank J. Wentz for his great help in our research. We are thankful for the support from the National Natural Science Foundation of China (41605016). We would like to express our gratitude to Edit Springs (https://www.editsprings.com/) for the expert linguistic services provided. We acknowledge WindSat in Remote Sensing Systems (RSS) for providing the data. The data, including the RSS WindSat Data Products, can be obtained online (http://www.remss.com/missions/windsat/).

Conflict of interest

The authors declare that the research was conducted in the absence of any commercial or financial relationships that could be construed as a potential conflict of interest.

Publisher's note

All claims expressed in this article are solely those of the authors and do not necessarily represent those of their affiliated organizations, or those of the publisher, the editors, and the reviewers. Any product that may be evaluated in this article, or claim that may be made by its manufacturer, is not guaranteed or endorsed by the publisher.

References

Ai, W., Feng, M., Chen, G., and Lu, W. (2020). Research on sea surface temperature retrieval by the one-dimensional synthetic aperture microwave radiometer, 1D-SAMR. *Acta Oceanol. Sin.* 39 (5), 115–122. doi:10.1007/s13131-020-1540-1

Bobylev, L. P., Leonid, E., ZabolotskikhElizaveta, V., Mitnikand Leonid, M. (2010). Atmospheric water vapor and cloud liquid water retrieval over the arctic ocean using satellite passive microwave sensing. *IEEE Trans. Geosci. Remote Sens.* 48, 283–294. doi:10.1109/TGRS.2009.2028018

Bettenhausen, M. H., Smith, C.K., Bevilacqua, R. M., Wang, N. Y., Gaiser, P. W., and Cox, S.(2006). A nonlinear optimization algorithm for WindSat wind-vector retrievals. *IEEE Trans. Geosci. Remote Sens.* 44(3), 597–610. doi:10.1109/tgrs.2005.862504

Brown, J., Simmonds, I., and Noone, D.(2006). Modeling delta O-18 in tropical precipitation and the surface ocean for present-day climate. *Journal of Geophysical Research-Atmospheres*. 111(D5). doi:10.1029/2004jd005611

Chelton, D. B., and Wentz, F. J. (2005). Global microwave satellite observations of sea surface temperature for numerical weather prediction and climate research. *Bull. Am. Meteorol. Soc.* 86 (8), 1097–1116. doi:10.1175/BAMS-86-8-1097

Corbella, I., Duffo, N., Vall-llossera, M., Camps, A., and Torres, F. (2004). The visibility function in interferometric aperture synthesis radiometry. *IEEE Trans. Geosci. Remote Sens.* 42 (8), 1677–1682. doi:10.1109/TGRS.2004.830641

Feng, M., Ai, W., Chen, G., Lu, W., and Ma, S. (2022). A multiple linear regression algorithm for sea surface temperature retrieval by one-dimensional synthetic aperture microwave radiometry. *J. Atmos. Ocean. Technol.* 37 (9), 1753–1761. doi:10.1175/JTECH-D-20-0003.1

Feng, M., Ai, W., Lu, W., Shan, C., Ma, S., and Chen, G. (2021). Sea surface temperature retrieval based on simulated microwave polarimetric measurements of a one-dimensional synthetic aperture microwave radiometer. *Acta Oceanol. Sin.* 40 (3), 122–133. doi:10.1007/s13131-021-1712-7

Goodberlet, M. A., Swift, C. T., and Wilkerson, J. C. (1990). Ocean surface wind speed measurements of the Special Sensor Microwave/Imager (SSM/I). *IEEE Trans. Geosci. Remote Sens.* 28 (5), 823–828. doi:10.1109/36.58969

Jin, R., Li, Q., and Liu, H. (2019). A subspace algorithm to mitigate energy unknown RFI for synthetic aperture interferometric radiometer. *IEEE Trans. Geosci. Remote Sens.* 58 (99), 227–237. doi:10.1109/TGRS.2019.2936005

Jordi, F., Camps, A., Andres, B., Martin-Neira, M., Boutin, J., Reul, N., et al. (2010). Smos: The challenging sea surface salinity measurement from space. *Proc. IEEE* 98 (5), 649–665. doi:10.1109/JPROC.2009.2033096

Koner, P. K., and Harris, A.(2015). " A deterministic inversion technique for sea surface temperature retrieval from MODIS radiances," in Conference on Ocean Sensing and Monitoring VII. doi:10.1117/12.2179868

Krasnopolsky, V. M., Gemmill, W. H., and Breaker, L. C.(2000). A neural network multiparameter algorithm for SSM/I ocean retrievals: Comparisons and validations. *Remote Sens. Environ.* 73 (2), 133–142. doi:10.1016/s0034-4257(00)00088-2

Lambrigtsen, B., Brown, S., Gaier, T., Kangaslahti, P., Tanner, A., and Wilson, W. (2006). "GeoSTAR : Developing a new payload for GOES satellites," in Aerospace Conference (IEEE).Big Sky, MT, March October 04–11, 2006

Le, V., and David, M. (1990). The sensitivity of synthetic aperture radiometers for remote sensing applications from space. *Radio Sci.* 25 (4), 441–453. doi:10.1029/rs025i004p00441

Le, V., Griffis, A., J., Swift, C., T., and Jackson, T. (1994). Estar: A synthetic aperture microwave radiometer for remote sensing applications. *Proc. IEEE* 82 (12), 1787–1801. doi:10.1109/5.338071

Li, Q., Ke, C., Wei, G., Liang, L., and Chen, L. (2008). "An aperture synthesis radiometer at millimeter wave band," in International Conference on Microwave & Millimeter Wave Technology, Nanjing, 21-24 April 2008.

Lise, K., Catherine, P., Filipe, A., Boutin, J., Heygster, G., Tonboe, R. T., et al. (2018). Expected performances of the copernicus imaging microwave radiometer (CIMR) for an all-weather and high spatial resolution estimation of ocean and sea ice parameters. *J. Geophys. Res. Oceans* 123 (110), 7564–7580. doi:10.1029/2018JC014408

Meissner, T., and Wentz, F. J. (2012). The emissivity of the ocean surface between 6 and 90 GHz over a large range of wind speeds and earth incidence angles. *IEEE Trans. Geosci. Remote Sens.* 50 (8), 3004–3026. doi:10.1109/TGRS.2011.2179662

Obligis, E., Labroue, S., Amar, A., Thiria, S., Crepon, M., and Mejia, C.(2005). RETRIEVING THE OCEAN SALINITY FROM SMOS OBSERVATIONS BY THE USE OF NEURAL NETWORKS.

Prigent, C., Aires, F., Bernardo, F., Orlhac, J. C., Goutoule, J. M., Roquet, H., et al. (2013). Analysis of the potential and limitations of microwave radiometry for the retrieval of sea surface temperature: Definition of MICROWAT, a new mission concept. *J. Geophys. Res. Oceans* 118 (6), 3074–3086. doi:10.1002/jgrc.20222

Ruf, C. S., Swift, C. T., Tanner, A. B., and Le Vine, D. M. (1988). Interferometric synthetic aperture microwave radiometry for the remote sensing of the Earth. *IEEE Trans. Geosci. Remote Sens.* 26 (5), 597–611. doi:10.1109/36.7685

RYLE (1962). The new cambridge radio telescope. *Nature* 194 (4828), 517–518. doi:10.1038/194517a0

Schanda, E. (1979). "Multiple wavelength aperture synthesis for passive sensing of the Earth's surface," in Antennas & Propagation Society International Symposium, Seattle, WA, USA, 18-22 June 1979, 597–611.

Ulaby, B., Moore, R. K., and Fung, A. K. (1981). Microwave remote sensing: Active and passive. Volume 1 - Microwave remote sensing fundamentals and radiometry.

Vine, D., Griffis, A., Swift, C. T., and Jackson, T. J. (1992). "Estar: A synthetic aperture microwave radiometer for measuring soil moisture," in International Geoscience & Remote Sensing Symposium. Houston, TX, May 26–29, 1992

Vine, D., Haken, M., and Swift, C. T. (2004). "Development of the synthetic aperture radiometer ESTAR and the next generation," in Geoscience and Remote Sensing Symposium, 2004. IGARSS '04. Proceedings (IEEE). Anchorage, AK, September 20–24, 2004

Vine, D. (2000). Synthetic aperture radiometer systems. *IEEE Trans. Microw. Theory Tech.* 47 (12), 2228–2236. doi:10.1109/22.808964

Wentz, F. J. (2000). Algorithm theoretical basis document (ATBD) AMSR ocean algorithm. EOS Project, Goddard Space Flight Center, National Aeronautics and Space Administration.

Wentz, F. J., and Meissner, T. (2007). Supplement 1: Algorithm theoretical basis document for AMSR-E ocean algorithms. Santa Rosa, CA: NASA.

Zine, S., Boutin, J., Font, J., Reul, N., Waldteufel, P., Gabarro, C., et al. (2008). Overview of the SMOS sea surface salinity prototype processor. *IEEE Trans. Geosci. Remote Sens.* 46 (3), 621–645. doi:10.1109/tgrs.2008.915543

frontiers | Frontiers in Earth Science

TYPE Original Research
PUBLISHED 03 January 2023
DOI 10.3389/feart.2022.1079369

OPEN ACCESS

EDITED BY
Feifei Shen,
Nanjing University of Information Science and Technology, China

REVIEWED BY
Xiaogang Huang,
National University of Defense Technology, China
Peng Chen,
Jiangsu Provincial Meteorological Bureau, China

*CORRESPONDENCE
Xin-Min Wang,
995378392@qq.com

SPECIALTY SECTION
This article was submitted to Environmental Informatics and Remote Sensing, a section of the journal Frontiers in Earth Science

RECEIVED 25 October 2022
ACCEPTED 05 December 2022
PUBLISHED 03 January 2023

CITATION
Li H, Xi L and Wang X-M (2023), A high-resolution numerical simulation of the "7.19" extraordinary heavy rainfall in Henan Province under topographic effect.
Front. Earth Sci. 10:1079369.
doi: 10.3389/feart.2022.1079369

A high-resolution numerical simulation of the "7.19" extraordinary heavy rainfall in Henan Province under topographic effect

Han Li[1,2], Le Xi[1,2] and Xin-Min Wang[3,4]*

[1]Key Laboratory of Agrometeorological Safeguard Application Technique, China Meteorological Administration, Zhengzhou, China, [2]Henan Provincial Meteorological Observatory, Zhengzhou, China, [3]Xiamen Key Laboratory of Straits Meteorology, Xiamen, China, [4]Xiamen Meteorological Observatory, Xiamen, China

Introduction: In this study, based on the ERA5 dataset, the orographic precipitation characteristics during an extraordinary heavy rainfall event in Henan Province on 19 July 2016 are analyzed.

Methods: In addition, by using the WRF model and the NCEP GDAS/FNL dataset, a high-resolution numerical simulation is carried out, including a series of sensitivity experiments on the Taihang Mountains, Yunmeng Mountain, and low-altitude areas.

Results and Discussion: The distribution of observed precipitation shows that the precipitation over the Taihang Mountains in northern Henan during the daytime on July 19 is significantly enhanced due to the topographic effect compared with that over the plain on the east. The simulation results demonstrate that the distribution of simulated precipitation over the steep terrains on the east side of the Taihang Mountains is closer to the observational precipitation when SRTM-90m is introduced to the WRF model. When the altitude of the Taihang Mountains is lowered by 50%, the accumulated precipitation along the Taihang Mountains in the daytime on July 19 decreases by 26%, accompanied by the northward movement of the heavy precipitation center over the northern Taihang Mountains. In addition, Yunmeng Mountain plays an important role in blocking or diverting the easterly and southeasterly low-level jet. When the terrain elevation of Yunmeng Mountain is reduced, the convergence zone of the wind field in the low level moves to the areas along the Taihang Mountains, which leads to the expansion of the area with heavy rainfall, with the average accumulated precipitation in mountain areas increasing by 7%. In addition, when the low altitude terrain in the study region is reduced by 50%, the center of heavy precipitation obviously moves westward. Combined with the diagnostic analysis of the topographically forced vertical velocity, the results show that the uplift of the low-level jet caused by the low-altitude terrain in northern Henan is one of the reasons that affect the location of the heavy rainfall center.

KEYWORDS

extraordinary heavy rainfall, topographic effect, numerical simulation, evolution mechanisms, low-level jet

1 Introduction

China is a country with complex terrains and diverse climates. On the whole, the terrain is high in the west and low in the east, and the mountain has a great influence on the weather and climate. Among them, topographic precipitation has always been the focus and difficulty in meteorological scientific research studies and forecasts.

Previous studies have revealed that topography plays a key role in precipitation formation, and the influences of different topographies on precipitation show different characteristics. The main influential mechanisms include dynamic forcings (uplift and convergence), thermal effects (heating on the underlying surface and latent heat release), and cloud microphysical processes influenced by topography (Liao et al., 2007; Houze, 2012; Huang et al., 2020). Moreover, the complex terrain is one of the crucial factors causing local extraordinary heavy rainfall. The intensity and distribution of the topographically forced precipitation vary under different environmental conditions (Ding, 2015; Wang et al., 2018). So far, there have been many significant achievements in deciphering the specific role of the terrain in affecting the precipitation. Based on a statistical analysis of the precipitation characteristics during 53 typhoon incidents affecting Taiwan during 1993–2013, Wu et al. (2015) pointed out that the hourly mean precipitation at the elevation of 500 m above is higher than that at the elevation of 500 m below. For a topographic precipitation process caused by Typhoon Morakot in 2013, Yu et al. (2013) proposed that the topographic effect in northern Taiwan is stronger than that in southern Taiwan on the enhancement of precipitation.

Moreover, the intensity of the topographic effect is related to the background precipitation and the mountainward wind speed caused by large-scale weather systems. Taking a low-pressure system as an example, the southwest warm and humid airflow on the front side and the northeast cold and dry airflow on the back side have different thermal properties and wind directions, resulting in heavy precipitation of different intensities and distributions when encountering mountain areas (Tsai et al., 2018). Meanwhile, forced topographic uplift and vertical wind shear caused by the terrain also can lead to the enhancement of thunderstorm downhill (Wang et al., 2017). Based on the relationship between the characteristics of hourly precipitation and the altitude in the Sichuan Basin, Zhou et al. (2019) indicates that the significant growth areas of precipitation and heavy rainfall days are mainly concentrated in the altitudes of 200–1,200 m. The diurnal changes in the mountain–valley wind can also cause increased night rain on the one side and frequent afternoon heavy rainfall on the other side of the mountain (Zhang et al., 2020). Therefore, the influences of different mountains, altitudes, and slopes on precipitation are different, and the influential mechanisms of different terrains on weather systems and associated precipitation are complex.

Due to the sparse distribution of observation stations and the poor representativeness of the data with low spatio-temporal resolution in mountainous regions with complex terrain, it is difficult to distinguish the effect of small- and medium-scale terrain on precipitation by conventional observations. Hence, many scholars have carried out analyses and research studies on the influence mechanisms of different terrains on precipitation through numerical simulation experiments (Chao et al., 2018; He et al., 2013; He et al., 2015; Wang et al., 2018). The research on multi-source observation data assimilation technology under complex terrain is also helpful to deeply understand the evolution mechanism of topographic precipitation (Shen et al., 2020; Zhong, 2020; Shen et al., 2021). Pontoppidan et al. (2017) conducted a series of simulation experiments with different resolutions on a heavy rainfall event in western Norway in October 2014. It is found that there is no significant improvement for the precipitation simulation by WRF with a finer resolution from 3 km to 1 km, and a reasonable resolution for the model should be related to the complexity of the terrain in the model domain. Milrad et al. (2017) designed a topographic sensitivity experiment for a heavy rainfall case in Alberta, western Canada, based on the WRF model. The results show that the intensity and location of the heavy rainfall center will change obviously when the terrain-smoothing exceeds 25%. Therefore, the numerical simulation is helpful to deeply analyze and effectively understand the critical role of different complex terrains in the evolution of local precipitation.

A regional rainstorm process occurred in North China from 18 to 21 July 2016, which has been widely studied, and meaningful results have been achieved (Lei et al., 2017; Yi et al., 2018; Zhao et al., 2018; Han et al., 2018; Jing et al., 2019). These research studies show that this rainstorm case is mainly affected by the vortex and the surface cyclone system. In particular, because the extraordinary heavy rainfall area is located on the complex terrain along the Taihang Mountains, the precipitation enhancement due to the topographic effect is significant. However, it is still necessary to research further and conduct a detailed study on the specific effect of multi-scale topographies on this rainstorm process, especially the internal relationship between terrain features and precipitation distribution, intensity and evolution, and the mechanism of terrain triggering the precipitation as well. Therefore, in this study, the WRF model is used to carry out high-resolution simulation experiments, and the topographically-forced vertical motion is also diagnostically analyzed. In addition, the characteristics and mechanisms for the influence of the large-

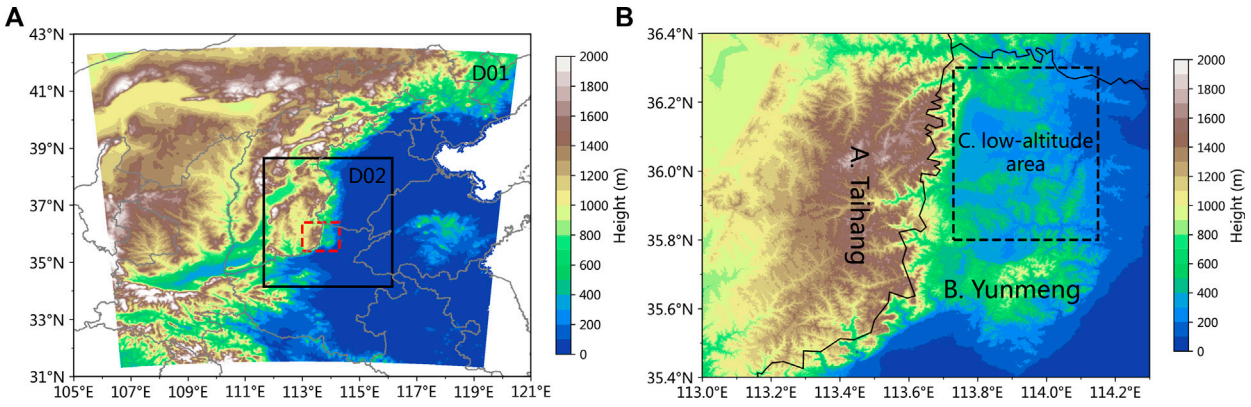

FIGURE 1
Coverage of model domains is denoted by D1 and D2, and the area within the red dotted box indicates the study area in Figure 1B **(A)**. Topographic features of the study area **(B)**.

scale terrain around the northern part of Henan Province and the local complex topography on the precipitation during the "7.19" process are focused on, aiming to enhance the recognition of the abnormal precipitation in mountainous areas of northern Henan Province and provide a necessary basis for the forecasts of precipitation hazards in mountainous areas.

2 Data and methods

2.1 Data

In this study, the data used for the analysis and diagnosis include the CMA multisource precipitation analysis system (CMPA-Hourly V2.0) dataset, which merges the observational data from automatic meteorological stations of the China Meteorological Administration and the precipitation data retrieved from satellite images from the National Oceanic and Atmospheric Administration (NOAA) adopting the Climate Prediction Center morphing technique (CMORPH) with a horizontal resolution of 0.05 × 0.05 (Yang et al., 2019); the fifth-generation reanalysis dataset from the European Centre for Medium-Range Weather Forecasts (ERA5) dataset; the National Centers for Environment Prediction final reanalysis data from the Global Data Assimilation System (NCEP GDAS/FNL), which are used as the background fields for the model, with a horizontal resolution of 0.25 × 0.25 and temporal resolution of 6 h (http://rda.ucar.edu/datasets/ds083.3); and the digital elevation model (DEM) data from the Shuttle Radar Topography Mission (SRTM, with a resolution of 90 m), which provides high-resolution terrain data for comparative experiments by high-resolution numerical simulation.

2.2 Design of numerical simulation schemes

The mesoscale model WRF V3.9.1 adopts the non-static equilibrium dynamic framework for double-nested simulations. The center point of the coarse grids is at 113°E, 37°N, and the horizontal grid intervals are 3 km for domain 1 (D01) and 1 km for domain 2 (D02), with the grid numbers for calculation being 401 × 401 and 451 × 451, respectively (Figure 1A). The vertical resolution is 50 layers, with the model top at 50 hPa. The time-step sizes of integration are 18 s for D01 and 6 s for D02, and the integration time for simulation is 36 h from 1200 UTC on 18 July 2016 to 0000 UTC on 20 July 2016. The physical schemes used in the model include the Morrison 2-mom scheme for microphysical processes (Morrison et al., 2009), the Mellor–Yamada–Janjic scheme (MYJ) for planetary boundary layer processes (Janjić, 1994), the rapid radiative transfer model (RRTM) (Mlawer et al., 1997) and the Dudhia schemes for longwave and shortwave radiation options (Dudhia, 1989), the MYJ Monin–Obukhov scheme for near-surface layer processes (Janjić, 1994), and the Noah land surface scheme (Tewari et al., 2004).

2.3 Design of comparative experiments

In this study, the terrains in the study area are mainly divided into three categories (Figure 1B). The first category is the Taihang Mountains, with a north–south orientation. The altitude of the main body of the Taihang Mountains exceeds 1,500 m, with shape slopes on its east and south sides, which mainly causes the topographically forced uplift and blocking-induced convergence of the low-level jet. The second category is

TABLE 1 Experimental schemes for terrains with different resolutions.

Name	Experimental scheme
Ctrl	Original terrain of WRF
Highres	Shuttle Radar Topography Mission (SRTM, with a resolution of 90 m)

TABLE 2 Schemes for sensitivity experiments with different terrain heights.

Name	Experimental scheme
Test1	Replace the area where the terrain height of SRTM-90 m is greater than 500 m within the range of 35.4°N~36.4°N and 113°E~113.8°E by 50%
Test2	Reduce the area where the terrain height of SRTM-90 m is greater than 200 m within the range of 35.4°N~35.8°N and 113.7°E~114.3°E by 50%
Test3	Reduce the area where the terrain height of SRTM-90 m is greater than 200 m within the range of 35.8°N~36.3°N and 113.8°E~114.3°E by 50%
Test4	Increase the area where the terrain height of SRTM-90 m is greater than 200 m within the range of 35.8°N~36.3°N and 113.8°E~114.3°E by 50%

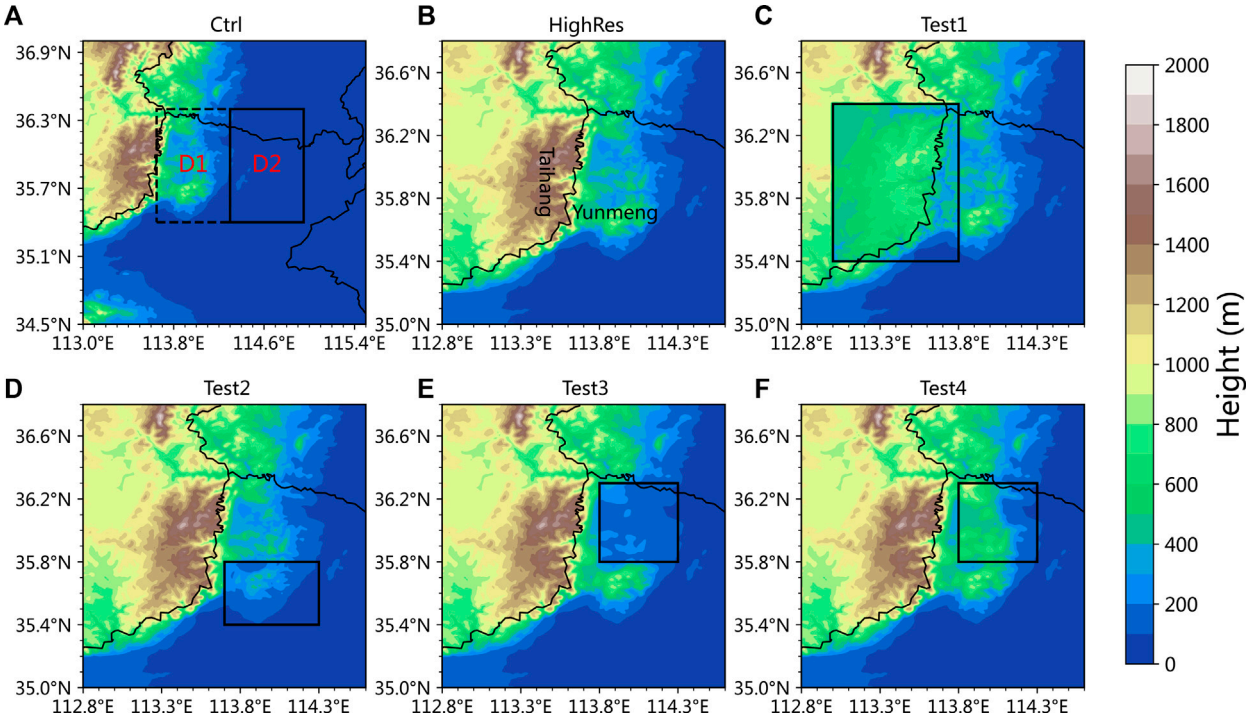

FIGURE 2
Terrains of the control experiment **(A)** and comparative experiment HighRes **(B)**, Test1 **(C)**, Test2 **(D)**, Test3 **(E)**, Test4 **(F)**. The area within the box indicates the terrain modification region or study region.

Yunmeng Mountain with relatively isolated and bell-shaped terrains, which is located to the south of the Taihang Mountains. The highest altitude is close to 1,000 m. The topographic gradient on its north side is relatively large, while the slope on its south side is relatively gentle. In addition to the topographically forced uplift, this terrain feature also causes the flow around the low-level jet. The third category is the region with complex terrain at low altitudes, which are shown in the dotted box in Figure 1B. The overall altitude is between 300 and 800 m, but the terrain surface fluctuates greatly, and the influential mechanism on the precipitation is complex in this region.

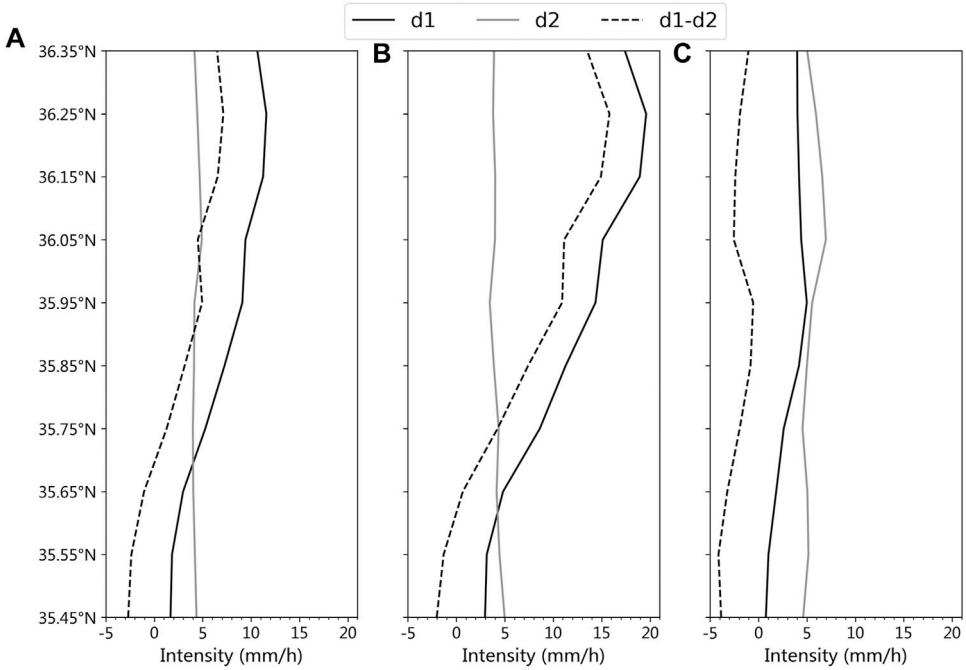

FIGURE 3
Hourly mean precipitation intensity in areas D1 and D2 indicated in Figure 2A and the difference between the two areas from **(A)** 0000 UTC on July 19 to 0000 UTC on July 20, **(B)** 0000 UTC on July 19 to 1200 UTC on July 19, and **(C)** 1200 UTC on July 19 to 0000 UTC on July 20.

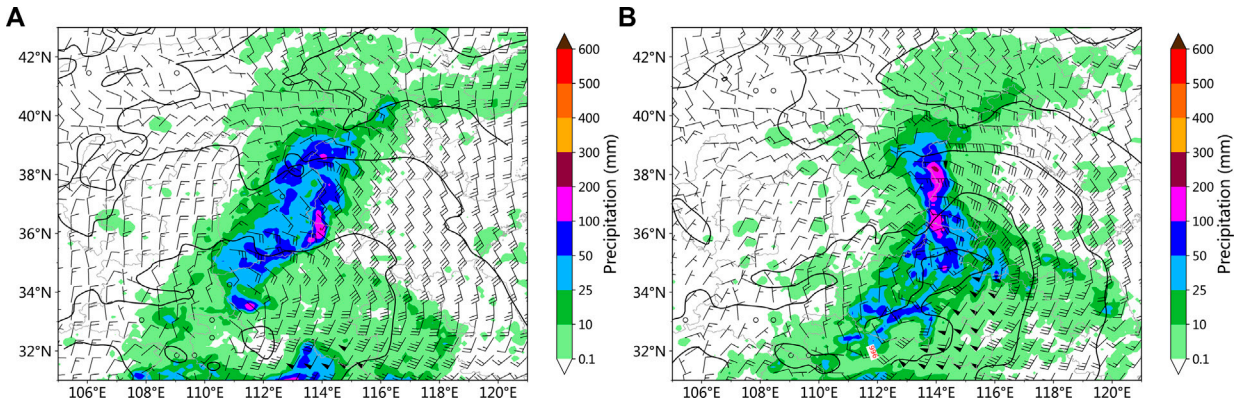

FIGURE 4
Wind field at 850 hPa and sea-level pressure (contour line) at 0000 UTC **(A)** and 0600 UTC **(B)** on 19 July 2016. Precipitation from 0000 UTC to 0600 UTC **(A)** and 0600 to 1200 UTC **(B)** on 19 July 2016. The wind field and sea-level pressure data are obtained from the ERA5 dataset.

In order to study the influences of the terrain data with different resolutions on numerical simulation results of the "7.19" precipitation process, first, the simulation results with the original terrain and SRTM-90 m terrain, respectively, adopted in the WRF model are compared and analyzed. The specific design schemes are shown in Table 1.

In order to study the influential mechanisms of the Taihang Mountains, Yunmeng Mountain, and the low-altitude region with complex terrain in the study area on this precipitation process, four groups of sensitivity experiments with different terrain heights are designed, and the specific schemes are shown in Table 2.

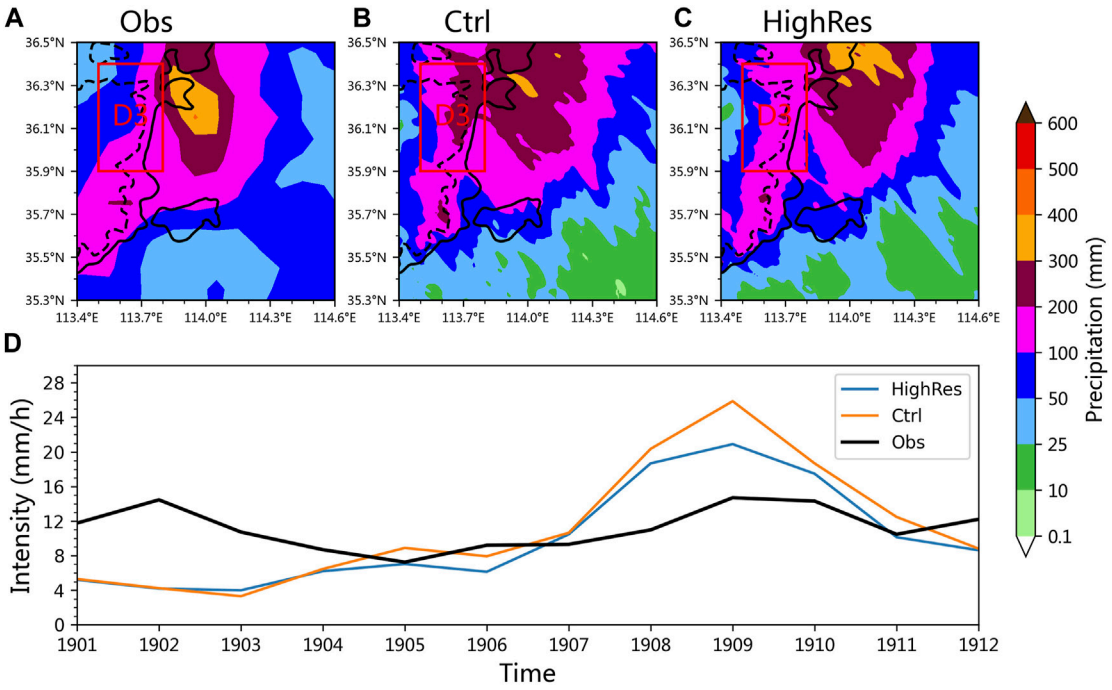

FIGURE 5
(A) Observational precipitation and simulated precipitation in **(B)** *Ctrl* and **(C)** *HighRes* experiments from 0000 to 1200 UTC on 19 July 2016. The black solid line denotes the 500 m contour line, and the black dotted line denotes the 1000 m contour line. **(D)** Time series of area-averaged hourly precipitation intensity in the area D1 from 0000 UTC on 19 July 2016 to 0000 UTC on 20 July 2016.

The terrains for the schemes of the aforementioned comparative experiments are shown in Figure 2.

3 Characteristics of observational topographic precipitation

The zonally averaged hourly mean rainfall intensity in areas D1 and D2 is shown in Figure 3. It can be seen that during the period from 0000 UTC on July 19 to 1200 UTC on July 19, the hourly mean rainfall intensity in the area D1 is significantly larger than that in the area D2, indicating that the topographic effect on the enhancement of precipitation in this case mainly occurs in the daytime on July 19. Similar results can also be found in the zonally averaged hourly rainfall intensity and 850-hPa wind field in areas D1 and D2. The heavy rainfall in the area D1 mainly occurs before 1200 UTC on July 19 and is significantly stronger than that in the area D2. In addition, the evolution of the 850-hPa wind field shows that there is a continuous easterly jet stream at the lower level in the study area (Figure 4). The sea-level pressure also indicates the development of a ground cyclone, which also represents an increase in ground wind speed. There was also evidence of topographic precipitation characteristics derived from the spatial distribution of observed rainfall, which further indicates that the terrain plays a key role in the enhancement of the precipitation during this stage.

4 Influence of the terrain resolution on precipitation simulation

The accumulated precipitation from 0000 to 1200 UTC on 19 July 2016 (Figures 5A–C) shows that the precipitation amount exceeding 100 mm appears in a wide region near the Taihang Mountains (marked as the area D3), while the precipitation amount over 200 mm mainly appears below the altitude of 500 m on the east side of the Taihang Mountains. In the *Ctrl* simulation experiments, the region with the precipitation of more than 100 mm is close to the observation, but the center of the region with the precipitation over 200 mm extends westward along the Taihang Mountains. By adopting the SRTM-90 m DEM for the *HighRes* experiment, the simulation results show similar distribution characteristics to the observed precipitation; that is, heavy rainfall (above 200 mm) mainly occurs in the area below the altitude of 500 m. In addition, the precipitation intensity in the area D3 is closer to the observation. Compared with the time series of hourly precipitation intensity simulated by the WRF model (Figure 5E), the Ctrl and HighRes experiments all show the

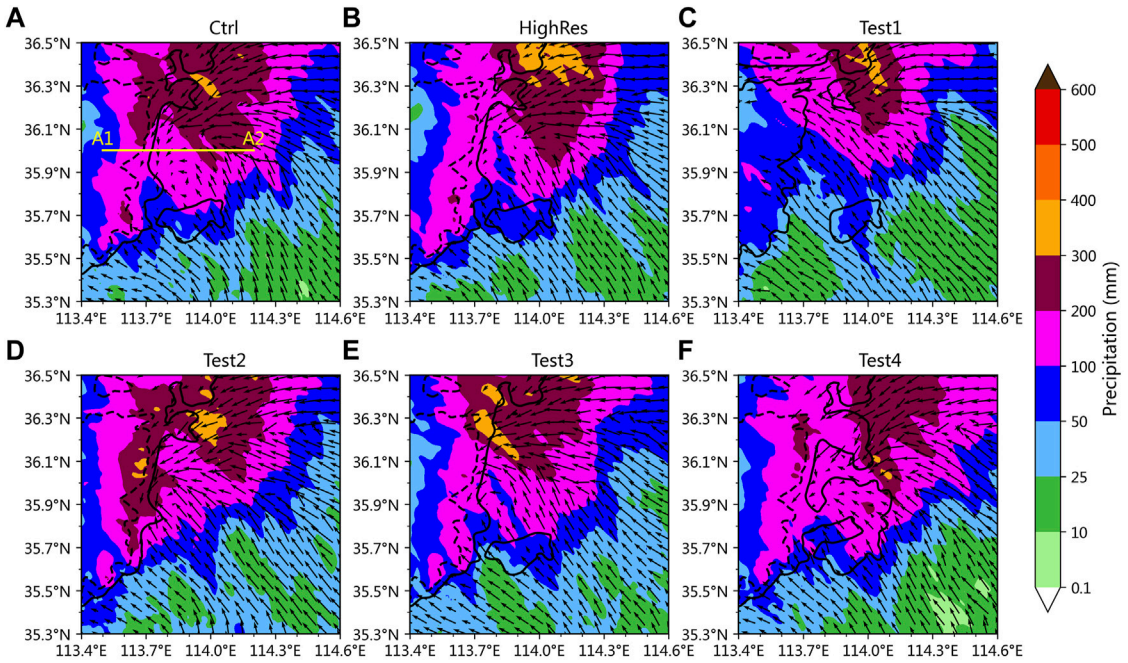

FIGURE 6
(A–F) Simulated precipitation by terrain sensitivity experiments from 0000 to 1200 UTC on 19 July 2016. The vector denotes the wind field at 925 hPa at 0900 UTC on 19 July 2016, simulated by each sensitivity experiment. The black solid line denotes the 500 m contour line, and the black dotted line denotes the 1000 m contour line.

characteristics of weak precipitation in the early daytime and strong precipitation in the late daytime on 19 July 2016. The comparison of the rainfall intensity during the period of heavy rainfall from 0700 to 1100 UTC on July 19 reveals that the simulation results from the HighRes experiment are closer to the observation. The aforementioned results indicate that by interpolating the SRTM-90 m terrain data to the grids with a resolution of 1 km, there is little difference between the interpolated terrain and the original terrain in the model. However, the model with the SRTM-90 m terrain data has a significant impact on the precipitation near the Taihang Mountains, and the distribution of the simulated precipitation is closer to the observation.

5 Influential mechanisms of the terrain on precipitation

Figure 2 shows that the terrains at high altitudes around the region with heavy rainfall, in this case, are the Taihang Mountains in the west and Yunmeng Mountain in the south. Yunmeng Mountain has an isolated and bell-shaped terrain with the highest altitude close to 1,000 m, while the highest altitude in the south of the Taihang Mountains is more than 1,500 m. In this study, four kinds of terrain sensitivity experiments are designed to study the influence of the terrains in northern Henan on this precipitation case. The schemes are shown in Table 2.

5.1 Influence of the topographic height of the Taihang Mountains on precipitation

Figure 6 shows the distribution of the accumulated precipitation from 0000 to 1200 UTC on 19 July 2016, simulated by each experiment. With the addition of SRTM-90 m terrain data, the simulated precipitation of *HighRes* in the D3 area reduced by 24% compared with that of *Ctrl*, which is much closer to the observation. The Taihang Mountains have a significant blocking effect on the easterly wind due to their high altitude. After the height of the Taihang Mountains is reduced by 50% (Figure 6C), the location and range of heavy precipitation ($\geq$ 100 mm) in the area D1 show no significant change compared with the *HighRes* experiment results, but the area-averaged accumulated precipitation decreases from 125.6 mm to 93.2 mm. Meanwhile, the precipitation at the border between the southern Taihang Mountains and Yunmeng Mountain significantly decreases, which corresponds to a reduction of 26% in the accumulated precipitation averaged in the area D3. According to the 925-hPa wind field at 0900 UTC on July 19, the wind field over the Taihang Mountains turns into a consistent

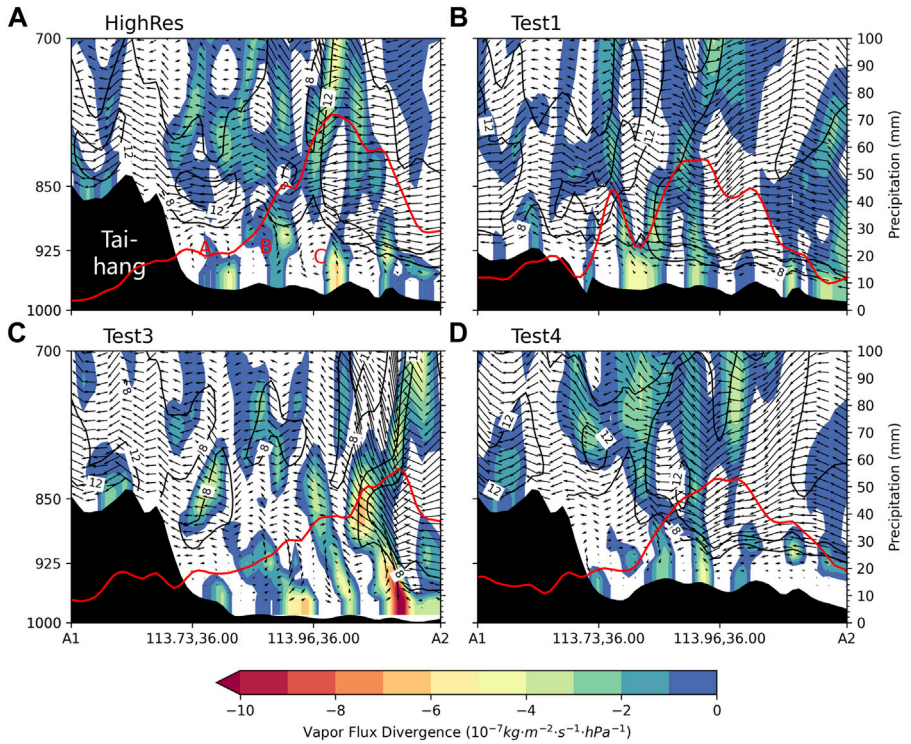

FIGURE 7
Vertical cross sections of the simulation experiment using the HighRes terrain **(A)**, Test1 **(B)**, Test3 **(C)** and Test4 **(D)** along the straight line between A1 and A2 (as shown in Figure 6A) at 0700 UTC on 19 July 2016. The red line indicates the hourly precipitation (0700–0800 UTC on 19 July 2016), and the wind vector is the combination of the U-wind component and the vertical velocity (W × 10). The black contour line indicates the U-wind speed exceeding 8 and 12 m/s. The shaded area indicates the vapor flux divergence (units: $10^{-7} \cdot kg \cdot m^{-2} \cdot s^{-1} \cdot hPa^{-1}$).

southeast wind without the blocking effect of the terrain. The precipitation produced only by the dynamic convergence of the environmental wind field is noticeably weaker than the observation. The comparison between the results of *Test1* (Figure 6C) and *Test3* (Figure 6E) reveals that the heavy rainfall area significantly shrinks northward or moves westward after removing the original topography of the heavy rainfall region.

According to the vertical cross sections along the straight line between A1 and A2 of the *HighRes*, the main precipitation area is located over the east side of the Taihang Mountains from 0700 UTC to 0800 UTC on July 19, rather than the region along the mountains (Figure 7A). The low-level wind field shows that due to the blocking effect of the Taihang Mountains, the mountainward airflow forms a vertical secondary circulation (as shown by A, B, and C in Figure 7A) at 925 hPa and below along the mountains, which blocks the westward movement of the low-level jet. When the terrain height of the Taihang Mountains is reduced by 50% (Figure 7B), the low-level vertical secondary circulation in front of the mountains disappears. Meanwhile, the low-level jet stream of 12 m/s moves down to 925 hPa, and the water vapor convergence center moves westward to the vicinity along the mountains, which leads to strong precipitation at the foot of the Taihang Mountains.

Under the background of extreme rainstorm weather circulation, even the low-altitude area still has a topographic uplift mechanism. By reducing the height of the low-altitude area (Figure 7C) in the *Test3* experiment, the precipitation intensity is weakened, and the water vapor convergence moves westward. The blocking effect of the Taihang Mountains is affected by the terrain height difference of the windward slope. In the *Test4* experiment (Figure 7D), the increase in the height of the low-altitude area leads to the weakening of vertical secondary circulation and the reduction of precipitation intensity. The aforementioned results show that the terrain features of high altitude of more than 1,000 m and steep slope for the Taihang Mountains have a significant blocking effect on the easterly or southeasterly wind, resulting in the variation of the convergence ascending region of the wind field in the lower layer. However, the precipitation intensity is also affected by the uplift mechanism of the low-altitude terrain on the east side of the Taihang Mountains.

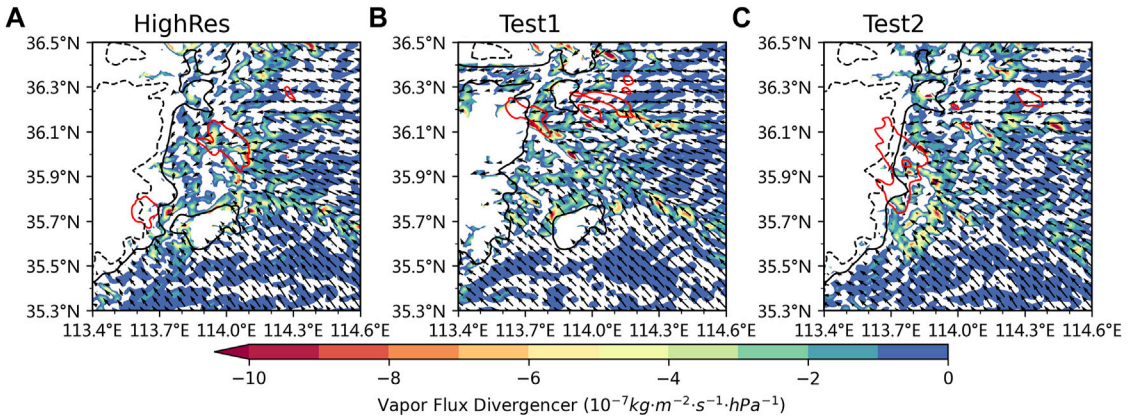

FIGURE 8
Simulated wind field at 925 hPa at 0800 UTC on July 19 and precipitation (red line) exceeding 50 mm/h (0800–0900 UTC on July 19) by HighRes terrain **(A)**, Test1 **(B)** and Test2 **(C)**. The black solid line denotes the 500 m contour line, and the black dotted line denotes the 1000 m contour line. The shaded area indicates the vapor flux divergence (units: $10^{-7} \cdot kg \cdot m^{-2} \cdot s^{-1} \cdot hPa^{-1}$).

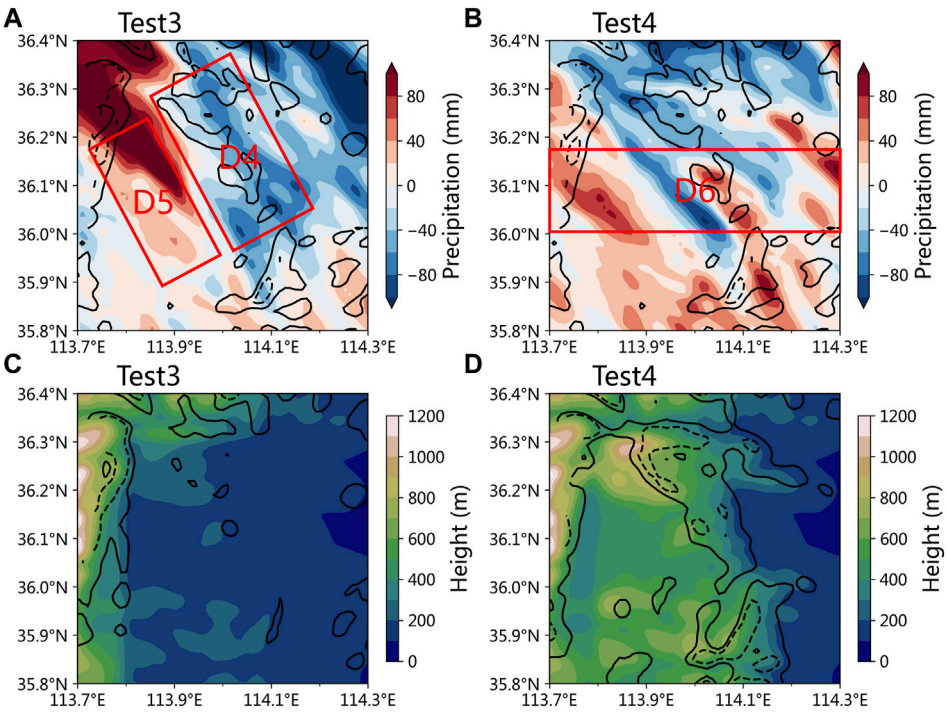

FIGURE 9
(A,B) Shaded regions indicate the difference in accumulated precipitation between the *Test3* or *Test4* experiment and the *HighRes* from 0000 UTC to 1200 UTC on July 19, 2016. The solid and dotted lines indicate the average vertical velocity forced by the terrain below 1,000 m in *HighRes* (contour; the interval is 0.1 m s^{-1} for the solid line and 0.3 m s^{-1} for the dashed line). **(C,D)** Shaded regions indicate the terrain height of the *Test3* and *Test4* experiments. The solid and dotted lines indicate the average vertical velocity forced by the terrain below 1,000 m in *Test3* and *Test4* experiments (contour; the interval is 0.1 m s^{-1} for the solid line and 0.3 m s^{-1} for the dashed line).

5.2 Influence of the bell-shaped terrain of Yunmeng Mountain on precipitation

When the terrain height of the Yunmeng Mountain is reduced by 50% while other terrains remain unchanged (Figure 6D), the region with precipitation over 200 mm extends southward along the Taihang Mountains, and the region with heavy rainfall on the north side of D1 becomes larger. The area-averaged accumulated precipitation of D1 increases by 7% compared with that in the *HighRes* experiment. The region with the most significant enhancement of precipitation is D3 located along the east side of the Taihang Mountains, with an average accumulated precipitation increasing by 64%. The results show that although the reduction of terrain height from Yunmeng Mountain makes the low-level jet more prone to move northward, it also leads to a decrease in precipitation intensity caused by topographic lifting or topographic turbulence convergence. From the 925-hPa wind field at 0900 UTC on 19 July 2016, it can be seen that the easterly or southeasterly in the lower layer is blocked or divided by Yunmeng Mountain. When the terrain height of Yunmeng Mountain is lowered, the convergence zone of the low-level wind field moves to the area along the Taihang Mountains, resulting in the westward movement of the heavy rainfall area.

Figure 8 shows the spatial distribution of the 925-hPa wind field, strong hourly precipitation, and water vapor convergence at 0800 UTC on July 19. In the *HighRes* experiment, the low-level southeast airflow is blocked and split by Yunmeng Mountain. Therefore, the low-level wind speed on the leeward slope of Yunmeng Mountain is weak, and the precipitation is mainly concentrated in the valley between Yunmeng Mountain and the Taihang Mountains. However, after reducing the terrain height of Yunmeng Mountain, the low-level southeast airflow continues to move to the Taihang Mountains (Figure 8C), and an area with the significant water vapor convergence center appears over the southeast side of the Taihang Mountains, resulting in an increase in precipitation. The aforementioned results show that the blocking effect of Yunmeng Mountain on the low-level jet causes the weakening of the low-level mountainward wind on the east side of the Taihang Mountains, thus leading to a decrease in precipitation intensity. The disturbed low-level jet produced by Yunmeng Mountain also affects the water vapor convergence, which leads to the change in the heavy rainfall center.

5.3 Influence of the dynamic uplift of complex terrain at low altitude on precipitation

In order to further analyze the dynamic effects of the complex terrain at low altitude on the precipitation in northern Henan during the "7.19" event, the variation in topographically forced vertical velocity is calculated. The variation in vertical velocity caused by the topographic lifting effect of the windward slope can be estimated by referring to previous studies (Sinclair, 1994; Yu et al., 2013; Cheng et al., 2019), and the formula is as follows:

$$W_{ter}(x,y,t) = \bar{u}(H,t)\frac{\partial H(x,y)}{\partial x} + \bar{v}(H,t)\frac{\partial H(x,y)}{\partial y}, \quad (1)$$

where H is the altitude of the terrain, $\bar{u}$ and $\bar{v}$ are the average zonal and meridional wind components below the altitude of H, respectively, and W_{ter} is the vertical velocity caused by the topographic uplift.

The contour lines in Figures 9A, B show the distribution of W_{ter} averaged from 0100 UTC to 1200 UTC on 19 July 2016 in the simulation experiment using the *HighRes* terrain. It can be seen that in addition to the dynamic effects of the Taihang Mountains and Yunmeng Mountain, the low-altitude terrain in the north of the area D1 is also an important factor causing noticeable changes in the vertical motion as well. Two large-value areas of orographic forced vertical velocity (W_{ter}) appear over the aforementioned regions. One is the uplift over the east side of the Taihang Mountains forced by the large-scale terrain of the Taihang Mountains, and the other is caused by the high altitude in D4. From the difference in the accumulated precipitation between the *HighRes* and *Test3* (Figure 9A) experiments, it can be seen that the accumulated precipitation decreases by 40–60 mm in the area D4 and increases by 40–80 mm in the area D5 from 0100 UTC to 1200 UTC on July 19, 2016, when the low-altitude terrain in the north of the area D1 is reduced by 50% and the terrains of the Taihang Mountains in the west and Yunmeng Mountain in the south remain unchanged (Figure 9C). The accumulated precipitation of the northern area in Figure 9B also reduced by about 60 mm, while the accumulated precipitation of the eastern area near 36.1°N increased due to the increase in orographic forced vertical velocity in *Test4* (Figure 9D).

When the low-altitude, complex terrain on the east side of the Taihang Mountains is reduced (Figure 10B), the original precipitation center during the two precipitation stages (0500 UTC and 0900 UTC on July 19) weakens and extends westward. From the variation in simulated vertical velocity before and after the modification of the terrains (Figures 10A, B), the large-value area with ascending motion in low altitude over the east side of the original terrain is mainly located to the east of 113.9°E, while the ascending motion center appears near 113.8°E in the *Test3* experiment. According to the changes in W_{ter}, around 0900 UTC on July 19, the wind in the lower layer of the area D6 gradually changes to the easterly airflow on the north side of the vortex, and the wind speed increases significantly. Correspondingly, there is also a significant topographically forced uplift area in the range of 114°E–114.1°E (filled by diagonal lines in Figure 10A). After increasing the height of the low-latitude area in *Test4*, the intensity and range of orographic forced vertical velocity enhanced (filled by

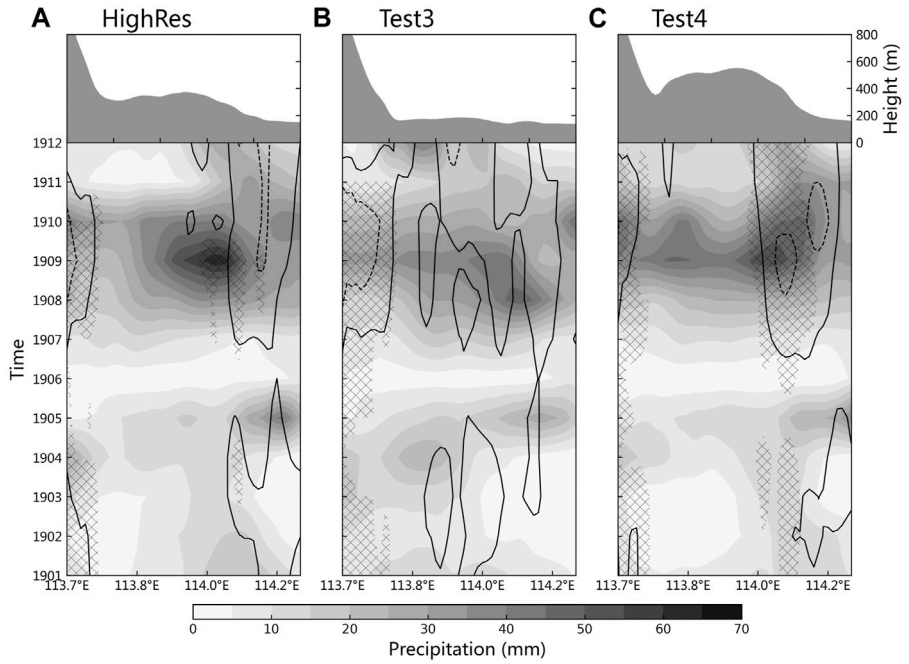

FIGURE 10
Meridionally averaged hourly precipitation, the average vertical velocity below the altitude of 1,000 m (contour; the interval is 0.1 m s^{-1} for the solid line and 0.3 m s^{-1} for the dashed line), the vertical velocity due to topographically forced uplift (shaded area filled by diagonal lines, unit: 0.1 m s^{-1}), and the meridionally averaged altitude in the area D6 from 0100 UTC to 1200 UTC on 19 July 2016 in the **(A)** *HighRes*, **(B)** *Test3*, and **(C)** *Test4* experiments.

diagonal lines in Figure 10C), resulting in the increase in precipitation of the east area. The aforementioned results indicate that, although the terrain height in the area D4 is low, it still has a great impact on the location of the heavy rainfall center due to orographic forcing uplift in this process.

6 Conclusion and discussion

In this study, based on the CMPA-Hourly V2.0 and ERA5 reanalysis datasets, the topographical precipitation characteristics during the "7.19" process are analyzed. In addition, the WRF V3.9.1 and NCEP GDAS/FNL reanalysis data are used for the high-resolution numerical simulations, and the SRTM-90 m terrain data are used to carry out high-resolution terrain simulation experiments. The influential mechanisms of different terrains on the precipitation in terrain sensitivity experiments by different schemes are compared. Finally, the vertical velocity forced by the terrain is diagnostically analyzed, and the influence of dynamic uplift forced by the complex terrain with low altitude on the precipitation is investigated. The main conclusions are as follows:

The observational precipitation characteristics show that under the condition of similar environmental dynamic fields (i.e., the wind field at 850 hPa), the precipitation over the mountainous area of northern Henan Province (area D1) is significantly stronger than that over the eastern plain (area D2) from 0000 UTC to 1200 UTC on July 19. The terrain of the northern mountain (area D1) plays an essential role in the precipitation increase during this heavy rainfall event.

he simulations by using terrain data with different resolutions show that there is little difference between the modified terrain and the original terrain of the model. However, by interpolating the SRTM-90 m terrain data to the grids with the resolution of 1 km, the refined terrain still has an obvious impact on the precipitation simulation results. The distribution characteristics of simulated precipitation are closer to the observations, while the lower-resolution terrain leads to the heavy precipitation area in D1 moving toward the region along the Taihang Mountains. Therefore, the refined terrain is beneficial to the model to effectively reproduce the distribution and evolution characteristics of local precipitation in the area with complex terrains.

The results of several terrain sensitivity experiments show that the terrain of the Taihang Mountains plays a crucial role in the precipitation along the mountains. After reducing the terrain by 50%, the accumulated precipitation along the mountains (area D3) during the daytime on July 19 decreases by 26%. However,

the terrain change in the Taihang Mountains has little effect on the precipitation over the northern part of the area D1. The precipitation in this region is mainly closely related to the complex terrains at a low altitude of about 500 m in the area D4. In addition, the low-level easterly jet uplifted by the local complex terrain at low altitudes also plays a key role in the variation in the intensity and distribution of heavy rainfall.

The southeasterly in the lower level is blocked or split by Yunmeng Mountain, which is not conducive to the movement of the low-level jet to the area along the Taihang Mountains and the westward movement of the heavy rainfall area. When the terrain height of Yunmeng Mountain is reduced by 50%, the low-level jet is prone to move to the area along the Taihang Mountains, resulting in a corresponding increase in the precipitation on the north side of Yunmeng Mountain and the east side of the Taihang Mountains, corresponding to the increases in the area-averaged accumulated precipitation in D1 by 7%.

The accumulated precipitation decreases by 40–60 mm in the area D4 and increases by 40–80 mm in the area D5 from 0100 to 1200 UTC on July 19 when the low-altitude terrain in the north of the area D1 is reduced by 50%, while the terrains of the Taihang Mountains in the west and Yunmeng Mountain in the south remain unchanged. Moreover, the heavy rainfall center significantly moves westward to the vicinity along the Taihang Mountains. The local terrain in the area D4 leads to remarkable changes in vertical movement, forming a local ascending motion region, which is one of the reasons for increasing the precipitation in this area and further affecting the location of the heavy precipitation center.

In this study, the WRF model is used to carry out the high-resolution terrain simulation experiments for the "7.19" extraordinary heavy rainfall process. The distribution characteristics of topographically forced vertical movement are analyzed, and the specific impact of complex terrain on the precipitation in northern Henan Province is studied. On this basis, some quantitative conclusions have been obtained, and the spatio-temporal variation characteristics of precipitation in different terrain sensitivity experiments have been analyzed. However, the aforementioned conclusions are only limited to the case of the "7.19" extraordinary heavy rainfall process, while the assessment and analysis for multiple cases have not been carried out yet. Therefore, it is necessary to systematically and quantitatively evaluate the precipitation changes caused by the topography-caused lifting, blocking, and convergence. In addition, it is also essential to further study the climatic characteristics for the influence of topography on the precipitation, the thermal effect of complex underlying surfaces related to topography, and the triggering and strengthening mechanisms of convective precipitation by topographic uplift.

Data availability statement

Publicly available datasets were analyzed in this study. These data can be found at: https://cds.climate.copernicus.eu/cdsapp#!/dataset/reanalysis-era5-pressure-levels?tab=overview.

Author contributions

HL: data analysis, visualization, and writing—original draft. XW: conceptualization, methodology, and investigation. LX: visualization and writing—review and editing.

Funding

This work was supported by China Meteorological Administration Innovation and Development Project (No. CXFZ2022J014), the 2020 National Supercomputing Zhengzhou Center Innovation Ecosystem Construction Technology Special Project (No. 201400210800), Joint Funds of Science and Technology Development of Henan Province (No. 222103810091), Key Project of Henan Meteorological Bureau (No. KZ202101).

Conflict of interest

The authors declare that the research was conducted in the absence of any commercial or financial relationships that could be construed as a potential conflict of interest.

Publisher's note

All claims expressed in this article are solely those of the authors and do not necessarily represent those of their affiliated organizations, or those of the publisher, the editors, and the reviewers. Any product that may be evaluated in this article, or claim that may be made by its manufacturer, is not guaranteed or endorsed by the publisher.

References

Chao, L., Cui, C., Jiang, X., Wang, X., Lai, A., and Wang, X. (2018). Mechanism analysis of the effect of special topography in middle-lower reaches of yangtze river on local severe precipitation in northeast hubei. *Meteor Mon.* 44 (09), 1117–1135.

Cheng, L. W., and Yu, C. K. (2019). Investigation of orographic precipitation over an isolated, three-dimensional complex topography with a dense gauge network, radar observations, and upslope model. *J. Atmos. Sci.* 76 (11), 3387–3409. doi:10.1175/jas-d-19-0005.1

Ding, Y. (2015). On the study of the unprecedented heavy rainfall in Henan Province during 4-8 August 1975: Review and assessment. *Acta Meteorol. Sin.* 73 (3), 411–424.

Dudhia, J. (1989). Numerical study of convection observed during the winter monsoon experiment using a mesoscale two-dimensional model. *J. Atmos. Sci.* 46 (20), 3077–3107. doi:10.1175/1520-0469(1989)046<3077:nsocod>2.0.co;2

Han, L., Wang, X., Zhang, X., Lv, L., and Xu, W. (2018). Analysis on extremity and characteristics of the 19 july 2016 severe torrential rainstorm in the north of henan Province. *Meteor Mon.* 44 (09), 1136–1147.

He, G., Peng, J., and Tu, N. (2015). Terrain construction and experiment for numerical model based on high resolution terrain data. *Plateau Meteor* 34 (4), 910–922. doi:10.7522/j.issn.1000-0534.2014.00022

He, G., Tu, N., and Zhang, L. (2013). Numerical experiment of terrain effect of vortex rainstorm process on east side of qinghai-xizang. *Plateau Meteor* 32 (06), 1546–1556. doi:10.7522/j.issn.1000-0534.2012.00150

Houze, R. A. (2012). Orographic effects on precipitating clouds. *Rev. Geophys.* 50 (1), RG1001. doi:10.1029/2011RG000365

Huang, X., Sun, J., and Liu, W. (2020). The interaction between low-level jet evolution and severe convective rainstorms under topographic effect. *Acta Meteorol. Sin.* 78 (4), 551–567.

Janjić, Z. I. (1994). The step-mountain eta coordinate model: Further developments of the convection, viscous sublayer, and turbulence closure schemes. *Mon. Wea. Rev.* 122 (5), 927–945. doi:10.1175/1520-0493(1994)122<0927:tsmecm>2.0.co;2

Jing, Z. Y., Zhou, Y., Shen, X., and Li, X. (2019). Evolution of dynamic and thermal structure and instability condition analysis of the extreme precipitation system in Beijing-Tianjin-Hebei on July 19 2016 [J]. *Chin. J. Atmos. Sci. (in Chinese)* 43 (4), 930–942. doi:10.3878/j.issn.1006-9895.1812.18231

Lei, L., Sun, J., He, N., Liu, Z., and Zeng, J. (2017). A study on the mechanism for the vortex system evolution and develop-ment during the torrential rain event in North China on 20 July 2016. *Acta Meteorologica Sinica* 75 (5), 685–699.

Liao, F., Hong, Y., and Zheng, G. (2007). Review of orographic influences on surface precipitation. *Meteor Sci Technol* 35 (03), 309–316.

Milrad, S. M., Lombardo, K., Atallah, E. H., and Gyakum, J. R. (2017). Numerical simulations of the 2013 Alberta flood: Dynamics, thermodynamics, and the role of orography. *Monthly Weather Review* 145 (8), 3049–3072. doi:10.1175/mwr-d-16-0336.1

Mlawer, E. J., Taubman, S. J., Brown, P. D., Iacono, M. J., and Clough, S. A. (1997). Radiative transfer for inhomogeneous atmospheres: RRTM, a validated correlated-k model for the longwave. *J. Geophys. Res.* 102 (14), 16663–16682. doi:10.1029/97jd00237

Morrison, H., Thompson, G., and Tatarskii, V. (2009). Impact of cloud microphysics on the development of trailing stratiform precipitation in a simulated squall line: Comparison of one- and two-moment schemes. *Mon. Weather Rev.* 137 (3), 991–1007. doi:10.1175/2008mwr2556.1

Pontoppidan, M., Reuder, J., Mayer, S., and Kolstad, E. W. (2017). Downscaling an intense precipitation event in complex terrain: The importance of high grid resolution. *Tellus A Dynamic Meteorology and Oceanography* 69 (1), 1271561. doi:10.1080/16000870.2016.1271561

Shen, F., Min, J., Li, H., Xu, D., Shu, A., Zhai, D., et al. (2021). Applications of radar data assimilation with hydrometeor control variables within the WRFDA on the prediction of landfalling hurricane IKE (2008). *Atmosphere* 12, 853. doi:10.3390/atmos12070853

Shen, F., Xu, D., Min, J., Chu, Z., and Li, X. (2020). Assimilation of radar radial velocity data with the WRF Hybrid 4DEnVar system for the prediction of Hurricane Ike (2008). *Atmospheric Research* 230, 104771. doi:10.1016/j.atmosres.2019.104771

Sinclair, M. R. (1994). A diagnostic model for estimating orographic precipitation. *J. Appl. Meteor.* 33 (10), 1163–1175. doi:10.1175/1520-0450(1994)033<1163:admfeo>2.0.co;2

Tewari, M., Chen, F., Wang, W., Dudhia, J., LeMone, M. A., Mitchell, K., et al. (January 2004). "Implementation and verification of the unified Noah land–surface model in the WRF model Paper," in Proceedings of the 20th Conference on Weather Analysis and Forecasting/16th Conference on Numerical Weather Prediction (Seattle, DC, USA: American Meteorological Society), 2165–2170.

Tsai, C. L., Kim, K., Liou, Y. C., Lee, G., and Yu, C. K. (2018). Impacts of topography on airflow and precipitation in the pyeongchang area seen from multiple-Doppler radar observations. *Monthly Weather Review* 146 (10), 3401–3424. doi:10.1175/mwr-d-17-0394.1

Wang, C., Yu, X., Li, Z., Li, H., and Wang, X. (2017). Investigation of extreme flash-rain events on the impact of Taihang mountain. *Meteor Mon* 43 (04), 425–433.

Wang, L., Miao, J., and Han, F. (2018). Overview of impact of topography on precipitation in China over last 10 years. *Meteor Sci Technol* 46 (01), 64–75.

Wang, Y., Miao, J., and Su, T. (2018). A numerical study of impact of topography on intensity and pattern of sea breeze precipitation over the Hainan Island[J]. *Plateau Meteor* 37 (1), 207–222. doi:10.7522/j.issn.1000-0534.2016.00135

Wu, C. C., Yen, T. H., Huang, Y. H., Yu, C. K., and Chen, S. G. (2015). Statistical characteristic of heavy rainfall associated with typhoons near taiwan based on high-density automatic rain gauge data. *Bulletin of the American Meteorological Society* 97 (8), 1363–1375. doi:10.1175/bams-d-15-00076.1

Yang, P. A. N., Junxia, G. U., Yu, J., Yan, S. H. E. N., Chunxiang, S. H. I., and Zhou, Z. (2018). Test of merging methods for multi-source observed precipitation products at high resolution over China[J]. *Acta Meteorologica Sinica* 76 (5), 755–766. doi:10.11676/qxxb2018.034

Yi, X., Chen, H., Sun, X., Wang, Y., Han, T., and Yun, L. (2018). Multi-scale configuration of the 20 july 2016 cyclone-induced severe torrential rain and its relationship with the development of MγCS. *Meteor Mon* 44 (07), 869–881.

Yu, C. K., and Cheng, L. W. (2013). Distribution and mechanisms of orographic precipitation associated with typhoon Morakot (2009). *J. Atmos. Sci.* 70 (9), 2894–2915. doi:10.1175/jas-d-12-0340.1

Zhang, H., Chen, H., Yu, H., and Zhang, X. (2020). Diurnal variations and causes of warm season precipitation in qinling and surrounding areas[J]. *Plateau Meteorol.* 39 (5), 935–946. doi:10.7522/j.issn.1000-0534.2019.00067

Zhao, S., Sun, J., Lu, R., and Fu, S. (2018). Analysis of the 20 july 2016 unusual heavy rainfall in North China and beijing. *Meteor Mon* 44 (03), 351–360.

Zhong, S. (2020). Advances in the study of the influencing mechanism and forecast methods for orographic precipitation. *Plateau Meteorology* 39 (5), 1122–1132. doi:10.7522/j.issn.1000-0534.2019.00083

Zhou, Q., Kang, L., Jiang, X., and Liu, Y. (2019). Relationship between heavy rainfall and altitude in mountainous areas of Sichuan Basin[J]. *Meteor Mon* 45 (6), 811–819. (in Chinese).

frontiers | Frontiers in Earth Science

TYPE Original Research
PUBLISHED 13 January 2023
DOI 10.3389/feart.2022.1037065

OPEN ACCESS

EDITED BY
Dongmei Xu,
Nanjing University of Information Science and Technology, China

REVIEWED BY
Ruichun Wang,
CMA Earth System Modeling and Prediction Centre, China
Guojie Wang,
Nanjing University of Information Science and Technology, China

*CORRESPONDENCE
Changliang Shao,
shchl1@163.com

SPECIALTY SECTION
This article was submitted to Environmental Informatics and Remote Sensing, a section of the journal Frontiers in Earth Science

RECEIVED 05 September 2022
ACCEPTED 14 November 2022
PUBLISHED 13 January 2023

CITATION
Shao C, Guo Y, Cao Y and Wang J (2023), A high-resolution soil moisture content analysis product in Jing-Jin-Ji using the successive correction method.
Front. Earth Sci. 10:1037065.
doi: 10.3389/feart.2022.1037065

A high-resolution soil moisture content analysis product in Jing-Jin-Ji using the successive correction method

Changliang Shao[1]*, Yakai Guo[2], Yunchang Cao[1] and Jiao Wang[3]

[1]CMA Meteorological Observation Centre, Beijing, China, [2]CMA Henan Meteorological Bureau, Zhengzhou, China, [3]Beijing Tianhe Xiangyun Culture Media Limited Company, Beijing, China

Two soil moisture content analysis products, each with a spatial resolution of 0.0625° and a temporal resolution of 1 h from 1 October 2015 to 1 October 2021 in the Jing-Jin-Ji area, have been developed and evaluated. Using a quality control (QC) scheme based on the biweight method and a successive correction method (SCM) with different weighting functions introduced from the Cressman and/or Barnes methods, the soil moisture collected from China Land Data Assimilation System version 2.0 was taken as the background data. Two soil analysis products with induced hourly station soil observations were constructed and further compared with *in situ* observations and satellite products. Results show that with the biweight method, the outliers of soil moisture could be identified, and that the number of these was less than 10% of the actual reported samples. The analysis product is more accurate with the Cressman weighting function than with the Barnes as the root mean square error was reduced by 30% to 0.06, while the correlation coefficient increased by 73% to 0.59, compared to the control. These results indicate that the Cressman product is a useful and promising soil moisture data set. The proposed Cressman method is computationally simple and efficient, so the product can be easily updated to keep pace with significant increases in the volume of soil moisture data. The methods used here for QC, SCM, and comparison could help evaluate and improve land surface models and their soil moisture products.

KEYWORDS

soil moisture, cross-validation, data assimilation, land surface model, quality control

1 Introduction

A regional climate can be affected by soil moisture, which can change the latent and sensible heat transported to the atmosphere, the reflectance of the surface, and the heat capacity of the ground. Soil moisture also plays an important role in medium- and small-scale atmospheric processes (Ma et al., 2001). Thus, it is important to properly use soil moisture data in the land surface model and to correctly understand the mechanisms underlying the interaction between the atmosphere and soil moisture (Pan and Mahrt,

1987; Chen et al., 1997; Gaertner et al., 2010; Seneviratne et al., 2010; Vereecken et al., 2014; Li et al., 2019; Shi et al., 2019; Song et al., 2019). The accurate measurement of soil moisture is very important for accurately understanding its role in atmospheric and climate processes. Good-quality soil moisture observation is also needed to improve a numerical model and soil moisture data assimilation (Kim and Wang, 2007; Li et al., 2012; Li et al., 2015; Ju et al., 2019). Research on soil moisture variation can be hindered because of the lack of observations with high temporal and spatial resolution (Seneviratne et al., 2010). Therefore, studies of soil moisture content usually depend on retrieved soil moisture data (Lai et al., 2014; Zhu et al., 2019). Remote sensing data from satellites can be used to produce a soil moisture product with high spatial resolution (Njoku et al., 2003; Parkinson, 2003; Qiao et al., 2007; Dabboor et al., 2019). However, low temporal resolution does reduce the accuracy of soil moisture retrieval when such data are used in numerical models (Lan et al., 2015; Fereidoon et al., 2019).

Powered by developing technologies for ground-based soil moisture monitoring, automatic devices have been developed and widely applied (Susha et al., 2014). Since 2004, the China Meteorological Administration has conducted a systematic project of generating soil moisture data using automatic monitoring devices. This project has been in operation since 2009. As of 2020, 2,400 observation stations had been established. In general, the automatic observation system for monitoring soil moisture in China has been developed mainly based on frequency domain reflectometry (Minet et al., 2010). In addition, the data volume and coverage have exceeded all previous traditional manual soil moisture observations. Recently, a growing number of researchers have been utilizing those automatically measured soil moisture data (Zhu and Shi, 2014; Wang and Gong, 2018).

However, automatic soil moisture stations are still sparse, and the spatial distribution of observations from the station system is nonuniform. These constraints have resulted in poor applications of the station data. Thus, a gridded analysis product with soil observations is needed, whereas the successive correction method (SCM) could be selected as a primary regular way of merging station data when considering applications in grid space. The advantage of SCM is that signals with different scales can be captured according to predefined weighting factors. Unlike other assimilation methods such as OI, 3DVAR, and EnKF, SCM needs neither the background error covariance nor the assumption of Gaussian errors of background and observation. Thus, given the sparse distribution of soil moisture data and the nonlinearity of the land surface model or the system, SCM is easier for implementing gridded product analysis and updates to keep pace with large increases in the volume of soil moisture data. In this work, the Cressman scheme (Cressman, 1959; Li, et al., 2017) and the Barnes scheme (Koch, 1983) are used as weighting factors. On this basis, the automatic soil moisture data for the areas of Beijing city, Tianjin city, and Hebei province were integrated into the China Land Data Assimilation System (CLDAS) version 2.0 dataset (Shi et al., 2014) to conduct the hourly soil moisture analysis from 1 October 2015 to 1 October 2021. This area is called Jing-Jin-Ji for short and is located in the middle of northern China. The newly constructed gridded analysis datasets were compared and evaluated against *in situ* data and Soil Moisture Active Passive (SMAP) satellite retrievals (Entekhabi et al., 2010). Ultimately, the dataset with higher quality can be used for further process studies, as well as for the validation and evaluation of other soil moisture products.

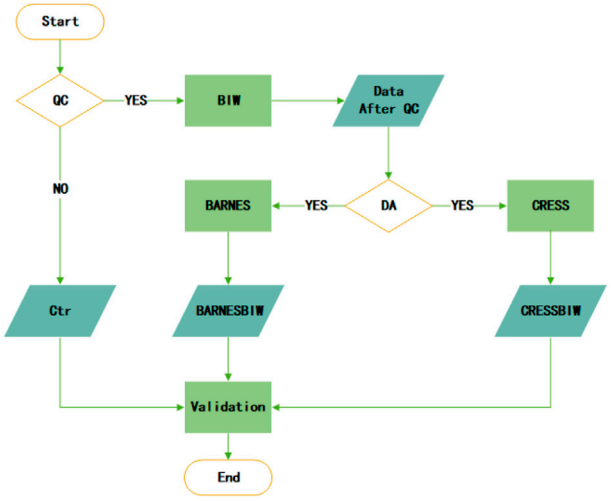

FIGURE 1
Experimental flowchart.

In the following sections, we first introduce the background data from CLDAS V2.0 and the station data (Section 2.1). The quality control (QC) methods are presented (Section 2.2). The algorithms for SCM and validation (Section 2.3) and the experimental design (Section 2.4) are then described. In Section 3, we describe several synthetic experiments to investigate their performances. In Section 4, the results of these cases are discussed. Conclusions are drawn last, in Section 5.

2 Experiments

2.1 CLDAS soil data and station soil data

The CLDAS V2.0 dataset, established and updated by CMA, contains hourly 0.0625° near-surface meteorological variables for mainland China from 2008 to 2021. This dataset merges surface measurements from over 2,400 national automatic weather stations and approximately 40,000 regional CMA automatic weather stations with 0.125° 3-hourly numerical analysis/

predicted products from the European Centre for Medium-Range Weather Forecasts to produce the near-surface wind speed, air temperature, and specific humidity. Using these ongoing near-surface data to force the offline land surface model, the finer land products were determined, the accuracy of which depends mainly on the quality of the atmospheric forcing data (Liu, et al., 2019). For this study, the soil moisture product from CLDAS V2.0 was selected as background data to combine with the station soil moisture observations.

This study observed soil moisture volumetric content on the hourly scale, as measured by the automatic soil moisture observation system, including 417 stations lying loosely in the Jing-Jin-Ji area, as shown in Figure 1. It should be noted that all raw soil moisture data used here are *in situ* observations.

2.2 Quality control

First, extreme values of soil moisture content (larger than 65%) and missing data from the raw data were eliminated. Then, to check the consistency of the background, the biweight technique—which was first described by Lanzante (1996) and further introduced into high spatial-temporal resolution soil moisture applications by Shao et al. (2020)—was applied to remove occasional outliers. The biweight function was defined using the following equation:

$$\omega_i = \frac{X_i - M}{7.5 \times MAD} \tag{1}$$

where the observation bias X_i is defined as $X_i = y_i^o - y_i^b$, where $i = 1, 2, \ldots, n$, n is the total number of the samples, i is the i^{th} sample, y_i^o is the observed value, and y_i^b is the background value. M is the median of X_i, and MAD is the median of $|X_i - M|$. When $|\omega_i| > 1$, $\omega_i = 1$, the biweight mean $\overline{X_{bw}}$, the biweight standard deviation $BSTD$, and Z_i are defined by the following equations:

$$\overline{X_{bw}} = M + \frac{\sum_{i=1}^{n} (X_i - M)\left(1 - \omega_i^2\right)^2}{\sum_{i=1}^{n} \left(1 - \omega_i^2\right)^2} \tag{2}$$

$$BSTD = \frac{\left[n \sum_{i=1}^{n} (X_i - M)^2 \left(1 - \omega_i^2\right)^4\right]^{0.5}}{\left|\sum_{i=1}^{n} \left(1 - \omega_i^2\right)\left(1 - 5\omega_i^2\right)\right|} \tag{3}$$

$$Z_i = \frac{\left|X_i - \overline{X_{bw}}\right|}{BSTD} \tag{4}$$

For a given value of Z_T, the i^{th} observed value was identified as an outlier when $Z_i \geq Z_T$. Generally, the value of Z_T was empirically set to be 1.5, 2.0, or 3.0, and the selection of Z_T ensured that the percentage of elements removed was about 10% of the actual reported elements (Shao et al., 2020). Thus, the Z_T was set to 2.0.

2.3 Data fusion and validation

The SCM can be generally written as follows:

$$f_i^{n+1} = f_i^n + \frac{\sum_{b=1}^{k_i^n} w_{ib}^n \left(f_b^o - f_b^n\right)}{\sum_{b=1}^{k_i^n} w_{ib}^n} \tag{5}$$

The i, b, and n in equation (Eq. hereafter) (Eq. 5) represent the i^{th} grid point, the b^{th} observation point, and the n^{th} iteration number. f_i^n is the analysis field after the n^{th} iteration at the i^{th} grid point, and f_b^o is the b^{th} observation within a predefined scan radius R_n, called the influence distance. For the n^{th} iteration interpolation with the location of the b^{th} observation, k_i^n is the total number of observations collected within R_n of the i^{th} grid point. Due to different weighting factors, w_{jb}^n, different data fusion schemes were defined. Two data fusion schemes used in this study, based on the Cressman and Barnes methods, are briefly described in the following.

The Cressman scheme is defined as follows:

$$\begin{cases} w_{ib}^n = \dfrac{R_n^2 - r_{ib}^2}{R_n^2 + r_{ib}^2}, r_{ib}^2 < R_n^2 \\ w_{ib}^n = 0, r_{ib}^2 \geq R_n^2. \end{cases} \tag{6}$$

In Eq. 6, r_{ib} is the distance between the i^{th} grid point and the b^{th} observation, while R_n is usually taken to be several times the value of r_{ib}. According to Cressman (1959), to resolve small-scale signals, R_n should be gradually decreased with successive iterations. Moreover, to ensure that a large-scale signal is retained, R_{n-1} should be set to a relatively large value.

The Cressman scheme with three iterations (Eqs 5, 6) was used in this study to conduct the hourly soil moisture analysis. The scan radii R_1, R_2, and R_3 were set to 281.25, 93.75, and 31.25 Km, respectively (Li et al., 2017).

In the meantime, a refined Barnes scheme was used for comparison. This scheme was originally proposed and refined by Barnes (1964, 1973) and is similar to the Cressman scheme. The main difference between the methods is how they compute the weighting factor, w_{jb}^n. A Gaussian function is used to compute w_{jb}^n in the Barnes scheme. Barnes (1973) refined this method by proposing the modified weighting factor

$$\begin{cases} w_{ib}^n = exp\left(\dfrac{-r_{ib}^2}{\chi\gamma}\right), r_{ib}^2 < R_n^2 \\ w_{ib}^n = 0, r_{ib}^2 \geq R_n^2, \end{cases} \tag{7}$$

where r_{jb}^2 and R_n are defined as in Eq. 6, γ is the convergence factor, and χ is the filtering constant. The number of iterations required to reach a stable solution can typically be reduced by this modified weighting factor. Prior to the analysis (Koch, 1983), the parameters χ and γ were set at 5.052 and 0.25, as one or two iterations should be used. We selected a two-pass (two-iteration) analysis in the scheme. Thereby, the scan radii were set to 281.25 (the overall radii of our study area) and 93.75 (1/3 of the overall radii, for a quick convergence) Km.

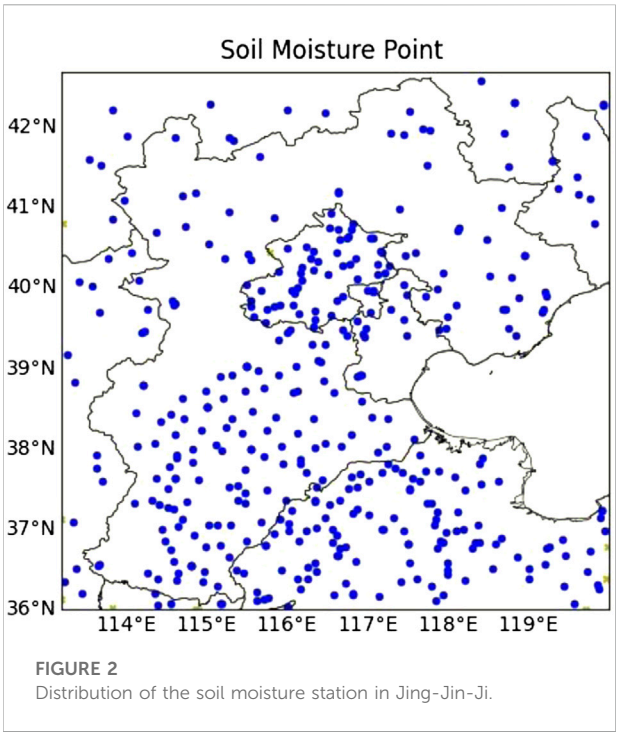

FIGURE 2
Distribution of the soil moisture station in Jing-Jin-Ji.

In this study, SMAP retrievals and station observations were used to compare against and/or validate the analysis obtained from each experiment over various temporal and spatial scales. Four metrics (i.e., root mean square error [RMSE], correlation coefficient [Corr], skewness [SKEW], and kurtosis [KURT]) were calculated as follows.

$$RMSE = \sqrt{\frac{\sum_{i=1}^{n}(y_i - x_i)^2}{n}} \tag{8}$$

$$Corr = \frac{\sum_{i=1}^{n}(y_i - \bar{y})(x_i - \bar{x})}{\sqrt{\sum_{i=1}^{n}(x_i - \bar{x})^2}\sqrt{\sum_{i=1}^{n}(y_i - \bar{y})^2}} \tag{9}$$

$$SKEW = \frac{n}{(n-1)(n-2)}\sum_{i=1}^{n}\left(\frac{x_i - \bar{x}}{s}\right)^3$$

$$KURT = \left\{\frac{n(n+1)}{(n-1)(n-2)(n-3)}\sum_{i=1}^{n}\left(\frac{x_i - \bar{x}}{s}\right)^4\right\} - \frac{3(n-1)^2}{(n-2)(n-3)} \tag{10}$$

where x_i is the reference data point, y_i is the corresponding data point to be validated, n is the sample size, and $\bar{x}$ ($\bar{y}$) is the mean value of x (y) of n values. In this article, the cross-validation method is presented using both station soil moisture observation and SMAP Level-2 gridded soil moisture product as validation data.

2.4 Experiment description

To efficiently induce the station soil moisture data into the grid products, QC and assimilation (DA) were the primary assignment. A brief description of the main procedures of this work is given in Figure 1. The QC process based on the biweight method was carried out using the available station observations. The Ctr was first taken as a comparison candidate and was conducted to generate two comparison candidates, following the assimilation process based on SCM with the diversity of weighting factor. Finally, cross-validation among the different candidate products and validation data was further conducted.

The hourly CLDAS V2.0 soil moisture product was used as the ongoing background data during station soil moisture assimilation. All types of datasets, including CLDAS V2.0, SMAP data, and station data in this study, concentrated on the area 113.2E~120.0E, 36.0N~42.7N, which covers Jing-Jin-Ji, as shown in Figure 2.

In addition, as shown in Table 1, data in the Ctr experiment (known as the control experiment) collected from the CLDAS V2.0 soil moisture product had no QC nor assimilation. Meanwhile, the experiments BARNESBIW and CRESSBIW both used the biweight method during QC and applied the SCM method with Barnes and Cressman weight factors, respectively, during observation assimilation. Moreover, to objectively verify the differences between various grid products, station observation and SMAP retravel data were used to compare against the three products, using evaluation indicators including RMSE, Corr, SKEW, and KURT.

TABLE 1 Experimental design.

Expr	Name	QC	WF	Assimilation
1	Ctr	—	—	No
2	CRESSBIW	QCBIW	Cressman	Yes
3	BARNESBIW	QCBIW	Barnes	Yes

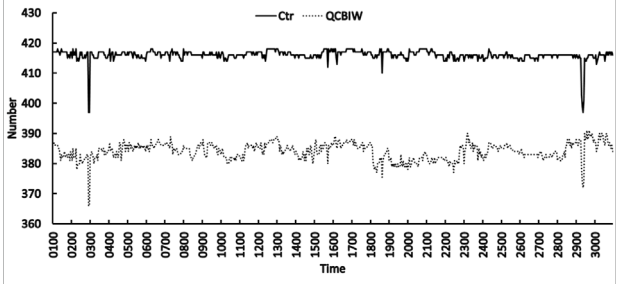

FIGURE 3
Hourly numbers of actual reported (solid line) and valid samples after QC (dotted line) from 1 September to 1 October 2020.

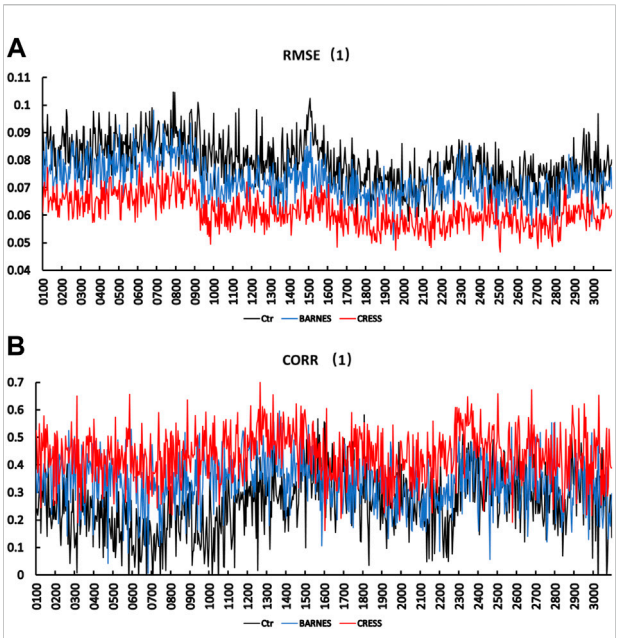

FIGURE 4
Hourly RMSEs **(A)** and Corrs **(B)** between station observations and products of each experiment from 1 September to 1 October 2020, including Ctr (black lines), BARNES (blue lines), and CRESS (red lines).

3 Results

3.1 QC of the station soil moisture

QC was conducted before assimilation as the CLDAS V2.0 grid data are continuously spatial and temporal, whereas raw station observations are discrete, to avoid assimilation distortion induced by countless differences with non-Gaussian noises between background and observation. When all observation and background samples were compared at the station points, the non-Gaussian noises could be greatly improved (Shao et al., 2020).

As shown in Figure 3, our datasets include a total of 720 hourly observations collected at 417 stations from 1 September to 1 October 2020, with one observation record per hour at each station. A total of 300,240 elements were recorded. After rejecting extreme values and missing data, the number of actual records was 292,308, accounting for about 97.36% of the actual reported elements, while after QCBIW, the number of rejected records was 276,518 and the corresponding percentages among actually reported records about 7.7%. Overall, about 10% of the raw data were rejected in total.

It should be noted that the ongoing results show more consistent behavior during QC, as compared to former research (Shao et al., 2020), because the actual reported rate during the whole QC procedure was higher in this paper. This indicates that SCMs assimilate more realistic soil moisture data into CLDAS V2.0 products.

TABLE 2 Average calculation of hourly RMSEs and Corrs between station observations and each product of Ctr, CRESSBIW, and BARNESBIW.

Expr	RMSE	Corr
Ctr	0.079341	0.261252
BARNESBIW	0.072546	0.338715
CRESSBIW	0.063091	0.425357
ESSMRA	0.104727	0.369636

3.2 Comparisons against station observations

To assess how the two schemes behave differently during the DA process, it was necessary to compare analysis data with station data. Station soil moisture data were used to calculate the RMSEs and Corrs of experiment results. Eighty percent of the whole-station data records after QC (Section 3.1) were used in data fusion, while the remaining 20% were used for additional independent validation. Next, we take the first soil layer, with more temporal-spatial variants, as an example.

The RMSE and Corr between the station and gridded data during the first soil layer [e.g., RMSE (1) and Corr (1)] for each experiment are shown in Figure 4. While distinguished boundary gaps can be found among different soil moisture products, both the CRESS and BARNES experiments can produce better soil moisture than the background (Ctr); at the same time, it is also clear that CRESS is superior to BARNES. In addition, we compared the available ESSMRA data (Naz et al., 2020), which provides long-term surface soil moisture at a high spatiotemporal resolution, with our results. Satellite-derived soil moisture data were assimilated into the community land model (CLM3.5) using an ensemble Kalman filter scheme in ESSMRA. Table 2 shows the average RMSE and Corr values for each experiment, as well as the ESSMRA results. It also shows that the CRESS scheme is superior to the Ctr, BARNES scheme, and ESSMRA, which coincides with the result shown in Figure 4.

Overall, these results show improved station scale soil moisture when observation was properly induced (e.g., smaller RMSE and larger Corr in CRESS, when compared to observations, than for both in BARNES or Ctr). This indicates that the widely used Cressman weighting factor (e.g., ocean data assimilation) is also suitable for the soil moisture data fusion scheme, and the results of the station scale promise to be statistically improved.

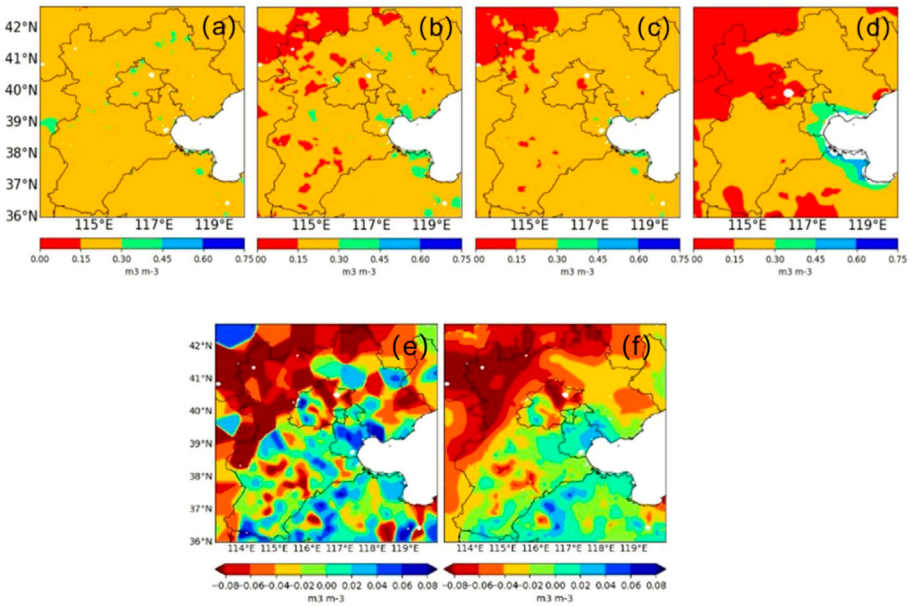

FIGURE 5
Distribution of monthly averages from Ctr **(A)**, BARNES **(B)**, CRESS **(C)**, and SMAP **(D)**. Difference between analysis [i.e., BARNES minus Ctr **(E)** and CRESS minus Ctr **(F)**].

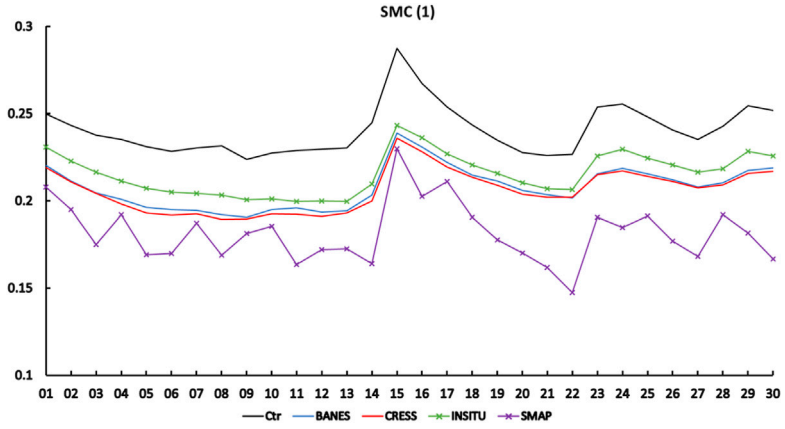

FIGURE 6
Daily average soil moisture content of SMAP (violet cross), station data (green cross), Ctr (black line), BARNES (blue line), and CRESS (red line) from 1 September to 1 October 2020.

3.3 Comparisons against the SMAP grid dataset

Preliminary validation studies have suggested that SMAP is meeting its performance targets (Chan et al., 2016; Pan et al., 2016), and therefore, the SMAP products were used for cross-validation here. However, the SMAP data records are on a daily scale while the assimilation results are on an hourly scale. Thus, the hourly values for the analysis have been averaged into daily values before validation. As we can see, the spatial distributions of the two analysis products were both more similar to the SMAP than to the background or Ctr, as shown in Figures 5A–F. Thereby, as seen from the difference between analysis and Ctr, the Cressman scheme clearly has a smoother

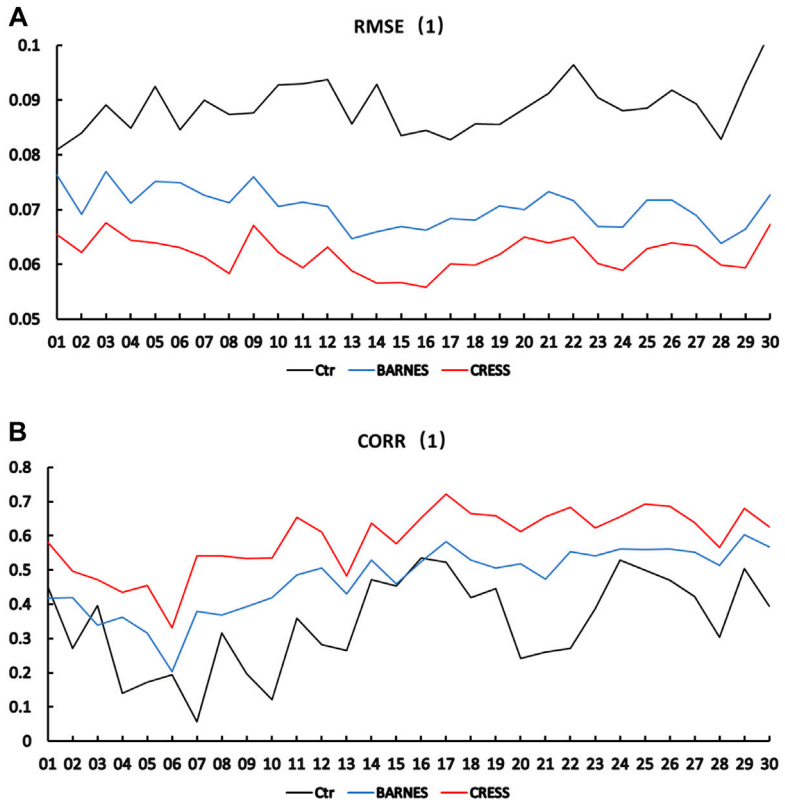

FIGURE 7
Daily RMSEs **(A)** and Corrs **(B)** between SMAP and products of each experiment from 1 September to 1 October 2020, including Ctr (black lines), BARNES (blue lines), and CRESS (red lines).

TABLE 3 Comparison of SMAP with Ctr, BARNESBIW, CRESSBIW, ASCAT, and AMSR2.

Expr	RMSE	Corr
Ctr	0.089	0.345
BARNESBIW	0.070	0.472
CRESSBIW	0.062	0.590
AMSR2	0.091	0.407
ASCAT	0.112	0.649

and more reasonable spatial distribution than does the Barnes scheme.

In addition, as the daily spatial average surface soil moisture content (Figure 6) suggests, the two analysis products are both closer to the SMAP than to the Ctr and *in situ* observation. Also, a consistent variant tendency among all products can be observed (e.g., the sudden increase of soil moisture around 15 September), indicating that SMAP agrees well with the others on domain-averaged daily scales. While lower surface soil moisture values can be found in SMAP retrievals than in station data, this should explain the quite different probe methods and also indicates that soil moisture data fusion is necessary.

Furthermore, as shown in the daily RMSEs and Corrs (Figure 7) and the averaging during the analysis of daily RMSEs and Corrs between SMAP and the analysis of each experiment (Table 3), the Cressman scheme is clearly superior to the Barnes scheme when lower RMSEs and larger Corrs can be found; this is consistent with the results of comparisons against station data. Also, as shown in both the probability density distribution (Figure 8) and the values of skewness and kurtosis (Table 4), the analysis using the Cressman scheme is closest to the Gaussian distribution and has the smallest SKEW and KURT for all validation candidates.

Notably, Burgin et al. (2017) have compared SMAP with products of AMSR2 and ASCAT using the same statistical evaluation indicators, as shown in Table 4. It is clear that the

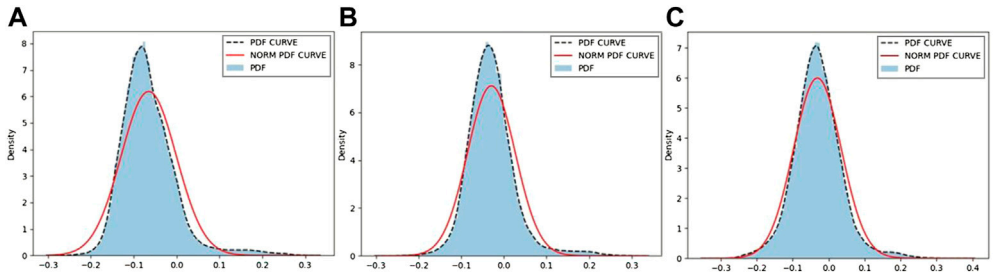

FIGURE 8
Probability density function of deviations between SMAP and products of each experiment from 1 September to 1 October 2020, including Ctr **(A)**, BARNES **(B)**, and CRESS **(C)**.

TABLE 4 Skewness and kurtosis of each product of Ctr, CRESS, and BARNES.

Expr	SKEW	KURT
Ctr	1.424943	4.077481
BARNESBIW	1.117530	3.779297
CRESSBIW	0.427401	1.806810

CRESSBIW product is superior to the AMSR2 product. Compared with ASCAT, although the Corr of CRESSBIW is smaller by 9.1%, the RMSE is smaller by 44.6%. Therefore, the CRESSBIW product can capture the comparative daily scale characteristics as satellite-gridded retrievals. In general, all the aforementioned results indicate that the CRESSBIW product is a good choice with a simple SCM assimilation method and a quality promised gridded dataset.

4 Conclusion and discussions

In this work, we developed and evaluated two analysis products using SCMs with Barnes and Cressman weight factors. The hourly CLDAS V2.0 soil moisture content product was adopted as background data, and the hourly automatic soil moisture station data as observations to be assimilated. QC was conducted using the biweight method with the result of eliminating less than 10% of the actual reported data. Then, two hourly soil moisture content analysis products were produced using two schemes, including Barnes and Cressman, with a spatial resolution of 0.0625°. All validation results showed that the analysis product using the Cressman scheme had smaller RMSE and larger Corr than that using the Barnes scheme. In addition, the probability density distribution of deviations from the Cressman scheme analysis was closer to a normal or Gaussian distribution than was that of the Barnes scheme analysis, which should be attributed to the weighting factor. Finally, the Cressman scheme is recommended for use in analysis production with the sources of CLDAS V2.0 soil moisture content product and automatic soil moisture station data in the Jing-Jin-Ji area.

The dataset presented here provides hourly surface soil moisture analysis at a high spatiotemporal resolution and will be beneficial for many hydrological applications across the Jing-Jin-Ji region. Our results indicate that the Cressman product is a useful and promising soil moisture dataset. The proposed Cressman scheme is computationally simple and efficient, so the product can be easily updated to keep pace with large increases in the volume of soil moisture data. These findings will help evaluate and improve numerical models and their corresponding products. The comparison and evaluation steps employed in this work can also be applied to other data sources, for example, to satellite remote sensing products and to soil moisture products produced in other ways. It is noted that the iterations and scan radius specified in this work may be altered when the resolution of the data changes. In the future, new methods for assimilating soil moisture data and optimal weighting factors will be developed to further improve the analysis product.

Data availability statement

The datasets presented in this article are not readily available because they were authorized by China Meteorological Administration. Requests to access the datasets should be directed to Shao Changliang, shchl1@163.com.

Author contributions

SC contributed to the conception and design of the study, organized the database, performed the statistical analysis, and wrote the first draft of the manuscript. SC and GY wrote sections of the manuscript. CY and WJ analysis the data and revised the manuscript. All authors contributed to manuscript revision, and read and approved the submitted version.

Funding

This work was supported by the China Environmental Protection Foundation Blue Mountain Project (CEPFQS202169-28).

Conflict of interest

The author WJ was employed by Beijing Tianhe Xiangyun Culture Media Limited Company.

The remaining authors declare that the research was conducted in the absence of any commercial or financial relationships that could be construed as a potential conflict of interest.

Publisher's note

All claims expressed in this article are solely those of the authors and do not necessarily represent those of their affiliated organizations, or those of the publisher, the editors, and the reviewers. Any product that may be evaluated in this article, or claim that may be made by its manufacturer, is not guaranteed or endorsed by the publisher.

References

Barnes, S. L. (1964). A technique for maximizing details in numerical weather map analysis. *J. Appl. Meteor.* 3, 396–409. doi:10.1175/1520-0450(1964)003<0396:atfmdi>2.0.co;2

Barnes, S. L. (1973). *Mesoscale objective analysis using weighted time series observations, NOAA Tech. Memo ERL NSSL-62.* Norman, Okla: Natl. Severe Storms Lab., 41.

Burgin, M. S., Colliander, A., Njoku, E. G., Chan, S. K., Cabot, F., Kerr, Y. H., et al. (2017). A comparative study of the SMAP passive soil moisture product with existing satellite-based soil moisture products. *IEEE Trans. Geosci. Remote Sens.* 55 (5), 2959–2971. doi:10.1109/tgrs.2017.2656859

Chan, S. K., Bindlish, R., O'Neill, P. E., Njoku, E., Jackson, T., Colliander, A., et al. (2016). Assessment of the SMAP passive soil moisture product. *IEEE Trans. Geosci. Remote Sens.* 54 (8), 4994–5007. doi:10.1109/tgrs.2016.2561938

Chen, F., Janjić, Z., and Mitchell, K. (1997). Impact of atmospheric surface-layer parameterizations in the new land-surface scheme of the NCEP mesoscale eta model. *Boundary-Layer Meteorol.* 85 (3), 391–421. doi:10.1023/a:1000531001463

Cressman, G. P. (1959). An operational objective analysis system[J]. *Mon. Wea. Rev.* 87, 367–374. doi:10.1175/1520-0493(1959)087<0367:aooas>2.0.co;2

Dabboor, M., Sun, L., Carrera, M. L., Friesen, M., Merzouki, A., McNairn, H., et al. (2019). Comparative analysis of high-resolution soil moisture simulations from the soil, vegetation, and snow (SVS) land surface model using SAR imagery over bare soil. *Water* 11 (3), 542. doi:10.3390/w11030542

Entekhabi, D., Njoku, E. G., O'Neill, P. E., Kellogg, K. H., Crow, W. T., Edelstein, W. N., et al. (2010). The soil moisture active passive (SMAP) mission. *Proc. IEEE* 98, 704–716. doi:10.1109/jproc.2010.2043918

Fereidoon, M., Koch, M., and Brocca, L. (2019). Predicting rainfall and runoff through satellite soil moisture data and SWAT modelling for a poorly gauged basin in Iran. *Water* 11, 594. doi:10.3390/w11030594

Gaertner, M. A., Domínguez, M., and Garvert, M. (2010). A modelling case-study of soil moisture-atmosphere coupling. *Q. J. R. Meteorol. Soc.* 136 (S1), 483–495. doi:10.1002/qj.541

Ju Fan Rand Sun, Y. (2019). Immune evolution particle filter for soil moisture data assimilation. *Water* 11, 211. doi:10.3390/w11020211

Kim, Y. J., and Wang, G. L. (2007). Impact of initial soil moisture anomalies on subsequent precipitation over North America in the coupled land–atmosphere model CAM3–CLM3. *J. Hydrometeorol.* 8 (3), 513–533. doi:10.1175/jhm611.1

Koch, S. E., Desjardins, M., and Kocin, P. J. (1983). An interactive Barnes objective map analysis scheme for use with satellite and conventional data. *J. Clim. Appl. Meteor.* 22, 1487–1503. doi:10.1175/1520-0450(1983)022<1487:aiboma>2.0.co;2

Lai, X., Wen, J., Ceng, S. X., Song, H. Q., and Huang, X. (2014). Numerical simulation and evaluation study of soil moisture over China by using CLM4.0 model [J]. *Chin. J. Atmos. Sci. (in Chinese)* 38 (3), 499–512.

Lan, X., Guo, Z., Tian, Y., Xia, L., and Wang, J. (2015). Review in soil moisture remote sensing estimation based on data assimilation [J]. *Advances in Earth Science* 30 (6), 668–679.

Lanzante, J. R. (1996). Resistant, robust and non-parametric techniques for the analysis of climate data: Theory and examples, including applications to historical radiosonde station data [J]. *Int. J. Climatol.* 16, 1197–1226. doi:10.1002/(sici)1097-0088(199611)16:11<1197::aid-joc89>3.0.co;2-l

Li, D. Q., Duan, Y. X., and Zhang, S. W. (2012). Soil moisture measurement and simulation: A review [J]. *Advances in Earth Science* 27 (4), 424–434.

Li, H., Xu, F., Zhou, W., Wang, D., Wright, J. S., Liu, Z., et al. (2017). Development of a global gridded Argo data set with Barnes successive corrections. *J. Geophys. Res. Oceans* 122, 866–889. doi:10.1002/2016jc012285

Li, Y., Wang, Y., Zheng, J., and Yang, M. (2019). Investigating spatial and temporal variation of hydrological processes in western China driven by CMADS. *Water* 11, 435. doi:10.3390/w11030435

Li, Z., Zhou, T., Chen, H., Ni, D., and Zhang, R. (2015). Modelling the effect of soil moisture variability on summer precipitation variability over East Asia. *Int. J. Climatol.* 35 (6), 879–887. doi:10.1002/joc.4023

Liu, J., Shi, C., Sun, S., Liang, J., and Yang, Z. L. (2019). Improving land surface hydrological simulations in China using CLDAS meteorological forcing data. *J. Meteorol. Res.* 33 (6), 1194–1206. doi:10.1007/s13351-019-9067-0

Ma, Z. G., Fu, C. B., Xie, L., Chen, W. H., and Tao, S. W. (2001). Some problems in the study on the relationship between soil moisture and climatic change. *Advance in Earth Sciences (in Chinese)* 16 (4), 563–568.

Minet, J., Lambot, S., Delaide, G., Huisman, J. A., Vereecken, H. A., and Vanclooster, M. A. (2010). A generalized frequency domain reflectometry modeling technique for soil electrical properties determination. *Vadose Zone Journal* 9, 1063–1072. doi:10.2136/vzj2010.0004

Naz, B. S., Kollet, S., Franssen, H. J. H., Montzka, C., and Kurtz, W. (2020). A 3 km spatially and temporally consistent European daily soil moisture reanalysis from 2000 to 2015. *Sci. Data* 7, 111. doi:10.1038/s41597-020-0450-6

Njoku, E. G., Jackson, T. J., Lakshmi, V., Chan, T. K., and Nghiem, S. V. (2003). Soil moisture retrieval from AMSR-E. *IEEE Trans. Geosci. Remote Sensing* 41 (2), 215–229. doi:10.1109/tgrs.2002.808243

Pan, H. L., and Mahrt, L. (1987). Interaction between soil hydrology and boundary-layer development. *Boundary-Layer Meteorol.* 38 (1-2), 185–202. doi:10.1007/bf00121563

Pan, M., Cai, X., Chaney, N. W., Entekhabi, D., and Wood, E. F. (2016). An initial assessment of SMAP soil moisture retrievals using high-resolution model simulations and *in situ* observations. *Geophysical Research Letters* 43, 9662–9668. doi:10.1002/2016gl069964

Parkinson, C. L. (2003). Aqua: An earth-observing satellite mission to examine water and other climate variables. *IEEE Trans. Geosci. Remote Sensing* 41 (2), 173–183. doi:10.1109/tgrs.2002.808319

Qiao, P. L., Zhang, J. X., and Wang, C. H. (2007). Soil moisture retrieving by AMSR-E microwave remote sensing data [J]. *Journal of China University of Mining & Technology* 36 (1), 262–265. (in Chinese).

Seneviratne, S. I., Corti, T., Davin, E. L., Hirschi, M., Jaeger, E. B., Lehner, I., et al. (2010). Investigating soil moisture-climate interactions in a changing climate: A review. *Earth-Science Reviews* 99 (3), 125–161. doi:10.1016/j.earscirev.2010.02.004

Shao, C., Wu, D., and Guo, Y. (2020). Comparison of high spatiotemporal-resolution soil moisture observations with CLM4.0 simulations. *Meteorol. Appl.* 27 (3), e1912. doi:10.1002/met.1912

Shi, C. X., Jiang, L. P., Zhang, T., Xu, B., and Han, S. (2014). Status and plans of CMA land data assimilation system (CLDAS) project. *Geophysical Research Abstracts* 16, EGU2014–5671.

Shi, Z., Tao, Y., Jian, Z., and Wu, F. T. (2019). A modeling study of the influence of initial soil moisture on summer precipitation during the East Asian summer monsoon. *Dynamics of Atmospheres and Oceans* 85, 72–82. doi:10.1016/j.dynatmoce.2018.12.003

Song, Y., Lu, Y., Guo, Z., Xu, X., Liu, T., Wang, J., et al. (2019). Variations in soil water content and evapotranspiration in relation to precipitation pulses within desert steppe in inner Mongolia, China. *Water* 11, 198. doi:10.3390/w11020198

Susha, L. S. U., Singh, D. N., and Baghini, M. S. (2014). A critical review of soil moisture measurement. *Measurement* 54 (8), 92–105. doi:10.1016/j.measurement.2014.04.007

Vereecken, H., Huisman, J. A., Pachepsky, Y., Montzka, C., Kruk, J. V. D., Bogena, H., et al. (2014). On the spatio-temporal dynamics of soil moisture at the field scale. *Journal of Hydrology* 516 (17), 76–96. doi:10.1016/j.jhydrol.2013.11.061

Wang, L. L., and Gong, J. D. (2018). Application of two OI land surface assimilation techniques in GRAPES meso. *Meteorological Monthly* 44 (7), 857–868.

Zhu, Y., Li, X., Pearson, S., Wu, D., Sun, R., Johnson, S., et al. (2019). Evaluation of fengyun-3C soil moisture products using *in-situ* data from the Chinese automatic soil moisture observation stations: A case study in henan province, China. *Water* 11, 248. doi:10.3390/w11020248

Zhu, Z., and Shi, C. X. (2014). Simulation and evaluation of CLDAS and GLDAS soil moisture data in China. *Science Technology and Engineering* 14 (32), 138–144.

frontiers | Frontiers in Earth Science

TYPE Original Research
PUBLISHED 19 January 2023
DOI 10.3389/feart.2023.1106204

OPEN ACCESS

EDITED BY
Yunheng Wang,
University of Oklahoma, United States

REVIEWED BY
Nannan Qin,
Fudan University, China
Donglei Shi,
China University of Geosciences, China

*CORRESPONDENCE
Ruifang Wang,
ruifwang@zjnu.edu.cn

SPECIALTY SECTION
This article was submitted to Environmental Informatics and Remote Sensing, a section of the journal Frontiers in Earth Science

RECEIVED 23 November 2022
ACCEPTED 04 January 2023
PUBLISHED 19 January 2023

CITATION
Bi M, Wang R, Li T and Ge X (2023), Effects of vertical shear on intensification of tropical cyclones of different initial sizes. *Front. Earth Sci.* 11:1106204. doi: 10.3389/feart.2023.1106204

Effects of vertical shear on intensification of tropical cyclones of different initial sizes

Mingyu Bi[1], Ruifang Wang[2]*, Tim Li[3] and Xuyang Ge[1]

[1]Key Laboratory of Meteorological Disaster, Ministry of Education (KLME) / Collaborative Innovation Center on Forecast and Evaluation of Meteorological Disasters (CIC-FEMD), Nanjing University of Information Science and Technology, Nanjing, China, [2]College of Geography and Environmental Sciences, Zhejiang Normal University, Jinhua, China, [3]Department of Atmospheric Sciences, University of Hawai'i at Manoa, Honolulu, HI, United States

Idealized experiments were conducted to examine the impacts of moderate vertical wind shear (VWS, i.e., magnitude of 12 m s^{-1}) on the intensification of tropical cyclones (TCs) of different initial sizes. The results showed that the intensity of all the simulated TCs decreased at the first 12-hour integration after imposing the shear. Larger TCs resumed intensification earlier, whereas smaller ones re-intensified more slowly or even failed to intensify. The differences in the intensification rate are likely due to the tilting magnitude. Under VWS, the upper-level TC center exhibited a horizontal displacement relative to the low-level circulation. In general, this displacement was smaller in larger TCs, indicating that larger TCs are less susceptible to VWS. Thermodynamically, the intrusion of mid-level low moist entropy also played a role in suppressing upshear convection. This negative impact was pronounced in smaller TCs. By using the PV-ω equation, the resilience of TC to VWS was compared. The second circulation forced by both dry dynamic and diabatic heating acted to restore the system to a vertically upright position. For larger TCs, more extensive convection was prolific on the downshear side, and its corresponding forced second circulation offset a larger part of the low- to mid-level environmental shear, which made larger TCs more resilient to VWS; i.e., larger TCs produced stronger low to middle counter shear circulation and facilitated vertical realignment. In contrast, for smaller TCs, the updrafts forced by dry dynamic and diabatic heating were deeper but narrower at the initial time, which did not efficiently reduce the mid-level VWS, resulting in greater tilting of the TC, thus making the smaller TCs more vulnerable to VWS.

KEYWORDS

TC intensity, tropical cyclone, size, intensification, vertical wind shear

1 Introduction

Although much work has been carried out to understand changes in intensity of tropical cyclones (TCs), improvement of accuracy in TC forecast is still needed. Difficulties in TC intensity prediction may arise from the complexities of dynamic processes and the various factors involved in modifying TC structure, such as sea surface temperature, environmental vertical wind shear (VWS) and humidity, TC size, and environmental temperature profile. Each aforementioned factor may change TC intensity, but their combined effect remains a major challenge for prediction of TC intensity.

Environmental VWS has long been considered one of the most detrimental factors in TC intensity change. For instance, VWS can modify TC structure and precipitation distribution. VWS may impair TC intensity in several ways. First, the warm core of a TC in the upper levels

may be advected apart from the center of the low-level vortex, which leads to a sea level pressure rise according to the hydrostatic equation (Simpson et al., 1958). Second, VWS may directly magnify the mixing of the dry mid-level air into the moist TC inner core, reducing the amount of work produced by the TC power machine (Tang and Emanuel, 2010; Tang and Emanual, 2012). Third, the shear induced downdrafts may transport mid-level low moist entropy air into the boundary layer, then minimize convection in the eyewall (Riemer et al., 2010). Generally, the detrimental effect of VWS on TC intensity change is roughly proportional to its magnitude (Reasor et al., 2013). Weak vertical shear (with smaller than 5 m s^{-1} between 850 and 250 hPa) has little effect on TC intensity. When the magnitude of VWS increases, the probability of TC intensification decreases. However, the magnitude of VWS alone cannot account for changes in TC intensity. Different TCs under VWS of the same magnitude may have different growth curves, even if their differences are tiny stochastic disturbances in mass or wind fields (Zhang and Tao, 2012; Chen et al., 2019). In addition, VWS also heightens the sensitivity of TC intensity to other dynamic and thermodynamic factors (Emanuel et al., 2004). For instance, if dry air is cyclonically advected into the downshear area, convection on the downshear side, where vigorous convection occurs, will be substantially suppressed (Ge et al., 2015). In short, the development of TC intensification is slowed, or even decays, due to the combined effects of VWS and humidity. In addition, a TC with a small Coriolis parameter is more susceptible to vertical shear, and its development is suppressed much more than it would otherwise be without shear (Bi et al., 2018).

In reality, it is not only the magnitude of VWS that relates to TC intensity change; its vertical profile can also affect TC intensity. When a TC is exposed to VWS of shallow depth, the TC is more prone to fail to develop (Finocchio et al., 2016). The height of VWS also influences the TC intensification rate. VWS in upper levels seems to have diminished effects in impeding the development of TCs (Finocchio et al., 2016; Dai et al., 2021). Numerous simulations have shown that by specifying the same magnitude of VWS, but changing rotations with height, the TC intensifies at a higher rate than the anticlockwise rotating mean wind (Onderlinde and Nolan, 2014). The authors argued that it is the helicity of environmental wind that acts to modulate the TC intensification rate (Chen et al., 2006). The orientation of low-level mean flow with respect to the vertical shear also has a relationship with TC intensification and expansion (Chen et al., 2019; Chen et al., 2021). Meanwhile, surface environmental wind plays a role in modulating the locations of convection excited in the core region (Rappin and Nolan, 2012). If the surface zonal wind is negative under westerly shear, the convection preferentially happens in the downshear left semicircle. This process favors the updrafts propagating cyclonically into the upshear region and constrains the magnitude of the vortex tilt, thus acting to reduce the adverse effect of vertical shear (Shi and Chen, 2021; Huang et al., 2022). The evolution of TCs of different size shows diversity under the same VWS. Although previous studies have implied that strong TCs are more resilient to VWS (Reasor et al., 2004; Zhang, 2005; Zhang and Kieu, 2006; Reasor and Montgomery, 2015), one remaining issue is whether the process is size-dependent. Through this study, we revealed underlying processes affecting structural changes under VWS, with the main purpose of identifying the effects of VWS modulated by TC size.

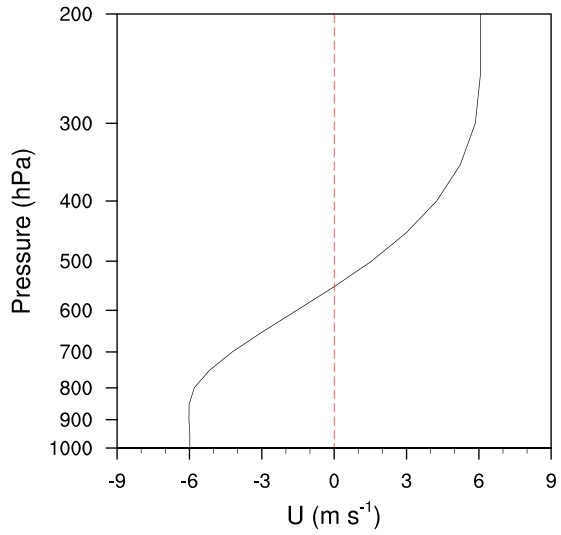

FIGURE 1
Vertical profile of environmental zonal wind (m s^{-1}).

The remainder of this article is organized as follows. Section 2 describes the configurations of the experimental simulations and the preliminary results. Section 3 shows the major differences of the dynamic and thermodynamic aspects of relatively small and large TCs under similar VWS. Section 4 describes use of the PV-ω equation to characterize shear induced vertical motion, for which we provide possible mechanisms accounting for intensity change associated with the effect of VWS. Conclusions and discussion are included in the final section.

2 Experimental design

In this study, the WRF_ARW model (version 4.2) was employed to investigate the changes in intensity of TCs of different sizes under a westerly VWS of 12 m s^{-1} between 850 and 200 hPa. Following Bi et al. (2018), the zonal environmental wind was introduced according to

$$u(p) = \begin{cases} u_b & p > p_b, \\ \cos\left(\dfrac{p - p_t}{p_b - p_t}\pi\right).(u_t - u_b)\Big/2 & p_t < p < p_b, \\ u_t & p < p_t, \end{cases} \quad (1)$$

where u is zonal wind, p is pressure, u_b, the wind at low levels, is set to −6 m s^{-1}, u_t, the wind at tropopause, is set to 6 m s^{-1}, p_b is 850 hPa, and p_t is 250 hPa. Using the NCEP final analysis data, the sounding was obtained by averaging over the region (120-140 °W, 10-25 °N) during the TC season (June–October) from year 2010 to 2020. Figure 1 shows the vertical profile of the VWS. In other words, the mean wind was easterly in the low levels and westerly in the upper levels.

The model domains were triply nested. The three domain resolutions were 18, 6, and 2 km, and the domain sizes were 361x361, 451x451, and 451x451, respectively. The model vertical level was 41. The innermost two nests had two-way interaction. The physical parameterization schemes in cumulus, microphysics, boundary, and longwave and shortwave radiation were Grell–Freitas

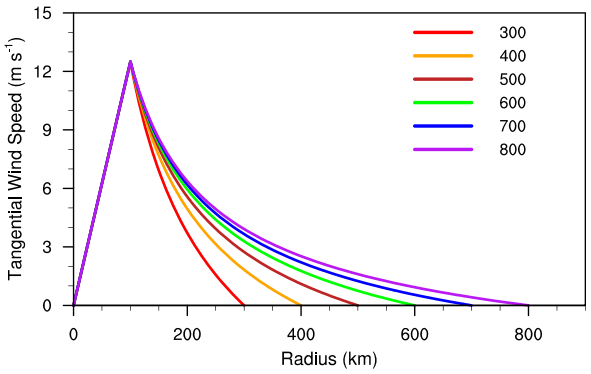

FIGURE 2
Initial surface tangential wind profiles in EXP300 (red), EXP400 (orange), EXP500 (brown), EXP600 (green), EXP700 (blue), and EXP800 (purple).

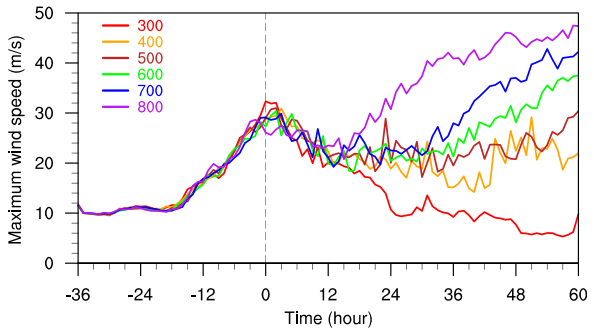

FIGURE 3
Time series of maximum surface winds of the experiments (m s^{-1}). The red dashed line indicates the imposed shear time. The red, orange, brown, green, blue, and purple solid lines indicate the intensity changes of TCs in EXP300, EXP400, EXP500, EXP600, EXP700, and EXP800, respectively.

(Grell and Freitas, 2014), WSM6 (Hong and Lim, 2006), YSU (Hong et al., 2006), and RRTMG (Iacono et al., 2008), respectively.

Six vortexes with the same maximum surface wind but different sizes were separately embedded in a quiescent environment. SST was uniformly set to 29°C, and the Coriolis parameter was set to the value of latitude of 15 oN across the domain. The initial wind profiles of the six vortexes at the surface are shown in Figure 2. The wind profile was developed based on the modified Rankine vortex (Wang and Li, 1992), and the formula used to generate the wind profile of a TC is as follows:

$$v = \begin{cases} v_m\left(\frac{r}{r_m}\right) & (r \le r_m), \\ v_m\left(\frac{r}{r_m}\right)^{-b} - \left|\frac{r - r_m}{r_0 - r_m}\right| v_m\left(\frac{r}{r_m}\right)^{-b} & (r_m < r \le r_0), \end{cases} \quad (2)$$

where v is the tangential wind, r_m is the radius of maximum wind, v_m is the magnitude of maximum wind, and b is a parameter control of the shape of wind profile, respectively. The variable r_0 is the radius of wind vanishing. The variables v_m, r_m, and b were set to 12 m s^{-1}, 100 km, and 0.75, respectively. The only difference among the initial vortexes was r_0. More specifically, r_0 was set to 300, 400, 500, 600, 700, or 800 km. For simplicity, these experiments will be hereafter referred to as EXP300, EXP400, EXP500, EXP600, EXP700, and EXP800, respectively.

Provided that a larger TC will maintain its larger size in observation and simulation (Wang and Holland, 1996; Wang et al., 1997; Xu and Wang, 2010a; Lee et al., 2010), a vortex with a larger initial size could generate a larger TC in the first 36 h integration, during which the model spins up the storm. After the spin up period, the VWS was imposed. The wind and temperature in the outermost domain were nudged to ensure the VWS could continuously exert its influence on the TC circulation. Because a TC may deflect from its original position during integration (Wu and Emanuel, 1993; Wang and Holland, 1996), the two innermost domains were configured vortex following.

3 The simulated results

The resultant changes in intensity of the experimental TCs are shown in Figure 3. All the vortexes intensified at roughly the same rate (Xu and Wang, 2010b; Ge et al., 2015). After the VWS was added, the intensity of the smaller TCs dropped more rapidly than their larger counterparts despite a small TC (in EXP300) that had higher maximum surface wind at the time that shear was imposed. The larger TCs resumed intensification earlier than the smaller ones, while the smaller TCs had more delayed intensification or failed to intensify.

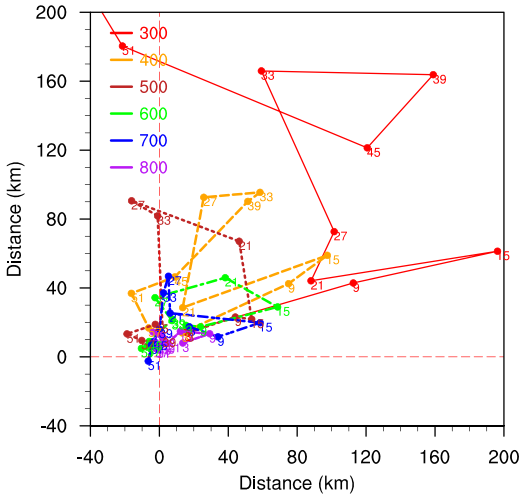

FIGURE 4
Position of the vortex center at 8 km relative to the vortex center at 2 km in EXP300, EXP400, EXP500, EXP600, EXP700, and EXP800. The numbers indicate the simulation time, and the relative positions are labeled every 6 h.

Previous studies have shown that the realignment of the TC vortex is essential for a TC to intensify (Reasor et al., 2004; Finocchio et al., 2016). To this end, Figure 4 describes the evolution of the process of tilting under shear. At the early stage, the vortex centers tilted northeastward in all the experiments. The magnitudes of tilting in all experiments increased during the first 12 h. Thereafter, the larger TCs became less tilted, whereas the smaller TCs displayed a large amount of tilt without any precession and realignment processes.

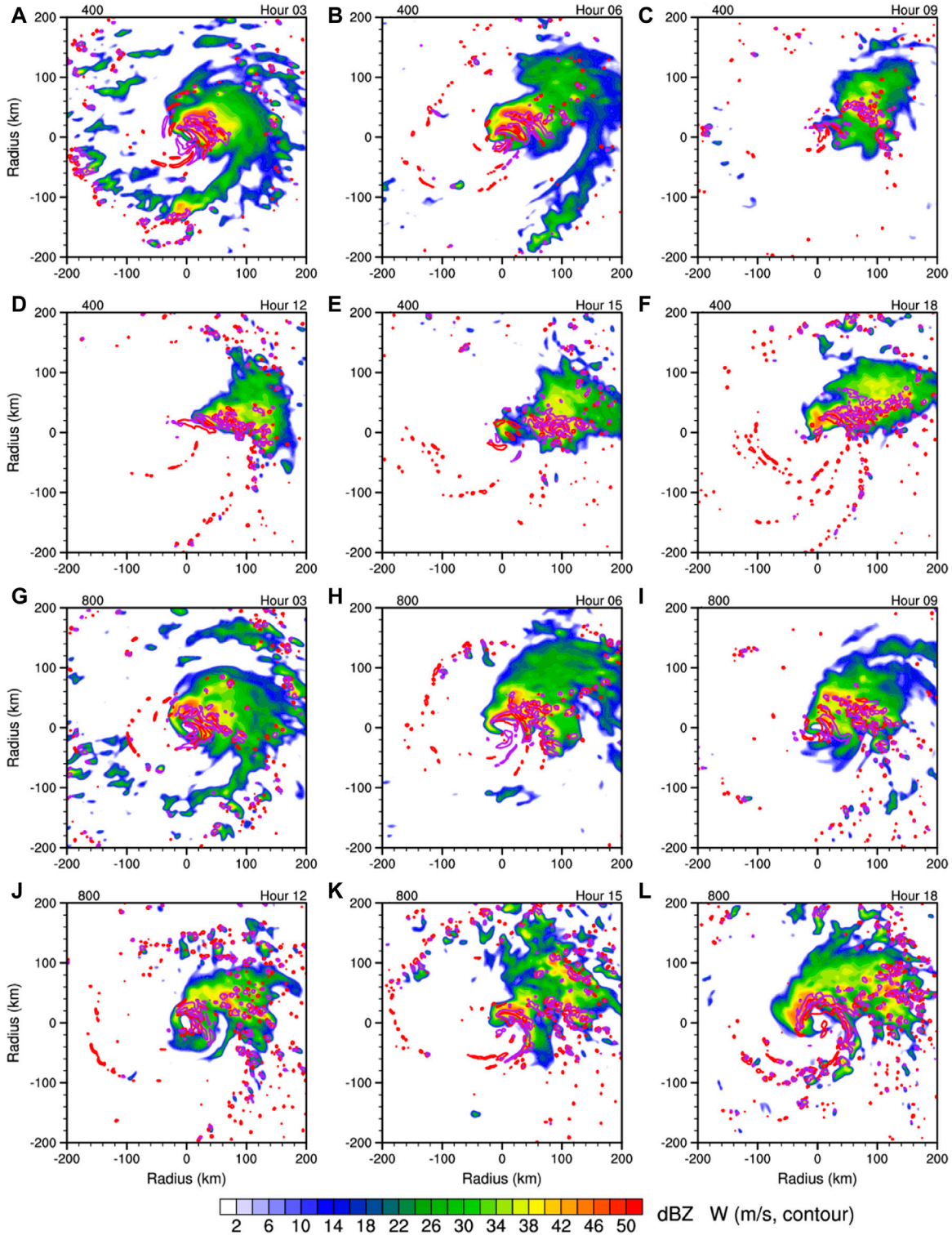

FIGURE 5
Evolution of the radar reflectivity (shaded, dBZ) at 1.5 km and vertical velocity (contour at 0.5 m s^{-1}) at 1.5 (red) and 5 (purple) km in the first 18 h. **(A–F)** Data from EXP400. **(G–L)** Data from EXP800.

Comparison of tilting magnitude in Figure 4 and the change in intensity in Figure 3 indicated that the configuration of tilting upshear was coincident with the onset of intensification. It was clear that the initially larger TCs had smaller magnitude of tilting and realigned more rapidly compared to the smaller ones. These results agree with results reported by Finocchio et al. (2016), which indicated that tilting into the upshear-left quadrant can be considered a precursor to intensification.

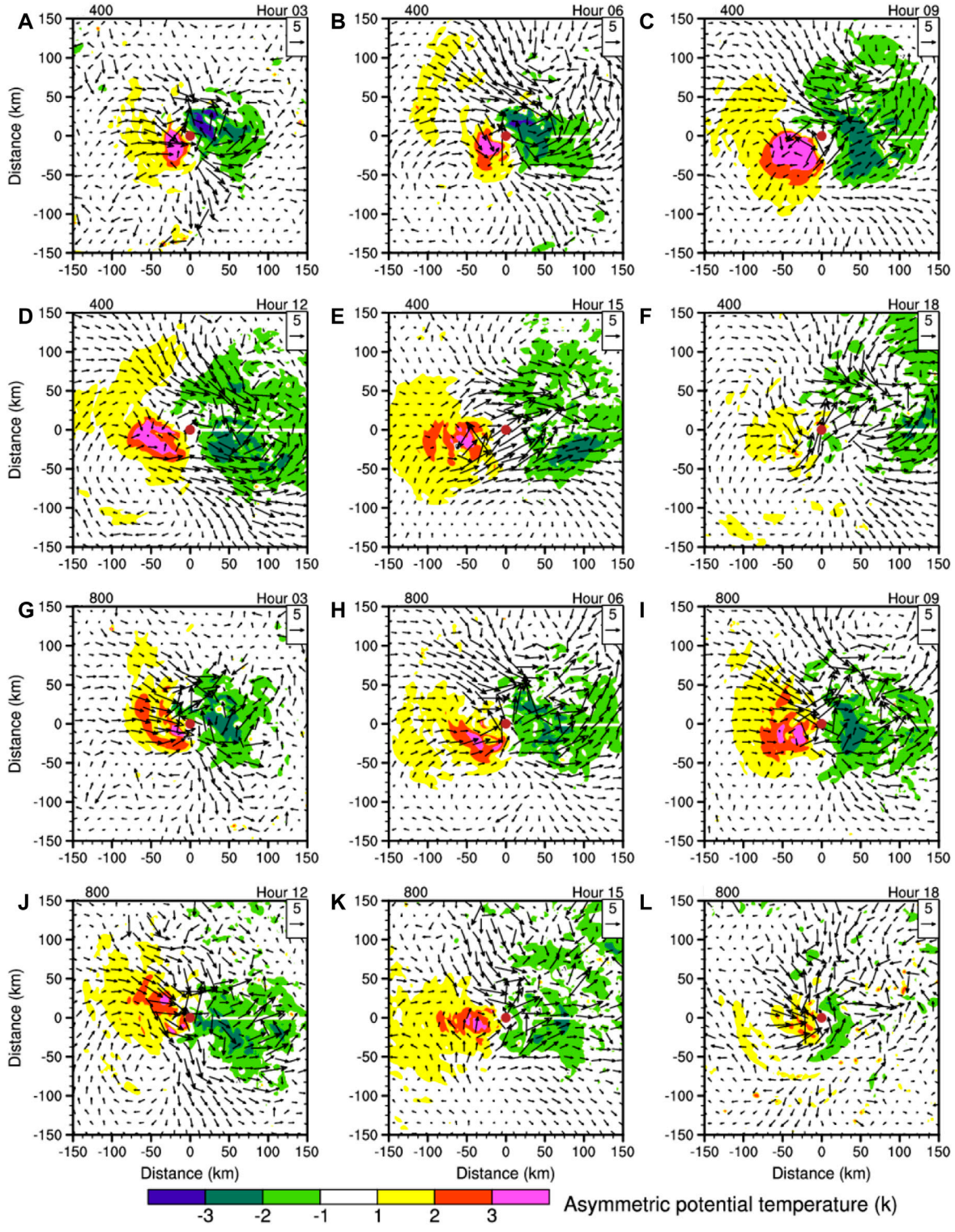

FIGURE 6
Evolution of diabatic heating (k hour^{-1}) at 3 km, asymmetric potential temperature (blue contours at −3, −2, and −1 K and red contours at 1, 2, and 3 K) at 5 km, and asymmetric winds (vector, m s^{-1}) at 5 km at hour 3, 6, 9, 12, 15, and 18. **(A–F)** Data from EXP400. **(G–L)** Data from EXP800. Brown dots indicate the vortex centers at 5 km.

After the VWS was imposed, the maximum surface wind of all the experiments showed a drop off in the first 12 h. To demonstrate this feature, two experiments, EXP800 and EXP400, were selected to represent large and small TCs, respectively. EXP800 began to intensify at hour 15, while EXP400 persisted in low intensity. As a result, a remarkable difference in TC structure was observed in the first 15 h. The radar reflectivity of these two cases is compared in Figure 5. Most convection in the outer core region in both cases was enhanced

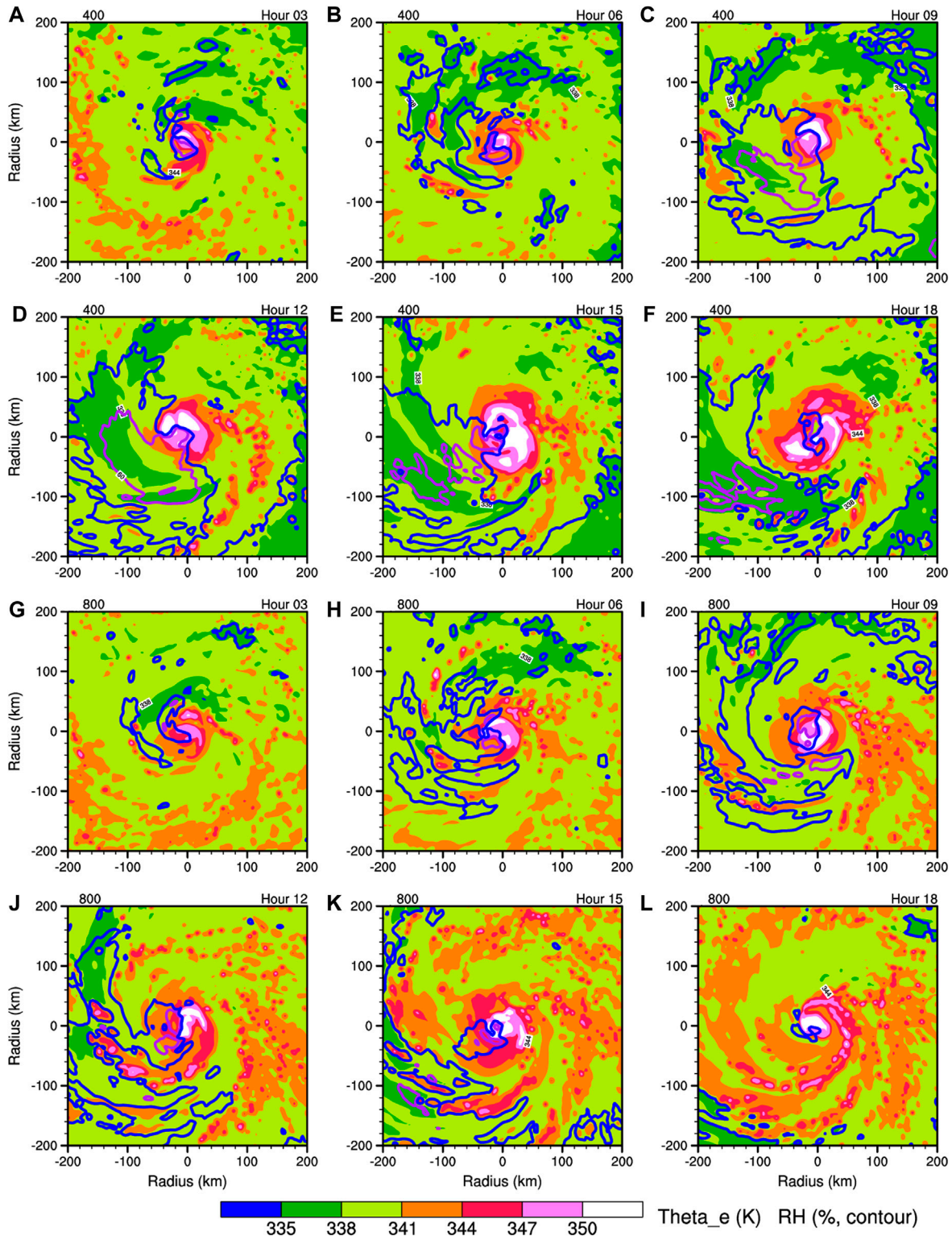

FIGURE 7
Evolution of θ_e (shaded, K) and relative humidity (contour) at 3 km at hour 3, 6, 9, 12, 15, and 18. Purple and blue contours are at 60 and 70%, respectively. **(A–F)** Data from EXP400. **(G–L)** Data from EXP800.

on the downshear side, especially in the downshear-left quadrant. In EXP400, the convection shrank rapidly in the first 12 h. In contrast, the convection in EXP800 seemed more vigorous. Although the upshear semicircle was unfavorable for the development of convective cells, the convection in larger TCs was able to survive the adverse condition and eventually propagate cyclonically into the upshear left quadrant. Huang et al. (2022) pointed out that the corresponding divergence wind of upshear convection counteracts

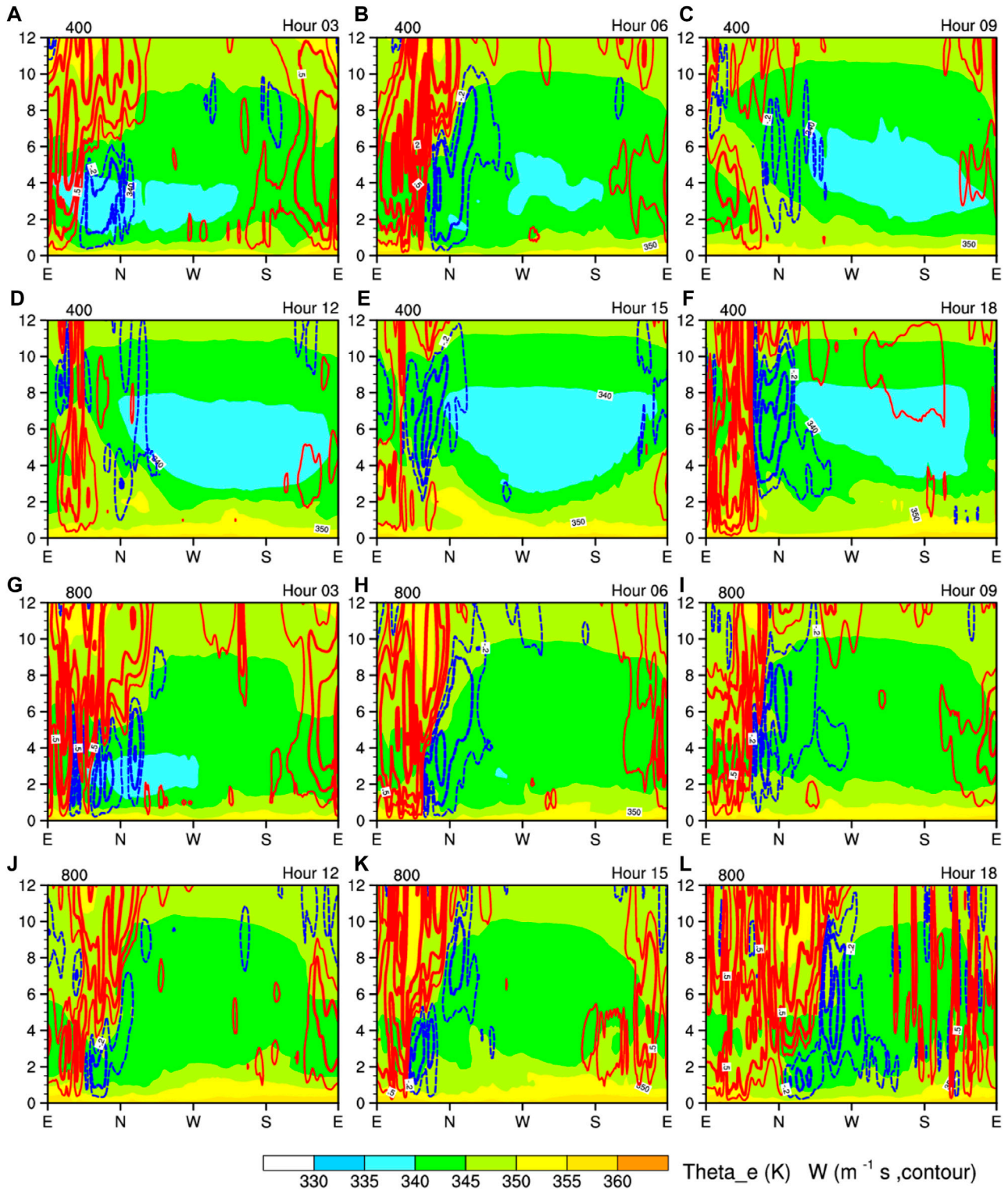

FIGURE 8
Vertical section of θ_e (K, shaded) and vertical velocity (m s^{-1}, contour) of ring-band average between radii at 30–80 km at hour 3, 6, 9, 12, 15, and 18. The contours are at -4, -2, -1, -0.5, -0.2, 0.2, 0.5, 1.0, 2, and 4 m s^{-1}. The E, N, W, S on the *X*-axis indicate the east, north, west, and south directions, respectively. **(A–F)** Data from EXP400. **(G–L)** Data from EXP800.

the storm-relative flow, thus decreasing the magnitude of VWS and minimizing the detrimental effects of VWS. This is also called the "outflow blocking" effect (Ryglicki et al., 2019; Shi and Chen, 2021). In this regard, the vertical velocities at different levels were compared (Figure 5). Basically, the updrafts on the upshear side were significantly suppressed. The low-level updrafts were generated in

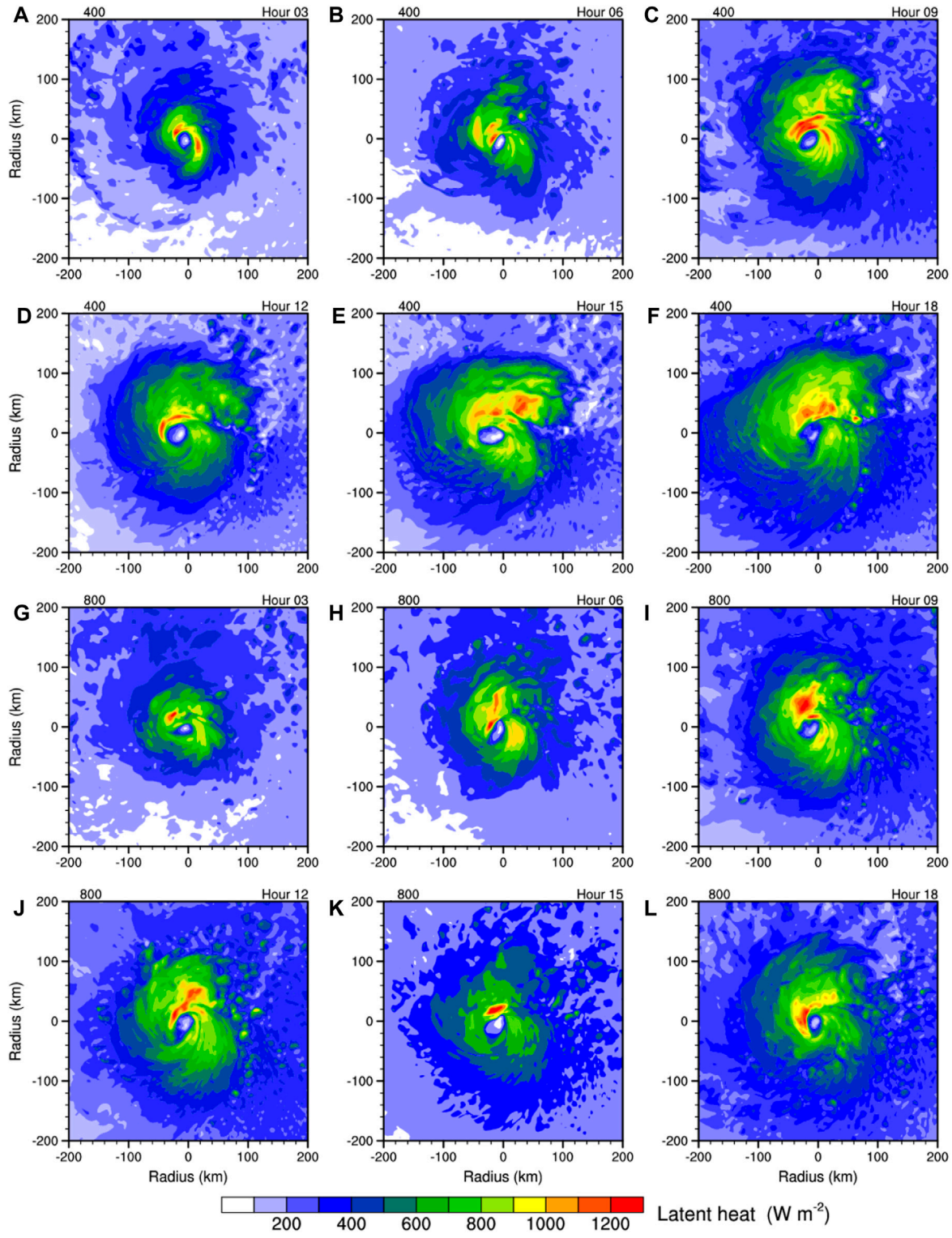

FIGURE 9
Evolution of latent heat (W m^{-2}) flux from the surface in EXP400 **(A–F)** and EXP800 **(G–L)**.

the vicinity of the TC, whereas the majority of updrafts in the upshear semicircle failed to penetrate the middle and upper troposphere, or were advected far away from the low-level vortex center in small TCs after hour 9. Conversely, the vertical motions in EXP800 at 5 km were much closer to the vortex center and eventually propagated into the upshear quadrant.

Jones (1995) argued that a balanced positive potential temperature θ anomaly exists in the middle levels over the low-level storm center,

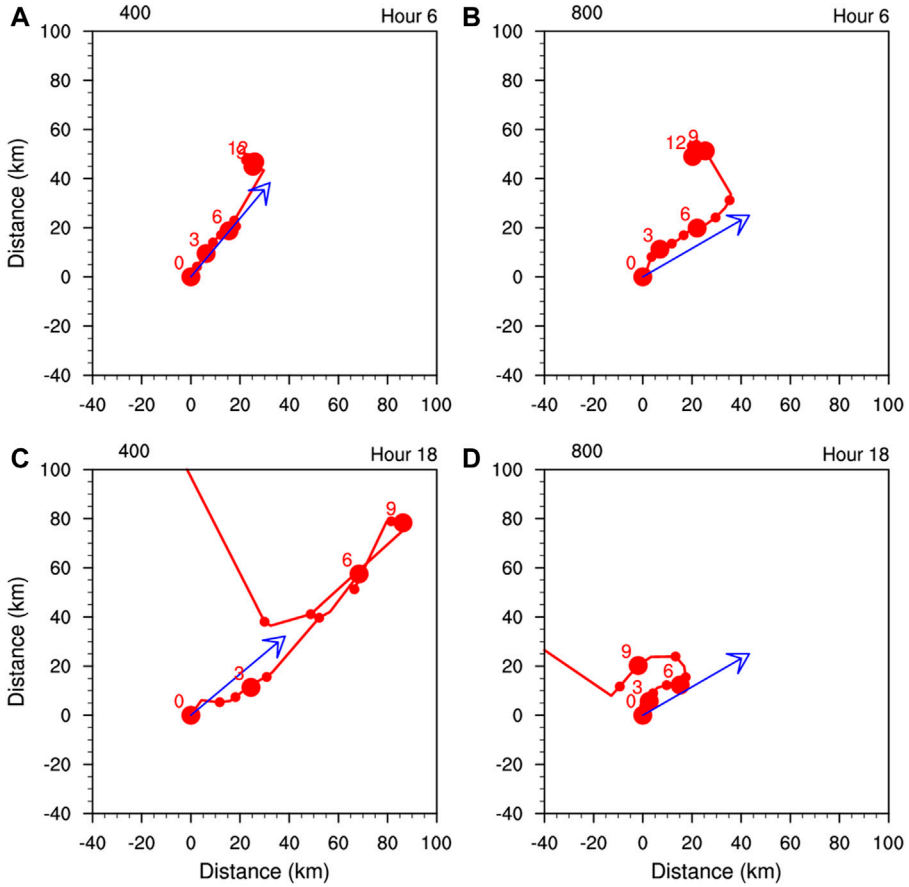

FIGURE 10
Hodographs of the vortex centers at different heights (km); **(A,C)** show data from EXP400 and **(B,D)** show data from EXP800; **(A,B)** are at hour 6 and **(C,D)** are at hour 18. Small dots are plotted every 1 km, and large dots are plotted every 3 km. Numbers indicate the height (km) of the vortex center. The titling direction is indicated by the blue vector.

corresponding to the tilting vortex. This θ anomaly acts to reduce the updrafts on the upshear side. The diabatic heating, asymmetric θ, and asymmetric flow are also shown in Figure 6. Physically, the temperature anomalies shown in Figure 6 are more related to the adiabatic warming and cooling of descent and ascent forced by the vertical shear (Zhang, 2005; Zhang and Kieu, 2006). The diabatic heating seemed to contribute little to this upshear warming and downshear cooling signature since positive heating presented in the negative θ anomaly region. The upshear warming and downshear cooling signature was not pronounced at lower and higher levels (figure not shown), which is probably due to the confounding effects of diabatic condensation heating and evaporation cooling. The θ anomalies resulted in an isentropic rise on the downshear side and lowering on the upshear side. Therefore, the cyclonic rotated air parcels along the isentropes tended to rise on the right of shear and descend on the left of shear. Assuming there is no diabatic heating or cooling, the cyclonically rotated air parcel near the TC center will ascend in the north semicircle and descend in the south semicircle along the slantwise θ surface. By this reasoning, the ascent to the right of VWS in EXP400 would be expected to be larger than that in EXP800, owing to the larger magnitude of the gradient of θ along the azimuth. Nevertheless, the ascent on the left-of-shear side was more restrained in EXP400, which was due to the intrusion of low equivalent potential temperature θ_e from middle levels. The distributions of θ_e at 3 km are shown in Figure 7. The initial distributions of θ_e were roughly the same pattern, and there was no significant discrepancy between the two initial fields. Over time, the difference in θ_e between the two cases became more apparent. The low θ_e gradually covered the upshear region and eventually intruded into the eyewall region at 12 hours in EXP400. This undoubtedly dampened the development of convection. This mid-level ventilation of low moist entropy diluted the inner core, which lessened the work carried out by the Carnot cycle and thus resulted in a reduction in kinetic energy transformed, as well as decreased intensity of the TC in terms of surface maximum wind (Riemer et al., 2010; Tang and Emanuel, 2010).

The radial band average of θ_e and vertical velocity between the radii at 30–80 km indicated that strong positive vertical velocities were excited on the downshear side (Figure 8). On the left-of-shear side, the strong low- and mid-level downdrafts were likely related to diabatic cooling associated with stratiform precipitation. In EXP800, at 15 hours, the cyclonic spiring up of updrafts finally reached the upshear direction. These updrafts acted to reduce the effects of VWS *via* two main pathways. First, the release of diabatic heating in the ascent on the upshear side contributed to the pressure fall at middle levels, which favored the realignment of the TC; second, the

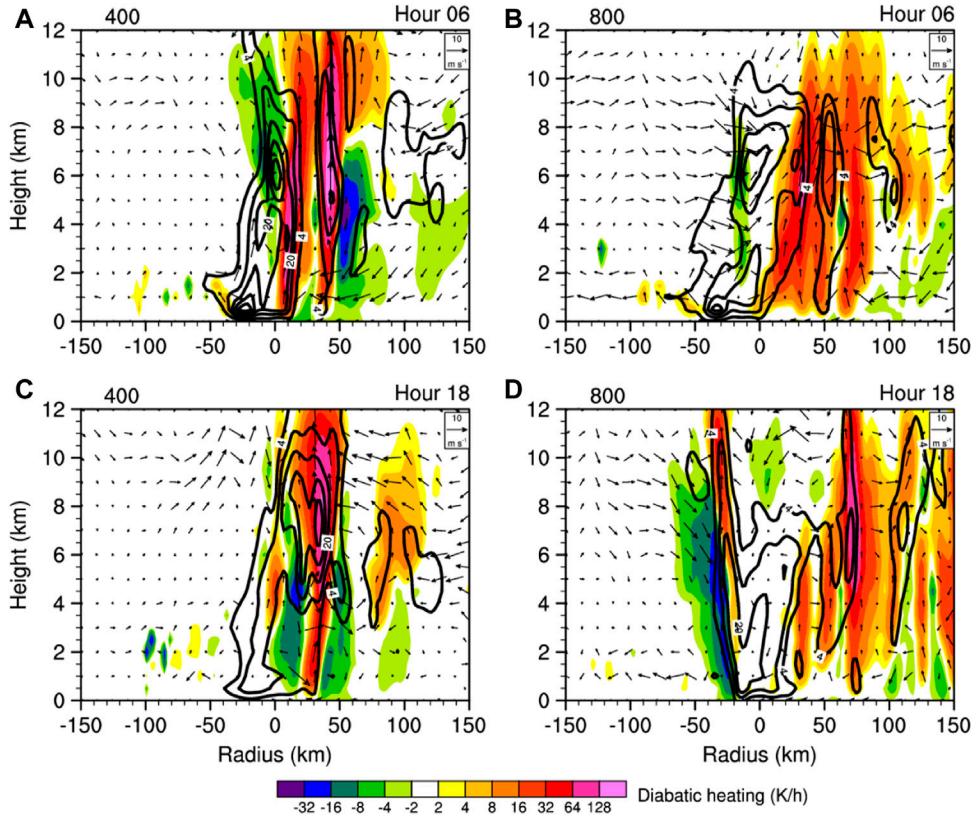

FIGURE 11
Vertical section of diabatic heating (k h^{-1}) and potential vorticity (contours at 4, 12, 20, and 28 PVU) across the TC center along the vector shown in Figure 10. **(A,C)** Data from EXP400 at hour 6 and 18, respectively. **(B,D)** Data from EXP800 at hour 6 and 18, respectively.

upper-level divergence wind induced by the updrafts reduced the storm-relative flow, hence minimizing the detrimental effects of VWS. The presence of rotating updrafts in the upshear direction was coincident with the onset of intensification in Figure 3, which can be considered a precursor to intensification. Unlike in EXP800, the updrafts in EXP400 did not continually rotate cyclonically into the upshear region and failed to cancel out the detrimental effects of VWS. Not only were the updrafts in the upshear left quadrant suppressed but also the ascent on the right-of-shear side was influenced by the lower θ_e. In EXP400, the upshear mid-level θ_e was particularly low, which may have been caused by the downward transport of the environmental mid-level θ_e. The ascent excited at low levels may have been diluted by the relatively dry surrounding air and thereby lost its potential to rise further. Therefore, even though a relatively large θ_e existed on the shear right side, the upward motions were only active in the lower levels in this region in EXP400. Previous studies proposed that upward projection of a low-level vortex and downward projection of an anticyclone make the TC mid-vortex center rotate cyclonically with respect to the low-level center (Wu and Emanuel, 1993; Jones, 1995; Riemer et al., 2010). In this study, the asymmetric flow in the mid-level seemed disordered and unsystematic and did not show significant northwestward transverse flow across the vortex center arising from the projection of low- and high-level vortexes.

Energy input from the surface may have significant effects on convection near the TC center (Xu and Wang, 2010a; Chan et al., 2019). The surface latent flux was not significantly different near the TC center when comparing large and small TCs (Figure 9), indicating that the surface latent heat flux did not directly influence the changes in intensity and that those changes were more related to the dynamic and thermodynamic processes associated with VWS.

4 Evaluation of the forced second flow

The vortex centers at each level were examined to characterize vortex tilting magnitude and direction (Figure 10). The vortex center did not rotate cyclonically with height and tilted almost linearly at low and middle levels. It is interesting that the upshear shifting of the upper-level center preceded that of the low and middle levels. This is counterintuitive considering that the upper levels have the largest storm-relative wind, and the vortex centers in these levels would be advected farther. Moreover, small TCs tilted more northward, and the tilting magnitude of large TCs decreased, whereas that of small TCs increased, over time.

Corbosiero and Molinari (2002) argued that the resilience of TCs to VWS was subject to the Vortex Rossby wave, which acted as a precession process to offset the detrimental effects of VWS. Nevertheless, we believe the shear-induced structural changes of TCs themselves resist the shear since the prominent feature of a shear TC is enhanced quasi-steady convection to the left-of-shear, which does not exhibit obvious wave-like characteristics.

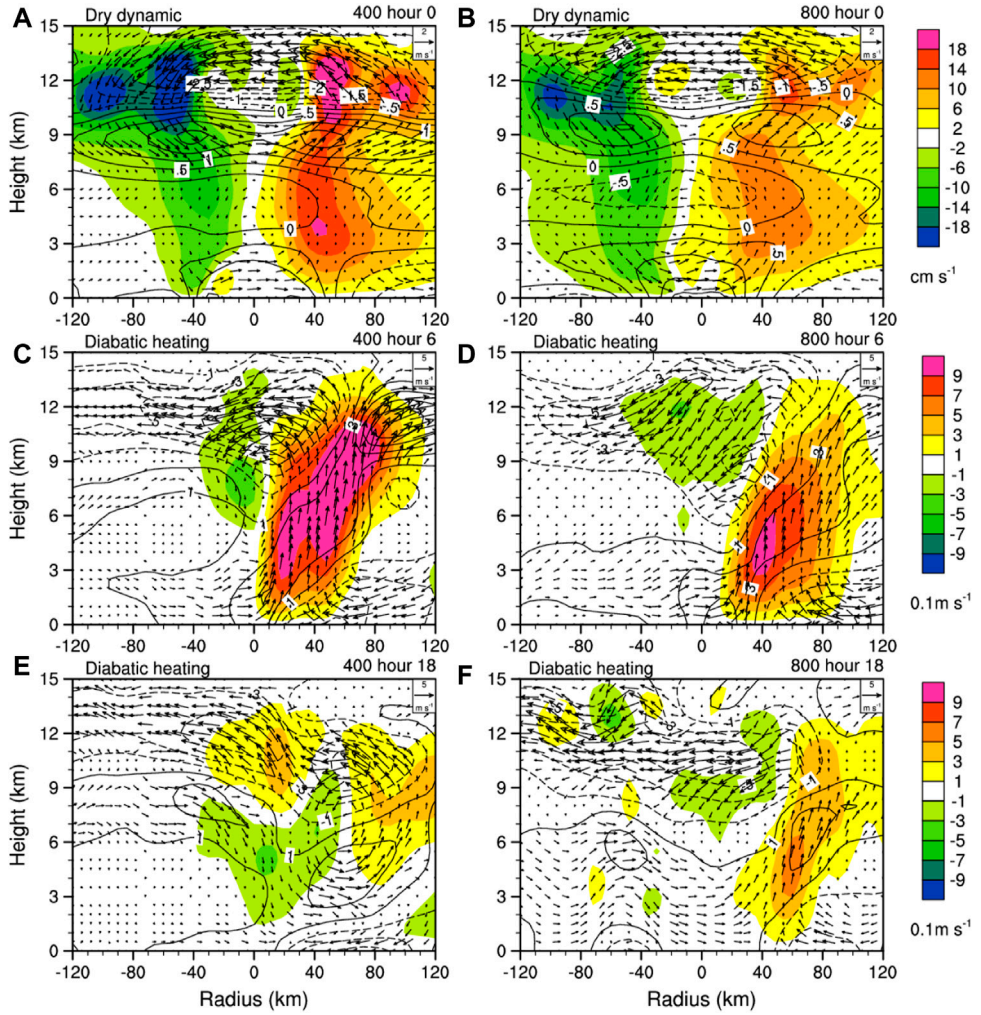

FIGURE 12
Shear induced second circulation. Shading indicates the induced vertical velocities (m s^{-1}), the vectors denote the in plane horizontal and vertical winds, and the contours indicate the magnitudes of divergence wind. The top panels are the dry dynamic-induced vertical velocity at hour 0 in EXP400 **(A)** and EXP800 **(B)**. **(C–F)** Vertical section of the diabatic heating induced divergence wind and vertical wind (vector) along the tilting vector shown in Figure 10.

To evaluate the changes of second circulation of TCs, the PV-ω equation was used (DeHart et al., 2014). This equation describes the vertical motions forced by dry dynamic and diabatic heating and friction, given a non-divergent balanced vortex. Once ω is derived, its corresponding divergence and convergence winds can be obtained.

The diabatic heating in the west–east direction in the eyewall region was slightly greater and extended vertically higher in EXP400 than in EXP800 at 6 hours, whereas the horizontal distribution of diabatic heating in EXP800 became wider (Figure 11). In EXP800, the broader diabatic heating may have arisen from stronger surface heat flux induced by stronger outer core surface winds (Xu and Wang, 2010b). This broader convection may have induced more extensive low-level convergence and mid-to high-level divergence. The corresponding divergence winds may have influenced the shifting of the vortex center, and thus sequential vertical realignment.

First, we tested the resilience of different sized TCs under the same VWS in an adiabatic framework. At the initial time point, since the inserted TC was symmetric, there was no asymmetric second circulation forced by diabatic heating. When the VWS was imposed on the initial vortex (hour 0), the ascent was excited on the downshear side and the descent on upshear side (Figures 12A, B). Since the maximum tangential wind of TC in EXP400 was a little larger and closer to the TC center than that in EXP800, the vorticity maxima of the TC in EXP400 was larger as well. According to the PV-ω equation, the vertical velocity is proportional to the vertical differential of horizontal vorticity advection. The horizontal gradient of vorticity was certainly larger in EXP400, thus leading to greater vorticity advection and then greater magnitude of vertical velocities. Furthermore, the environmental temperature gradient point to right-of-shear, reflecting the horizontal advection of temperature, was positive (negative) on the downshear (upshear) side. This led to the generation of updrafts downshear (downdrafts upshear). Both processes accounted for the generation of forced secondary circulation (FSC). Meanwhile, diabatic heating played an important role in producing the FSC. Figure 12 shows second circulation forced by diabatic heating along the tilting vector. Apparently, the divergence wind induced by the dry dynamics and

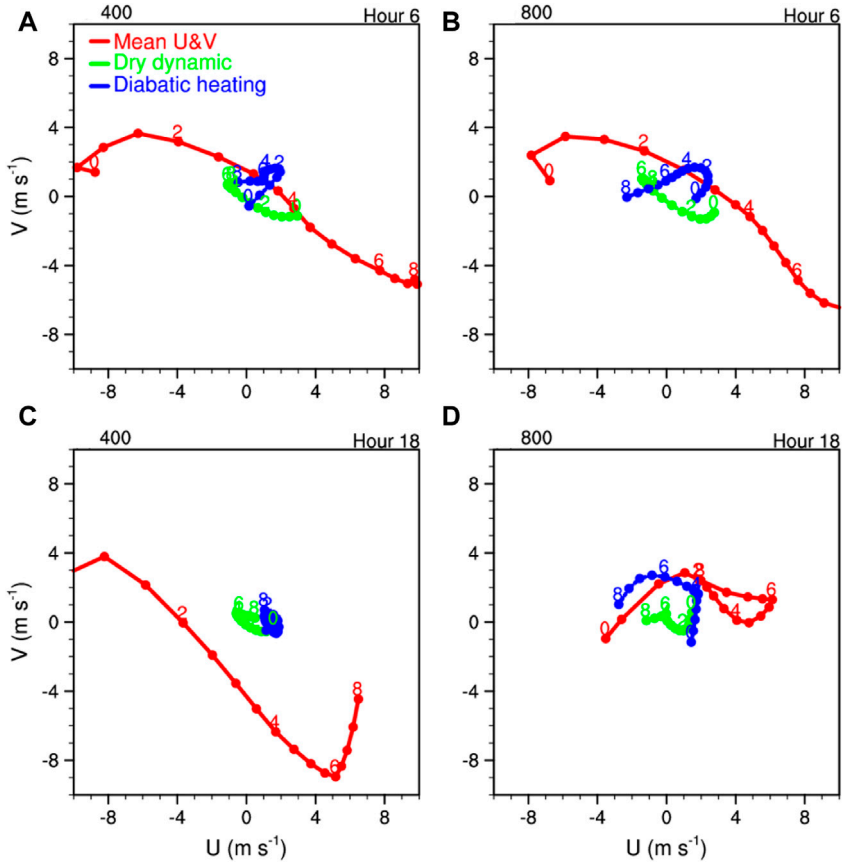

FIGURE 13
Hodographs of the divergence wind forced by dry dynamic heating (green), diabatic heating (blue), and the mean horizontal wind (red) averaged within a 50-km radius centered in the eye. Each dot indicates a 0.5 km height increment, beginning at the surface and ending at 8 km. **(A,C)** Data from EXP400. **(B,D)** Data from EXP800. **(A,B)** are at hour 6, and **(C,D)** are at hour 18.

diabatic heating acted to oppose the tilting and helped move the vortex back toward vertical realignment.

The broader inner core vorticity in the larger TC produced a wider second circulation. Although the larger TC had a smaller vertical wind maximum, its ascent in the eyewall region was wider and shallower, which provided stronger convergence wind at low levels and divergence wind at middle and upper levels. As shown in Figure 12, although smaller TCs can excite stronger vertical velocity maxima, their ascending flow extends into high levels and the divergence and convergence winds nearly all concentrate at very high and low altitudes. Specifically, the divergence wind at middle levels in smaller TCs was considerably weaker than that in larger TCs. As a result, the convergence and divergence winds corresponding to the updrafts and downdrafts in the core region could offset more detrimental effects of environmental shear at low and middle levels. The mean induced divergence wind forced by dry dynamics and diabatic heating and the total mean winds are shown in Figure 13. The magnitude of mean winds averaging a radius of 50 km forced by dry dynamic and diabatic heating were almost all on the same order, and both dry dynamic and diabatic heating acted to offset the environmental shear. Indeed, the counter shear circulation is slightly greater in larger TCs. In smaller TCs, the induced second circulation could not efficiently offset the low- and mid-level VWS, which made the smaller TCs tilt significantly and become more susceptible to VWS. The reason we focused on shear in the low and middle levels is that the detrimental effects of shear at upper levels have been shown to be relatively weak (Finocchio et al., 2016; Dai et al., 2021). The wind shear at upper levels can be easily offset by the outflow of asymmetric convective activities. This was demonstrated by the shifting of the vortex center at upper levels. In both small and large TCs, the shifting of vortex centers toward the upshear direction at upper levels precedes the shifting at low and middle levels, which is pronounced in the hour 18 data presented in Figure 10.

5 Conclusions and discussion

In this study, we modeled the effects of initial TC size on storm intensity in the presence of VWS. By specifying the same sounding and uniform SST, under the same VWS, we demonstrated size-dependent evolution of TC intensity. That is, the intensity of smaller TCs tended to decrease more rapidly than that of larger TCs. Detailed examination of the structure of the simulated TCs showed that the vortex center tilted more in smaller TCs. The re-intensification of a TC is indicated by the process of the TC eyewall resuming an upright position. An erect eyewall can not only produce stronger vertical motions but also reduce the interface area between the eyewall and the environment, thus decreasing the entrainment of environmental low entropy air into the eyewall.

Possible mechanisms are proposed. It was expected that the adjustment of the TC in response to VWS would act to oppose the shear forced tilting. Use of the PV- ω equation illustrated that, in the presence of VWS, both dry dynamic and diabatic heating can produce second circulation. The ascent and descent were excited on the downshear and upshear sides, respectively. As a consequence, the corresponding divergence (convergence) wind at upper (low) levels and convergence (divergence) wind at low (upper) levels, combining the updrafts downshear and downdrafts upshear, resulted in counterclockwise circulation across the eye. This counterclockwise circulation canceled out part of the environmental VWS, thus decreasing the actual magnitude of VWS.

The larger TC eyewall resumed its upright status faster than did the smaller TC. First, the counter shear circulation induced by asymmetric vertical motion was shallower in larger TCs due to the relative shallow extent of vertical convection; therefore, the cross eye counter shear circulation was shallower than that in small TCs. As a result, the environmental vertical shear was reduced more at low and middle levels. Hence, larger TCs can survive the destructive effects of VWS. Second, the larger TC has a larger eyewall radius. Even with the same magnitude of vortex center tilt, there is more opportunity for the convection to cyclonically rotate into the upshear region in larger TCs due to the larger eyewall radius. The slantwise rising ascent and its divergence and convergence winds act to oppose the shear forced tilt and account for the resilience of the vortex to VWS. In dry model framework, Black et al. (2002) pointed out that, in the absence of diabatic heating, VWS can result in downdrafts and updrafts on the downshear and upshear sides. The downdrafts and updrafts associated divergence wind may also help move the vortex back toward vertical orientation. This accounts for the precession process and provides a rationale for why the vortex center was not advected further by the environmental shear. In the presence of diabatic heating, the VWS at upper levels was strongly offset by the shear forced circulation. The horizontal branch of counter shear circulation was remarkably strong at the upper levels, which was recognized as the outflow blocking effect, which substantially reduced, or even reversed, the advection storm center at upper levels. In short, our data demonstrates that larger TCs have stronger forced second circulation and are therefore more resilient to the detrimental effects of VWS.

The intrusion of upshear low moist entropy may also play a role in weakening small TCs. That is, the downward deposition of low moist entropy flux can reduce emergence into the eyewall region, thus weakening the TC. When the low entropy approached the upshear eyewall, it was transported downward by shear forced downdrafts or diabatic cooled descent. Once this low moist entropy air was advected into the eyewall, the intensity of the TC deceased significantly. Further study is needed to investigate these ventilation pathways in more detail, and to assess to what extent low moist entropy can change the intensity of TCs.

Data availability statement

The raw data supporting the conclusion of this article will be made available by the authors, without undue reservation.

Author contributions

MB prepared all the figures in the manuscript, RW completed all diagnostic analyses, XG contributed significantly to writing the manuscript, and TL provided many useful ideas and comments.

Funding

This work was jointly sponsored by the National Natural Science Foundation of China (42088101), the National Science Foundation of China (Grants 41805039 and 42175003), and the Natural Science Foundation of Zhejiang Province (LQ22D050002).

Acknowledgments

The authors acknowledge the High Performance Computing Center of Nanjing University of Information Science and Technology for their support of this work.

Conflict of interest

The authors declare that the research was conducted in the absence of any commercial or financial relationships that could be construed as a potential conflict of interest.

Publisher's note

References

Bi, M., Ge, X., and Li, T. (2018). Dependence of tropical cyclone intensification on the latitude under vertical shear. *J. Meteor. Res.* 32, 113–123. doi:10.1007/s13351-018-7055-4

Black, M. L., Gamache, J. F., Marks, F. D., Samsury, C. E., and Willoughby, H. E. (2002). Eastern pacific hurricanes jimena of 1991 and olivia of 1994: The effect of vertical shear on structure and intensity. *Mon. Weather Rev.* 130, 2291–2312. doi:10.1175/1520-0493(2002)130<2291:ephjoa>2.0.co;2

Chan, K. T. F., Wang, D., Zhang, Y., Wanawong, W., He, M., and Yu, X. (2019). Does strong vertical wind shear certainly lead to the weakening of a tropical cyclone? *Environ. Res. Commun.* 1, 015002. doi:10.1088/2515-7620/aaecac

Chen, B.-F., Davis, C. A., and Kuo, Y.-H. (2019). An idealized numerical study of shear-relative low-level mean flow on tropical cyclone intensity and size. *J. Atmos. Sci.* 76, 2309–2334. doi:10.1175/jas-d-18-0315.1

Chen, B.-F., Davis, C. A., and Kuo, Y.-H. (2021). Examination of the combined effect of deep-layer vertical shear direction and lower-tropospheric mean flow on tropical cyclone intensity and size based on the ERA5 reanalysis. *Mon. Weather Rev.* 149, 4057–4076. doi:10.1175/MWR-D-21-0120.1

Chen, S. S., Knaff, J. A., and Marks, F. D. (2006). Effects of vertical wind shear and storm motion on tropical cyclone rainfall asymmetries deduced from TRMM. *Mon. Weather Rev.* 134, 3190–3208. doi:10.1175/mwr3245.1

Corbosiero, K. L., and Molinari, J. (2002). The effects of vertical wind shear on the distribution of convection in tropical cyclones. *Mon. Weather Rev.* 130, 2110–2123. doi:10.1175/1520-0493(2002)130<2110:teovws>2.0.co;2

Dai, Y., Majumdar, S. J., and Nolan, D. S. (2021). Tropical cyclone resistance to strong environmental shear. *J. Atmos. Sci.* 78, 1275–1293. doi:10.1175/jas-d-20-0231.1

DeHart, J. C., Houze, R. A., and Rogers, R. F. (2014). Quadrant distribution of tropical cyclone inner-core kinematics in relation to environmental shear. *J. Atmos. Sci.* 71, 2713–2732. doi:10.1175/jas-d-13-0298.1

Emanuel, K., DesAutels, C., Holloway, C., and Korty, R. (2004). Environmental control of tropical cyclone intensity. *J. Atmos. Sci.* 61, 843–858. doi:10.1175/1520-0469(2004)061<0843:ecotci>2.0.co;2

Finocchio, P. M., Majumdar, S. J., Nolan, D. S., and Iskandarani, M. (2016). Idealized tropical cyclone responses to the height and depth of environmental vertical wind shear. *Mon. Weather Rev.* 144, 2155–2175. doi:10.1175/mwr-d-15-0320.1

Ge, X., Xu, W., and Zhou, S. (2015). Sensitivity of tropical cyclone intensification to inner-core structure. *Adv. Atmos. Sci.* 32, 1407–1418. doi:10.1007/s00376-015-4286-5

Grell, G. A., and Freitas, S. R. (2014). A scale and aerosol aware stochastic convective parameterization for weather and air quality modeling. *Atmos. Chem. Phys.* 14, 5233–5250. doi:10.5194/acp-14-5233-2014

Hong, S.-Y., Noh, Y., and Dudhia, J. (2006). A new vertical diffusion package with an explicit treatment of entrainment processes. *Mon. Weather Rev.* 134, 2318–2341. doi:10.1175/mwr3199.1

Hong, S. Y., and Lim, J.-O. J. (2006). The WRF single-moment 6-class microphysics scheme (WSM6). *Asia-pacific J. Atmos. Sci.* 42, 129–151.

Huang, Q., Ge, X., and Bi, M. (2022). Simulation of rapid intensification of super typhoon lekima (2019). Part II: The critical role of cloud-radiation interaction of asymmetric convection. *Front. Earth Sci.* 9, 832670. doi:10.3389/feart.2021.832670

Iacono, M. J., Delamere, J. S., Mlawer, E. J., Shephard, M. W., Clough, S. A., and Collins, W. D. (2008). Radiative forcing by long-lived greenhouse gases: Calculations with the AER radiative transfer models. *J. Geophys. Res. Atmos.* 113, D13103. doi:10.1029/2008jd009944

Jones, S. C. (1995). The evolution of vortices in vertical shear. I: Initially barotropic vortices. *Q. J. Roy. Meteor Soc.* 121, 821–851. doi:10.1002/qj.49712152406

Lee, C.-S., Cheung, K. K. W., Fang, W.-T., and Elsberry, R. L. (2010). Initial maintenance of tropical cyclone size in the western north pacific. *Mon. Weather Rev.* 138, 3207–3223. doi:10.1175/2010mwr3023.1

Onderlinde, M. J., and Nolan, D. S. (2014). Environmental helicity and its effects on development and intensification of tropical cyclones. *J. Atmos. Sci.* 71, 4308–4320. doi:10.1175/jas-d-14-0085.1

Rappin, E. D., and Nolan, D. S. (2012). The effect of vertical shear orientation on tropical cyclogenesis. *Q. J. Roy. Meteor Soc.* 138, 1035–1054. doi:10.1002/qj.977

Reasor, P. D., and Montgomery, M. T. (2015). Evaluation of a heuristic model for tropical cyclone resilience. *J. Atmos. Sci.* 72, 1765–1782. doi:10.1175/jas-d-14-0318.1

Reasor, P. D., Montgomery, M. T., and Grasso, L. D. (2004). A new look at the problem of tropical cyclones in vertical shear flow: Vortex resiliency. *J. Atmos. Sci.* 61, 3–22. doi:10.1175/1520-0469(2004)061<0003:anlatp>2.0.co;2

Reasor, P. D., Rogers, R., and Lorsolo, S. (2013). Environmental flow impacts on tropical cyclone structure diagnosed from airborne Doppler radar composites. *Mon. Weather Rev.* 141, 2949–2969. doi:10.1175/mwr-d-12-00334.1

Riemer, M., Montgomery, M. T., and Nicholls, M. E. (2010). A new paradigm for intensity modification of tropical cyclones: Thermodynamic impact of vertical wind shear on the inflow layer. *Atmos. Chem. Phys.* 10, 3163–3188. doi:10.5194/acp-10-3163-2010

Ryglicki, D. R., Doyle, J. D., Hodyss, D., Cossuth, J. H., Jin, Y., Viner, K. C., et al. (2019). The unexpected rapid intensification of tropical cyclones in moderate vertical wind shear. Part III: Outflow–Environment interaction. *Mon. Weather Rev.* 147, 2919–2940. doi:10.1175/mwr-d-18-0370.1

Shi, D., and Chen, G. (2021). The implication of outflow structure for the rapid intensification of tropical cyclones under vertical wind shear. *Mon. Weather Rev.* 149, 4107–4127. doi:10.1175/MWR-D-21-0141.1

Simpson, R. H., Bureau, U., and Riehl, H. (1958). "Mid-tropospheric ventilation as a constraint on hurricane development and maintenance," in Preprints, Tech. Conf. on Hurricanes, 12-June 1958 (Miami Beach, FL: Amer. Meteor. Soc.), 1–10.

Tang, B., and Emanuel, K. (2012). A ventilation index for tropical cyclones. *Bull. Am. Meteorological Soc.* 93, 1901–1912. doi:10.1175/bams-d-11-00165.1

Tang, B., and Emanuel, K. (2010). Midlevel ventilation's constraint on tropical cyclone intensity. *J. Atmos. Sci.* 67, 1817–1830. doi:10.1175/2010jas3318.1

Wang, B., and Li, X. (1992). The beta drift of three-dimensional vortices: A numerical study. *Mon. Weather Rev.* 120, 579–593. doi:10.1175/1520-0493(1992)120<0579:tbdotd>2.0.co;2

Wang, B., Li, X., and Wu, L. (1997). Direction of hurricane beta drift in horizontally sheared flows. *J. Atmos. Sci.* 54, 1462–1471. doi:10.1175/1520-0469(1997)054<1462:dohbdi>2.0.co;2

Wang, Y., and Holland, G. J. (1996). Tropical cyclone motion and evolution in vertical shear. *J. Atmos. Sci.* 53, 3313–3332. doi:10.1175/1520-0469(1996)053<3313:tcmaei>2.0.co;2

Wu, C.-C., and Emanuel, K. A. (1993). Interaction of a baroclinic vortex with background shear: Application to hurricane movement. *J. Atmos. Sci.* 50, 62–76. doi:10.1175/1520-0469(1993)050<0062:ioabvw>2.0.co;2

Xu, J., and Wang, Y. (2010a). Sensitivity of the simulated tropical cyclone inner-core size to the initial vortex size. *Mon. Weather Rev.* 138, 4135–4157. doi:10.1175/2010mwr3335.1

Xu, J., and Wang, Y. (2010b). Sensitivity of tropical cyclone inner-core size and intensity to the radial distribution of surface entropy flux. *J. Atmos. Sci.* 67, 1831–1852. doi:10.1175/2010jas3387.1

Zhang, D.-L., and Kieu, C. Q. (2006). Potential vorticity diagnosis of a simulated hurricane. Part II: Quasi-balanced contributions to forced secondary circulations. *J. Atmos. Sci.* 63, 2898–2914. doi:10.1175/jas3790.1

Zhang, D.-L. (2005). Shear-forced vertical circulations in tropical cyclones. *Geophys. Res. Lett.* 32, L13822. doi:10.1029/2005gl023146

Zhang, F., and Tao, D. (2012). Effects of vertical wind shear on the predictability of tropical cyclones. *J. Atmos. Sci.* 70, 975–983. doi:10.1175/jas-d-12-0133.1

frontiers | Frontiers in Environmental Science

TYPE Original Research
PUBLISHED 03 February 2023
DOI 10.3389/fenvs.2023.1112266

OPEN ACCESS

EDITED BY
Yunheng Wang,
University of Oklahoma, United States

REVIEWED BY
Youcun Qi,
Institute of Geographic Sciences and Natural Resources Research (CAS), China
Hui Xiao,
Guangzhou Institute of Tropical and Marine Meteorology (GITMM), China
Man Zhang,
Weather News America, United States

*CORRESPONDENCE
Xiaoli Liu,
liuxiaoli2004y@nuist.edu.cn

SPECIALTY SECTION
This article was submitted to Environmental Informatics and Remote Sensing, a section of the journal Frontiers in Environmental Science

RECEIVED 30 November 2022
ACCEPTED 19 January 2023
PUBLISHED 03 February 2023

CITATION
Li Y, Liu X and Yuan C (2023), The numerical study on the sensitivity of different auto-conversion parameterization to CCN concentration. *Front. Environ. Sci.* 11:1112266. doi: 10.3389/fenvs.2023.1112266

The numerical study on the sensitivity of different auto-conversion parameterization to CCN concentration

Yi Li[1], Xiaoli Liu[2]* and Chaoyu Yuan[3]

[1]College of Atmospheric Physics, Nanjing University of Information Science and Technology, Nanjing, China, [2]Key Laboratory for Aerosol-Cloud-Precipitation of China Meteorological Administration, Collaborative Innovation Center on Forecast and Evaluation of Meteorological Disasters, Nanjing University of Information Science and Technology, Nanjing, China, [3]Changzhou Benniu International Airport, Changzhou, China

The auto-conversion from cloud droplet to raindrop is a process whereby rain drops formed by collision-coalescence of cloud droplets. As an essential link connecting aerosol-cloud interaction, it significantly influences the changes in cloud morphology and precipitation. In order to explore the sensitivity of auto-conversion schemes to cloud condensation nuclei (CCN) concentration, using the auto-conversion scheme in the Thompson scheme (TH-AU) and Milbrandt-Yau scheme (MY-AU), we set four groups of CCN concentrations to simulate a strong convection process in Ningxia region of China. The results show that: The sensitivity of different auto-conversion schemes to changes in CCN concentrations varies significantly, and the aerosol-induced changes in precipitation and convection strongly depend on the auto-conversion scheme. With the increase of CCN concentration, the mixing ratio of cloud droplets increases, and the particle size decreases, resulting in a decrease in the auto-conversion intensity for the two schemes, which makes more supercooled water participate in the ice phase process. Compared with the TH-AU, the MY-AU has lower auto-conversion intensity at the same CCN concentration, the proportion of supercooled cloud droplets participating in the ice phase process is higher than that in the TH-AU, which leads to the raindrop mixing ratio of 4000–6000 m in MY-AU is lower than that in TH-AU at the same CCN concentration, and the mixing ratio of ice phase particles in MY-AU scheme is higher in the convective mature stage, especially snow and graupel particles, and the graupel particle generation height of MY-AU is lower than that of TH-AU. In terms of dynamic structure, with the increase of CCN concentration, more cloud droplets are activated and frozen which makes the enhancement of updraft mainly occur in the upper layer in both schemes, but the stronger gravitational drag caused by graupel particles in MY-AU may enhance the downdraft in the middle and lower layers, which makes the convection of MY-AU decay early at higher CCN concentration. In addition, changes in microphysical processes also lead to differences in cumulative precipitation and accumulated ground graupel-fall of the two schemes. The cumulative precipitation and the accumulated ground graupel-fall of the MY-AU decrease strongly with the increase of CCN concentration because the warm rain process of MY-AU is strongly inhibited. Compared with MY-AU, the warm rain process of TH-AU is not significantly inhibited, which leads to the cumulative precipitation and the accumulated ground graupel-fall of the TH-AU scheme increases when the CCN concentration is 50–200 cm^{-3} and slightly decreases when the CCN concentration is 200–10000 cm^{-3}.

KEYWORDS

auto-conversion parameterization, CCN concentration, numerical simulation, convection, microphysical process

1 Introduction

Cloud and precipitation development processes are a critical source of uncertainty in numerical simulations of meteorological and climatic conditions (Houghton, 2001; Li et al., 2016). As cloud condensation nuclei (CCN), aerosols can influence cloud microphysical processes and albedo by activating cloud droplets, which affects the development of cloud structure and lifetime (Rosenfeld, 2000). As social and economic development progresses, the effect of increasing anthropogenic aerosol on the weather becomes more pronounced (Rosenfeld et al., 2014). The increase in CCN concentration triggers an increase in cloud droplet number concentration, accompanied by a decrease in cloud droplet size (Köhler, 1936).

While initial cloud droplet changes due to increasing concentrations of CCN have been elucidated (Reutter et al., 2009; Twomey, 1977), many studies have shown that the subsequent responses of convective clouds to changes in CCN concentrations are complex and even contradictory (Khain et al., 2005; Barthlott and Hoose, 2018; Lim and Hong, 2010; Saleeby et al., 2016). CCN-induced reduction of cloud droplet size makes the cloud droplet collision-coalescence process less efficient, and the cloud to rain auto-conversion process is inhibited (Albrecht, 1989), which weakens the warm rain process and reduces surface precipitation (Wang, 2005; Marinescu et al., 2017; Kovačević, 2018; Lerach and Cotton, 2018).

However, there are contrasting findings of Alizadeh-Choobari and Gharaylou (2017), which found that at high CCN concentrations, a large number of small cloud droplets are more easily transported to the upper layers for freezing. Thus, the precipitation in the weak convective process was inhibited, while the precipitation in the strong convective process was enhanced. Besides, Gryspeerdt et al. (2014) also found, based on satellite observation, that aerosol optical thickness was positively correlated with spatial variability in precipitation or convective cloud formation. This effect's magnitude varies depending on cloud, aerosol, concentration, and environmental conditions (Khain et al., 2008; Hande et al., 2017).

In addition, changes in microphysical processes caused by aerosols can also lead to changes in cloud convection structure. Seinfeld and Lebo, 2011 showed that the convective intensity of clouds with suppressed precipitation might be enhanced later in the process. Overall, the strength of updrafts in convective clouds appears to increase at higher concentrations of CCN (Khain et al., 2005; Wang, 2005). However, the reason for the enhanced updraft at higher CCN concentrations is also controversial.

Several studies suggest that the increase in updrafts of clouds at relatively high CCN concentrations is primarily due to the enhanced release of latent heat from cloud droplet condensation (Sheffield et al., 2015; Morrison et al., 2018). However, other studies suggest that the additional latent heat from the more substantial freezing process is the primary reason for the increase in updraft velocity (van den Heever, 2018; Andreae and Ronsenfeld, 2008). In contrast, other studies have found that updrafts of some deep convective clouds remain unchanged or weaken at higher concentrations of CCN (Fan et al., 2009; Lebo and Seinfeld 2011; Barthlott and Hoose 2018). This discrepancy has been attributed to differences in cloud types and weather conditions.

For the warm rain process mentioned above, cloud droplets are generated by the activation of aerosols and grow by condensation and collision coalescence. Auto-conversion is a microphysical process in which the collision-coalescence of cloud droplets forms raindrops. As an essential link connecting aerosol-precipitation interaction, cloud to rain auto-conversion significantly influences the changes in cloud morphology and precipitation caused by aerosols (Ghan et al., 2011; Lee et al., 2012; Tao et al., 2012; Xie and Liu, 2015). Rosenfeld, (2000) found that clouds with cloud-top heights higher than 10 km can produce only half as much precipitation as clouds that reach the same cloud-top height if collision-coalescence processes are suppressed. Precipitation is found sensitive to changes in CCN concentration in Xie and Liu (2015) by use of three auto-conversion schemes. Michibata and Takemura's (2015) simulations reflect that cloud optical thickness and liquid-water path are highly sensitive to the auto-conversion parameterization scheme. In summary, there are significant differences in aerosol-induced changes in clouds and precipitation when using different auto-conversion parameterization schemes (White et al., 2017; Barthlott and Hoose, 2021).

Given the complexity of the dynamic and thermodynamic processes involved in the auto-conversion process, the knowledge of cloud microphysical processes limits the development of the auto-conversion parameterization. There are still many empirical values or assumptions in the model, which renders the simulation results reasonably sensitive to the setting of the microphysics schemes (van den Heever et al., 2021). So, there has been a great deal of interest in this territory over the last few decades (Khain et al., 2015; Morrison et al., 2020).

Kessler pioneered a simple scheme to calculate the auto-conversion rate by cloud water content (Kessler, 1969). However, Hu and Cai, (1979) pointed out that Kessler's auto-conversion rate was higher than the observed value. The scheme proposed by Manton and Cotton (1977) based on Kessler (1969) considered both liquid water content and cloud droplet concentration. The results of Wang and Xie, 2009 show that the simulation results using this scheme of Manton and Cotton (1977) are consistent with the observed value. A representative scheme was proposed by Berry (1969), which calculated the auto-conversion efficiency as a function of cloud droplet number concentration, cloud water content, cloud droplet size, and spectral shape parameters; Ghosh and Janas, (1998) has proposed an auto-conversion parametrization scheme combining the benefits of Kessler's (1969) and Berry (1969) schemes, which can be applied to different types of clouds. As a result of more in-depth studies of microphysical processes, others have derived new auto-conversion schemes based on more complicated microphysical models (Seifert et al., 2010; Lei et al., 2020). In recent years, Kogan and Ovchinnikov (2020) and Naegar et al. (2020) have considered the effect of turbulence in auto-conversion parameterization.

In order to explore the sensitivity of different auto-conversion schemes to CCN concentration, this paper uses the Thompson scheme embedded in WRF v 3.7.1 model as a microphysics scheme simulating strong convective processes. One group of simulations uses the original auto-conversion scheme of the Thompson et al. (2008) scheme (TH-AU), and the other group uses the Milbrandt and Yau (2005) (MY) scheme's auto-conversion scheme (MY-AU). Both auto-

conversion schemes follow Berry (1968). However, there are apparent differences in the intensity of the auto-conversion rate due to different conversion thresholds and rain-characteristic particle size calculations. On this basis, four sets of CCN concentrations, 50, 200, 2,000, and 10,000 cm^{-3}, are set as the initial CCN concentrations of the model, which refer to the studies of Xie and Liu (2015) and Liu et al. (2021), and can represent several typical CCN concentrations. Moreover, a strong convective process is simulated in Ningxia, China.

2 Model description and experimental design

2.1 Design of simulation

WRFV3.7.1 is used for the numerical simulations in this paper, and the ECMWF reanalysis data is used as the initial field, updated every 6 h with a resolution of 0.75°*0.75°. A two-level nesting is implemented in the simulation area with a central location of 37.3°N, 106°E, and a grid number of 481*481. The Thompson scheme is used as the microphysics scheme, with a topographic resolution of 3 km and 1 km and a simulation duration of 18 h. All the simulation settings are kept consistent except for the auto-conversion scheme.

The Mellor–Yamada–Janjic (MYJ) scheme is the physics scheme of the planetary boundary layer (PBL). The cumulus parameterization options are turned off. We use the Rapid Radiative Transfer Model (RRTM) for the Global Climate Model (GCM) as the Shortwave and Longwave schemes. The Unified Noah Land and Surface Model are chosen as the surface land scheme, and the Eta Similarity Scheme as the surface layer scheme.

2.2 Introduction of microphysics scheme and auto-conversion scheme

The Thompson scheme used in this paper is a modification of Reisner et al. (1998) and produces better simulation results. The scheme has six in-cloud components: water vapor, cloud droplets, rain droplets, ice crystals, snow, and graupel. Predictions for snow and graupel are made only in terms of the mixing ratio. Predictions for clouds, rain, and ice crystals include the number concentration and the mixing ratio.

In the Thompson scheme, raindrop particles originate from the auto-conversion on the one hand and the melting of ice phase particles on the other. The size of raindrops can vary significantly depending on whether they originate from the ice phase or warm rain process, and the auto-conversion process in the Thompson scheme is set as follows:

The TH-AU follows Berry (1969) scheme except for the droplet spectrum, which uses a gamma distribution, and the characteristic diameter is derived by calculation rather than assumption. The conversion rate of cloud water to rainwater is expressed as:

$$\frac{dr_r}{dt} = \frac{0.027\rho q_c\left(\frac{1}{16}\times D_b^3 D_f - 0.4\right)}{\frac{3.72}{\rho q_c}\left(\frac{1}{2}\times 10^6 D_b - 7.5\right)^{-1}} \tag{1}$$

r_r is the water content of raindrops, ρ is the density of moist air, q_c is the mass mixing ratio of cloud drops, D_b, D_f is the characteristic particle size of cloud drops distribution which is calculated as follows:

$$D_f = \left(\frac{6\rho q_c}{\pi\rho N_c}\right)^{1/3} \tag{2}$$

$$D_g = \frac{\left[\frac{\Gamma(\mu_c+7)}{\Gamma(\mu_c+4)}\right]^{1/3}}{\lambda_c} \tag{3}$$

$$D_b = \left(D_f^3 D_g^3 - D_f^6\right)^{1/6} \tag{4}$$

N_c is number concentration of cloud water droplets, μ_c is the gamma size distribution shape parameter of cloud, λ_c is the gamma size distribution slope parameter of cloud.

The raindrop number concentration of TH-AU is consistent with the MY-AU scheme, which will be described later.

The conversed water content of cloud droplets into rain droplets in the MY-AU follows that of Cohard and Pinty (2000):

$$QCN = 2.7\times 10^{-2}\rho q_c\left(\frac{1}{16}\times 10^{20}\sigma_c^3 D_c - 0.4\right) \tag{5}$$

$$\tau = 3.7\frac{1}{\rho q_c}\left(0.5\times 10^6\sigma_c - 7.5\right)^{-1} \tag{6}$$

$$\frac{dQCN}{d\tau} = -max\left(QCN/\tau, 0.\right) \tag{7}$$

and,

$$Dc = \frac{1}{\lambda_c}\frac{\Gamma\left(\nu_c + 3/\alpha_c\right)}{\Gamma(\nu_c)}^{1/3} \tag{8}$$

$$\sigma_c = \frac{1}{\lambda_c}\frac{\Gamma\left(\nu_c + 6/\alpha_c\right)}{\Gamma(\nu_c)} - \left[\frac{\Gamma\left(\nu_c + 3/\alpha_c\right)}{\Gamma(\nu_c)}\right]^2{}^{1/6} \tag{9}$$

QCN is the water content of auto-conversion, ρ is the density of moist air, q_c is the cloud droplet mixing ratio, σ_c is the standard deviation of cloud droplet distribution, D_c is the mean cubic root diameter of ca loud droplet, τ is the time scale of auto-conversion, α_c and ν_c is the dispersion parameter of the generalized gamma distribution law for the cloud droplets, λ_c is slope of cloud.

The raindrop number concentration of the MY-AU:

$$NCN_{cr} = \left(\frac{\rho}{m_{x0}}\right)QCN_{cr} \tag{10}$$

NCN_{cr} denotes the auto-conversion number concentration, QCN_{cr} is the auto-conversion water content, ρ is the density of moist air, m_{x0} is the rain particle mass. The above part is the same as the auto-conversion number concentration of TH-AU schemes.

In addition, the MY-AU scheme has special settings for particle size. For the newly generated particles with number concentration of NCN_{cr}, there exists a constraint on the particle size:

$$D_{mr\_aut} = \frac{1.26\times 10^{-3}}{(0.5\times 10^6)\sigma_c - 3.5} \tag{11}$$

The mass-weighted average diameter of existing raindrop particles D_{mr} is calculated as:

$$D_{mr} = \left[\left(\rho q_r/c_r N_{Tr}\right)\right]^{1/3} \tag{12}$$

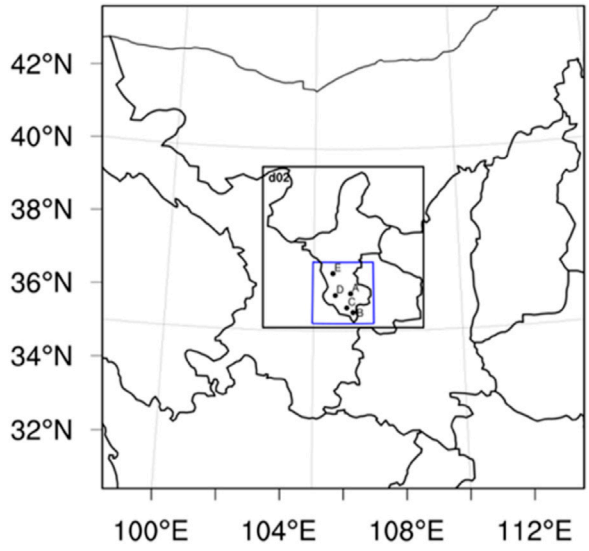

FIGURE 1
Simulation setting (A) Guyuan City (B) Jingyuan County (C) Longde County (D) Xiji County (E) Haiyuan County (F) Zhongwei City, the blue area is the area affected by the convection.

N_{Tr} is the otal number concentration of raindrops, c_r is the mass parameter for raindrops, q_r is the cloud droplet mixing ratio, ρ is the density of moist air.

If $D_{mr} > D_{mr\_aut}$, newly generated raindrop particle size $D_{mr\_new} = D_{mr}$. Otherwise, $D_{mr\_new} = D_{mr\_aut}$.

Three characteristic particle sizes are considered in the TH-AU scheme. D_f is related to mthe ean size of cloud droplet, D_g is related to reflectivity, D_b combines the two influences. Therefore, the TH-AU scheme is more sensitive to the cloud droplet particles of large particle size. In the MY-AU scheme, the spectral dispersion of cloud droplets is considered in the auto-conversion calculation, which is more sensitive to the overall particle size difference of cloud droplets.

2.3 Statistical parameters

The observed precipitation used in this article combines the hourly precipitation of the China automatic station and CMORPH (Climate Prediction Center Morphing technique) integrated precipitation data. The simulated hourly precipitation intensities are analyzed using the Root Mean Squared Error (RMSE), calculated as follows:

$$RMSE = \sqrt{\frac{1}{n}\sum_{i=1}^{n}(P_i - O_i)^2} \tag{13}$$

n represents the number of data groups, P_i, O_i denote the ith group of observed value and simulation results, respectively.

It measures the deviation between the simulated value and the observed value. In general, the RMSE value of less than 2 proves that the simulated value is more reliable.

2.4 The mass-weighted average diameter

Since the forecast output of the Thompson scheme does not include the particle size, a gamma function for the particle size distribution is introduced, and the mean particle size is calculated using the mixing ratio and the number concentration of the hydrometeor particles.

The particle size distribution of hydrometeor particles is represented by the gamma function as:

$$N(D) = N_0 D^{\mu} e^{-\lambda D} \tag{14}$$

N_0 is the intercept, μ is the shape parameter of the particle, and λ is the slope.

$$M_x = \int_0^{\infty} D^x N(D) dD \tag{15}$$

M_x is the Xth order moment of particle size and D is the particle diameter. From this, the 3rd, 4th and 6th order moments of the particle size in the liquid phase can be calculated. Then, the spectral parameters can be expressed as:

$$N_0 = \frac{\lambda^{\mu+4} M_3}{\Gamma(\mu+4)} \tag{16}$$

$$\lambda = \frac{(4+\mu)(3+\mu)M_3}{M_4} = \frac{m+4}{D_m} \tag{17}$$

Γ is a gamma function, D_m is the mass-weighted average diameter, and the unit is mm.

2.5 Description of the convective process

Figure 1 shows that the strong convective process in this paper occurred on 7 June 2017, in the southern region of Ningxia Hui Autonomous Region, China. Ningxia Hui Autonomous Region is located on the Loess Plateau, near the upper reaches of the Yellow River, and has a semiarid temperate continental climate. The precipitation process is accompanied by hail, with the maximum hail diameter reaching 1.5 cm and the accumulated hail reaching 2–3 cm.

The earliest precipitation in Ningxia appeared at 03:00 UTC on 7 June, mainly concentrated in the southern region. At 10:00 UTC, the maximum intensity of the precipitation appeared with a precipitation intensity of 10–20 mm. The precipitation process began weakening after 10:00 UTC and gradually moved southward. At 14:00 UTC on the 07th day, the precipitation process finally moved out of Ningxia territory.

3 Macroscopic simulation results

3.1 Radar echo

The composite radar reflectivity is shown in Figure 2, and the detection data are from the C band radar. At 04UTC, an intense radar echo center began to appear in the south-central region of Ningxia as the echo range developed and gradually moved southeastward. At 07UTC, the strongest radar echo appeared with a reflectivity intensity of approximately 54dBZ. During the southward motion of the echo, several strong echo

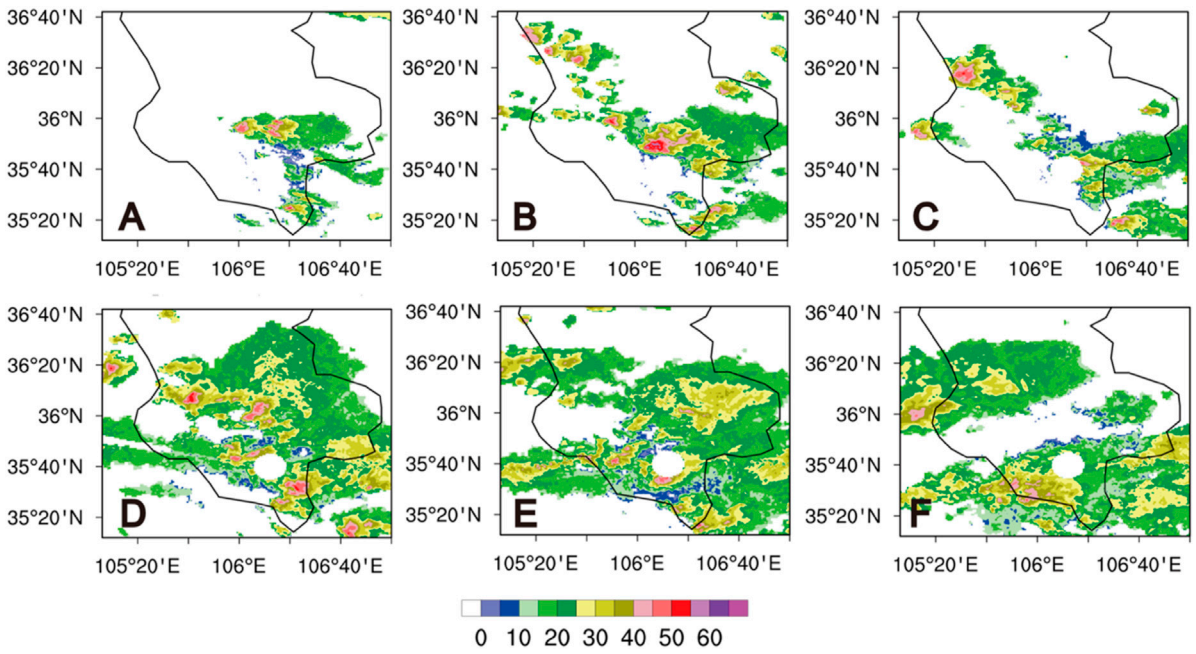

FIGURE 2
Observed composite radar reflectivities (Unist: dBZ) at **(A)** 0600 UTC **(B)** 0700 UTC **(C)** 0800 UTC **(D)** 0900 UTC **(E)** 1000 UTC **(F)** 1100 UTC.

centers merged. At 0730UTC, three strong radar echo centers emerged to the northwest of Guyuan city. At 09UTC, the earliest radar echo center moved out of Ningxia territory and gradually dissipated.

Figures 3, 4 shows that the simulated convective development is close to the real case, and the center of the radar echo corresponds to the convective center. Concerning radar echo distribution, the simulation results are more southerly than real. As the concentration of CCN increases, the distribution of strong radar echoes beyond 40 dBZ is more concentrated in both schemes, and the reflectivity of the echo center is lessened. Compared with TH-AU, the intensity of the radar reflectivity center of MY-AU attenuates more with the increase of CCN concentration. In addition, at the CCN concentration of 10,000 cm^{-3}, the convection of MY-AU entered the decay stage earlier. This is related to the early dissipation of convection in the MY-AU scheme at high CCN concentration.

3.2 Comparison of precipitation results

There are significant differences between the two schemes concerning cumulative precipitation with changes in CCN which can be found in Figure 5. The precipitation distribution is more consistent with the location of the convective centers. For the simulation results of the two schemes, the cumulative precipitation of TH-AU does not change monotonically with increasing concentrations of CCN, which increases gradually as the CCN concentration increases from 50 to 200 cm^{-3}, and reduces from 200 to 10,000 cm^{-3}. This is related to the fact that the warm rain process of the TH-AU scheme is not significantly inhibited when the CCN concentration is 50–200 cm^{-3} but is inhibited when the CCN concentration is 200–10,000 cm^{-3}, which is consistent with the research results of Khain et al. (2005) and van den Heever et al. (2006). Compared to MY-AU, there is a merging trend in precipitation centers in TH-AU. On the contrary, as the CCN concentration increases, the cumulative precipitation of MY-AU decreases. This is consistent with the trend that the increase of CCN concentration continuously strongly inhibits the warm rain process of the MY-AU scheme.

We also use observed precipitation to assess hourly rainfall intensity and assessed it by calculating RMSE, which is shown in Figure 6. The RMSE for both schemes is less than 2, providing that the simulated hourly rainfall intensity is credible. The RMSE of the TH-AU scheme was similar except for the CCN concentration of 50 cm^{-3}, indicating that hourly precipitation in the TH-AU scheme was not sensitive to CCN concentration changes. On the contrary, the RMSE of the four groups in the MY-AU scheme is significantly different, which proves that hourly precipitation in the MY-AU scheme is more sensitive to CCN concentration changes.

3.3 Accumulated ground graupel-fall

Figure 7 shows the accumulated ground graupel-fall from simulations at 1600UTC. With the increase of CCN concentration, the maximum value of accumulated ground graupel-fall in the TH-AU scheme gradually increases. On the contrary, accumulated ground graupel-fall in the MY-AU scheme decrease with the increase of CCN concentration. The maximum accumulated ground graupel-fall quantity is at the CCN concentration of 50 cm^{-3}.

4 Differences in convection development

Figure 8 shows the distribution of maximum updraft and average downdraft with height with time. The process of convective

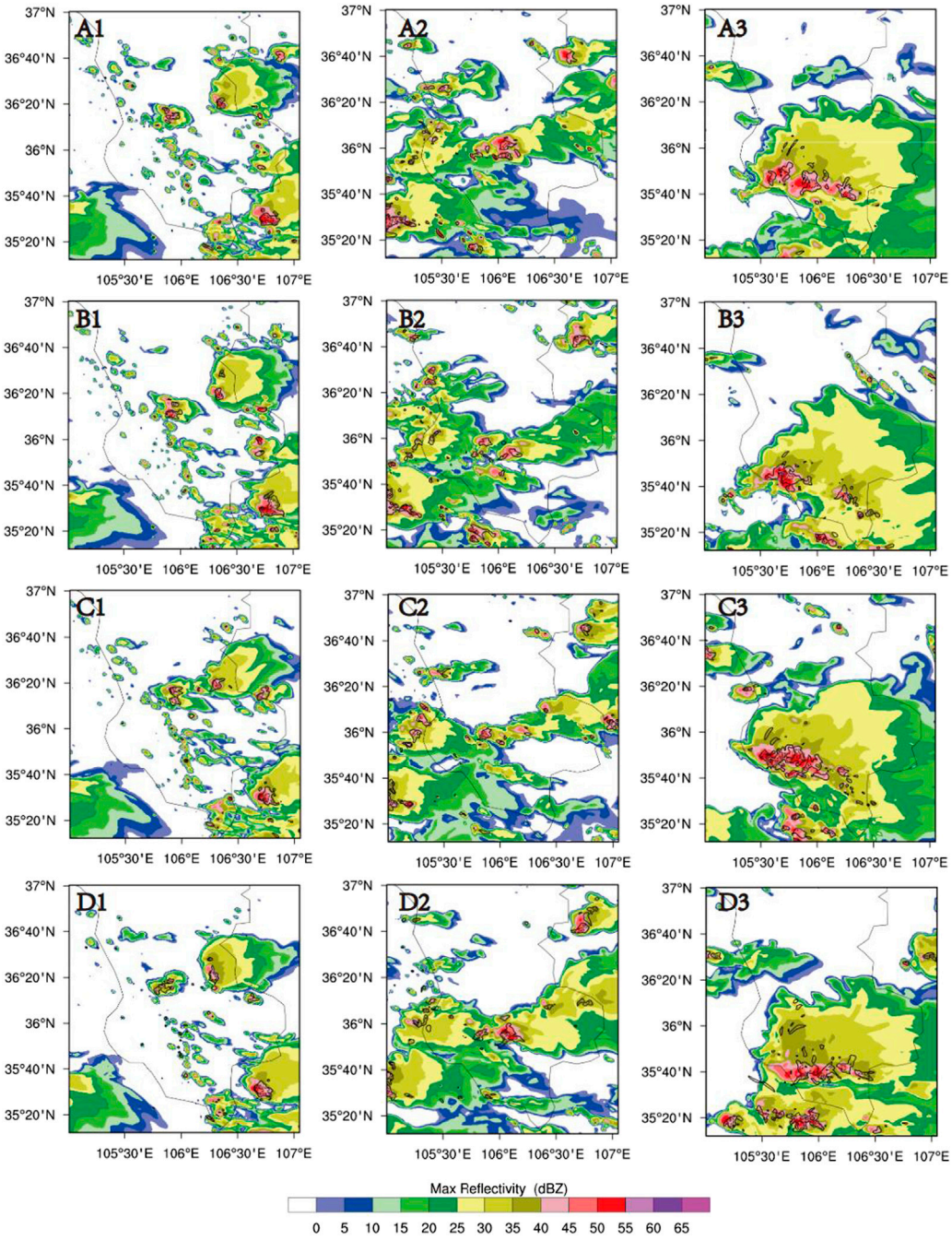

FIGURE 3
Composite radar reflectivity (Unit: dBZ) simulated with TH-AU scheme, with the solid line as the area where the updraft is greater than 5 m/s: **(A)** NCCN 50 **(B)** NCCN 200 **(C)** NCCN 2000 **(D)** NCCN 10000; **(1)** 0600 **(2)** 0800 **(3)** 1000 UTC.

development can be roughly divided into three stages based on changes in hourly precipitation and updraft intensity: stage of development (3-6UTC), stage of maturity (6-10UTC), and stage of dissipation (10-16UTC).

First, with the increased CCN concentration, more latent heating releases, resulting in more buoyant updrafts due to higher concentrations of cloud droplets that form. In addition, the cloud to rain auto-conversion process is inhibited at higher CCN concentrations (details are discussed in Section 5), suppressing the collision rate of rain to cloud. Because of that, more supercooled cloud water participates in freezing and riming, releasing more latent heat and promoting updraft development. This phenomenon is similar to the study of Khain et al. (2005), Seifert and Beheng (2005a) and Seifert and Beheng (2005b).

Therefore, as can be seen from Figures 8, 9, with the increase of CCN concentration and the weakening of cloud to rain auto-conversion intensity, the effect that cloud droplets are transported to the upper level to freeze, causing the upper-level updraft to

10.3389/fenvs.2023.1112266

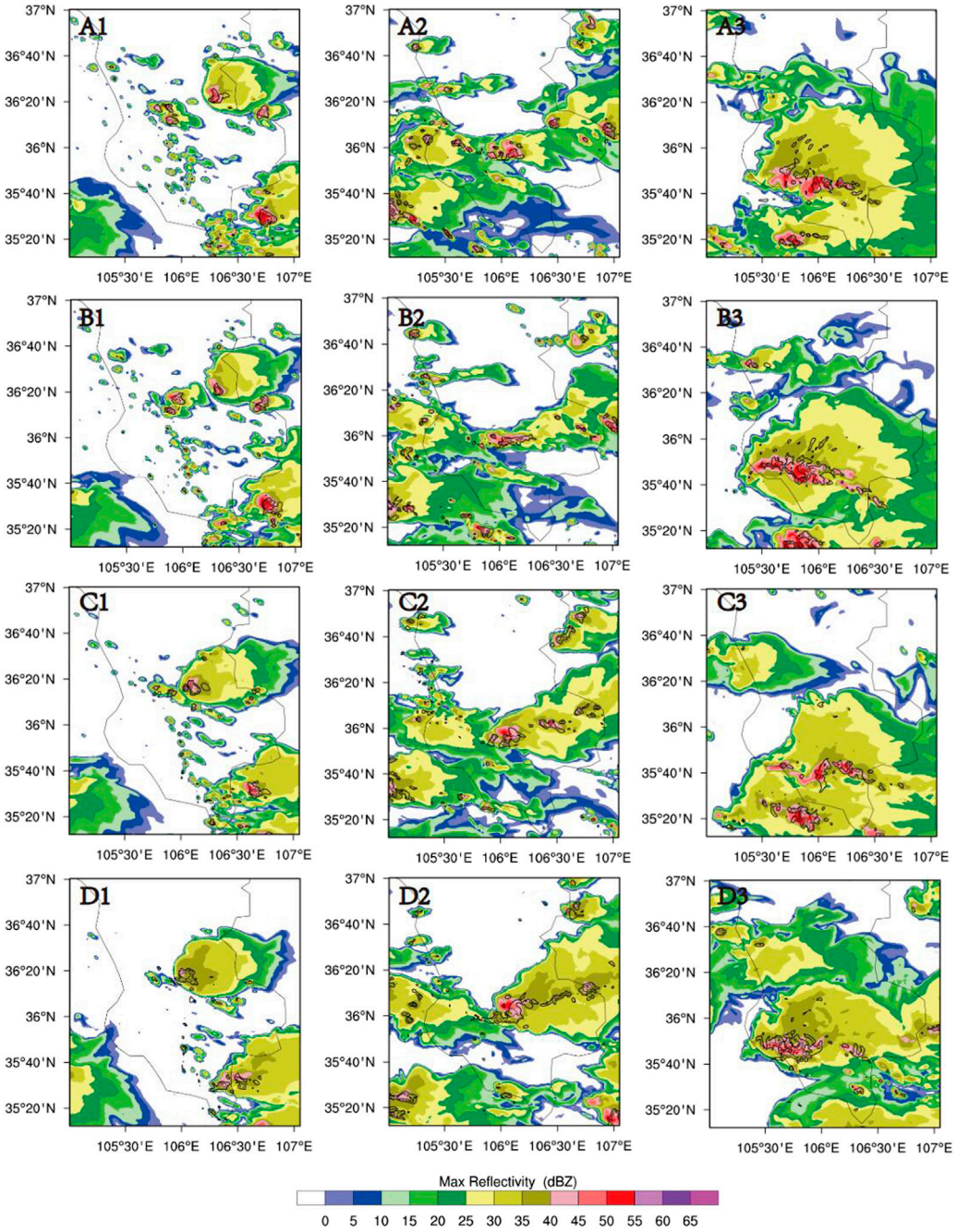

FIGURE 4
Composite radar reflectivity (Unit: dBZ) simulated with MY-AU scheme, with the solid line as the area where the updraft is greater than 5 m/s: **(A)** NCCN 50 **(B)** NCCN 200 **(C)** NCCN 2000 **(D)** NCCN 10000; **(1)** 0600UTC **(2)** 0800UTC **(3)** 10000 UTC.

strengthen has increased in the development and maturity stage, which also appears in the study of Fan (2007) and Fan et al. (2018), Lebo and Morrison (2014). On this basis, the simulation results show that in the process of increasing CCN concentration, the enhancement of updraft mainly occurs in the upper layer, while the increase of graupel particles in this height layer may enhance the downdraft in the middle and lower layers.

However, there is a clear difference in the stage of maturity and the stage of dissipation for the two schemes. At first, the updraft of 8,000–10,000 m in the MY-AU scheme has much higher growth than TH-AU in the mature stage, which is most significant with a CCN concentration of 10,000 cm^{-3}. Moreover, compared with the TH-AU scheme, the decay of convection in the MY-AU is earlier when the CCN concentration is 10,000 cm^{-3}. In addition, there are differences in the range of strong convection ($w > 15$ m/s) grids. When the concentration of CCN is the same, the range of strong convection grids above 8,000 m for MY-AU is more extensive than that for TH-AU, which indicates that the strong convection scale of the MY-AU scheme is larger than that of the TH-AU scheme.

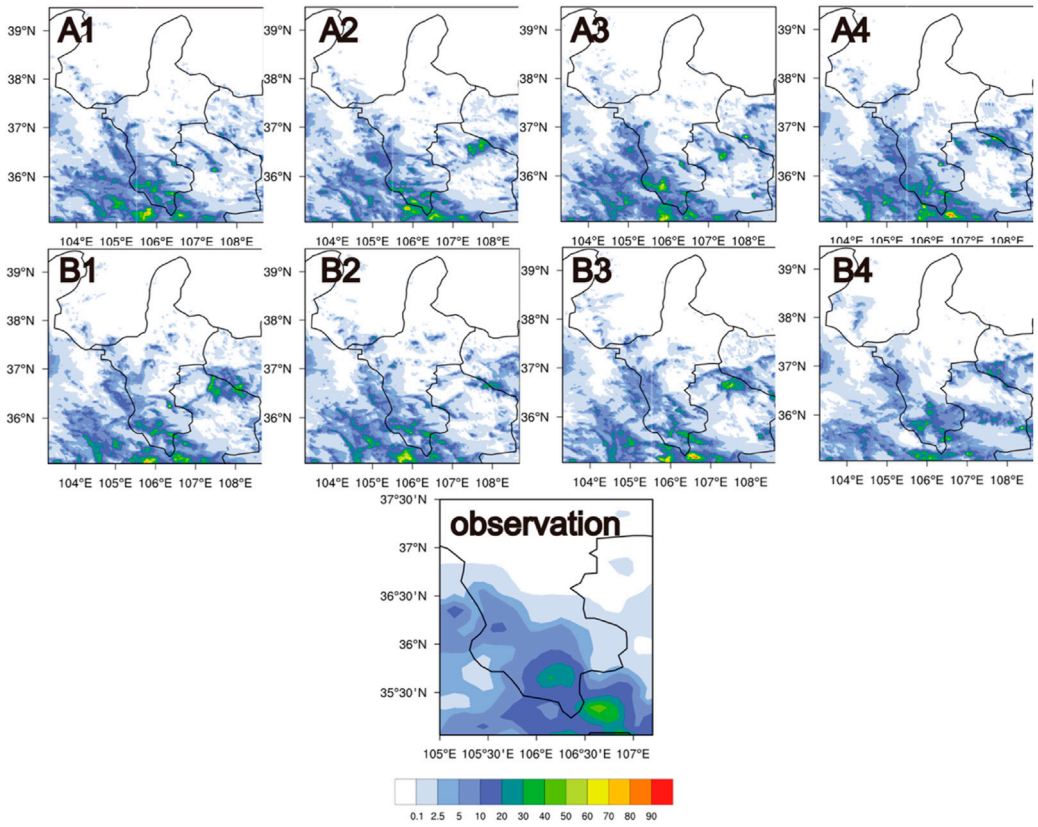

FIGURE 5
Simulated and observed precipitation accumulation (Unit: mm) at 1600 UTC: **(A)** TH-AU; **(B)** MY-AU; **(1)** NCCN 50 **(2)** NCCN200 **(3)** NCCN 2000 **(4)** NCCN10000.

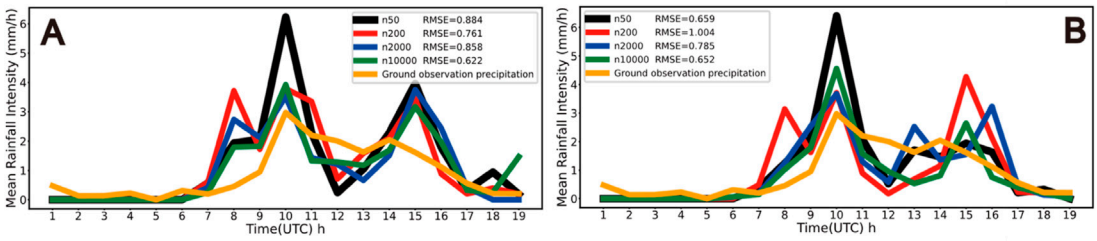

FIGURE 6
Hourly rainfall intensity (Unit: mm s^{-1}): **(A)** TH-AU; **(B)** MY-AU.

5 Analysis of microphysical processes

As the CCN concentration increases, the mixing ratio of cloud droplets is significantly increased in both schemes (Figure 10). This phenomenon indicates that increasing the number of hygroscopic aerosols will produce more cloud droplets generated by aerosol activation, consistent with numerical studies (Khain et al., 2005; Lee et al., 2012). As a result of increased cloud droplet activation and water vapor competition, condensation growth of cloud droplet become complicated, resulting in a decrease in the particle size of cloud droplets. More and smaller cloud droplets induced by aerosols can hinder the auto-conversion process of clouds from raining (Xie et al., 2013). The auto-conversion intensities of both schemes decades with increasing concentrations of CCN, as shown in Figure 11. Because of that, it is shown in Figure 12 that more cloud droplets can be transported and enhance the ice phase processes, thus forming more ice hydrometeors, which is the same as Woodley et al. (2003).

However, in Figure 12, it can be found that the distribution of supercooled cloud water of the two schemes at the same CCN concentration is significantly different. At the same CCN concentration, a more significant proportion of supercooled clouds in the MY-AU scheme are frozen into ice crystals and involved in riming of snow crystals and graupel particles. Considering that the two schemes adopt the same cloud droplet activation calculation, this

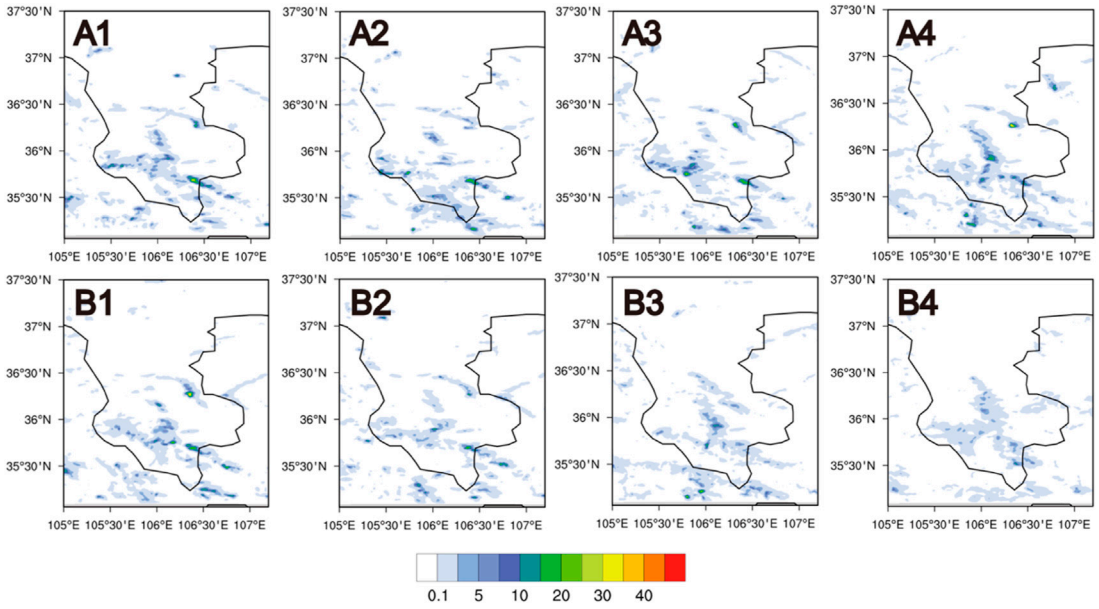

FIGURE 7
Accumulated ground graupel-fall from simulations (Unit: mm) at 1600 UTC: **(A)** TH-AU; **(B)** MY-AU, **(1)** NCCN 50 **(2)** NCCN200 **(3)** NCCN2000 **(4)** NCCN10000.

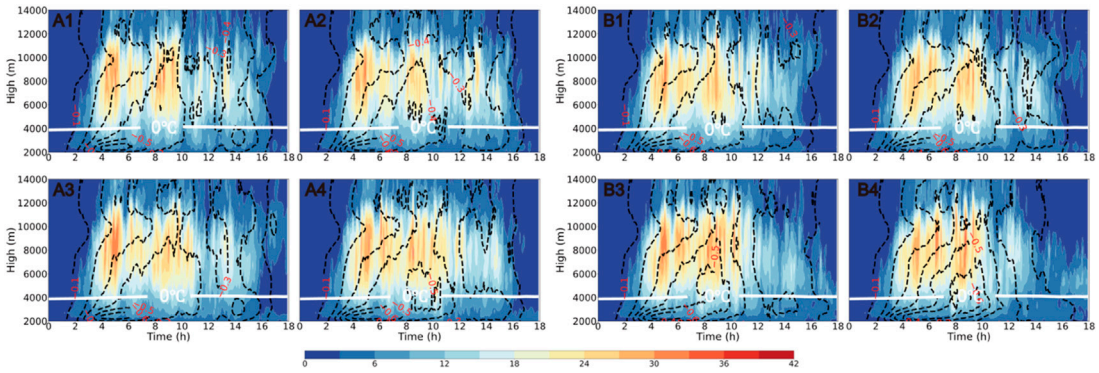

FIGURE 8
Time variation of height distribution of maximum updraft (Unit: m s^{-1}) with the contour of height distribution of hourly mean downdraft (Unit: m s^{-1}), and the solid white line is the height of 0°C: **(A)** TH-AU. **(B)** MY-AU; **(1)** NCCN50 **(2)** NCCN200 **(3)** NCCN 2000 **(4)** NCCN10000.

phenomenon comes from the different distribution of supercooled cloud water caused by the different sensitivity of the two auto-conversion schemes to the CCN concentration. In Figure 11, we can see that the auto-conversion intensity of MY-AU is more strongly inhibited as the concentration of CCN increases. Compared with the TH-AU scheme, the warm rain process is more strongly inhibited in the MY-AU scheme at the same CCN concentration, resulting in more supercooled cloud water participating in the ice phase process in the MY-AU scheme than in the TH-AU scheme.

Because the cloud water involved in ice crystal freezing increases slightly with the increase of CCN concentration in the TH-AU scheme, the ice-crystal mixing ratio does not change significantly with increasing CCN concentration. In contrast, with the rise of CCN concentration, the number of ice crystals generated by cloud water freezing in the MY-AU scheme increases significantly, the intensity of auto-conversion of ice to snow also increases significantly with the increase of CCN concentration (Figure Omitted), the ice-crystal mixing ratio in Figure 13 does not obviously increase with increasing CCN concentration. In addition, the downdraft of 4,000–6,000 m in the MY-AU scheme is enhanced when the CCN concentration is 2,000–10,000 cm^{-3} at dissipating stage, which weakens the transport of supercooled cloud droplets to the upper level and leads to the decrease of ice-crystal mixing ratio above 8,000 m.

In terms of dynamics, more cloud droplet freezing above 8,000 m also brings additional latent heat release. With the increase of CCN concentration, the updraft above 8,000 m of the two schemes is

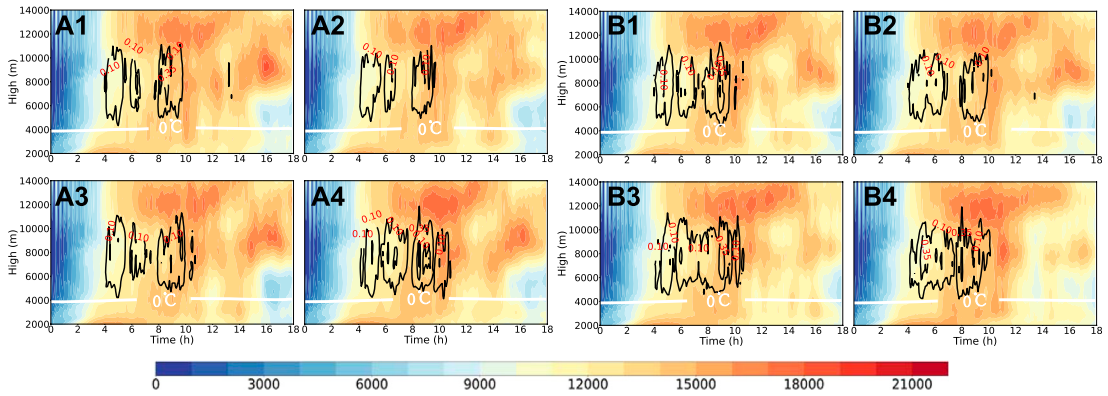

FIGURE 9
Time variation of height distribution of the number of updraft grids ($w > 0.1$ m s^{-1}) with the contour of the proportion of updraft greater than 15 m s^{-1} in the total updraft, and the solid white line is the height of 0 degrees Celsius: **(A)** TH-AU. **(B)** MY-AU; **(1)** NCCN50 **(2)** NCCN200 **(3)** NCCN2000 **(4)** NCCN10000.

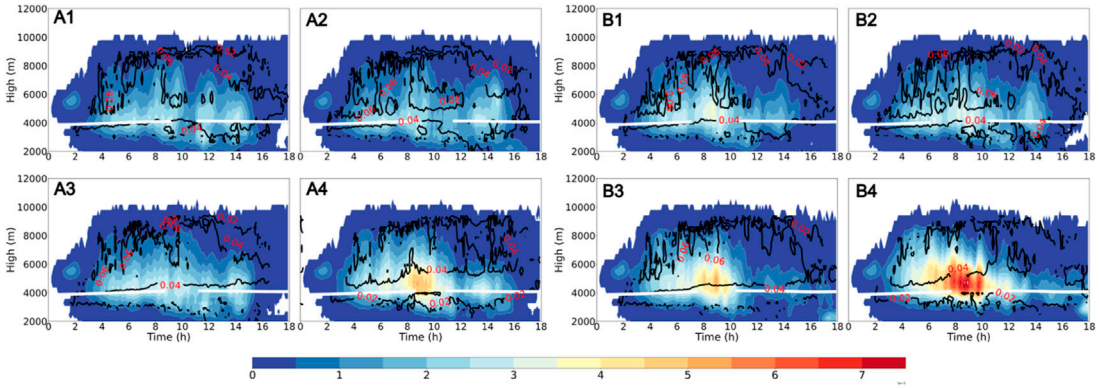

FIGURE 10
Time variation of the height distribution of cloud droplet mixing ratio (Unit:10^{-5} g kg^{-1}) with the contour of the mass-weighted average diameter (Unit: mm), and the solid white line is the height of 0°C **(A)**.TH-AU **(B)**.MY-AU; **(1)** NCCN50 **(2)** NCCN200 **(3)** NCCN 2000 **(4)** NCCN10000.

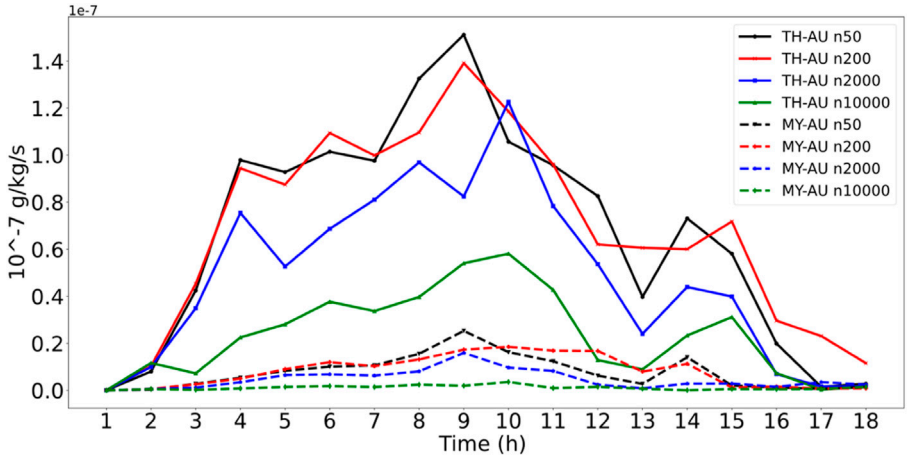

FIGURE 11
Time variation of auto-conversion rate from cloud water to rainwater (Unit: 10^{-7} g kg^{-1} s^{-1}).

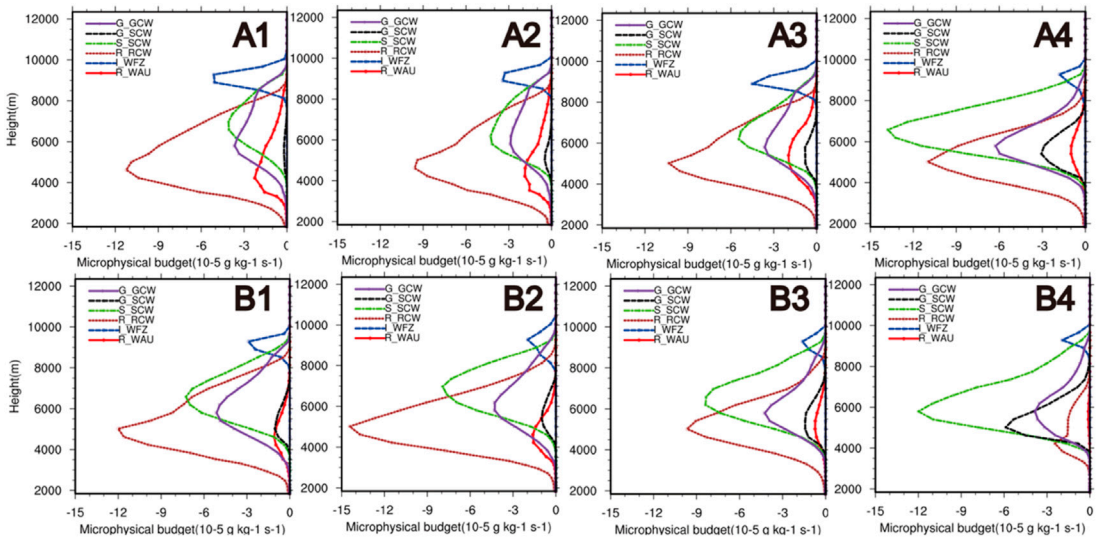

FIGURE 12
Height distribution of microphysical budget of cloud particles at 0930 UTC (Unit: 10^{--5} g kg^{-1} s^{-1}): **(A)** TH-AU **(B)** MY-AU; **(1)** NCCN50 **(2)** NCCN200 **(3)** NCCN 2000 **(4)** NCCN10000; G_GCW is the riming of graupel particles to cloud drops, G_SCW is the snow crystal s rime cloud droplets to generate graupel particles, S_SCW is the snow crystals rime cloud droplets to generate snow particles, R_RCW is the collision-coalescence of rain to cloud, I_WRF is the cloud droplets freeze into ice crystals, R_WAU is the cloud to rain auto-conversion.

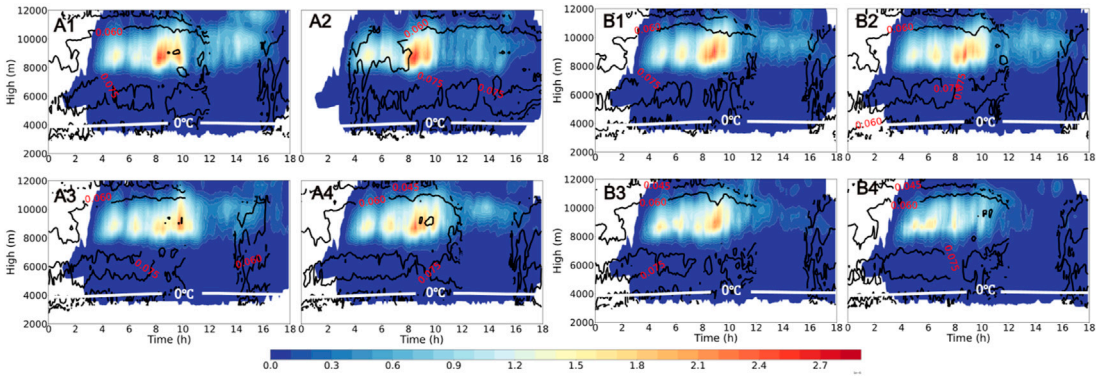

FIGURE 13
Time variation of the height distribution of ice particle mixing ratio (Unit:10^{-6} g kg^{-1}) with the contour of the mass-weighted average diameter (Unit: mm), and the solid white line is the height of 0°C **(A)** TH-AU. **(B)** MY-AU; **(1)** NCCN50 **(2)** NCCN200 **(3)** NCCN 2000 **(4)** NCCN10000.

enhanced. In particular, more cloud droplets freeze above 8,000 m in the MY-AU scheme, resulting in stronger updraft above 8,000 m at the same CCN concentration than in the TH-AU scheme.

In addition to cloud and ice particles, the auto-conversion process has more complex effects on snow and graupel particles. From the development stage to the maturity stage, with the increase of CCN concentration, the riming of cloud droplets to snow crystals increases obviously at 6,000–10,000 m (Figure Omitted), and more ice crystals also result in a greater auto-conversion of ice to snow crystals, which leads to the mixing ratio of snow particles increases at 6,000–8,000 m (Figure 14). At the same concentration of CCN, more supercooled cloud droplets participate in the ice phase process, causing the mixing ratio of snow crystals in MY-AU is significantly higher than that of TH-AU at the mature stage. In addition, when the convection enters the dissipative stage from the mature stage, the intensity of downdraft increases obviously with the increase of CCN concentration at 4,000–6,000 m. Along with the strengthening of the downdraft, the snow mixing ratio in both schemes above 6,000 m decreases because the strong downdraft makes it challenging to transport supercooled water to the upper-level in the dissipative stage. When the CCN concentration is 2,000–10,000 cm^{-3}, the stronger downdraft in the MY-AU scheme makes the mixing ratio of the snow crystals lower than that in TH-AU at the same CCN concentration.

In fact, from the change in the mixing ratio of ice and snow crystals, we can see that the effect of increasing CCN number concentration on the ice phase process and vertical airflow in the cloud has different effects at different stages of convection. In the convective development stage, with the increase of CCN concentration

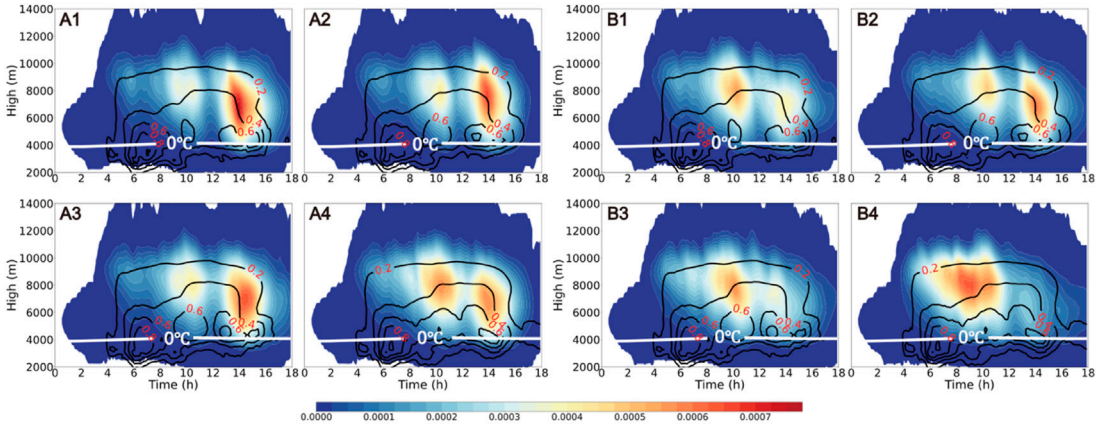

FIGURE 14
Time variation of the height distribution of snow particle mixing ratio (Unit: g kg^{-1}) with the contour of the mass-weighted average diameter (Unit: mm), and the solid white line is the height of 0°C **(A)** TH-AU. **(B)** MY-AU; **(1)** NCCN50 **(2)** NCC N200 **(3)** NCCN 2000 **(4)** NCCN10000.

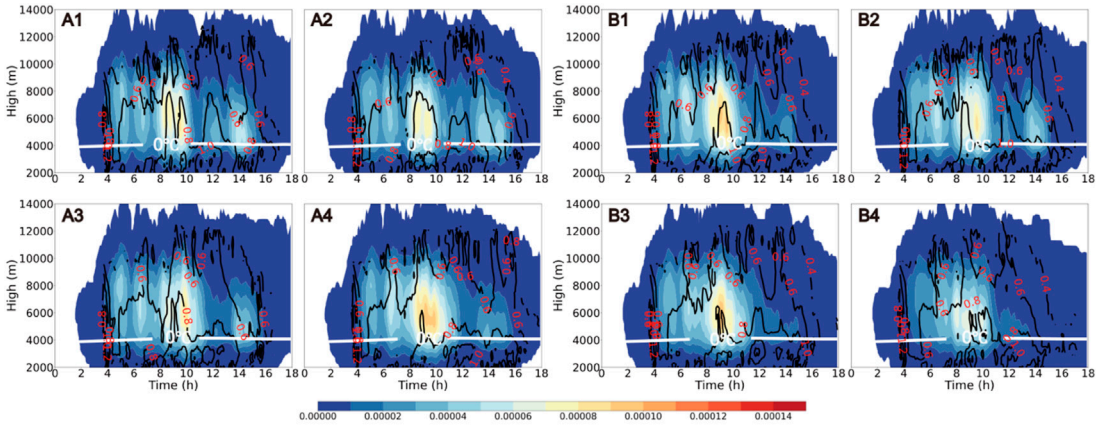

FIGURE 15
Time variation of the height distribution of graupel particle mixing ratio (Unit: g kg^{-1}) with the contour of the mass-weighted average diameter (Unit: mm), and the solid white line is the height of 0°C **(A)** TH-AU. **(B)** MY-AU; **(1)** NCCN50 **(2)** NCCN200 **(3)** NCCN 2000 **(4)** NCCN10000.

and the weakening of the auto-conversion intensity of cloud to rain, the mixing ratio of ice and snow crystals in the upper layer increases, and the updraft also increases. However, in the dissipation stage of convection, the increase of CCN concentration and the weakening of the auto-conversion intensity of cloud to rain may strengthen the downdraft in the middle of the cloud, resulting in a weakening of the upward transport of supercooled water, which is not conducive to the increase of ice and snow grains in the upper part of the convection.

In addition, for ice particles, the differences between the two schemes due to auto-conversion are more significant for graupel particles. The microphysical scheme of Thompson assumes that graupel particles are primarily produced by the freezing of raindrops and the riming of snow particles, and grow by riming supercooled water. Because the intensity of auto-conversion is not significantly inhibited, TH-AU still has a large number of tiny raindrops generated by the warm rain process. These raindrops can be transported to more than 8,000 m by the updraft and frozen into graupel particles. In addition, with the increase of CCN concentration, snow crystals can rime more cloud water. Because of this, as the concentration of CCN increases, the mixing ratio of graupel increases significantly.

On the contrary, for the MY-AU, the warm rain process is strongly suppressed at the CCN concentration of 50–10,000 cm^{-3} (Figure 15), resulting in the almost raindrops being from the melting of snow crystals and graupel particles. Only sporadic tiny raindrops can freeze into graupel particles above 8,000 m. Therefore, graupel particles in MY-AU are mainly concentrated below 6,000 m, which are generated by the riming of the snow crystal to cloud droplets. Because of that, the mixing ratio of graupel particles in MY-AU decreases with the increase in CCN concentration. At the same time, the particle size of the graupel decreases due to limited growing space, which makes graupel particles more likely to melt completely in the falling process. In

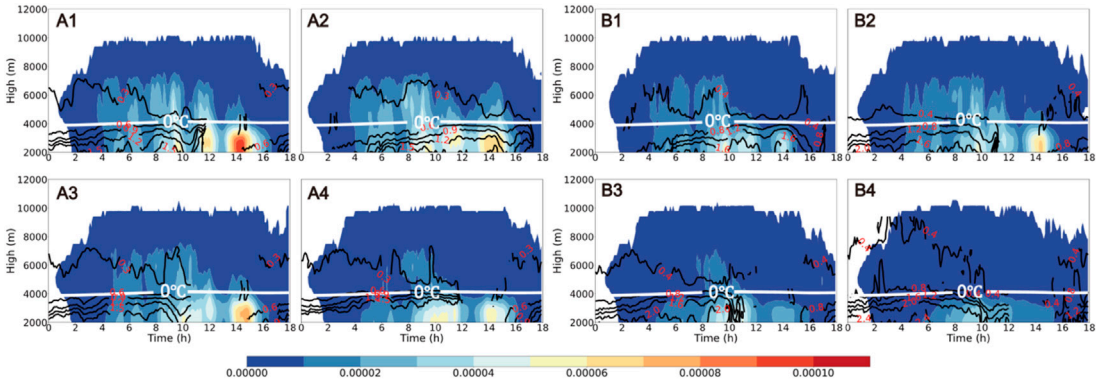

FIGURE 16
Time variation of the height distribution of rain particle mixing ratio (Unit: g kg^{-1}) with the contour of the mass-weighted average diameter (Unit: mm), and the solid white line is the height of 0°C **(A)** TH-AU. **(B)** MY-AU; **(1)** NCCN50 **(2)** NCC N200 **(3)** NCCN 2000 **(4)** NCCN10000.

addition, a large number of graupel particles fall below 6,000 m, enhancing the downdraft in MY-AU when the CCN concentration is 2,000–10,000 cm^{-3}.

At last, there are a series of changes in the microphysical processes that lead to a significant difference in precipitation between the two schemes. It is shown in Figure 16 that the mixing ratio of raindrops at the height of 4,000–8,000 m in the MY-AU scheme decreases with the increase of CCN concentration, but the raindrop mixing ratio at 4,000–8,000 m in the TH-AU scheme does not monotonically change with CCN concentration. Besides, the raindrop mixing ratio of the MY-AU scheme with the same CCN concentration is higher than TH-AU. In fact, raindrops at 4,000–8,000 m mainly come from warm rain processes, including cloud to rain auto-conversion and the collisional-coalescence process of cloud to rain. When the concentration of CCN is 50–200 cm^{-3}, the auto-conversion intensity of the TH-AU scheme changes little. Simultaneously, with the increase of CCN concentration, the activation of cloud droplets increases, which accelerates the warm rain process. Therefore, when the CCN concentration of the TH-AU scheme is 200 cm^{-3}, the raindrop mixing ratio increases at 4,000–8,000 m. However, when the CCN concentration is 200–10,000 cm^{-3}, the auto-conversion intensity in the TH-AU scheme begins to decrease, resulting in a decrease in the raindrop mixing ratio at the height of 4,000–8,000 m. On the contrary, the auto-conversion intensity of the MY-AU scheme is significantly inhibited with the increase of CCN concentration, and the warm rain process is continuously weakened.

The difference in the raindrop transformation process also affects the macroscopic convection process, manifested as the difference of ground accumulated precipitation between the two schemes. Due to the non-monotonic response of the warm rain process with CCN concentration in the TH-AU scheme, the cumulative precipitation increases with the increase of the warm rain process when the CCN concentration is 50–200 cm^{-3}. However, when the CCN concentration is 2,000–10,000 cm^{-3}, the melting precipitation of the TH-AU scheme does not increase significantly, and the attenuation of the warm rain process leads to a decrease in cumulative precipitation. On the contrary, in the MY-AU scheme, accumulative precipitation decreases with the increase in CCN concentration.

6 Discussion

Due to the limited knowledge of microphysical processes in clouds and the complexity of aerosol-cloud interactions, there are still some controversial findings on the sensitivity of clouds to rain auto-conversion schemes with CCN concentrations in strong convective simulations.

In terms of dynamic structure, with the increased CCN concentration, more supercooled water participates in freezing and riming, which releases more latent heat. The updraft in the two schemes increases with the increase of CCN concentration between 6,000 and 12,000 m. This is most likely to the simulation results of Rosenfeld et al. (2014) and Stevens and Feingold (2009). However, in this paper, the increase in CCN concentration does not lead to the extension of a convective lifetime, as Rosenfeld et al. (2014) mentioned. Moreover, the convective lifetime decreases with the increase of CCN concentration in both schemes, and this phenomenon is more evident in the MY-AU scheme. In fact, it is because the simulation of Rosenfeld et al. (2014) does not consider the buoyancy consumption caused by hydrometeor particles' fall. In the simulation results of MY-AU, with the increase of CCN concentration, the fall of more graupel particles and large raindrops enhances the development of downdraft in the mature stage at 4,000–6,000 m, which leads to the early dissipation of convection.

In addition, the influence of CCN on precipitation has also been controversial in previous studies. Khain and Pokrovsky (2004) and Teller and Levin (2006) changed the number of concentrations of CCN and found decreases in cumulative precipitation for higher concentrations of CCN. However, this is contrary to the study by Wang (2005) and Khain et al. (2005). In this work, with the increase of CCN concentration, the mixing ratio of ice particles increases, and the proportion of melting precipitation in total precipitation increases in both schemes. Because the auto-conversion intensity of the TH-AU scheme is less inhibited with CCN concentration, the melting precipitation has little difference. When the CCN concentration is low, the accumulated precipitation increases due to the strengthening of the warm rain process. However, when the CCN concentration is high, the accumulated precipitation decreases with the inhibition of the warm rain process.

On the contrary, for the MY-AU scheme, the proportion of supercooled water participating in the ice phase process is higher than in the TH-AU scheme when the concentration of CCN increases. Due to the decrease in the particle size of ice phase particles, especially when the concentration of CCN is 10,000 cm^{-3}, the melting process of snow crystals and graupel particles increases with the increase of CCN concentration, which is similar to the study of Khain et al. (2008) and Khain et al. (2015). Accompanied by the more suppressed warm rain processes, cumulative precipitation decreases.

7 Conclusion

In summary, the sensitivity of different auto-conversion schemes to changes in CCN concentrations varies significantly, and the aerosol-induced changes in precipitation and convection are strongly dependent on the auto-conversion scheme, with the following conclusions:

(1) Different auto-conversion scheme has a different sensitivity to changes in CCN concentrations, hence differences in the distribution of supercooled water in clouds. As the concentration of CCN increases, the particle size of cloud droplets decreases, resulting in the inhabitation of the auto-conversion process, which leads to more supercooled cloud water participate in the ice phase process. The MY-AU scheme is more sensitive to variation in CCN concentration, as the auto-conversion intensity decays more with the increase of CCN concentration, and auto-conversion intensity is only one-tenth of the TH-AU scheme. In the MY-AU scheme, more supercooled water participates in the ice-phase process at the same concentration of CCN.

(2) As the concentration of CCN increases, more cloud droplets freeze and release latent heat, which strengthens the updraft above 8,000 m for both schemes, and the proportion of updraft greater than 15m/s increases. The MY-AU has more cloud droplets freezing at the same CCN concentration than the TH-AU. Above 8,000 m, the updraft intensity is significantly greater than that of the TH-AU scheme in the mature phase, leading to a higher freezing height of supercooled water in the MY-TH scheme. In addition, at the same CCN concentration, the MY-AU scheme's graupel particles are produced at a lower height, which leads to more graupel particles falling at 4,000–6,000 m. The dragging effect makes the downdraft enhanced and convective decay advanced.

(3) Effects of CCN concentration on precipitation and ground graupel-fall show a significant dependence on the auto-conversion process. The cumulative precipitation and the accumulated ground graupel-fall of the TH-AU scheme increases when the CCN concentration is 50–200 cm^{-3} and slightly decreases when the CCN concentration is 200–10000 cm^{-3}. In contrast, as the CCN concentration increases, the cumulative precipitation with accumulated ground graupel-fall of the MY-AU scheme decreases, and the hourly rainfall intensity fluctuates wildly.

In this paper, the auto-conversion schemes are derived from the Thompson microphysics scheme, and in the other case, from Milbrandt-Yau. In addition, many auto-conversion schemes describe the cloud to rain auto-conversion process differently, and their conversion efficiency differs. More in-depth studies on other microphysical schemes are expected in future work. Moreover, it has been pointed out that meteorological elements such as vertical wind shear, atmospheric radiation, and turbulence strength can also affect the aerosol-cloud-precipitation interaction (Fan et al., 2009; Morrison et al., 2011; Tao et al., 2012). The interaction is not limited to the auto-conversion process. In this paper, we focus on the direction of microphysical parameterization and consider the response of different auto-conversion schemes to CCN concentration changes, hoping that the research can be helpful for future numerical simulation work in the field of aerosol-cloud interactions.

Data availability statement

The raw data supporting the conclusions of this article will be made available by the authors, without undue reservation.

Author contributions

Under the supervision by XL, YL conducted data analysis and article writing, and CY performed numerical simulation and data preparation. XL did further investigation and revises. All authors read and contributed to the manuscript.

Funding

This work was supported by the National Natural Science Foundation of China (Grant Nos. 42061134009 and 41975176).

Acknowledgments

In addition, we acknowledge the High Performance Computing Center of Nanjing University of Information Science and Technology for their support of this work.

Conflict of interest

Author CY was employed by Changzhou Benniu International Airport.

The remaining authors declare that the research was conducted in the absence of any commercial or financial relationships that could be construed as a potential conflict of interest.

Publisher's note

References

Albrecht, B. A. (1989). Aerosols, cloud microphysics, and fractional cloudiness. *Science* 245 (4923), 1227–1230. doi:10.1126/science.245.4923.1227

Alizadeh-Choobari, O., and Gharaylou, M. (2017). Aerosol impacts on radiative and microphysical properties of clouds and precipitation formation. *Atmos. Res.* 185, 53–64. doi:10.1016/j.atmosres.2016.10.021

Andreae, M. O., and Rosenfeld, D. (2008). Aerosol–cloud–precipitation interactions. part 1. the nature and sources of cloud-active aerosols. *Earth-Science Rev.* 89 (1-2), 13–41. doi:10.1016/j.earscirev.2008.03.001

Barthlott, C., and Hoose, C. (2018). Aerosol effects on clouds and precipitation over Central Europe in different weather regimes. *J. Atmos. Sci.* 75 (12), 4247–4264. doi:10.1175/jas-d-18-0110.1

Berry, E. X. (1969). A mathematical framework for cloud models. *J. Atmos. Sci.* 26 (1), 109–111. doi:10.1175/1520-0469(1969)026<0109:amffcm>2.0.co;2

Cohard, J.-M., and Pinty, J.-P. (2000). A comprehensive two-moment warm microphysical bulk scheme. I: Description and tests. *Q. J. R. Meteorological Soc.* 126 (566), 1815–1842. doi:10.1256/.56613

Fan, J., Yuan, T., Comstock, J. M., Ghan, S., Khain, A., Leung, L. R., et al. (2009). Dominant role by vertical wind shear in regulating aerosol effects on deep convective clouds. *J. Geophys. Res.* 114 (D22), D22206. doi:10.1029/2009jd012352

Fan, X., Xia, X., and Chen, H. (2018). Can Modis detect trends in aerosol optical depth over land? *Adv. Atmos. Sci.* 35 (2), 135–145. doi:10.1007/s00376-017-7017-2

Fan, Y. (2007) "The interaction between cloud, radiation and convection self-aggregation." *institutional Repos.* 46. doi:10.14711/thesis-991012980216303412

Ghan, S. J., Abdul-Razzak, H., Nenes, A., Ming, Y., Liu, X., Ovchinnikov, M., et al. (2011). Droplet nucleation: Physically-based parameterizations and comparative evaluation. *J. Adv. Model. Earth Syst.* 3 (4). doi:10.1029/2011ms000074

Ghosh, S., and Jonas, P. R. (1998). On the application of the classic Kessler and Berry Schemes in large eddy simulation models with a particular emphasis on cloud autoconversion, the onset time of precipitation and droplet evaporation. *Ann. Geophys.* 16 (5), 628–637. doi:10.1007/s00585-998-0628-2

Gryspeerdt, E., Stier, P., and Partridge, D. G. (2014). Links between satellite-retrieved aerosol and precipitation. *Atmos. Chem. Phys.* 14 (18), 9677–9694. doi:10.5194/acp-14-9677-2014

Hande, L. B., Hoose, C., and Barthlott, C. (2017). Aerosol- and droplet-dependent contact freezing: Parameterization development and case study. *J. Atmos. Sci.* 74 (7), 2229–2245. doi:10.1175/jas-d-16-0313.1

Houghton, J. (2001). "Climate change," measuring environmental degradation [Preprint]. doi:10.4337/9781781950715.00018

Hu, Z., and Cai, L. (1979). Cumulus warm rain process and its salt powder catalyzed parameterized numerical simulation (in China). *Chin. J. Atmos. Sci.* 3 (4), 334–342.

Kessler, E. (1969) *On the distribution and continuity of water substance in atmospheric circulations*, pp. 1–84. doi:10.1007/978-1-935704-36-2_1

Khain, A. P., Beheng, K. D., Heymsfield, A., Korolev, A., Krichak, S. O., Levin, Z., et al. (2015). Representation of microphysical processes in cloud-resolving models: Spectral (bin) microphysics versus bulk parameterization. *Rev. Geophys.* 53 (2), 247–322. doi:10.1002/2014rg000468

Khain, A. P., BenMoshe, N., and Pokrovsky, A. (2008). Factors determining the impact of aerosols on surface precipitation from clouds: An attempt at classification. *J. Atmos. Sci.* 65 (6), 1721–1748. doi:10.1175/2007jas2515.1

Khain, A., and Pokrovsky, A. (2004). Simulation of effects of atmospheric aerosols on deep turbulent convective clouds using a spectral microphysics mixed-phase cumulus cloud model. part II: Sensitivity study. *J. Atmos. Sci.* 61 (24), 2983–3001. doi:10.1175/jas-3281.1

Khain, A., Rosenfeld, D., and Pokrovsky, A. (2005). Aerosol impact on the dynamics and microphysics of deep convective clouds. *Q. J. R. Meteorological Soc.* 131 (611), 2639–2663. doi:10.1256/qj.04.62

Kogan, Y., and Ovchinnikov, M. (2020). Formulation of autoconversion and drop spectra shape in shallow cumulus clouds. *J. Atmos. Sci.* 77 (2), 711–722. doi:10.1175/jas-d-19-0134.1

Köhler, H. (1936). The nucleus in and the growth of hygroscopic droplets. *Trans. Faraday Soc.* 32, 1152–1161. doi:10.1039/tf9363201152

Kovačević, N. (2018). Hail suppression effectiveness for varying solubility of natural aerosols in water. *Meteorology Atmos. Phys.* 131 (3), 585–599. doi:10.1007/s00703-018-0587-4

Lebo, Z. J., and Morrison, H. (2014). Dynamical effects of aerosol perturbations on simulated idealized squall lines. *Mon. Weather Rev.* 142 (3), 991–1009. doi:10.1175/mwr-d-13-00156.1

Lebo, Z. J., and Seinfeld, J. H. (2011). Theoretical basis for convective invigoration due to increased aerosol concentration. *Atmos. Chem. Phys.* 11 (11), 5407–5429. doi:10.5194/acp-11-5407-2011

Lee, S.-S., Feingold, G., and Chuang, P. Y. (2012). Effect of aerosol on cloud–environment interactions in trade cumulus. *J. Atmos. Sci.* 69 (12), 3607–3632. doi:10.1175/jas-d-12-026.1

Lei, H., Guo, J., Chen, D., and Yang, J. (2020). Systematic bias in the prediction of warm-Rain Hydrometeors in the WDM6 microphysics scheme and modifications. *J. Geophys. Res. Atmos.* 125 (4). doi:10.1029/2019jd030756

Lerach, D. G., and Cotton, W. R. (2018). Simulating southwestern U.S. desert dust influences on supercell thunderstorms. *Atmos. Res.* 204, 78–93. doi:10.1016/j.atmosres.2017.12.005

Lim, K.-S. S., and Hong, S.-Y. (2010). Development of an effective double-moment cloud microphysics scheme with prognostic cloud condensation nuclei (CCN) for weather and climate models. *Mon. Weather Rev.* 138 (5), 1587–1612. doi:10.1175/2009mwr2968.1

Liu, X., Yuan, C., Sang, J., and Ma, S. (2021). Effect of cloud condensation nuclei concentration on a hail event with weak warm rain process in a semi-arid region of China. *Atmos. Res.* 261, 105726. doi:10.1016/j.atmosres.2021.105726

Li, Z., Lau, W., Ramanathan, V., Wu, G., Ding, Y., Manoj, M., et al. (2016). Aerosol and monsoon climate interactions over Asia. *Reviews of Geophysics* 54 (4), 866–929. doi:10.1002/2015rg000500

Manton, M. J., and Cotton, W. R. (1977). *Formulation of approximate equations for modeling moist deep convection on the mesoscale*. Fort Collins, CO: Department of Atmospheric Science, Colorado State University.

Marinescu, P. J., van den Heever, S. C., Saleeby, S. M., Kreidenweis, S. M., and DeMott, P. J. (2017). The microphysical roles of lower-tropospheric versus midtropospheric aerosol particles in mature-stage MCS precipitation. *J. Atmos. Sci* 74 (11), 3657–3678. doi:10.1175/jas-d-16-0361.1

Michibata, T., and Takemura, T. (2015). Evaluation of autoconversion schemes in a single model framework with satellite observations. *J. Geophys. Res. Atmos.* 9570–9590. Preprint. doi:10.1002/2015jd023818-t

Milbrandt, J. A., and Yau, M. K. (2005). A multimoment bulk microphysics parameterization. part I: Analysis of the role of the spectral shape parameter. *J. Atmos. Sci.* 62 (9), 3051–3064. doi:10.1175/jas3534.1

Morrison, H., de Boer, G., Feingold, G., Harrington, J., Shupe, M. D., and Sulia, K. (2011). Resilience of persistent arctic mixed-phase clouds. *Nat. Geosci.* 5 (1), 11–17. doi:10.1038/ngeo1332

Morrison, H., van Lier-Walqui, M., Fridlind, A. M., Grabowski, W. W., Harrington, J. Y., Hoose, C., et al. (2020). Confronting the challenge of Modeling Cloud and precipitation microphysics. *J. Adv. Model. Earth Syst.* 12 (8), e2019MS001689. doi:10.1029/2019ms001689

Morrison, H., Witte, M., Bryan, G. H., Harrington, J. Y., and Lebo, Z. J. (2018). Broadening of modeled cloud droplet spectra using bin microphysics in an Eulerian spatial domain. *J. Atmos. Sci.* 75 (11), 4005–4030. doi:10.1175/jas-d-18-0055.1

Naeger, A. R., Colle, B. A., Zhou, N., and Molthan, A. (2020). Evaluating warm and cold rain processes in cloud microphysical schemes using Olympex Field Measurements. *Mon. Weather Rev.* 148 (5), 2163–2190. doi:10.1175/mwr-d-19-0092.1

Reisner, J., Rasmussen, R. M., and Bruintjes, R. T. (1998). Explicit forecasting of supercooled liquid water in winter storms using the MM5 mesoscale model. *Q. J. R. Meteorological Soc.* 124 (548), 1071–1107. doi:10.1002/qj.49712454804

Reutter, P., Su, H., Trentmann, J., Simmel, M., Rose, D., Gunthe, S. S., et al. (2009). Aerosol- and updraft-limited regimes of cloud droplet formation: Influence of particle number, size and hygroscopicity on the activation of cloud condensation nuclei (CCN). *Atmos. Chem. Phys.* 9 (18), 7067–7080. doi:10.5194/acp-9-7067-2009

Rosenfeld, D., Sherwood, S., Wood, R., and Donner, L. (2014). Climate effects of aerosol-cloud interactions. *Science* 343 (6169), 379–380. doi:10.1126/science.1247490

Rosenfeld, D. (2000). Suppression of rain and snow by urban and industrial air pollution. *Science* 287 (5459), 1793–1796. doi:10.1126/science.287.5459.1793

Saleeby, S. M., Heever, S. C., Marinescu, P. J., Kreidenweis, S. M., and DeMott, P. J. (2016). Aerosol effects on the anvil characteristics of mesoscale convective systems. *Journal of Geophysical Research: Atmospheres* 121 (18). doi:10.1002/2016jd025082

Seifert, A., and Beheng, K. D. (2005a). A two-moment cloud microphysics parameterization for mixed-phase clouds. part 2: Maritime vs. Continental Deep convective storms. *Meteorology Atmos. Phys.* 92 (1-2), 67–82. doi:10.1007/s00703-005-0113-3

Seifert, A., and Beheng, K. D. (2005b). A two-moment cloud microphysics parameterization for mixed-phase clouds. part 1: Model description. *Meteorology and Atmospheric Physics* 92 (1-2), 45–66. doi:10.1007/s00703-005-0112-4

Seifert, A., Nuijens, L., and Stevens, B. (2010). Turbulence effects on warm-rain autoconversion in precipitating shallow convection. *Q. J. R. Meteorological Soc.* 136 (652), 1753–1762. doi:10.1002/qj.684

Seinfeld, J. H., and Lebo, Z. J. (2011). Theoretical basis for convective invigoration due to increased aerosol concentration. *Atmospheric Chemistry and Physics* 11 (11), 5407–5429. doi:10.5194/acp-11-5407-2011

Sheffield, A. M., Saleeby, S. M., and van den Heever, S. C. (2015). Aerosol-induced mechanisms for Cumulus Congestus growth. *J. Geophys. Res. Atmos.* 120 (17), 8941–8952. doi:10.1002/2015jd023743

Stevens, B., and Feingold, G. (2009). Untangling aerosol effects on clouds and precipitation in a buffered system. *Nature* 461 (7264), 607–613. doi:10.1038/nature08281

Tao, W.-K., Chen, J. P., Li, Z., Wang, C., and Zhang, C. (2012). Impact of aerosols on convective clouds and precipitation. *Rev. Geophys.* 50 (2). doi:10.1029/2011rg000369

Teller, A., and Levin, Z. (2006). The effects of aerosols on precipitation and dimensions of subtropical clouds: A sensitivity study using a numerical cloud model. *Atmos. Chem. Phys.* 6 (1), 67–80. doi:10.5194/acp-6-67-2006

Thompson, G., Field, P. R., Rasmussen, R. M., and Hall, W. D. (2008). Explicit forecasts of winter precipitation using an improved bulk microphysics scheme. part II: Implementation of a new snow parameterization. *Mon. Weather Rev.* 136 (12), 5095–5115. doi:10.1175/2008mwr2387.1

van den Heever, S. (2018) "Aerosol effects on the anvil characteristics, cold pool forcing and stratiform-convective precipitation partitioning and latent heating of mesoscale convective systems." doi:10.2172/1482383

van den Heever, S. C., Carrio, G. G., Cotton, W. R., DeMott, P. J., and Prenni, A. J. (2006). Impacts of nucleating aerosol on Florida storms. part I: Mesoscale simulations. *J. Atmos. Sci.* 63 (7), 1752–1775. doi:10.1175/jas3713.1

van den Heever, S. C., Grant, L. D., Freeman, S. W., Marinescu, P. J., Barnum, J., Bukowski, J., et al. (2021). The Colorado state university convective cloud outflows and updrafts experiment (C3LOUD-EX). *Bull. Am. Meteorological Soc.* 102 (7), E1283–E1305. doi:10.1175/bams-d-19-0013.1

Wang, C., and Xie, Y. (2009). Study on cloud micro-physical processes and precipition formative mechanisms of a mesoscale convective system in Meiyu Front in June 2004 (in China). *J. Meteorological Sci.* 29 (4), 434–446.

Wang, C. (2005). A modeling study of the response of tropical deep convection to the increase of cloud condensation nuclei concentration: 1. Dynamics and microphysics. *J. Geophys. Res.* 110 (D21), D21211. doi:10.1029/2004jd005720

White, B., Gryspeerdt, E., Stier, P., Morrison, H., Thompson, G., and Kipling, Z. (2017). Uncertainty from the choice of microphysics scheme in convection-permitting models significantly exceeds aerosol effects. *Atmos. Chem. Phys.* 17 (19), 12145–12175. doi:10.5194/acp-17-12145-2017

Woodley, W. L., Rosenfeld, D., and Silverman, B. A. (2003). Results of on-top glaciogenic cloud seeding in Thailand. part I: The demonstration experiment. *J. Appl. Meteorology* 42 (7), 920–938. doi:10.1175/1520-0450(2003)042<0920:roogcs>2.0.co;2

Xie, X., and Liu, X. (2015). Aerosol-cloud-precipitation interactions in WRF model: Sensitivity to autoconversion parameterization. *J. Meteorological Res.* 29 (1), 72–81. doi:10.1007/s13351-014-4065-8

Xie, X. N., and Liu, X. D. (2013). Analytical studies of the cloud droplet spectral dispersion influence on the first indirect aerosol effect. *Adv. Atmos. Sci.* 30, 1313–1319. doi:10.1007/s00376-012-2141-5

frontiers | Frontiers in Earth Science

TYPE Original Research
PUBLISHED 03 February 2023
DOI 10.3389/feart.2023.1110898

OPEN ACCESS

EDITED BY
Yunheng Wang,
University of Oklahoma, United States

REVIEWED BY
Omid Memarian Sorkhabi,
University of Isfahan, Iran
Junhu Zhao,
National Climate Center, China

*CORRESPONDENCE
Yutong Ma,
1034472773@qq.com
Mei Liu,
lmkerry@163.com

SPECIALTY SECTION
This article was submitted to Environmental Informatics and Remote Sensing, a section of the journal Frontiers in Earth Science

RECEIVED 29 November 2022
ACCEPTED 10 January 2023
PUBLISHED 03 February 2023

CITATION
Jin X, Ma Y, Liu M and Zhong S (2023), Evolution characteristics of impact weather system and SST signals during years of anomalous Meiyu onset over the Yangtze-Huaihe River Basin.
Front. Earth Sci. 11:1110898.
doi: 10.3389/feart.2023.1110898

Evolution characteristics of impact weather system and SST signals during years of anomalous Meiyu onset over the Yangtze-Huaihe River Basin

Xiaoxia Jin[1], Yutong Ma[2]*, Mei Liu[1]* and Shanshan Zhong[2]

[1]Jiangsu Meteorological Observatory, Nanjing, China, [2]School of Atmospheric Sciences, Nanjing University of Information Science and Technology, Nanjing, China

This article investigates the climatic characteristics of Meiyu over the Yangtze-Huaihe River Basin and the primary impact system based on Meiyu onset data from 1954 to 2020, precipitation during the Meiyu Period, NCEP/NCAR reanalysis data, sea surface temperature (SST) data of NOAA, and western Pacific subtropical high (sub-high) data provided by the National Climate Center. The main analytical method used is synthetic analysis. The results indicate that the Meiyu onset date has enormous interannual variation. The date of the earliest Meiyu emergence is 27 days prior to the latest. There is a strong relationship between the duration of Meiyu and rainfall. The start of Meiyu correlates with the northward motion of the South Asia High, the northward jump of the westerly jet, the northward jump of the subtropical high, and the northward motion of the low-level jet. In the early Meiyu years featured in this study, the northward jump of the aforementioned systems occurred earlier and the position of the westerly jet shifted from 34–35°N to 38–40°N, which is much further north than its position under typical climatic circumstances. From late May to early June, the subtropical high was extraordinarily powerful, the ridgeline reached 20°N, and its position was further to the north. In years with a late Meiyu onset, the position of the westerly jet and the ridgeline were further south than the climatological average from early to late June; the jump to the north was not evident until late June. In addition, SST anomalies of the Indian Ocean and Pacific Ocean are significant external forcing variables that influence the Meiyu start date. The high SST of the equatorial Indian Ocean and the equatorial tropical eastern Pacific in the autumn of the preceding year and the high SST of the equatorial Indian Ocean in the spring of that year are prophase indicators of an early Meiyu start in the Yangtze-Huaihe River Basin.

KEYWORDS

Meiyu over the Yangtze-Huaihe River Basin, Meiyu onset date, abnormal circulation, subtropical high, South Asia high

1 Introduction

Meiyu is a climatic phenomenon characterized by persistent rainfall in June and July in the middle and lower reaches of the Yangtze River in China, Taiwan, south-central Japan, and southern Korea (Ding et al., 2007). The seasonal rainy period in early summer in East Asia is described differently in different regions and is referred to as Meiyu in China, Baiu in Japan (Takaya et al., 2020), and the "Changma" season in Korea (Choi et al., 2020). Meiyu is closely related to the interannual variability of the East Asian summer wind circulation; the early start

and duration of Meiyu and the amount of rainfall it brings are significantly influenced by East Asian atmospheric circulation (Huang et al., 2012; Sun and Li, 2019; Tang and Li, 2020). According to extensive previous studies, China's rainbands experience two northward jumps and three stagnations (Ding et al., 2007), and in early June, the East Asian summer winds advance northward and the rain belt moves from South China to the Jianghuai basin. The summer Meiyu anomaly is the main cause of flooding in eastern China (Liu et al., 2013), and flooding can bring great harm to various industries (Zhou et al., 2019). Therefore, there is great significance, for short-term climate prediction, in studying the climatic characteristics of Meiyu anomaly years and analyzing the influence of the East Asian summer wind, so as to make accurate forecasts for Meiyu anomaly years, which can greatly reduce people's losses.

Many previous studies have been conducted on the influence of East Asian summer winds on anomalous Meiyu years. According to previous studies, the main influence systems in the upper troposphere are the South Asian high and the subtropical westerly jet stream. The time of the northward jump, the area, and the intensity of the South Asian high and the time of the two northward jumps of the subtropical westerly jet are closely related to the duration of Meiyu in China (Liu et al., 2007) and the time of Meiyu onset (Li et al., 2015). The influence system of the middle troposphere is mainly the large-scale circulation and western Pacific subtropical high. The subtropical high transports a large amount of water vapor to the eastern part of China, so the time of the westward extension and the northward jump of the subtropical high have a significant influence on the location of the main rain belt in China (Zhao et al., 2018), and while the circulation at middle and high latitudes determines whether the cold air moves southward, both determine the duration of Meiyu (Luo et al., 2019). Low-level circulation mainly determines whether the location of the low-level jet is conducive to precipitation. Chinese Meiyu is influenced by the early and late outbreak of the Somali rapids and the South China Sea summer winds (Li and Wu, 2002). In addition, Meiyu is also influenced by precursors, including SST anomaly, soil moisture anomaly, snow cover anomaly, *etc.* (Chen et al., 2020; Xu et al., 2021; Zhao et al., 2021). SST anomaly is one of the most important factors; by influencing the circulation system of the East Asian summer monsoon, it further affects Meiyu over the Yangtze-Huaihe River Basin. The interannual variation of the East Asian summer wind circulation and sea surface temperature led to a significant difference in the start and end dates of Meiyu in the Jianghuai region between 1954 and 2020. This paper discusses the following questions: what are the characteristics of the early and late entry and exit of Meiyu in the Jianghuai region in the past 67 years; what are the characteristics of the East Asian monsoon circulation in the anomalous years; and what is the influence of the precursor SST on Meiyu, and which region's SST has a greater impact.

This paper analyzes the climatic characteristics of Meiyu in Jianghuai regions from 1954 to 2020, focusing on the climatic characteristics of the start and end of Meiyu anomalies and the systematic analysis of East Asian summer winds. On this basis, the correlation between the Meiyu onset date and the SST in different periods is analyzed. The key SST area was selected to analysis the influence of SST on the western Pacific subtropical high index and the start and end dates of Meiyu. The conclusion has great significance in predicting Meiyu in the Yangtze-Huaihe River Basin.

2 Data and methods

In order to display the contribution of the weather system and SST, the following datasets are employed:

(1) According to the division of Meiyu regions provided by the National Climate Center's "Operational Regulations for Meiyu Monitoring," the Meiyu regions in China are divided into three regions: Jiangnan region, Yangtze region, and Jianghuai region. In this paper, analysis is mainly carried out on Meiyu in the Jianghuai region, represented by Jiangsu and Anhui, and data relating to Meiyu onset dates in Jiangsu and Anhui from 1954 to 2020 are collated and used. (2) The first set of reanalysis data from the National Centers for Environmental Prediction and National Center for Atmospheric Research (NCEP/NCAR): height field, wind field, and relative humidity field with a horizontal resolution of 2.5° × 2.5°; (3) the global ERSST_V5 SST reconstruction data from the National Oceanic and Atmospheric Administration (NOAA) with a horizontal resolution of 2.0° × 2.0°; and (4) the western Pacific subtropical high intensity, area, ridge line, and westward-extending ridge point information provided by the National Climate Center. (5) The climatic averages of height and wind fields in this paper are adopted from 1981 to 2010.

In order to analyze the influence of key weather systems on the annual pattern of Meiyu and explore the indicators of forecasting significance, this paper conducts a synthetic analysis of the circulation situation in the years that saw abnormal Meiyu onset, focusing on the differences between the circulation situation in the early and late years of Meiyu on June 5 (the average Meiyu start date in early years), June 17 (the average Meiyu start date in climatic average years), and June 28 (the average Meiyu start date in the late years) respectively, and analyzes the influence of key systems on the day of Meiyu entry.

3 Anomalous characteristics of the start date of Meiyu in Jianghuai

The standardization of the Meiyu onset date, the duration of the Meiyu period, and the interannual variation of the amount of rainfall during Meiyu in the Jiangsu Province from 1954 to 2020 (the figure of Anhui Province is omitted) are shown in Figure 1. There are significant interannual variations in the onset date of Meiyu, the duration of the Meiyu period, and the amount of rainfall during Meiyu in the Jianghuai region, and there is a significant correlation between the onset date of Meiyu, the duration of the Meiyu period, and the amount of rainfall during Meiyu. The correlation coefficients of the onset date of Meiyu and the duration of the Meiyu period in Anhui and Jiangsu are −0.47 and −0.53, respectively. The correlation coefficients of the onset date of Meiyu and the amount of rainfall during Meiyu are −0.24 and −0.30, respectively. Thus, the duration of the Meiyu period is usually longer and the amount of rainfall during Meiyu is generally greater when the onset date of Meiyu is early, so it can be seen that early and late Meiyu start dates have greater influence on the duration of the Meiyu period and the amount of rainfall during Meiyu in that year, especially in years when the onset date of Meiyu is unusually early and late, which is a key factor in the ruling of "extreme Meiyu." At the same time, it can be found that the correlation between the start date of Meiyu and the duration of

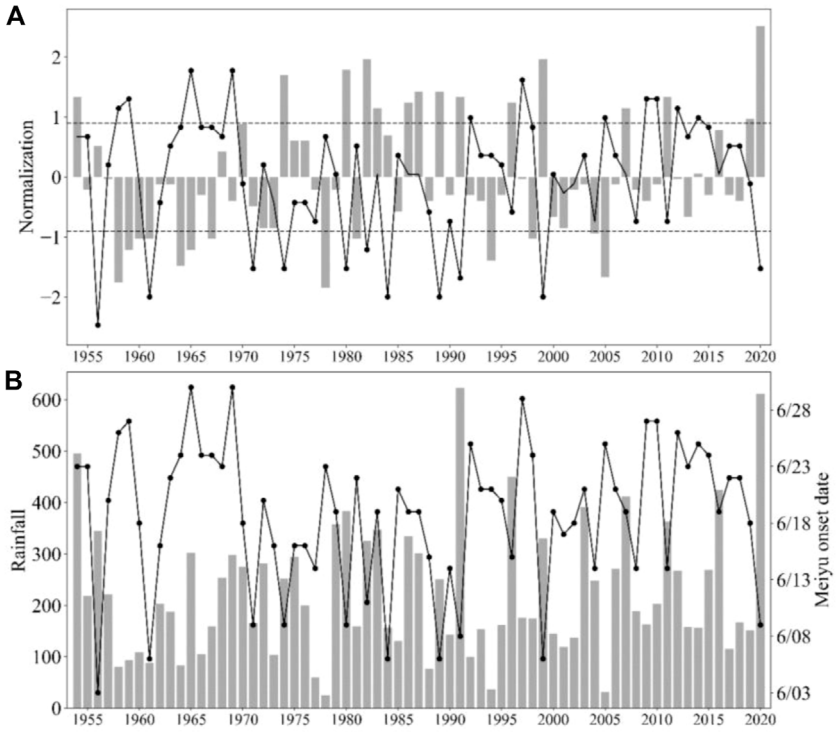

FIGURE 1
(A) Standardized time series of the onset date of Meiyu and the duration of Meiyu (the dotted line represents 0.9 times the standard deviation) in Jiangsu from 1954 to 2020 **(B)** Rainfall during Meiyu period and the onset date of Meiyu (The bar represents the duration of Meiyu and rainfall during Meiyu, and the broken line represents the onset date of Meiyu).

TABLE 1 Statistics of the Meiyu onset dates over the Yangtze-Huaihe River Basin from 1954 to 2020.

	Meiyu onset
Earliest (year)	3 June (1956)
Latest (year)	30 June (1965)
Climatic average	17 June
Unusually early	1956, 1961, 1971, 1980, 1984, 1989, 1999, 2020
Unusually late	1959, 1965, 1969, 2005, 2010, 2014

Meiyu is higher than its correlation with the amount of rainfall duringMeiyu, mainly because the early onset of Meiyu generally causes the end of Meiyu rain to occur later, and the amount of rainfall during Meiyu rain is related to the precipitation characteristics during the Meiyu period. Therefore, the analysis of the anomalous characteristics of Meiyu is important for the prediction of the Meiyu onset date. Taking 0.9 times standard deviation as the standard, the year when the two provinces' Meiyu onset days were less than 0.9 times standard deviation was selected as the early year, and the year when the two provinces' Meiyu onset days are more than 0.9 times standard deviation was selected as the late year of Meiyu onset. See Table 1 for abnormal years. The average onset date of Meiyu in the last 67 years in Jiangsu and Anhui was June 17, and the average end date was July 12. Among them, the earliest start date was June 3 (1956) and the latest was June 30 (1965), with a difference of 27 days between the earliest and latest entry dates. This shows that the onset date varies significantly each year. According to the statistics, early and late years of Meiyu onset are 8 and 6 years, respectively.

4 The relationship between the Meiyu start date and key weather systems

Summer wind activity in East Asia has a significant influence on the interannual variation of Meiyu. Different levels of circulation systems change significantly before and after the onset and end of Meiyu, such as the northward enhancement of South Asian high pressure and the northward jump of subtropical high pressure; accompanied by the stabilization and maintenance of the low-level jet and the formation of the Meiyu bands, this is a comprehensive reflection of the multi-scale weather systems. Therefore, different levels of weather systems play key roles in the formation of the rainy season, and changes in these systems determine the beginning and end of the rainy season.

4.1 The influence of the upper tropospheric South Asia High on Meiyu anomaly

The main influence system of the upper troposphere for Meiyu is South Asian high pressure, located in southern Asia, which is a strong and stable center of atmospheric activity and is an important

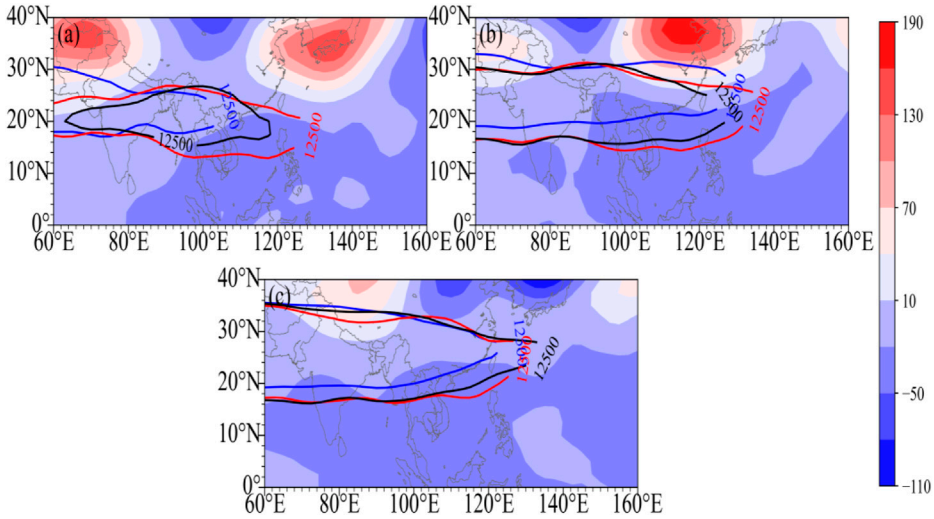

FIGURE 2
Comparative analysis of 200 hPa geopotential height **(A)**. June 5th, **(B)**. June 17th, **(C)**. June 28th, unit: gpm) (Shaded area: the difference between early years and late years, contour: South Asia High (12500 gpm), blue: early years, red: late years, black: climatic average).

part of the Meiyu weather system. The time, area, and intensity of South Asian high pressure starting to jump north and east in summer are closely related to the time of Meiyu onset in China (Liu et al., 2007). Figure 2 displays the analysis of the 200 hPa height occasion at different times of Meiyu; it shows that on June 5, the west ring of South Asian high pressure in the early Meiyu year was further west and slightly further north compared with climatic average years and the average late year, indicating that South Asian high pressure was established in the early Meiyu year and moved northward earlier, but its east ring does not show a strong advantage. On June 17, South Asian high pressure in the early Meiyu onset year was further north compared with the climatic average year and the average late year, and the east ring, in particular, was more pronounced. The position of the ridge of South Asian high pressure was close to that of -climatic average years and the late year, the position of the eastern extension of South Asian high pressure was close to that during climatic average years and the early year, and the ridge of South Asian high pressure in climatic average years and the late year was further north and east compared with June 5. On June 28, there was little difference between the position of the ridge line of South Asia high pressure in the early year, climatic average years, and the late year, indicating that Meiyuonset occurred at this time in each of the years. The changes and differences in the positions of South Asian high pressure on the anomalous and average onset days indicate that South Asian high pressure has a close relationship with the beginning and the progress of Meiyu, and the early and late jump of inSouth Asian high pressure to the north affects the early and late start of Meiyu.

Another difference between the early and late years is that 200 hPa height fields also have obvious features and differences at certain times, the most obvious being that between June 5 and 17 on the north side of the high pressure in South Asia, distribution is "+-+", the Iranian plateau and the vicinity of Japan show a significant positive distribution, and the rest of the areas have negative distribution. The positive center on June 17 in the Iranian plateau decreased compared with the central value on June 5, and the positive center on the island of Japan increased compared with the 5th, and the center moved westward to the north China plain area. By June 28, there was no obvious positive or negative zone between the two height differences, and the situation was already relatively close in different years. Therefore, the difference between the early and late 200 hPa height fields is mainly manifested in early and mid-June, and the early height field near Japan is strongly correlated with the early onset of Meiyu, which is indicative of the early arrival of Meiyu.

The East Asian subtropical westerly rapid is a high-value wind speed zone located in north of the South Asian high pressure. Generally speaking, the time of the second northward jump of the westerly jet stream is closely related to the time of Meiyu onset in Jianghuai (Li et al., 2004). This article presents a synthetic analysis of the subtropical westerly jet stream in the years of early and late Meiyu onset. As shown in Figure 3, in the early onset year (Figure 3A), the center of the westerly rapid and the climatic mean state were close to each other before June 4, but after June 4, there was an obvious northward jump, and the rapid axis jump from 34°N to 38°N was obviously further north than the climatic mean state of the westerly rapid, which corresponded to the early start of the Meiyu in Jianghuai and Huaihua. In the late onset year (Figure 3B), the position of the westerly rapids from early to mid-June was stable at nearly 35°N, which was close to the climatic average position, and the wind speed of the rapids axis was slightly lower than that in the early onset year, with the central wind speed about 35 m/s. In late June, the westerly rapids axis jumped significantly northward, which corresponded to the late onset date. Therefore, the differences in the distribution of 200 hPa latitudinal winds between the early year, climatic average years, and the late year are obvious, fully reflecting the close relationship between the westerly rapids and the early and late onset of Meiyu.

The differences between South Asian high pressure and the westerly jet stream in the upper troposphere in the abnormal Meiyu

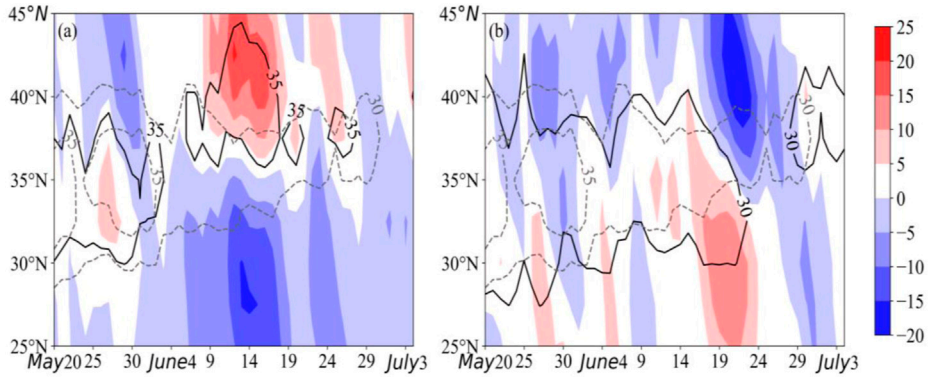

FIGURE 3
East Asia 110°-120°E average of 200 hPa zonal wind anomaly (unit: m/s) time-latitude cross sections in abnormal years of Meiyu onset **(A)**: early years **(B)**: late years The shaded area is the anomaly, and the dashed (solid) line represents the 30 m/s, 35 m/s contour of the climatic average in abnormal years.

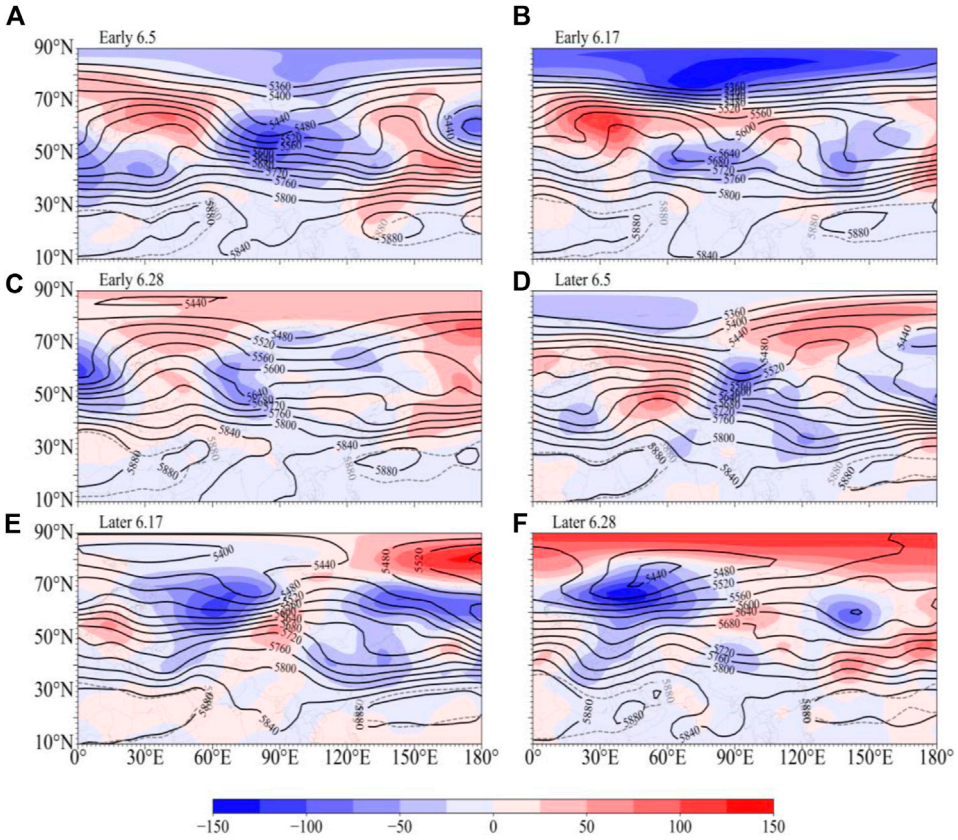

FIGURE 4
The characteristics of the 500 hPa geopotential height (unit: gpm) in the early and late years of the Meiyu onset date in the Yangtze-Huaiher River Basin (Shaded area: anomaly, black solid line: height field, gray dotted line: climatic average position of subtropical high). **(A)**: June 5th in early years **(B)**: June 17th in early years **(C)**: June 28th in early years **(D)**: June 5th in later years **(E)**: June 17th in later years **(F)**: June 28th in later years.

onset year show that before the onset of Meiyu in the Jianghuai region, the upper East Asian summer wind circulation system underwent a rapid adjustment, with the southern high pressure gradually pushing northward, strengthening the center and increasing the area; the westerly jet stream took a second jump northward, from 34–35°N to 38–40°N, and maintained its position steadily or gradually moved northward. In general, in early Meiyu onset years, high pressure in South Asia is north-westerly and the westerly rush adjusts northward earlier, while the opposite is true of late Meiyu onset years.

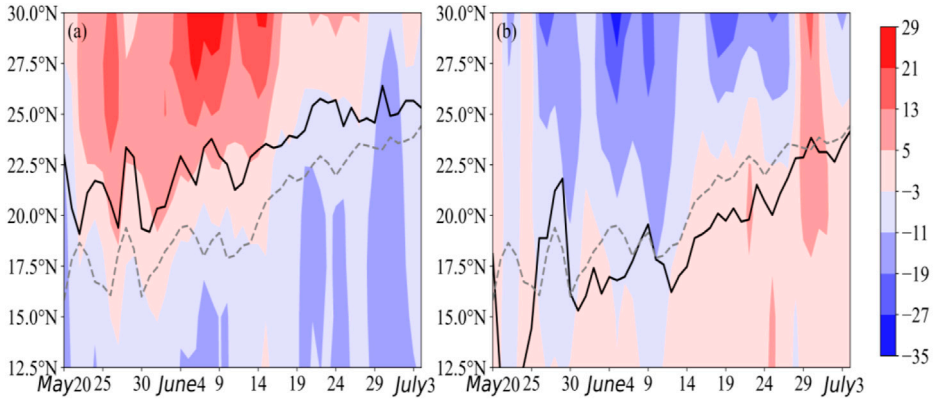

FIGURE 5
110°-140°E average of 500 hPa geopotential height time-latitude cross sections in the early and late years of Meiyu onset **(A)**: early years **(B)**: late years (The shaded area is the anomaly, and the dashed (solid) line represents the climatic average position (abnormal year) of the subtropical high ridgeline).

4.2 The influence of mid-level subtropical high pressure on Meiyu anomaly

The 500 hPa height field is representative of the mid-tropospheric circulation system, and the main object of study is the large-scale circulation situation and the characteristics of the western Pacific sub-high. The analysis of the 500 hPa height field at different times in anomalous years (Figure 4) shows that on June 5, in early Meiyu onset years, the blockage in the middle and high latitudes of Europe and Asia is obvious, the positive height leveling area is located in the Ural Mountains and the East Siberian mountains, and the negative leveling area is located from the West Siberian plain to the Central Siberian plateau; the position of the sub-high is further west and north than the climatic average position, but the intensity is weaker than in climatic average years (Figure 4A). On June 17, the circulation situation in the middle and high latitudes of Eurasia still maintained an obvious double blocking high pressure, and the positive height deviation level located in the Ural Mountains was further strengthened, the ridge position and westward extension of the ridge point of the sub-high was close to that in climatic average years, and the intensity was less than in climatic average years (Figure 4B). On June 28, the blockage of the circulation in the middle and high latitudes of Eurasia weakened, the flat westerly zone was dominated by the circulation, and the position of the sub-high was close to the climatic average position (Figure 4C). In summary, the early westward extension of the sub-high's northward jump is conducive to the early onset of Meiyu in the Jianghuai and Huaihua areas. In addition, the early onset of Meiyu shows a clear blockage of high-latitude circulation at different times in June, while mid-latitude circulation is flatter and straighter, and the sub-high maintains a longer period of stability and less movement.

The situation surrounding circulation in the middle troposphere and the characteristics of the western Pacific subsurface are significantly different to those in the early year; the position of the sub-high in the late year, on June 5 (Figure 4D), is significantly more easterly and southerly than the climatic average position, and the latitudinal circulation is dominant at high latitudes, and the coastal trough is controlled in the Jianghuai region, which is not conducive to the onset of Meiyu in the Jianghuai region. On June 17, the position and intensity of the sub-high (Figure 4E) were close to those in climatic average years, but the height field in the middle and high latitudes of Eurasia became obviously negative, and the coastal trough was still controlling the Jianghuai area. By June 28 (Figure 4F), the sub-high was close to normal, and the coastal trough in the JH region disappeared and turned into a flatter trough fluctuation type. The circulation situation is conducive to the onset of Meiyu.

The blockage is a prerequisite for the onset of Meiyu as it is conducive to the accumulation of cold air and provides favorable cold air transport for the occurrence of heavy rainfall during the Meiyu period. The characteristics of the western Pacific sub-high are also significant in the onset of Meiyu in Jianghuai and Huaihua, and it, therefore, deserves further discussion. The study shows that the time of the second northward jump of the subsurface corresponds with the end of Meiyu in Jianghuai (Liu et al., 2013). As shown in Figure 5, the ridge of the sub-high in the early year (Figure 5A) was significantly further north than in climatic average years and it was generally maintained north of 19°N. Between June 25 and June 29, the sub-high suddenly jumped north, and the ridge position was adjusted from 19°N to 23°N (Figure 5B), which was the same time as the northward jump of the upper jet at this time in the late Meiyu onset year in the Jianghuai region. It can be seen that the position and time of the northward jump of the sub-high ridge have a strong relationship with the start of Meiyu in the Jianghuai region. The sub-high ridge jumps northward early and stably maintains a more northerly position in the year of early Meiyu onset, while the sub-high ridge is more southerly than the climatic average position in the year of abnormally late Meiyu onset and surpasses 20°N later.

4.3 Influence of the low-level jet on the early and late onset of Meiyu

The trans-equatorial flow in the low-level system, the early and late summer wind outbreak in the South China Sea, and the strength of the low-level rapids all reflect the water vapor supply, which has a

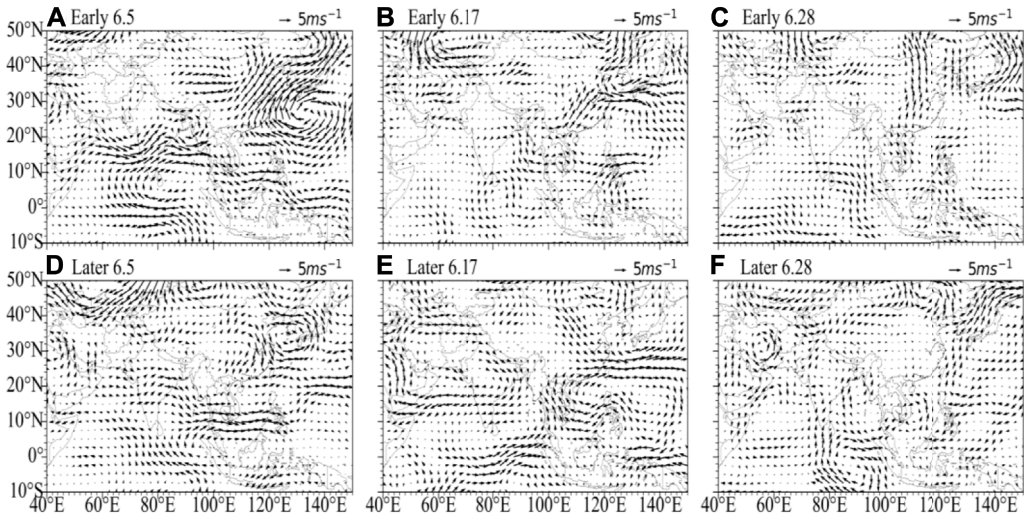

FIGURE 6
850 hPa wind field (unit: m/s) anomalies in the early years **(A)**, **(B)**, **(C)** and late years **(D)**, **(E)**, **(F)** of the Yangtze-Huaihe River **(A)**, **(D)**: June 5th; **(B)**, **(E)**: June 17th; **(C)**, **(F)**: June 28th).

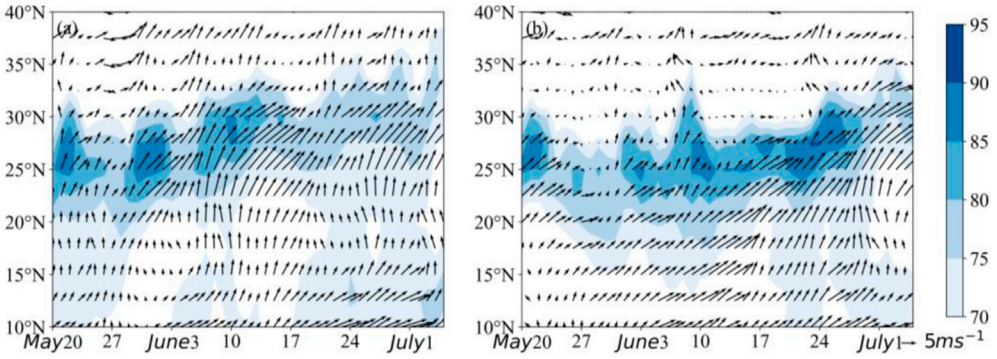

FIGURE 7
110°-120°E average of 850 hPa relative humidity (shadow, unit: %) and wind field (unit: m/s) time-latitude cross sections in the early and late years of Meiyu onset **(A)**: early years **(B)**: late years.

significant influence on the early and late onset of Meiyu and the amount of precipitation in the Jianghuai region of China. According to Li Chongyin (Li and Wu, 2002), Ding Yihui (Ding et al., 2007), and others, the Bay of Bengal-Central Indian Peninsula-South China Sea region is the main water vapor supply zone during the Meiyu period in China, and the time of the summer wind outbreak in the South China Sea, the time of the establishment of the Somali equator crossing, and the date of Meiyu onset are closely related. Figure 6 shows the comparison of the 850 hPa wind field at different stages of the years of the Meiyu onset anomaly. As shown in the figure, on June 5 of the early year (Figure 6A), there was a southwest wind anomaly in the Somali Basin, a significant westerly wind anomaly in the water vapor conveyor belt of the Bay of Bengal-Central Indian Peninsula-South China Sea, and significant anticyclonic anomalous circulation over the western Pacific Ocean off the eastern coast of China. In the late year (Figure 6D), there was a northwesterly wind anomaly on the sea surface of the southern coast of China and cyclonic abnormal circulation on the sea surface of the eastern coast; thus, the outbreak of trans-equatorial flow in the early year was earlier than in the late year, and the anticyclone intensity east of the Philippines was stronger than in the late year. The supply of low-level water vapor was more abundant on June 5 in the early year, which was favorable to Meiyu onset. On June 17 (Figure 6B), when Meiyu began, the southwesterly low-level jet in Guangxi and the middle and lower reaches of the Yangtze River were unusually strong, which was conducive to the transport of water vapor and the maintenance of Meiyu in the Jianghuai region. The low-level wind field from the Bay of Bengal to the Indian Peninsula and the South China Sea is controlled by anticyclones, and the west of Jianghuai is controlled by an abnormally strong northwesterly wind field. The low-level circulation configuration is still unfavorable for water vapor transportation to the Jianghuai

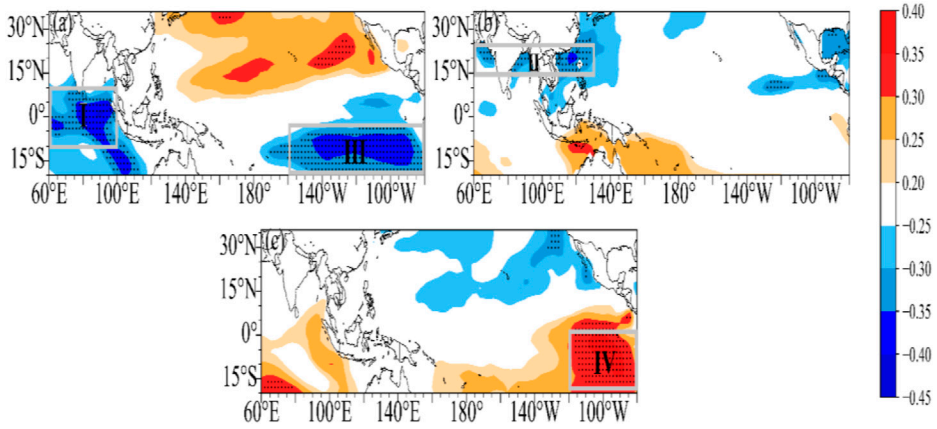

FIGURE 8
The distribution of correlation coefficients between the sea surface temperature in the early autumn **(A)**, winter **(B)**, and spring **(C)**, and the Meiyu onset date from 1954 to 2020 (the dotted area passed the 99% T-test).

area, which, in turn, is unfavorable to the onset of Meiyu in the Jianghuai area. On June 28, in both abnormally early Meiyu years and abnormally late Meiyu years, there are no obvious system and element anomalies in low-level circulation, which means that both are closer to the average-climate situation.

The location, duration, and high humidity zone of the low-level rapids determine the time of the onset of Meiyu and the duration of the Meiyu period, and the change of the 850 hPa high relative humidity zone is an indicator of the distribution of water vapor, and is a reference basis on which the start and end of Meiyu can be determined. In the early year (Figure 7A), from late May to early June, the high relative humidity zone was stable at nearly 26°N. The low-level jet was enhanced from early June, the southwesterly wind was obviously strengthened, and a steady stream of water vapor was transported to the Jianghuai region. The high relative humidity zone was pushed northward to around 28–32°N on June 7, when Meiyu started in Jianghuai, and a continuous high humidity and rapid convergence zone appeared in the region. In the late year (Figure 7B), before June 20, the low-level jet in the range of 110°–120°E was not significantly enhanced, the southwesterly wind was obviously weak, and the high relative humidity zone was located around 25–28°N until late June. When the low-level rapids appeared significantly northerly, the high humidity zone was pushed further north to around 28–30°N, and Meiyu began in the Jianghuai and Huaihua areas.

From the above analysis, it can be concluded that the strength of the trans-equatorial jet stream—especially the Somali rapids, the early and late outbreak of the South China Sea summer winds, and the location and intensity of the Philippine anticyclone—has important effects on the levels of water vapor in the Jianghuai region. When the Somali rapids and the South China Sea summer winds break out early, and when the intensity of the Philippine anticyclone is greater, water vapor in the Jianghuai region of China is more abundant, which is conducive to the earlier onset of Meiyu. Meanwhile, the distribution of low level water vapor and the northward jump of low-level rapids also have a strong correspondence with the time of Meiyu onset.

5 Precursor signal of early and late Meiyu in the JAC region

In addition to the internal dynamic processes, atmospheric circulation anomalies are also influenced by external forcing signals. For China, SST, snow cover, and soil moisture are the main factors considered, and this paper focuses on the influence of SST anomalies on the day of Meiyu onset in the Jianghuai region. As shown in Figure 8A, the day of Meiyu onset in the Jianghuai region is significantly negatively correlated with the tropical Indian Ocean and the central-eastern equatorial Pacific Ocean and significantly positively correlated with the north Pacific Ocean in the previous autumn (September-November). The correlation between the day of Meiyu onset and the SST in the previous winter (December-February) (Figure 8B) has changed significantly compared with the spring, with a negative correlation in the ocean north of the equator and a positive correlation in the ocean south of the equator; the area with the strongest correlation is the Arabian Sea-Gulf of Bengal—South China Sea area, with a significant negative correlation. The correlation distribution between the day of Meiyu onset and pre-spring (March-May) SSTs (Figure 8C) is almost opposite to that in autumn, with a positive correlation in the Indian Ocean and South Pacific regions and a negative correlation in the North Pacific region.

The Indian Ocean and Pacific Ocean SST anomalies mainly affect the East Asian subtropical summer wind, which, in turn, affects summer precipitation in the Jianghuai region (Li et al., 2007). The Indian Ocean transports a large amount of warm and humid water vapor to China, which can significantly affect precipitation in the middle and lower reaches of the Yangtze River. In the following spring and summer, the ENSO signal is retained through a “discharge” effect, which causes the western Pacific subsurface to maintain an abnormally strong state, favoring the weak Indian summer winds and high summer precipitation in the middle and lower reaches of the Yangtze River (Wang et al., 2000; Yang et al., 2008). Therefore, the key SST zones in the Indian and Pacific Oceans are selected for analysis of their influence on the day of Meiyu onset.

From the analysis of Figure 9, it is clear that early and late Meiyu onset dates are best correlated with the Indian Ocean and the eastern

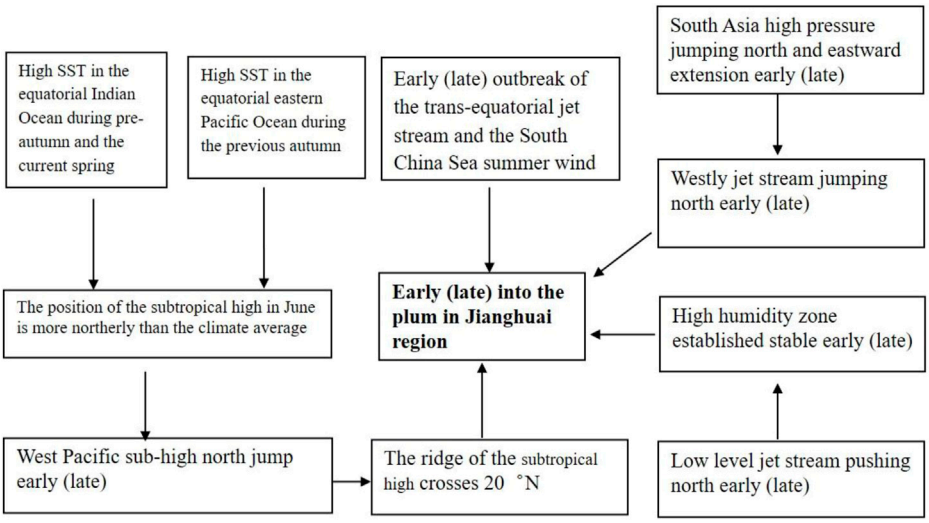

FIGURE 9
Conceptual diagram of the key influence system for the Meiyu onset date over the Yangtze-Huaihe River Basin.

TABLE 2 Correlation coefficients between partial seasonal SST anomalies in Zone I (Equatorial Indian Ocean), Zone II (Bay of Bengal-South China Sea), Zone III, and Zone IV (Eastern Pacific) from 1954 to 2020; the Western Pacific subtropical high in June of the following year; and the Meiyu onset date.

SST critical zone	Zone I		Zone II		Zone III		Zone IV	
	Autumn	Winter	Spring	Winter	Autumn	Spring	Autumn	Spring
Sub-high intensity/hPa	0.143	0.213*	0.192	−0.03	0.059	0.079	0.046	0.08
Sub-high area	0.128	0.227*	0.2	−0.026	0.052	0.09	0.041	0.085
Sub-high ridge line/°N	0.209	−0.03	−0.271**	0.23*	0.257**	−0.246**	0.249**	−0.257**
West extension ridge point/°E	−0.131	−0.255**	−0.078	−0.098	−0.12	−0.012	−0.113	−0.001
Meiyu start date	−0.374***	−0.089	0.238*	−0.34***	−0.363***	0.327***	−0.332***	0.346***

*** for passing α=0.01 reliability test, ** for passing α=0.05 reliability test, * for passing α=0.1 reliability test.

Pacific Ocean. The mean SSTA of the (10°S- 10°N, 60°- 100°E) region is selected to represent the equatorial Indian Ocean region (Zone I); the mean SSTA of the (15°-25°N, 60°-130°E) region represents the Bay of Bengal—South Sea region (Zone II); the (5°S-20°S, 150°-80°W) region and the (0°-20°S, 120°-80°W) region represent eastern equatorial Pacific region (Zones III and IV). The correlation coefficients of autumn, winter, and spring SSTs in key zones with the characteristic parameters of the western Pacific subtropical high pressure in June and the day of Meiyu onset are further analyzed, and the data of the more strongly correlated parts are shown in Table 2. As can be seen in Table 2, the correlation between autumn SST and subtropical high parameters in zone I is not strong, but there is a strong negative correlation with the day of Meiyu onset; this means that the higher the SST in Zone I in autumn, the earlier the day of Meiyu onset in the Jianghuai area in the following year. Although the correlation coefficient of winter SST in Zone I with the day of Meiyu onset is small, it is positively correlated with the high intensity and area of the sub-high and negatively correlated with the westward extension of the sub-high ridge; this means that the higher the SST in this area in winter, the higher the intensity and area of the sub-high in June of the following year and the more southerly the position of the sub-high. Therefore, the winter SST in Zone I has a significant influence on the western Pacific sub-high, but because the intensity and area are positively correlated and the position is negatively correlated, it is generally not strongly correlated with the day of Meiyu onset. In the correlation coefficients of SSTs in key areas (table omitted), the correlation between spring SSTs in Zone I and winter SSTs in Zone II is stronger, and they are negatively and positively correlated with the ridge of the sub-high and positively and negatively correlated with the day of Meiyu onset respectively; this means that the lower the spring SSTs in Zone I, the higher the winter SSTs in Zone II and the more northerly the position of the sub-high in June of the following year. It also results in the transport of water vapor to the middle and lower reaches of the Yangtze River in China being more adequate than the same period and the day of Meiyu onset being earlier in the Jianghuai area. The SSTs of Zone III and Zone IV are significantly correlated, and the correlation between them and the parameters of the sub-high and the day of Meiyu onset is also consistent, both of them are positively correlated with the sub-high ridge and negatively correlated with the day of Meiyu onset in autumn and negatively correlated with the sub-high ridge and positively correlated with the day of Meiyu onset in spring. This indicates

that the higher the SST in the eastern equatorial Pacific in autumn, the lower the SST in the following spring, and the more northerly the position of the sub-high in June, the earlier the onset of Meiyu in the Jianghuai region. Thus, SST is an important precursor of early and late Meiyu onset in the Jianghuai region.

6 Conclusion and discussion

The prediction of the beginning and end of Meiyu has always been the focus of forecasters. The onset of Meiyu in the Yangtze-Huaihe River basin is closely related to changes in different levels of weather systems and their advance to the north; in particular, being able to determine what is an "abnormal year" plays a key role and can provide scientific and technical support to the government, agriculture, and water conservancy as well as supporting other decision-making. In this paper, we analyze the characteristics of the changes in the key influencing systems of anomalous Meiyu onset years in Jiangsu and Anhui in the past 67 years using data on Meiyu, combined with NCEP/NCAR reanalysis data, and provide reference indicators and signals for Meiyu forecasting from different weather systems and SST. The results are as follows.

1) In the past 67°years, the time of Meiyu onset in the Jianghuai region has varied significantly inter-annually. Meiyu start time, duration, and total rainfall have a strong correlation; generally, early Meiyu leads to its longer duration and greater rainfall. The time of the northward movement of South Asian high pressure, the northward jump of the westerly rapids, the northward jump of the paramount, the high-value area of the low-level relative humidity, and the northward movement of the low-level rapids are closely related to the time of Meiyu onset.
2) In years with unusually early Meiyu onset, the South Asian high pressure and the western Pacific sub-high jumped significantly north from late May to early June, and the westerly rapids jumped from 34–35°N to 38–40°N and remained stable at higher latitudes and significantly further north compared with its climatic average position. The sub-high was unusually strong at the beginning of June, and the position of the ridge of the sub-high was significantly further north and surpassed 20°N between late May and early June compared with the climatic average position, and the time of the enhanced northward push of the low-level jet was also significantly early. In the late year, the westerly jet and the ridge of the sub-high were slightly further south than the climatic average position from early June to late June and did not jump significantly north until late June.
3) SST anomaly in the early stages is an important external forcing factor affecting the early and late onset of Meiyu, among which, the impact of SST anomaly in the Indian Ocean and the Pacific Ocean is the most significant. When the SST of the equatorial Indian Ocean is high in the autumn, Meiyu starts early in the Jianghuai region. When the SST of the equatorial Indian Ocean is high in the spring, the SST of the Bay of Bengal-South China Sea is usually low in winter, and the position of the sub-high in June of the following year is further north compared with the climatic average position, which leads to Meiyu starting early in the Jianghuai region. When the SST of the eastern equatorial Pacific Ocean is high in the autumn, the SST of the region is often low in the spring of the following year, and the position of the sub-high in June is further north, so Meiyu starts early in the Jianghuai region. When the SST of the eastern equatorial Pacific region is high in the early autumn, the SST of the region is often low in the following spring, and the position of the sub-high is further north, so Meiyu starts early in the Jianghuai region.
4) The key systems and pre-SSTs that affect the date of Meiyu onset in the Yangtze-Huaihe River basin are combined in Figure 9 to establish the conceptual map of key influencing systems for early and late Meiyu onset in the Yangtze-Huaihe River basin, respectively, to provide ideas for Meiyu forecasting.

This study mainly focuses on the climatic characteristics and influence systems of anomalies in the start and end times of Meiyu in the Jianghuai region, but there are many issues, particularly the influence of the precursor, SST on the Meiyu onset date, which need to be further investigated.

Data availability statement

Publicly available datasets were analyzed in this study. This data can be found here: data.cma.cn.

Author contributions

XJ completed the analysis of the climatic characteristics of the Meiyu onsetdata in Jianghuai region, YM completed the analysis of the characteristics of the weather system, ML completed the analysis of the sea temperature signal, and SZ completed the data calculation.

Funding

This work is sponsored by the Yangtze River Basin Meteorological Open Fund (CJLY 2022Y02) and the Key Projects of the Jiangsu Meteorological Bureau (KZ202101).

Conflict of interest

The authors declare that the research was conducted in the absence of any commercial or financial relationships that could be construed as a potential conflict of interest.

Publisher's note

References

Chen, B., Jiang, Y., Li, D., and Tang, Y. (2020). Response of Meiyu in Jianghuai region on the process of East Asian subtropical summer monsoon and sea surface temperature anomaly. *J. Meteorological Sci.* 40 (5), 669–678. doi:10.3969/2020jms.0072

Choi, J.-W., Kim, H.-D., and Wang, B. (2020). Interdecadal variation of Changma (Korean summer monsoon rainy season) retreat date in Korea. *Int. J. Climatol.* 40 (3), 1348–1360. doi:10.1002/joc.6272

Ding, Y., Liu, J., Sun, Y., Liu, Y., He, J., and Song, Y. (2007). A study of the synoptic-climatology of the Meiyu system in East Asia. *Chin. J. Atmos. Sci.* 31 (6), 1082–1101. doi:10.3878/j.issn.1006-9895.2007.06.05

Huang, Q., Wang, L., Li, Y., and He, J. (2012). Determination of the onset and ending of regional Meiyu over Yangtze-Huaihe River valley and its characteristics. *J. Trop. Meteorology* 28 (5), 749–756. doi:10.3969/j.issn.1004-4965.2012.05.015

Li, C., Han, G., Liu, M., Sun, H., and Zhou, L. (2015). Relationship between East Asia jet anomaly and Meiyu onset over yangtze-HuaiheRiver valley. *J. Meteorological Sci.* 35 (2), 176–182. doi:10.3969/2014jms.0043

Li, C., Wang, Z., Lin, Z., and Cho, H. (2004). The relationship between east Asian summer monsoon activity and northward jump of the upper westerly jet location. *Chin. J. Atmos. Sci.* 28 (5), 641–658. doi:10.3878/j.issn.1006-9895.2004.05.01

Li, C., and Wu, J. (2002). Important role of the somalian cross-equator flow in the onset of the South China Sea summer monsoon. *Atmos. Sci.* 26 (2), 185–192. doi:10.3878/j.issn.1006-9895.2002.02.04

Li, Y., Wang, Y., and W, D. (2007). Effects of anomalous SST in tropical Indian Ocean and Pacific Ocean on next june rainfall over the Yangtze River Basin and area south of the basin. *Acta Meteorol.* 65 (3), 393–405. doi:10.11676/qxxb2007.037

Liu, M., Hu, L., and Pu, M. (2007). Study on change of South Asia high and response of other weather system during summer. *Sci. Meteorol. Sin.* 27 (3), 294–301. doi:10.3969/j.issn.1009-0827.2007.03.009

Liu, Y., Hong, J., Liu, C., and Zhang, P. (2013). Meiyu flooding of Huaihe River valley and anomaly of seasonal variation of subtropical anticyclone over the Western Pacific. *Chin. J. Atmos. Sci.* 37 (2), 439–450. doi:10.3878/j.issn.1006-9895.2012.12.313

Luo, L., Xu, M., and He, D. (2019). Interdecadal characteristics of summer precipitation over HuaiheRiver Basin and the associated atmospheric circulation anomalies since 2000. *J. Arid Meteorology* 37 (4), 540–549. doi:10.11755/j.issn.1006-7639(2019)-04-0540

Sun, S., and Li, D. (2019). Morphological variation of the Western Pacific subtropical high and its possible thermodynamic causes under the background of climate warming. *Acta Meteorol. Sin.* 77 (1), 100–110. CNKI:SUN:QXXB.0.2019-01-008.

Takaya, Y., Ishikawa, I., Kobayashi, C., Endo, H., and Ose, T. (2020). Enhanced meiyu-baiu rainfall in early summer 2020: Aftermath of the 2019 super IOD event. *Geophys. Res. Lett.* 47 (22), 090671. doi:10.1029/2020GL090671

Tang, Y., and Li, D. (2020). The relationship between the Meiyu in the Yangtze-Huaihe Region and the variation of the East Asiansubtropical summer monsoon process. *J. Meteorological Sci.* 40 (2), 169–179. CNKI:SUN:QXKX.0.2020-02-003.

Wang, B., Wu, R., and Fu, X. (2000). Pacific-East asian teleconnection: How does ENSO affect East Asian climate. *J. Clim.* 13 (9), 1517–1536. doi:10.1175/1520-0442(2000)013<1517:PEATHD>2.0.CO;2

Xu, B., Chen, H., Gao, C., Zeng, G., and Huang, Q. (2021). Abnormal change in spring snowmelt over Eurasia and its linkage to the East Asian summer monsoon:The Hydrological effect of snow cover. *Front. Earth Sci.* 8 (594656). doi:10.3389/feart.2020.594656

Yang, M., Ding, Y., Li, W., and Mao, H. (2008). The leanding mode of Indian Ocean SST and its impacts on asian summer monsoon. *Acta Meteorol. Sin.* 22 (1), 31–41. CNKI:SUN:QXXW.0.2008-01-004.

Zhao, J., Chen, L., and Wang, D. (2018). Characteristics and causes analysis of abnormal Meiyu in China in 2016. *Chin. J. Atmos. Sci.* 42 (5), 1055–1066. doi:10.3878/j.issn.1006-9895.1708.17170

Zhao, J., Wang, A., and Wang, H. (2021). Soil moisture memory and its relationship with precipitation characteristics in China region. *Chin. J. Atmos. Sci.* 45 (4), 799–818. doi:10.3878/j.issn.1006-9895.2007.20149

Zhou, Y., Peng, T., and Shi, R. (2019). Research progress on risk assessment of heavy rainfall and flood disasters in China. *Torrential Rain Disasters* 38 (5), 494–501. doi:10.3969/j.issn.1004-9045.2019.05.011

frontiers | Frontiers in Environmental Science

TYPE Original Research
PUBLISHED 16 February 2023
DOI 10.3389/fenvs.2023.1083517

OPEN ACCESS

EDITED BY
Yuefei Zeng,
Nanjing University of Information Science and Technology, China

REVIEWED BY
Chunsong Lu,
Nanjing University of Information Science and Technology, China
Yongbo Zhou,
Nanjing University of Information Science and Technology, China
Zeyi Niu,
China Meteorological Administration, China

*CORRESPONDENCE
Zhixian Luo,
luozx_kj@js.gov.cn

SPECIALTY SECTION
This article was submitted to Environmental Informatics and Remote Sensing, a section of the journal Frontiers in Environmental Science

RECEIVED 29 October 2022
ACCEPTED 19 January 2023
PUBLISHED 16 February 2023

CITATION
Shi Y, Luo Z, Chen X, Zhang Q, Liu Y and Liu C (2023), Effects of joint assimilation of FY-4A AGRI and ground-based microwave radiometer on heavy rainfall prediction. *Front. Environ. Sci.* 11:1083517. doi: 10.3389/fenvs.2023.1083517

Effects of joint assimilation of FY-4A AGRI and ground-based microwave radiometer on heavy rainfall prediction

Yinglong Shi[1], Zhixian Luo[2]*, Xiangguo Chen[1], Qian Zhang[3], Yin Liu[4,5] and Chun Liu[6]

[1]College of Meteorology and Oceanography, National University of Defense Technology, Changsha, China, [2]Jiangsu Provincial Department of Science and Technology, Nanjing, China, [3]College of Atmosphere and Remote Sensing, Wuxi University, Wuxi, China, [4]Jiangsu Meteorological Observation Center, Nanjing, China, [5]Key Laboratory of Atmosphere Sounding, Chengdu, China, [6]Anhui Meteorological Observatory, Hefei, China

As the latest generation of Chinese Geostationary Weather Satellites, Fengyun-4 carries the Advanced Geosynchronous Radiation Imager (AGRI), which has more spectral bands and higher temporal and spatial resolution than the Visible Infrared Spin-Scan Radiometer (VISSR) onboard geostationary satellite FY-2. Direct assimilation of the FY-4A AGRI datasets has been proved to be an efficient way to improve heavy rainfall simulation. We aim to assess the joint assimilation of AGRI infrared radiance and ground-based MWR (Microwave Radiometer) data on short-duration heavy rainfall prediction. RTTOV (Radiative Transfer for the TIROS Operational Vertical Sounder) is used as the observational operator for FY-4A AGRI data assimilation. The data assimilation interface is built in WRFDA 4.3 to achieve direct assimilation of FY4A AGRI radiance. The forecasting effectiveness of the joint assimilation for a typical heavy rainfall event over northern China is analyzed with four simulation experiments. The main conclusions are: 1) Assimilating MWR data can improve the initial humidity condition in the middle-lower layers, while AGRI radiance assimilation favors the initial humidity correction in the middle-upper layers. The joint assimilation of two datasets can remarkably improve the initial humidity condition in the entire column. 2) Data assimilation effectively improves the 6-h accumulated rainfall simulation. The joint assimilation of AGRI radiance and MWR data is superior to assimilating either of them. The joint assimilation significantly improves the rainfall forecast over the Beijing area, where the seven MWRs are distributed. 3) Data assimilation experiments present similar effects on predicted and initial humidity conditions. The MWR_DA experiment (only assimilate MWR data) markedly improves the humidity forecast in the middle-lower layers, while AGRI_DA (only assimilate AGRI data) is effective in the middle-upper layers. The joint assimilation of AGRI radiance and MWR data could skillfully correct the humidity distribution in the entire layers, allowing for more accurate heavy rainfall prediction. This paper provides a valuable basis for further improving the application of FY-4A AGRI radiance in numerical weather models.

KEYWORDS

joint, assimilation, FY-4A AGRI, ground-based microwave radiometer, heavy rainfall prediction

1 Introduction

To satisfy the massive demand for disaster prevention and mitigation, numeric weather prediction (NWP) has made remarkable progress with continuous advances in numerical simulation theory, computation capability, and comprehensive observation ability (Li et al., 2014). At present, great efforts are made to improve the forecast skill of high-resolution NWP in predicting disastrous mesoscale rainstorms triggered by multiscale weather systems (Qin et al., 2005; Shen et al., 2021; Xu et al., 2021). However, as the atmosphere is a highly non-linear system, the forecast errors of NWP models are susceptible to the initial conditions. Therefore, the data assimilation (DA) technique helps to fuse information from background field and observation data to obtain an optimal initial condition, which is a crucial issue in the research of NWP (Shen and Min, 2015; Xu et al., 2016; Kutty et al., 2018).

In addition to the continuous development of assimilation methods, research has been carried out on assimilating various observational data (De Souza et al., 2022; Ye et al., 2021; Ma et al., 2022; Wang et al., 2022). In particular, geostationary satellite data, due to its advantages of high spatial-temporal resolution and less susceptibility to geographic conditions, can effectively complement observations over land and ocean, and might optimize the initial conditions, which facilities the improvement of NWP (Yang et al., 2017; Wang et al., 2018; Xu et al., 2021). Launched on 11 December 2016, Fengyun-4A (FY-4A) is the first test satellite of the Fengyun-4 geostationary system, the second generation of the Chinese geostationary meteorological satellite system. The design of FY-4A thoroughly considers atmospheric, marine, and environmental science demands, showing broad application prospects (Dong, 2016). The meteorological instruments onboard FY-4A include the Advanced Geostationary Radiation Imager (AGRI), the Geostationary Interferometric Infrared Sounder (GIIRS), the Lightning Mapping Imager (LMI), and the Space Environment Monitoring Instrument Package (SEP) (Yang et al., 2017). Compared with the Visible Infrared Spin-Scan Radiometer (VISSR) onboard geostationary satellite FY-2, the FY-4A AGRI has more spectral bands and higher temporal and spatial resolution to provide more accurate atmospheric information. Assimilation of AGRI radiance could facilitate the development of NWP operations in China and promote the full use of China's meteorological satellite data (Zhang et al., 2022; Shen et al., 2021). Radiance assimilation was mostly limited in clear-sky conditions, although all-sky radiance, containing critical cloud and precipitation properties, is also of great significance for improving heavy rainfall simulation (Okamoto et al., 2019). The reason lies in the great challenges of assimilating all-sky radiance in handling strong non-linearity and low predictability of complicated cloud-related processes due to the high sensitivity of infrared radiances to clouds (Honda et al., 2018a; 2018b; Minamide and Zhang, 2018). Thus, clear-sky radiance assimilation has already been implemented at many operational centers, in terms of impact on numerical weather prediction skill (Okamoto et al., 2019).

As a passive remote sensing instrument, the ground-based microwave radiometer (MWR) provides continuous unattended operations and real-time accurate atmospheric observations under nearly all-weather conditions (Cimini et al., 2007; Löhnert and Maier, 2012). Furthermore, continuous observations of temperature and humidity profiles from MWR effectively complement sounding observations. Therefore, assimilating MWR data for NWP models can help improve weather forecasts. For example, 3-Dimensional Variational Assimilation (3DVAR) of data from seven ground-based MWRs has been attempted for a heavy rainfall case in Bejing (Qi et al., 2021). However, the current applications of MWR observations, particularly in numerical models, are still insufficient.

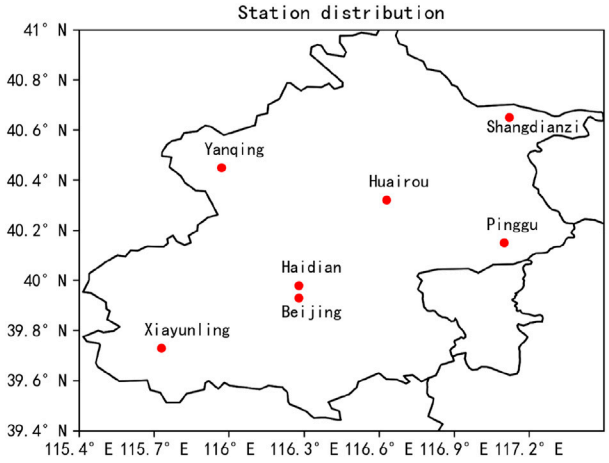

FIGURE 1
Locations of MWR sites.

Due to the high spatial and temporal inhomogeneous, the moisture field is hard to be described by initial conditions in NWP models (Shoji et al., 2011). However, moisture is the essential thermodynamic variable in the simulation of various physical processes. In the processes of cloud microphysics, radiative transfer, and cumulus convection, moisture-associated tri-state phase transformation of water could further affect the dynamic and thermodynamic conditions of the surrounding atmosphere. Meanwhile, atmospheric moisture is one of the essential factors dominating the initiation and development of deep convection. Therefore, initial moisture errors would directly influence the simulations of cloud distribution and subsequent precipitation. AGRI channels 9-10 are water vapor absorption channels depicting the actual moisture conditions in the middle-upper troposphere (Geng et al., 2020). The inability of AGRI to observe planet boundary layers (PBL) can be complemented using the ground-based MWR, which is designed for profile observation in PBL. The joint assimilation of FY-4A AGRI and ground-based MWR could effectively correct the initial moisture conditions in model simulations, which is crucial to the accuracy of weather forecasts (Xue, 2009).

The experiments of this study are based on the Weather Research and Forecasting model's Data Assimilation (WRFDA) v4.3. We choose the Radiative Transfer for the TIROS Operational Vertical Sounder (RTTOV) v12.1 as the AGRI observation operator. In addition, temperature and humidity profiles from the ground-based MWR are jointly assimilated. In this study, accurate convective rainfall forecasts can be achieved by the improved initial and simulated moisture conditions with the two datasets being jointly assimilated.

2 Model and data description

2.1 WRFDA and RTTOV model

As the assimilation system of the Weather Research and Forecasting model (WRF), WRFDA can assimilate observational

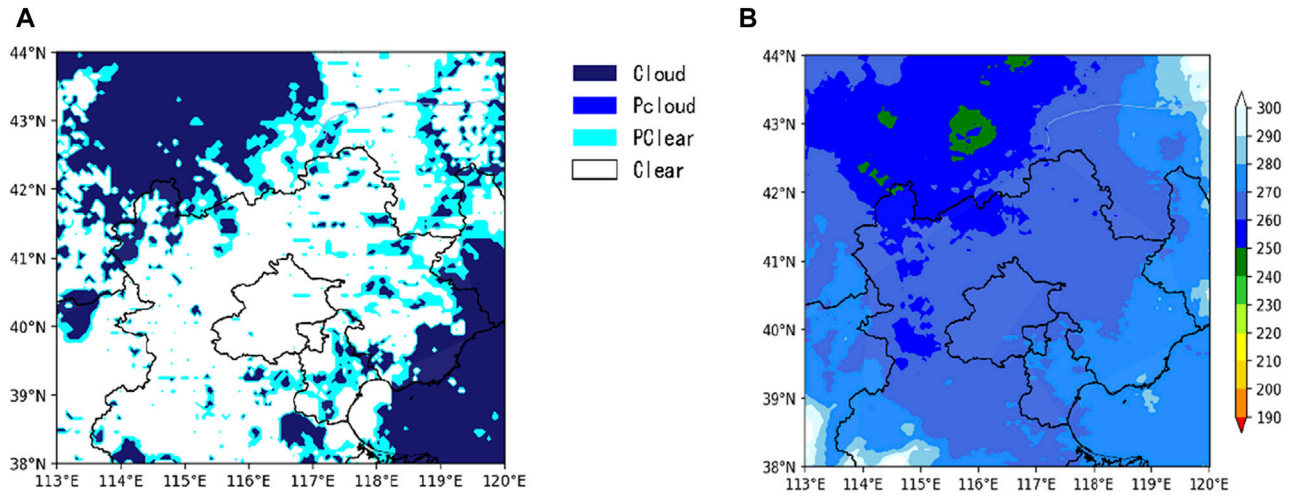

FIGURE 2
Distributions of AGRI **(A)** cloud detection (cloud, pcloud, pclear, and clear represent cloudy, probably cloudy, probably clear, and clear observations, respectively), **(B)** channel 9 brightness temperature before QC (units: K) at 00 UTC on 9 August 2019.

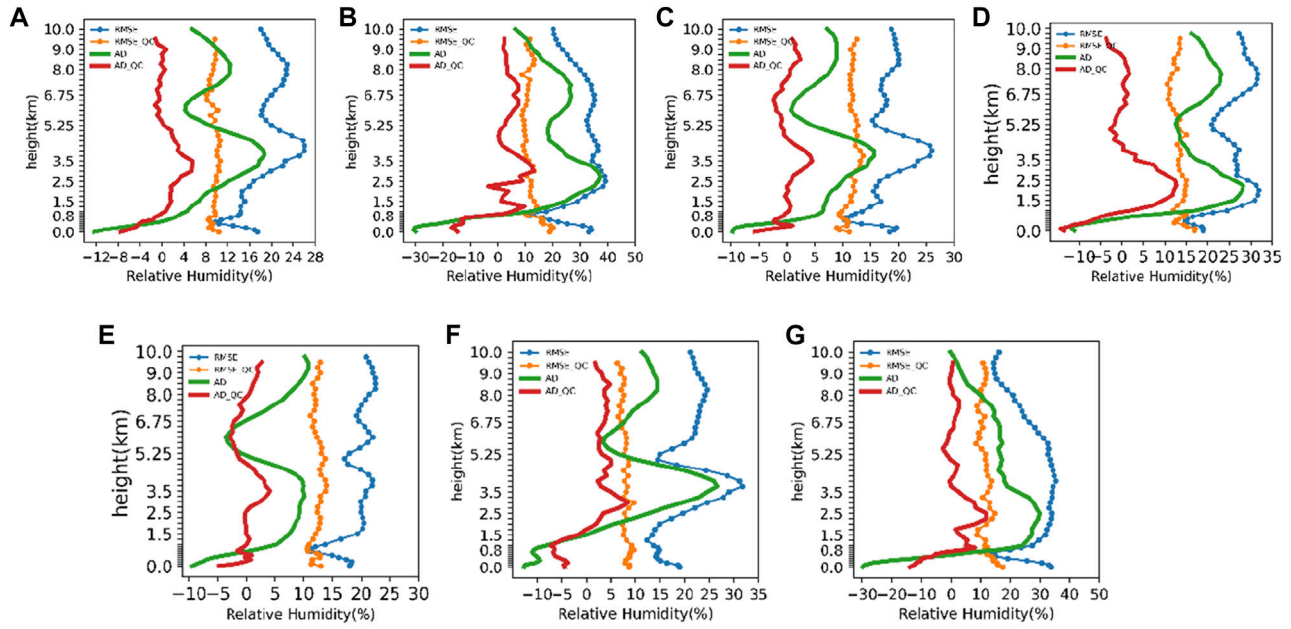

FIGURE 3
Average deviation (AD, red and green lines) and RMSE (blue and yellow lines) of relative humidity (%) between sounding and MWR observations at station **(A)**54399, **(B)** 54406, **(C)** 54419, **(D)** 54421, **(E)** 54424, **(F)** 54511, and **(G)** 54597. RMSE_QC and AD_QC are the RMSE and AD after data quality control, respectively.

data from comprehensive instruments, e.g., surface weather station, radiosonde, ground-based radar, and satellite, into the model simulations. WRFDA includes assimilation techniques such as 3DVar, four-Dimensional Variational (4DVar), and Ensemble-Variational (EnVar) methods. The assimilation experiments in this paper are based on incremental 3DVar. In addition, the conjugate gradient method is used to minimize the cost function in the analysis of control variables, estimating the atmospheric state. The equation is as follows:

$$J(\boldsymbol{x}) = \frac{1}{2}(\boldsymbol{x}-\boldsymbol{x}_b)^T\boldsymbol{B}^{-1}(\boldsymbol{x}-\boldsymbol{x}_b) + \frac{1}{2}(\boldsymbol{y}-\boldsymbol{H}(\boldsymbol{x}))^T\boldsymbol{R}^{-1}(\boldsymbol{y}-\boldsymbol{H}(\boldsymbol{x})). \quad (1)$$

In Eq. 1, $\boldsymbol{x}$ represents the atmospheric state vector, $\boldsymbol{x_b}$ stands for the background information, $\boldsymbol{H}$ is the observation operator, and $\boldsymbol{y}$ acts as the observation vector. The covariance matrixes of background error and observation error are represented by $\boldsymbol{B}$ and $\boldsymbol{R}$, respectively.

RTTOV is a radiative transfer model developed by the European Center for Medium Range Weather Forecasts (ECMWF) in the early 1990 s (Saunders et al., 1999; Saunders et al., 2018). The initial version

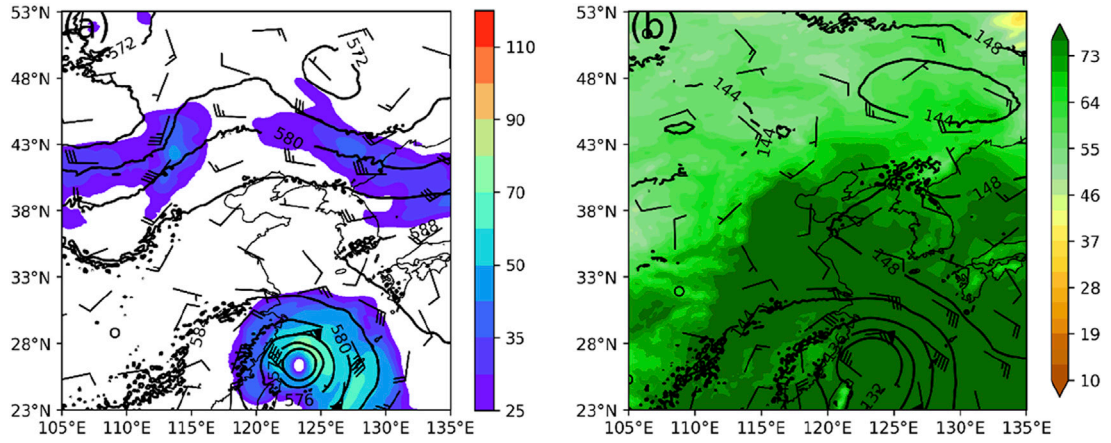

FIGURE 4
The NCEP FNL analysis at 00 UTC on 9 August 2019. **(A)** The 500 hPa geopotential height (contours; gpm), wind barbs (a full barb is 5 m/s), and horizontal wind speed (shading; m/s). **(B)** 850 hPa geopotential height (contours; gpm), wind barbs (a full barb is 5 m/s), and relative humidity (shading; %).

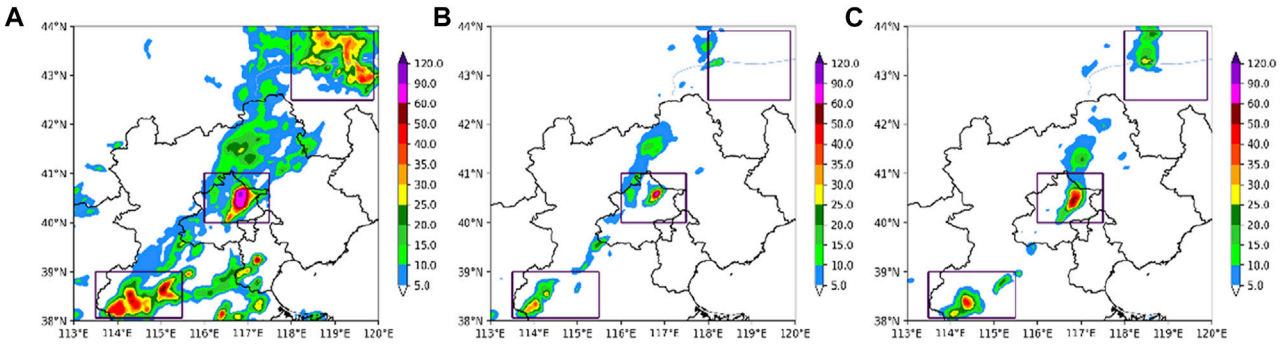

FIGURE 5
Distribution of **(A)** 6-hr accumulated rainfall starting from 06 UTC on 9 August 2019, and hourly rainfall on **(B)** 08 UTC, and **(C)** 09 UTC.

of RTTOV could only simulate bright temperature (BT) from TIROS Operational Vertical Sounder (TOVS). To date, RTTOV can simulate cloudy infrared and microwave radiance from dozens of meteorological satellites. Given a profile of atmospheric states such as temperature and atmospheric composition, RTTOV allows rapid simulation of the satellite radiance data. Therefore, we choose RTTOV v12.1 as the FY-4A radiance observation operator. The spectral response functions and coefficient files used in the simulation of the AGRI radiance are jointly provided by the National Satellite Meteorological Center (NSMC) and the University of Wisconsin-Madison's Space Science and Engineering Center (SSEC).

2.2 FY-4A AGRI radiance data

The AGRI radiance data used in this study is the GEO positioning data and full-disk L1-level raw data with a spatial resolution of 4 km. AGRI L1-level data is processed from Level-0 raw data after the quality check, geolocation check, and radiometric calibration. The 4 km full-disk data contains 2748 scan lines, with 2748 scan points on each line. We focus on the AGRI clear-sky radiances. Cloud mask is performed using the 4-km resolution L2-level Cloud Mask product (CLM), including a four-level (confidently clear, probably clear, probably cloudy, and confidently cloudy) product. Meanwhile, we use the full-disk Cloud Type (CLT) product to identify cloud classification, e.g., clear, water, super-cooled water, mixed, ice, cirrus, and overlap. The AGRI includes 14 channels in the visible, near-infrared, and infrared (IR) spectral bands and scans every 5 min with a subsatellite point resolution of 0.5–4 km (Yang et al., 2017). The spectral coverage, spectral bands, spatial resolution, and main applications for channels 8–14 can be found in Yang et al. (2017). The AGRI has a high temporal resolution, completing a full-disk observation in approximately 15 min, providing one full-disk image every 1 h, three consecutive full-disk images every 3 h (a total of 40 full-disk images per day), and one image of the Chinese region (10°–55°N, 70°–140°N) every 5 min (Zhang et al., 2017). In this study, FY-4A AGRI channels 9–14 are assimilated, including the water vapor channels 9-10 and the window channels 11–14.

2.3 Ground-based MWR observations

The MWR network over the Beijing region during May-September 2019, including seven RPG-HATPRO MWRs deployed in the southern suburbs, Xiayunling Village, Yanqing District, Haidian District, Huairou District, Shangdianzi Village,

TABLE 1 Model configurations.

Nested scheme	Double nested
Horizontal resolution	9 km, 3 km
Horizontal grid number	501 × 391, 622 × 48
Model top pressure	50 hPa
Microphysics scheme	WSM6
Boundary layer scheme	YSU
Longwave radiance scheme	RRTM
Shortwave radiance scheme	Goddard
Cumulus scheme	Kain-fritsch for d02, none for d01

and Pinggu District, has been carried out in this study. Figure 1 shows MWR locations and the simulation coverage in this paper. The RPG-HATPRO MWR has 14 channels, including seven channels in the K-band, for retrieving water vapor profiles, and seven channels in the V-band (oxygen band), for retrieving temperature profile. The level-2 products from the seven ground-based MWRs are obtained using inversion software from the MWR manufacturers, including the temperature and relative humidity profiles (Qi et al., 2021; Guo et al., 2022a). The level-2 products used in this paper are available at least once every 2 min with 41 levels from the surface up to 10 km above ground level (AGL). The vertical resolution below and above 1 km AGL are 100 m and 250 m, respectively. The NCEP FNL (0.25° × 0.25°) analysis field is used as the initial field for the model simulation. The observed rainfall includes the 0.1° × 0.1° hourly precipitation product from Chinese meteorological Data Sharing Service System (hereafter CMORPH-AWS data), which merged observations from more than 30,000 automatic weather stations (AWS) and CMORPH (CPC MORPHing technique) retrieved satellite data.

3 Data processing

3DVar requires that both the observation error and the background error can be characterized as unbiased Gaussian distributions (Dee, 2005). The optimal linear unbiased estimate of the atmospheric state is determined from the observation, the background condition, and their error covariance matrix (Zou and Zeng, 2006; Qin et al., 2010). When performing data assimilation, data quality control (QC) is an essential step to ensure the requirement of the assimilation system. The quality of QC directly affects the accuracy of numerical prediction (Min et al., 2000; Guo et al., 2022b).

3.1 QC of AGRI radiance data

The QC scheme in this paper is modified based on Geng et al. (2020). The original QC and bias correction schemes of Geng et al. (2020) are proposed for a typhoon case in which all the observations over land are removed. In this study, AGRI radiance observations over land are reserved because the deep convection case in this study occurred over land. The detailed QC methods are as follows.

1) Remove all the observations in the mixed surface channels, including mixed predominately sea, mixed predominately sea ice, mixed predominately land, and mixed predominately snow.
2) Only AGRI clear-sky radiance and satellite zenith angle less than 60° are selected.
3) Cloud liquid water paths in background fields exceeding 0.02 kg/m^2 are removed.
4) Exclude innovations (observed BT minus simulated BT) exceeding 15 K.
5) Exclude innovations exceeding three times the standard deviation of the observation error.

This study uses the variational bias correction (VarBC) method to reduce bias in the AGRI assimilation (Dee, 2005; Auligné et al., 2007).

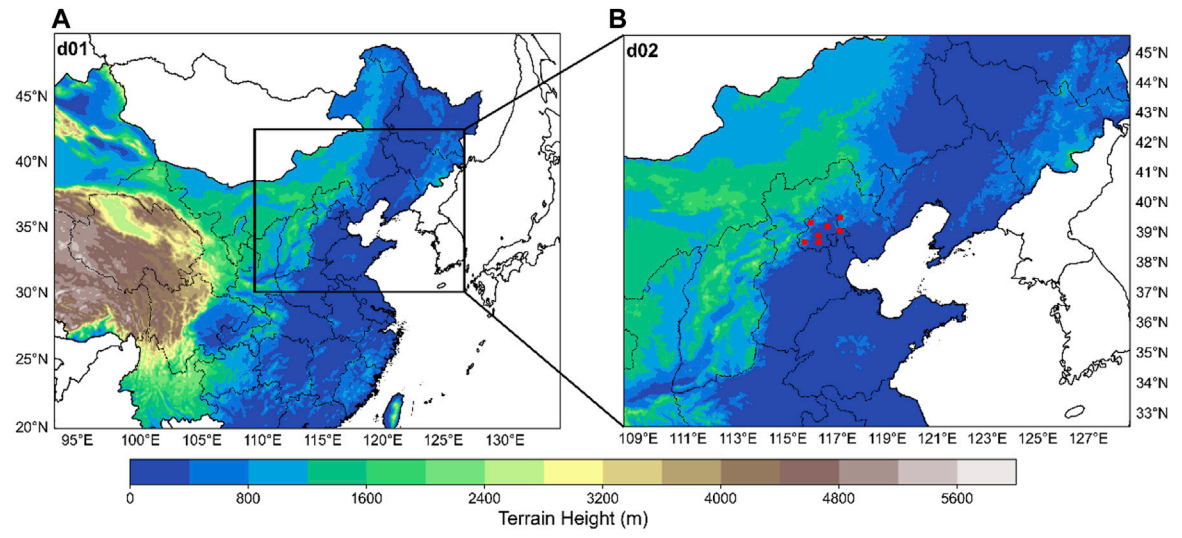

FIGURE 6
(A) The WRF model domain. Domain 2 (d02) is outlined by the black box. **(B)** Map of MWRs (red dots) located in d02. The colour shading represents topography.

TABLE 2 Assimilation scheme.

	Assimilated data	Assimilation interval
CTRL	No	1-h
MWR_DA	temperature and humidity profiles from seven MWRs	1-h
AGRI_DA	FY-4A AGRI radiance channels 9–14	1-h
A + M_DA	both FY-4A AGRI and MWR data	1-h

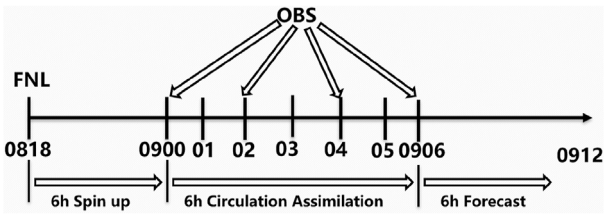

FIGURE 7
Workflow for assimilation experiments.

VarBC changes the observation operator by adding a correction term at each assimilation time step:

$$\tilde{\boldsymbol{H}}(\boldsymbol{x},\boldsymbol{\beta}) = \boldsymbol{H}(\boldsymbol{x}) + \boldsymbol{\beta}_0 + \sum_{i=1}^{N_p}\boldsymbol{\beta}_i\boldsymbol{p}_i \quad (2)$$

where $\boldsymbol{H}$ and $\tilde{\boldsymbol{H}}(\boldsymbol{x},\boldsymbol{\beta})$ are the observation operators before and after the bias correction, respectively. $\boldsymbol{x}$ represents the atmospheric state vector. $\boldsymbol{\beta_0}$ is the constant term of bias. p_i and $\boldsymbol{\beta_i}$ are the $\boldsymbol{i}$-**th** predictor and corresponding bias correction coefficients, respectively. N_p stands for the number of predictors.

According to the CLM product at 00 UTC on 9 August 2019 (Figure 2A), we only reserve the clear-sky BT. Figure 2B shows the channel 9 BT before QC, indicating that the clear-sky observed BT is higher than the cloudy observed BT.

3.2 QC of ground-based MWR data

The temperature and relative humidity profiles provided by the MWR network are used in this study. It has been widely reported that considerable observation errors might exist in the relative humidity retrieval from ground-based MWR (Pan et al., 2020; Posada et al., 2013). Therefore, QC of MWR observations is needed to run variational data assimilation. We use the QC scheme proposed by Fu and Tan, 2017, including extreme value check, time consistency check, and vertical consistency check. In addition, a bias correction approach using sounding observations should be applied to MWR profiles before data assimilations:

$$\tilde{\boldsymbol{x}}_M = \boldsymbol{x}_M + \frac{\sum_{i=1}^{n}\left(\boldsymbol{x}_M^i - \boldsymbol{x}_{TK}^i\right)}{\boldsymbol{n}} \quad (3)$$

Where $\boldsymbol{x}_M$ and $\tilde{\boldsymbol{x}}_M$ represent the MWR observation before and after bias correction, respectively. $\boldsymbol{x}_{TK}$ is the sounding observation. n is the number of samples observed simultaneously by MWR and sounding. Subsequently, temperature and relative humidity profiles obtained from seven MWRs from May to September 2019 are quality-controlled (Figures 3A,C–F). Temperature profiles after QC are not presented here due to minor observation errors. The relative humidity profiles from seven MWRs present large deviations from the sounding observations before QC (blue profiles in Figure 3), with the Root-Mean-Square-Error (RMSE) larger than 20% at each height. The maximum RMSE before QC can be as large as 40% in Figures 3B, G. After QC, the relative humidity RMSE decreases (orange profiles in Figure 3), especially at middle-upper layers. The relative humidity bias is basically distributed near a zero contour at all heights. Compared to the raw data, the quality-controlled relative humidity is closer to a Gaussian distribution, better meeting the requirements of the data assimilation system. Thus, the temperature and relative humidity profiles after QC can be used in this paper.

4 Data assimilation application

4.1 The heavy rainfall case

In the present study, we pick the heavy rainfall event that occurred over North China on 9 August 2019. Figure 4 shows the synoptic conditions where the heavy rainfall event occurs. At 00 UTC, the upper-level trough is distributed near 100°E (Figure 4A), presenting a 'trough-ridge-trough' atmospheric circulation pattern over the middle-higher latitude in East Asia. This rainfall event is situated to the south of the upper-level trough. Associated with the upper-level trough is a Northwest Pacific subtropical high over the southern Japan Sea, steering the warm southwesterly carrying ample moist air to the heavy rainfall area. This circulation situation is conducive to the production of this heavy rainfall event. Meanwhile, this heavy rainfall is closely associated with the landfalling typhoon 'Lekima'. At 850 hPa (Figure 4B), typhoon 'Lekima' transports sufficient water vapor to the heavy rainfall area.

The accumulated rainfall observation shows a northeast-southwest oriented rainfall belt with three heavy rainfall regions (black boxes in Figure 5A) over North China. The most extensive precipitation occurs in northeast Beijing, with a maximum rainfall accumulation exceeding 90 mm. The hourly rainfall distributions (Figures 5B, C) show that this heavy rainfall event is mainly produced in 2 hours. Thus, this rainfall process is a short-term heavy rainfall event over North China, with significant rainfall intensity and short rainfall duration.

4.2 Model configurations and experimental design

In this study, the experiment is carried out using WRFv4.3 and the associated 3DVAR system. Model

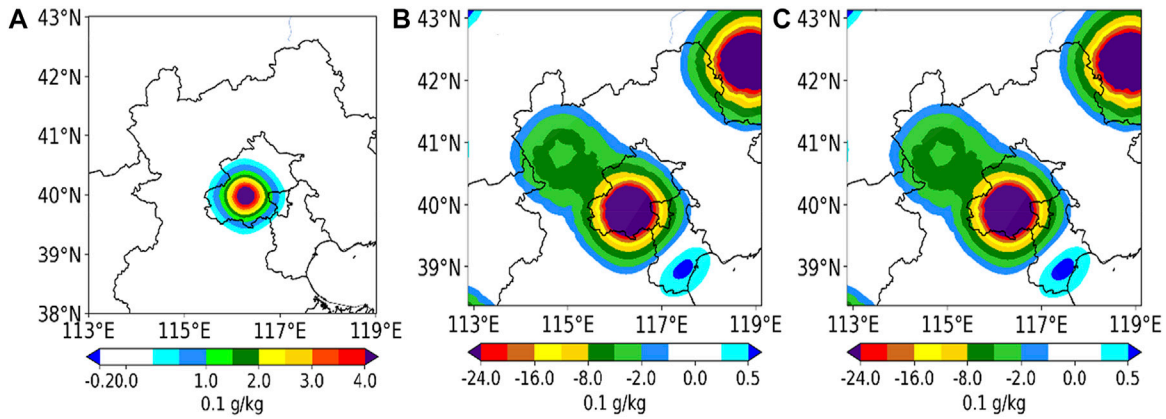

FIGURE 8
Initial specific humidity increments (unit: g/kg) after the first data assimilation from **(A)** MWR_DA at 850 hPa, **(B)** AGRI_DA at 500 hPa, **(C)** A + M_DA at 500 hPa.

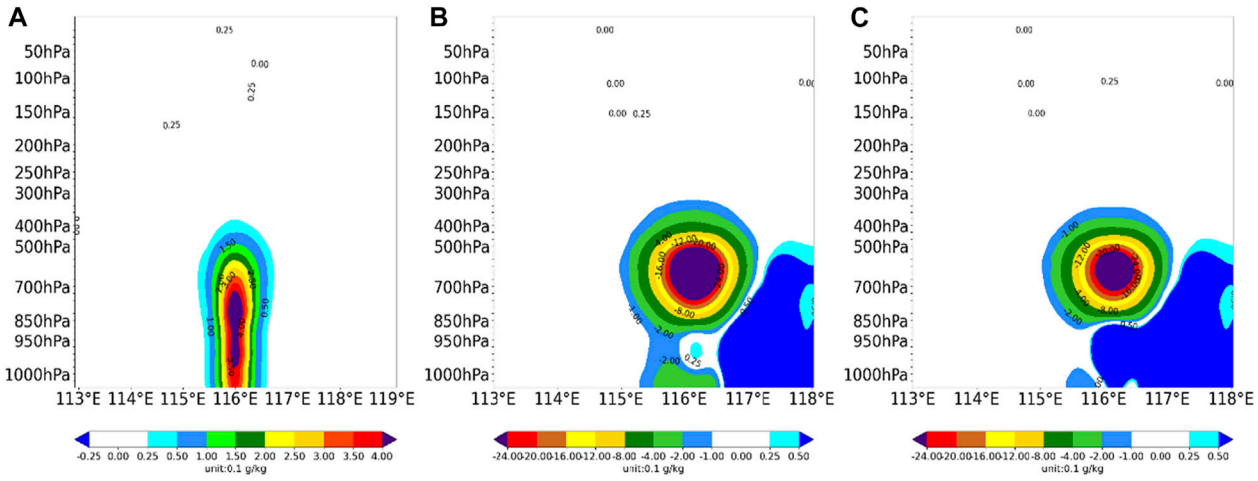

FIGURE 9
The cross sections of the specific humidity increments (shaded; unit: g/kg) along 40°N from **(A)** MWR_DA, **(B)** AGRI_DA, and **(C)** A + M_DA.

configurations are listed in Table 1. The simulated area for this case has two nested domains (Figure 6), with 501 × 391 grid points (9 km) for domain 1 (d01) and 622 × 481 grid points (3 km) for domain 2 (d02), with 51 vertical levels and a model top of 50 hPa. The physical parameterizations are as follows: WSM6 microphysics scheme, Yonsei University (YSU) planetary boundary layer scheme (Hong, 2010), Noah land-surface model (Yang et al., 2011), the Rapid Radiative Transfer Model (RRTM) longwave radiance scheme (Mlawer et al., 1997), Goddard shortwave radiance scheme (Chou et al., 2001), Kain-Fritsch cumulus scheme (Kain, 2004) for d02, but with cumulus parameterization for d01 switched off. All the simulation experiments share the same sets of parameters. The WSM6 microphysical scheme and the Kain-Fritsch cumulus scheme were chosen based on extensive previous studies (e.g., Tewari et al., 2022) showing that these two parameterization schemes are better able to produce heavy rainfall at mid-latitudes. In this paper, the Environmental Prediction (NCEP) Final (FNL) Operational Global Analysis data (available at https://rda.ucar.edu/datasets/ds083.2/, last access: 16 January 2023). NCEP FNL is selected to provide the initial field for the model simulation. Using the FNL analysis during 1–31 August 2019, the 24-h forecast is initialized at 00 UTC and 12 UTC daily. Background error covariance is then calculated by the National Meteorological Center (NMC) method (Parrish and Derber, 1992) based on the 24-h forecast results, using U and V as dynamic control variables (CV7). The variance scale factor and length factor are set to 0. 75 and 0.25, respectively.

The experiment in this paper starts at 18 UTC on 8 August. Data assimilation is conducted after the 6-h spin-up run. Table 2 lists four experiments, including the control (CTRL) run without data assimilation. The other three experimental runs assimilate FY-4A AGRI radiance only (AGRI_DA), temperature and humidity profiles from seven MWRs only (MWR_DA), and both FY-4A AGRI radiance and temperature and humidity profiles from the MWR network (A + M_DA). As depicted in Figure 7, FY-4A AGRI and MWR data are assimilated at 1-h intervals during 00–06 UTC on 9 August, after the 6-h spin-up run. Finally, a 6-h forecast is performed since 06 UTC on 9 August. FY-4A AGRI channels 9–14 are assimilated, including the

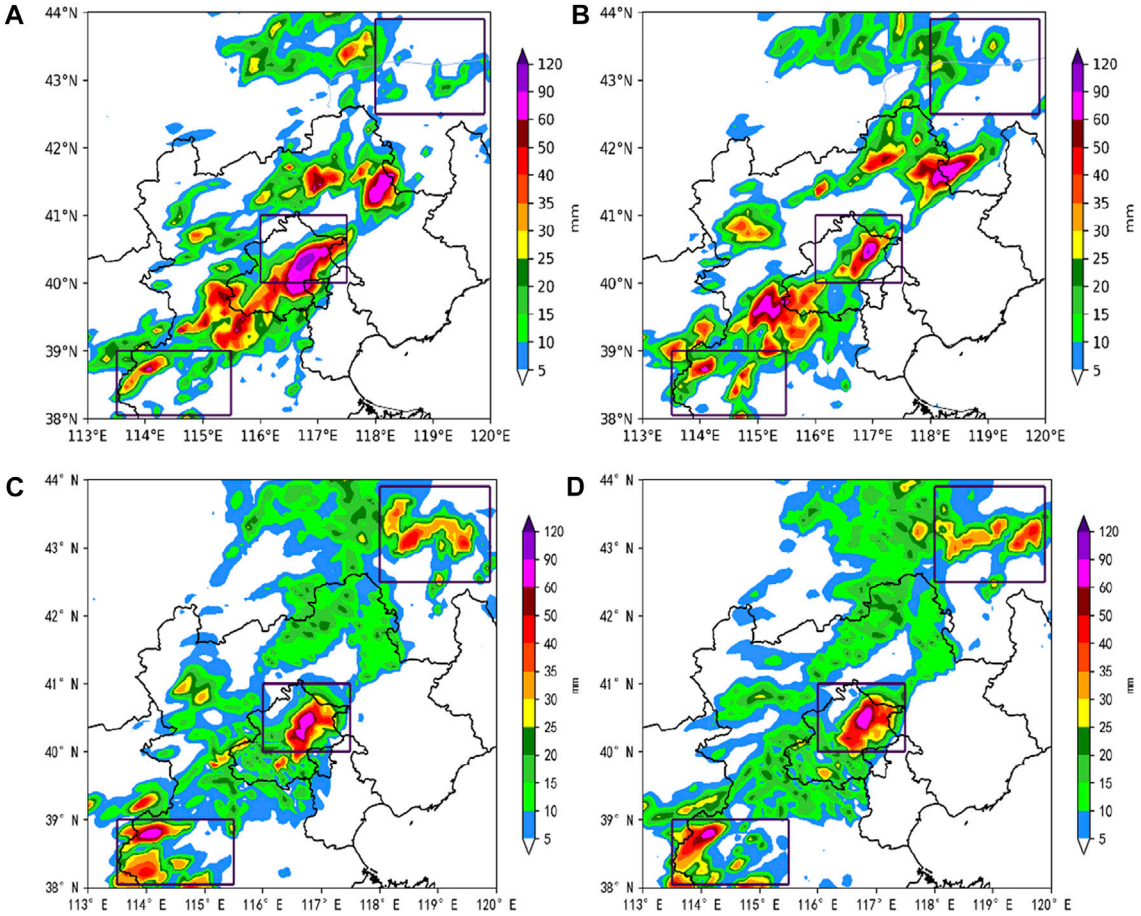

FIGURE 10
Simulated 6-h rainfall accumulation from **(A)** CTRL, **(B)** MWR_DA, **(C)** AGRI_DA, **(D)** A+M_DA.

water vapor channels 9-10 and the window channels 11–14, using a dilation of 30 km.

5 Results

5.1 Effects of data assimilation on the initial humidity condition

Analysis of initial humidity increments for the three data assimilation experiments is shown in Figure 8 and Figure 9 to determine the separate and simultaneous effect of two assimilated data sources. In the MWR_DA experiment, specific humidity increments on 850 hPa are distributed over the Beijing area, presenting a concentric-circles structure (Figure 8A). The vertical cross-section along 40°N from MWR_DA shows that the humidity increment is up to 400 hPa, with its maximum increment exceeding 0.4 g/kg at 850 hPa. The humidity increments in the AGRI_DA at 500 hPa are mainly distributed over the three heavy rainfall regions (as shown in Figure 5B) and to the southeast of Beijing. The assimilation of AGRI radiance strongly influences the initial humidity in the middle-upper troposphere between 850 hPa and 500 hPa (Figure 9B). In the A + M_DA experiment (Figure 8C), the humidity increments are consistent with that in the AGRI_DA experiment, indicating that the assimilation of AGRI radiance primarily influences the middle-upper layer moisture. The vertical profile further demonstrates the significant influence of AGRI radiance in the middle-upper troposphere and the evident humidity increments in the lower troposphere caused by MWR profiles. The joint assimilation of FY-4A AGRI and ground-based MWR could compensate for their lack of observations at lower and higher layers, respectively, providing effective initial moisture correction in model simulations.

5.2 Impact of data assimilation on the 6-h accumulated rainfall forecast

We choose a typical short-duration heavy rainfall event reaching a very heavy rainfall level (>60 mm) in all three heavy rainfall areas during a 2-h period (Figures 5B, C). Figure 10 shows the 6-h accumulated precipitation from four experiments. In the CTRL experiment (Figure 10A), the observed heavy rainfall amounts (Figure 5A) are not simulated in the north and south areas and are overestimated in the central area (Beijing). By conducting MWR assimilation in the MWR_DA experiment (Figure 10B), the 6-h rainfall forecasts in the Beijing area are effectively corrected. However, only a slight difference can be seen in the north and south areas compared to the CTRL experiment. In contrast, the rainfall distribution in the AGRI_DA experiment (Figure 10C) agrees better with the observation (Figure 5A). The overestimated rainfall near the Beijing area in the CTRL experiment is also effectively corrected in the

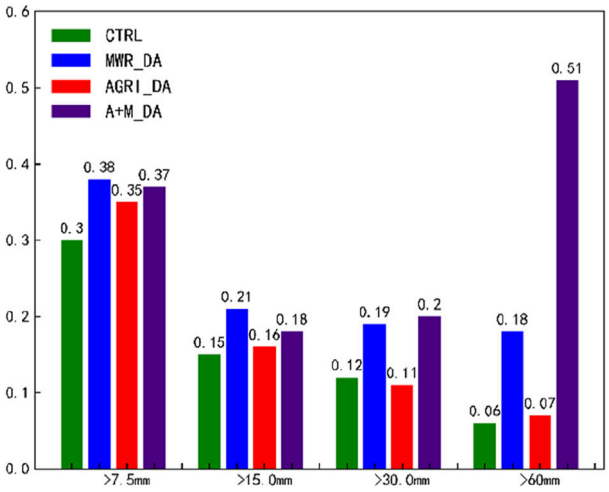

FIGURE 11
TS for 6-h rainfall forecasts from all four experiments at different rainfall thresholds.

AGRI_DA experiment. Moreover, the simulated maximum rainfall center and intensity in the AGRI_DA experiment are similar to the observation (Figure 5A). In the joint assimilation experiment of A + M_DA (Figure 10D), rainfall intensity and distribution are improved over the AGRI_DA experiment in the Beijing area. The simulated 6-h rainfall accumulation in the Beijing area is approximately comparable to the observed value (Figure 5A). At the very heavy rainfall level (>60 mm), the A + M_DA experiment gives a considerable TS enhancement than the other three experiments (Figure 11). The results indicate that such short-duration heavy rainfall prediction can be noticeably improved by the joint assimilation of AGRI radiance and ground-based MWR data.

5.3 Analysis of the impact on rainfall forecast

To explore the underlying reason for joint data assimilation facilitating the short-duration rainfall prediction, we analyze the essential meteorological elements dominating the initiation and development of convective storms, that is, temperature, relative humidity, and wind vector. Learn from the vertical cross-section along 40.5°N from the FNL analysis field (Figure 12A), there exists a moist

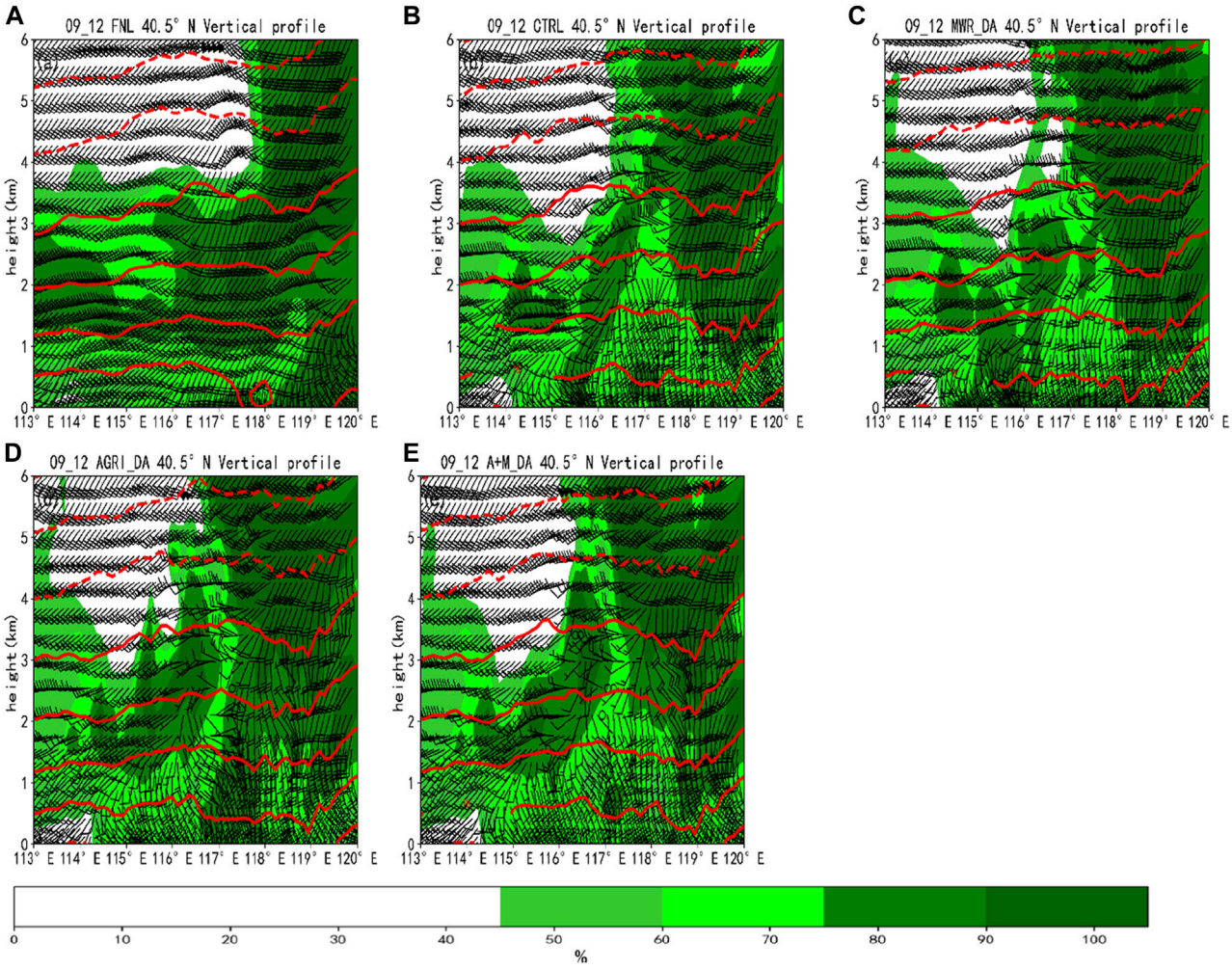

FIGURE 12
The vertical cross sections along 40.5°N from **(A)** FNL, **(B)** CTRL, **(C)** MWR_DA, **(D)** AGRI_DA, **(E)** A + M_DA at 1200 UTC, superimposed with the temperature (red contours), relative humidity (shaded), and horizontal wind barbs.

region (116°E–118°E) at 1–3 km height with the relative humidity exceeding 80%. The corresponding updraft could lift the moist air parcel, favoring the initiation of this convective precipitation. The same cross-section from the CTRL experiment fails to simulate the high humidity region at 1–3 km AGL, and overestimates the relative humidity below 1 km (Figure 12B). The MWR_DA experiment strengthens the relative humidity at 1–3 km AGL and below 1 km (Figure 12C). Compared to the CTRL experiment, the AGRI_DA experiment effectively corrects the underestimation at 1–3 km and the overestimation below 1 km AGL at 116°E–118°E (Figure 12D). However, data assimilation of AGRI radiance alone brings another humidity overestimation area at 117°E–118°E below 1 km. This humidity overestimation is successfully corrected by the joint data assimilation in the A + M_DA experiment, giving a predicted humidity condition approximately comparable to the observation (Figure 10E). The joint data assimilation of AGRI radiance and ground-based MWR data could skillfully correct the humidity distribution at lower and middle-upper layers, allowing for more accurate heavy rainfall prediction.

6 Conclusion and discussion

This paper uses RTTOV as the observational operator for FY-4A AGRI data assimilation. The data assimilation interface is built in WRFDA 4.3 to achieve direct assimilation of FY4A AGRI radiance. The effect of joint assimilation of AGRI radiance and ground-based MWR data on short-duration heavy rainfall prediction is investigated. Four data assimilation experiments are designed to explore the effects of the initial conditions and predicted variables of a typical short-duration heavy rainfall event in northern China. The main conclusions are as follows.

(1) The humidity increments caused by the assimilation of ground-based MWR data are mainly distributed in the middle-lower troposphere, with a horizontal influence radius of about 100 km, due to the less data amount of MWR. In contrast, the AGRI radiance assimilation affects the humidity over a large area, with the main effects distributed in the middle-upper troposphere. The joint assimilation of AGRI radiance and ground-based MWR data works together on the entire water vapor column, resulting in an improved initial humidity condition.
(2) All three data assimilation experiments effectively improve the 6-h accumulated rainfall forecast. The temperature and humidity profiles obtained from seven MWRs distributed across the Beijing area proved to be effective in correcting the heavy rainfall forecast over Beijing. AGRI radiance provides more skillful rainfall prediction over the three observed heavy rainfall regions. Compared to the AGRI_DA experiment, the joint assimilation experiment (A + M_DA) significantly improves the rainfall forecast over the Beijing area at a very heavy rainfall level. Thus, such short-duration heavy rainfall prediction can be noticeably improved by the joint assimilation of AGRI radiance and ground-based MWR data.
(3) The main reason for the improvement in precipitation forecasts from the assimilation experiments is the better forecast in humidity. The MWR_DA experiment can improve the humidity condition in the middle-lower layers, while AGRI_DA effectively provides a better humidity forecast in the middle-upper layers. The joint assimilation of AGRI radiance and ground-based MWR data could skillfully correct the humidity distribution in the entire layers, allowing for more accurate heavy rainfall prediction.

This paper explores the effect of joint assimilation of AGRI radiance and ground-based MWR data on deep convection prediction. Limited to the sparse distribution of MWR, mainly located in the Beijing area, the joint assimilation has remarkably improved the precipitation forecasts for the Beijing region and the other two rainfall regions to a lesser extent. This paper provides a basis for the joint assimilation of the two data sources as an efficient way to improve forecasts of such deep convective weather. It is a question for further study whether the results would be better if more MWRs were available for the joint assimilation with FY-4A AGRI.

Data availability statement

The original contributions presented in the study are included in the article/supplementary material, further inquiries can be directed to the corresponding author.

Author contributions

YS and ZL conceived and designed the study. YS wrote the main manuscript text. All authors contributed to the discussion of the results and reviewed the manuscript.

Funding

This research is jointly supported by the Natural Science Fundamental Research Project of Jiangsu Colleges and Universities (19KJB170024), the Youth Project of Natural Science Foundation of Anhui Province (2008085QD190), the Key Scientific Research Projects of Jiangsu Provincial Meteorological Bureau (KZ202203), and the fund of "Key Laboratory of Atmosphere Sounding, CMA" (2021KLAS01M).

Conflict of interest

The authors declare that the research was conducted in the absence of any commercial or financial relationships that could be construed as a potential conflict of interest.

Publisher's note

References

Auligné, T., McNally, A. P., and Dee, D. P. (2007). Adaptive bias correction for satellite data in a numerical weather prediction system. *Quarterly Journal of the Royal Meteorological Society*, 133 (624).

Chou, M. D., Suarez, M. J., Liang, X. Z., and Yan, M. M. H. (2001). A thermal infrared radiation parameterization for atmospheric studies. *NASA Tech. Memo.* 19, 55. 10,4606.

Cimini, D., Westwater, E. R., Gasiewski, A. J., Klein, M., Leuski, V. Y., and Liljegren, J. C. (2007). Ground-based millimeter-and submillimeter-wave observations of low vapor and liquid water contents. *IEEE Trans. Geoscience Remote Sens.* 45 (7), 2169–2180. doi:10.1109/tgrs.2007.897450

Dee, D. P. (2005). Bias and data assimilation. *Q. J. R. Meteorological Soc. A J. Atmos. Sci. Appl. meteorology Phys. Oceanogr.* 131 (613), 3323–3343. doi:10.1256/qj.05.137

De Souza, P. M. M., Vendrasco, E. P., Saraiva, I., Trindade, M., de Oliveira, M. B. L., Saraiva, J., et al. (2022). Impact of radar data assimilation on the simulation of a heavy rainfall event over manaus in the Central Amazon. *Pure Appl. Geophys.* 179, 425–440. doi:10.1007/s00024-021-02901-0

Dong, Y. H. (2016). FY-4 meteorological satellite and its application prospect. *Aerosp. Shanghai (In Chin.* 33 (02), 1–8. doi:10.19328/j.cnki.1006-1630.2016.02.001

Fu, X., and Tan, J. G. (2017). Quality control of temperature and humidity profile retrievals from ground-based microwave radiometer. *J. Appl. Meteorological Sci. (In Chinese)* 28 (2), 209–217. doi:10.11898/1001-7313.20170208

Geng, X. W., Min, J. Z., and Xu, D. M. (2020). Analysis of FY-4A AGRI radiance data bias characteristics and a correction experiment. *Chinese Journal of Atmospheric Sciences (In Chinese)* 44 (4), 679–694. doi:10.3878/j.issn.1006-9895.1907.18254

Guo, C., Ai, W., Hu, S., Du, X., and Chen, N. (2022a). Sea surface wind direction retrieval based on convolution neural network and wavelet analysis. *IEEE Journal of Selected Topics in Applied Earth Observations and Remote Sensing* 05, 3868–3876. doi:10.1109/jstars.2022.3173001

Guo, C., Ai, W., Zhang, X., Guan, Y., Liu, Y., Hu, S., et al. (2022b). Correction of sea surface wind speed based on SAR rainfall grade classification using convolutional neural network. *IEEE Journal of Selected Topics in Applied Earth Observations and Remote Sensing* 16, 321–328. doi:10.1109/JSTARS.2022.3224438

Honda, T., Kotsuki, S., Lien, G.-Y., Maejima, Y., Okamoto, K., and Miyoshi, T. (2018b). Assimilation of himawari-8 all-sky radiances every 10 minutes: Impact on precipitation and flood risk prediction. *Journal of Geophysical Research Atmospheres* 123, 965–976. doi:10.1002/2017jd027096

Honda, T., Miyoshi, T., Lien, G., Nishizawa, S., Yoshida, R., Adachi, S. A., et al. (2018a). Assimilating all-sky himawari-8 satellite infrared radiances: A case of typhoon soudelor (2015). *Monthly Weather Review* 146, 213–229. doi:10.1175/mwr-d-16-0357.1

Hong, S. Y. (2010). A new stable boundary-layer mixing scheme and its impact on the simulated East Asian summer monsoon. *J. Roy. Meteor. Soc.* 136 (651), 1481–1496. doi:10.1002/qj.665

Kain, J. S. (2004). The Kain-Fritsch convective parameterization: An update. *Journal of Applied Meteorology* 43 (1), 170–181. doi:10.1175/1520-0450(2004)043<0170:tkcpau>2.0.co;2

Kutty, G., Muraleedharan, R., and Kesarkar, A. P. (2018). Impact of representing model error in a hybrid ensemble-variational data assimilation system for track forecast of tropical cyclones over the Bay of Bengal. *Pure and Applied Geophysics* 175 (3), 1155–1167. doi:10.1007/s00024-017-1747-z

Li, Z. C., Bi, B. G., Jin, R. H., Xu, Z. F., and Xue, F. (2014). The development and application of the modern weather forecast in China for the recent ten years. *Acta Meteorologica Sinica (In Chinese)* 72 (6), 1069–1078. doi:10.11676/qxxb2014.090

Löhnert, U., and Maier, O. (2012). Operational profiling of temperature using ground-based microwave radiometry at Payerne: Prospects and challenges. *Atmos. Meas. Tech.* 5, 1121–1134. doi:10.5194/amt-5-1121-2012

Ma, S., Zhang, W., Cao, X. Q., Zhao, Y., and Liu, B. (2022). Assimilation of all-sky radiance from the FY-3 MWHS-2 with the Yinhe 4D-Var system. *J. Meteor. Res.* 36 (5), 750–766. doi:10.1007/s13351-022-1208-1

Min, L. Z., Sheng, T. L., Chen, H. S., and Sun, L. P. (2000). Numerical experiment on quality control and variational assimilation of satellite image retrieval. *Journal of Applied Meteorological Science (In Chinese)* 11 (4), 410–418.

Minamide, M., and Zhang, F. (2018). Assimilation of all-sky infrared radiances from himawari-8 and impacts of moisture and hydrometer initialization on convection-permitting tropical cyclone prediction. *Monthly Weather Review* 146, 3241–3258. doi:10.1175/mwr-d-17-0367.1

Mlawer, E. J., Taubman, S. J., Brown, P. D., Iacono, M. J., and Clough, S. A. (1997). Radiative transfer for inhomogeneous atmospheres: RRTM, a validated correlated-k model for the longwave. *Journal of Geophysical Research* 102, 16663–16682. doi:10.1029/97jd00237

Okamoto, K., Sawada, Y., and Kunii, M. (2019). Comparison of assimilating all-sky and clear-sky infrared radiances from Himawari-8 in a mesoscale system. *Quarterly Journal of the Royal Meteorological Society* 145 (719), 745–766. doi:10.1002/qj.3463

Pan, Y., Zhang, S., Li, Q., Ma, L., Jiang, S., Lei, L., et al. (2020). Analysis of convective instability data derived from a ground-based microwave radiometer before triggering operations for artificial lightning. *Atmospheric research* 243, 105005. doi:10.1016/j.atmosres.2020.105005

Parrish, D. F., and Derber, J. C. (1992). The National Meteorological Center's spectral statistical-interpolation analysis system. *Monthly Weather Review* 120 (8), 1747–1763. doi:10.1175/1520-0493(1992)120<1747:tnmcss>2.0.co;2

Posada, R., García-Ortega, E., López, L., and Marcos, J. L. (2013). A method to improve the accuracy of continuous measuring of vertical profiles of temperature and water vapor density by means of a ground-based microwave radiometer. *Atmospheric Research*, 122.

Qi, Y., Fan, S., Li, B., Mao, J., and Lin, D. (2021). Assimilation of ground-based microwave radiometer on heavy rainfall forecast in beijing. *Atmosphere* 13 (1), 74. doi:10.3390/atmos13010074

Qin, D. H., Sun, H. L., Sun, S., and Liu, Y. J. (2005). The strategy of Chinese meteorological Service and development: 2005-2020. *Advances in Earth Science* 20 (3), 268–274. (In Chinese).

Qin, Z. K., Zou, X., Li, G., and Ma, X. L. (2010). Quality control of surface station temperature data with non-Gaussian observation-minus-background distributions. *Journal of Geophysical Research Atmospheres* 115 (D16), D16312. doi:10.1029/2009jd013695

Saunders, R., Hocking, J., Turner, E., Rayer, P., Rundle, D., Brunel, P., et al. (2018). An update on the RTTOV fast radiative transfer model (currently at version 12). *Geosci. Model Dev.* 11, 2717–2737. doi:10.5194/gmd-11-2717-2018

Saunders, R., Matricardi, M., and Brunel, P. (1999). An improved fast radiative transfer model for assimilation of satellite radiance observations. *Quarterly Journal of the Royal Meteorological Society* 125 (556), 1407–1425. doi:10.1002/qj.1999.49712555615

Shen, F., and Min, J. (2015). Assimilating AMSU-A radiance data with the WRF hybrid En3DVAR system for track predictions of typhoon megi (2010). *Advances in Atmospheric Sciences* 32, 1231–1243. doi:10.1007/s00376-014-4239-4

Shen, F., Shu, A., Li, H., Xu, D., and Min, J. (2021). Assimilation of Himawari-8 imager radiance data with the WRF-3DVAR system for the prediction of Typhoon Soudelor. *Natural Hazards Earth Syst. Sci.* 21, 1569–1582. doi:10.5194/nhess-21-1569-2021

Shen, F., Xu, D., Li, H., Min, J., Liu, R., et al. (2021). Assimilation of GPM microwave imager radiance data with the WRF hybrid 3DEnVar system for the prediction of typhoon chan-hom (2015). *Atmospheric Research* 251, 105422. doi:10.1016/j.atmosres.2020.105422

Shoji, Y., Kunii, M., and Saito, K. (2011). Mesoscale data assimilation of Myanmar Cyclone Nargis. Part II: Assimilation of GPS-derived precipitable water vapor. *J. Meteor. Soc. Japan* 89, 67–88. doi:10.2151/jmsj.2011-105

Tewari, M., Chen, F., Dudhia, J., Ray, P., Miao, S., Nikolopoulos, E., et al. (2022). Understanding the sensitivity of WRF hindcast of Beijing extreme rainfall of 21 July 2012 to microphysics and model initial time. *Atmospheric Research*, 271. doi:10.1016/j.atmosres.2022.106085

Wang, D. C., You, W., Zang, Z. L., Pan, X. B., Hu, Y. W., and Liang, Y. F. (2022). A three-dimensional variational data assimilation system for aerosol optical properties based on WRF-chem v4.0: Design, development, and application of assimilating himawari-8 aerosol observations. *Geosci. Model. Dev.* 15, 1821–1840. doi:10.5194/gmd-15-1821-2022

Wang, Y., Liu, Z., Yang, S., Min, J., Chen, L., Chen, Y., et al. (2018). Added value of assimilating Himawari-8 AHI water vapor radiances on analyses and forecasts for "7.19" severe storm over north China. *Journal of Geophysical Research Atmospheres* 123 (7), 3374–3394. doi:10.1002/2017jd027697

Xu, D., Liu, Z., Fan, S., Chen, M., and Shen, F. (2021). Assimilating all-sky infrared radiances from himawari-8 using the 3DVar method for the prediction of a severe storm over NorthNorth China. *Adv. Atmos. Sci.* 38, 661–676. doi:10.1007/s00376-020-0219-z

Xu, D., Min, J., Shen, F., Ban, J., and Chen, P. (2016). Assimilation of MWHS radiance data from the FY-3B satellite with the WRF Hybrid-3DVAR system for the forecasting of binary typhoons. *Journal of Advances in Modeling Earth Systems* 8 (2), 1014–1028. doi:10.1002/2016ms000674

Xu, D., Shu, A., Li, H., Shen, F., Min, J., and Su, H. (2021). Effects of assimilating clear-sky FY-3D MWHS2 radiance on the numerical simulation of tropical storm ampil. *Remote Sens* 13 (15), 2873. doi:10.3390/rs13152873

Xue, J. S. (2009). Scientific issues and perspective of assimilation of meteorolo gical satellite data. *Acta Meteorologica Sinica (In Chinese)* 67 (6), 903–911. doi:10.3321/j.issn:0577-6619.2009.06.001

Yang, C., Min, J. Z., and Liu, Z. Q. (2017). The impact of AMSR2 radiance data assimilation on the analysis and forecast of typhoon son-tinh. *Chinese Journal of Atmospheric Sciences (in Chinese)* 41 (2), 372–384.

Yang, J., Zhang, Z., Wei, C., Lu, F., and Guo, Q. (2017). Introducing the new generation of Chinese geostationary weather satellites, Fengyun-4. *Bulletin of the American Meteorological Society* 98 (8), 1637–1658. doi:10.1175/bams-d-16-0065.1

Yang, Z.-L., Niu, G.-Y., Mitchell, K. E., Chen, F., Ek, M. B., Barlage, M., et al. (2011). The community Noah land surface model with multiparameterization options (Noah-MP): 2. Evaluation over global river basins. *Journal of Geophysical Research Atmospheres* 116 (D12), D12110. doi:10.1029/2010jd015140

Ye, H., Pan, X., You, W., Zhu, X., Zang, Z., Wang, D., et al. (2021). Impact of CALIPSO profile data assimilation on 3-D aerosol improvement in a size-resolved aerosol model. *Atmospheric Research* 264, 105877. doi:10.1016/j.atmosres.2021.105877

Zhang, X., Xu, D., Liu, R., and Shen, F. (2022). Impacts of FY-4A AGRI radiance data assimilation on the forecast of the super typhoon "in-fa" (2021). *Remote Sens* 14, 4718. doi:10.3390/rs14194718

Zhang, Z. Q., Lu, F., Fang, X., and Zhou, Y. Q. (2017). Application and development of FY-4 meteorological satellite. *Aerospace Shanghai (In Chinese)* 34 (04), 8–19. doi:10.19328/j.cnki.1006-1630.2017.04.002

Zou, X., and Zeng, Z. (2006). A quality control procedure for GPS radio occultation data. *Journal of Geophysical Research Atmospheres* 111 (D2), D02112. doi:10.1029/2005jd005846

frontiers | Frontiers in Earth Science

TYPE Original Research
PUBLISHED 27 March 2023
DOI 10.3389/feart.2023.1057299

OPEN ACCESS

EDITED BY
Yunheng Wang,
University of Oklahoma, United States

REVIEWED BY
Jean-Baptiste Renard,
UMR7328 Laboratoire de physique et chimie de l'environnement et de l'Espace (LPC2E), France
Chang Liu,
Guangdong Provincial Climate Center, China
Muyuan Li,
China Meteorological Administration, China
Feng Hu,
Chuzhou University, China

*CORRESPONDENCE
Xiaoli Xia,
xiaxiaoli051@163.com

SPECIALTY SECTION
This article was submitted to Environmental Informatics and Remote Sensing, a section of the journal Frontiers in Earth Science

RECEIVED 29 September 2022
ACCEPTED 06 March 2023
PUBLISHED 27 March 2023

CITATION
Xia X, Min J, Sun S and Chen X (2023), Simultaneous assimilation of Fengyun-4A and Himawari-8 aerosol optical depth retrieval to improve air quality simulations during one storm event over East Asia . *Front. Earth Sci.* 11:1057299. doi: 10.3389/feart.2023.1057299

Simultaneous assimilation of Fengyun-4A and Himawari-8 aerosol optical depth retrieval to improve air quality simulations during one storm event over East Asia

Xiaoli Xia[1,2]*, Jinzhong Min[3], Shangpeng Sun[2] and Xu Chen[2]

[1]Jiangsu Key Laboratory of Environmental Engineering, Jiangsu Provincial Academy of Environmental Science, Nanjing, China, [2]College of Tourism, Resources and Environment, Zaozhuang University, Zaozhuang, China, [3]Key Laboratory of Meteorological Disaster of Ministry of Education (KLME), Nanjing University of Information Science & Technology, Nanjing, China

Aerosols are the main components of air pollutants, which are closely related to haze, dust storm and air pollution. In this study, an aerosol data assimilation system was developed using Gridpoint Statistical Interpolation (GSI) system to assimilate the Aerosol Optical Depth (AOD) observations from FY4 and Himawari-8 for the first time and applied in the heavy dust case over east Asia in March 2018. Three parallel experiments assimilated AOD from FY4, Himawari-8 and both the FY4 and Himawari-8 respectively and a control experiment which did not employ DA were performed. The hourly aerosol analyses and forecasts are compared with the assimilated FY-4 AOD, Himawari-8 AOD and independent AOD from Aerosol Robotic Network (AERONET). The results showed that all forms of DA experiments improved a low Bias and the RMSE reduced about 20%. The aerosol data assimilation with observations from both the FY-4 and Himawari-8 satellites substantially improved aerosol analyses and subsequent forecasts with more abundant aerosol observation information, especially over the northwest of China. This study indicates that the new generation geostationary meteorological satellites have potential to dramatically contribute to air quality forecasting.

KEYWORDS

Fengyun-4A satellite, aerosol optical depth, geostationary meteorological satellites, data assimilation, Himawari-8

1 Introduction

With rapid economic growth and accelerated urbanization, subsequent air pollution is becoming increasingly serious (Zhao et al., 2020). Aerosols are the main components of air pollutants, are closely related to haze, dust storms, and air pollution, and are present in very small amounts in the composition of the earth's atmosphere. However, atmospheric aerosols have a direct impact on climate, including the energy budget of atmospheric radiation, changes in the microscopic and macroscopic characteristics of clouds, and indirect effects of atmospheric chemical processes (Hansen et al., 1997; Koren et al., 2004; Rosenfeld et al., 2008; Wilcox, 2012). Not only can they worsen air quality and reduce visibility, but they can

also have an impact on human health, the environment, and climate change (Tie et al., 2009; Chen et al., 2017; Sicard et al., 2017; Liu et al., 2018; Zhao et al., 2018).

With continuous progress in satellite detection technology, satellite remote sensing can play a vital role in the study of atmospheric aerosols. Satellite observation can partly make up for the deficiency of conventional observation. Many studies have found that data assimilation can improve the level of model prediction (e.g., Zhang and Reid, 2006; Shen et al., 2022; Xu et al., 2022). Meteorological satellites are usually classified as geostationary (in geosynchronous orbit) or polar-orbiting (in sun-synchronous orbit) according to their orbits (Zou et al., 2011; Xu et al., 2013; Yang et al., 2017; Wang et al., 2020). Polar orbit meteorological satellites orbit the earth's polar regions at an altitude of about 1,000 km. They are low-orbit satellites with an operating period of approximately 115 min. Polar-orbit satellites can monitor the global atmosphere and provide high-resolution products. However, they can only observe the same area twice a day and thus may miss rapidly developing dust storms. Conversely, geostationary satellites are high-orbit satellites, with an operational height of at least 35,786 km. Geostationary satellites have a large monitoring range and high temporal resolution, which are necessary for monitoring the development of rapidly evolving weather systems (Stengel et al., 2009; Yumimoto, 2013; Shen and Min, 2015; Li and Zou, 2017; Yang et al., 2017; Xia et al., 2019a). Many studies have found that meteorological data from geostationary satellites play an increasingly significant role in many weather applications, including monitoring heavy rain, severe weather, typhoons, and air pollution as a result of the high temporal resolution (Stuhlmann et al., 2005; Schmit et al., 2008; Yu et al., 2009; Goodman et al., 2012; Greenwald et al., 2016; Min et al., 2017).

In recent years, geostationary satellite data have been increasingly applied to air pollution and have had a positive influence on aerosol prediction. Yumimoto et al. (2016), Dai et al. (2019), and Xia et al. (2019b) presented data assimilation experiments, including aerosol optical depth (AOD), from the Himawari-8 satellite. Their results showed that data assimilation with rapid-update Himawari-8 observations improves aerosol analyses better than polar satellite observations. Niu et al. (2008) used the three-dimensional variational method (3DVAR) to assimilate the dust retrieval from the Fengyun-2 satellite (FY-2C). The results found that the dust aerosol data assimilation system could effectively improve the short-term prediction of dust weather. Wang et al. (2004) and Lee et al. (2016) employed AOD from the Goddard Earth Observing System-8 (GEOS-8) and the Geostationary Ocean Color Imager (GOCI) into a data assimilation (DA) system to evaluate efficiency, obtaining some significantly positive results.

The Fengyun-4 satellite (FY-4), which was successfully launched on 11 December 2016, is a new generation of geostationary orbit meteorological satellites for quantitative application to China. FY-4 is the realization of the upgrading and technological leap forward of China's geostationary orbit (GEO) meteorological satellites, with an overall performance reaching an internationally advanced level. FY-4 carries an advanced geosynchronous radiation imager (AGRI), a geostationary interferometric infrared sounder (GIIRS), and a lightning mapping imager (LMI) that can provide full-disk images for 14 spectral bands, with a temporal resolution of 15-min intervals and a spatial resolution of 0.5–4.0 km (Zhang et al., 2015; Min et al., 2017; Wang et al., 2019). The Japanese Himawari-8, a next-generation GEO satellite, was successfully launched in October 2014. In comparison with conventional geostationary satellites, the advanced Himawari imager (AHI) carried by Himawari-8 can provide more frequent observations and more aerosol-detectable channels (Bessho et al., 2016; Zhuge et al., 2017; Wang et al., 2018). Both FY-4 and the Himawari-8 belong to a new generation of advanced meteorological weather satellites. The effect of the Himawari-8 aerosol data assimilation system has been reported as mentioned previously. However, in regions such as northwest China, where Himawari-8 has little data coverage, it is necessary to assimilate both FY-4 and Himawari-8 aerosol data and conduct full research and analysis to improve the capability of air quality prediction.

In this study, we constructed a rapid-update aerosol data assimilation system to assimilate both FY-4 and Himawari-8 aerosol observations. This study is the first attempt to assimilate both these satellites' aerosol observations using Gridpoint Statistical Interpolation (GSI).

This study used the three-dimensional variational method (3DVAR) within a GSI system as a follow-up to the work of Liu et al. (2011), who assimilated the MODIS AOD observations with the GSI system; the impact of MODIS AOD data assimilation was demonstrated by its application to a dust storm of 17–24 March 2010 over East Asia. Yumimoto et al. (2016) showed the first application of AOD derived from Himawari-8 data to aerosol data assimilation that targeted transboundary pollutants and dust outflows over East Asia over 14–17 April 2011. Wang et al. (2012) presented a new method for the combined use of satellite-measured radiances and inverse modeling to spatially constrain the amount and location of dust emissions. The technique was illustrated by a case study in May 2008. As shown in the work of Peng et al. (2018), an ensemble Kalman filter data assimilation (DA) system was developed to improve air quality forecasts. This DA system was applied to simultaneously adjust the chemical initial conditions (ICs) during an extreme haze episode that occurred in early October 2014 over East Asia. Their results showed the positive impact of their assimilation approach on air quality prediction through its application to one dust event. In this study, the added value of assimilating AHI and AGRI aerosol data was applied to a severe dust case over East Asia in March 2018 to assess the effectiveness of analysis and prediction.

The remaining sections of this article are arranged as follows. The AOD data used in this study are introduced in the following section. Section 3 presents the dust storm case, the details of the aerosol DA system, the experimental design, and the background error covariance. The results are discussed in Section 4. The summary and discussion are given in Section 5.

2 Observation data

FY-4 was successfully launched on 11 December 2016 by the Satellite Meteorological Center of China Meteorological Agency.

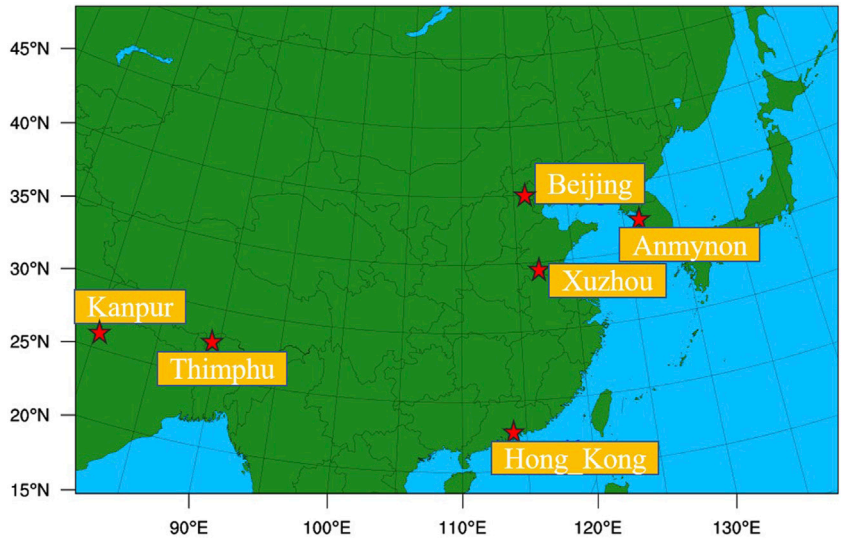

FIGURE 1
Experimental domain. Blue labeling indicates the locations of six AERONET sites used in this study.

FY-4 has realized the upgrading and technological leap forward of China's GEO meteorological satellites. It can provide geostationary images over a large area from 24.1°E to 174.7°W between 80.6°N and 80.6°S. FY-4 is equipped with four optical instruments: an advanced geosynchronous radiation imager (AGRI), a geostationary interferometric infrared sounder (GIIRS), a lightning mapping imager (LMI), and a Solar X-EUV Imaging Telescope (SXEIT). The highly improved AGRI onboard FY-4 has 14 spectral bands from visible to infrared and provides full-disk images with a temporal resolution of 15-min intervals and spatial resolutions of 1 km for nadir channels, 2 km for near-infrared channels, and 4 km for the rest of the infrared channels (Zhang et al., 2015; Min et al., 2017; Yang et al., 2017).

In this study, AOD observations from FY-4 were selected for the newly developed data assimilation system. The FY-4 AOD products are provided by the National Satellite Meteorological Center with 4 km resolution and were then refined to the same resolution as the initial grid of the model—25km. The total observation error for AOD was suggested by Zhang et al. (2008), in which observation errors were estimated to be the retrieval uncertainty attached to the FY-4A AOD products plus a standard deviation calculated as the representative error in the re-gridding. The assimilation time window is 1 h, and all the observation data in the assimilation time window are included in the assimilation system. Furthermore, only FY-4 AOD marked as the best quality control flag with values less than 2.5 could be assimilated, as suggested by Saide et al. (2014).

The latest version of the Himawari-8 AOD (Kikuchi et al., 2018; Yoshida, et al., 2018; Dai et al., 2019) was used for comparison in this study; it can be downloaded free from the internet (http://www.eorc.jaxa.jp/ptree/index.html) and was then processed to the same resolution as our model. Furthermore, the AErosol RObotic NETwork (AERONET) AOD observations were used for the validation; these are freely available at the website (http://aeronet.gsfc.nasa.gov/) (Holben et al., 1998). The locations of AERONET sites employed in this study are presented in Figure 1.

3 Aerosol data assimilation system and experimental setup

3.1 The severe dust storm case

A dust storm affecting most regions of East Asia during 26–30 March 2018 was selected for this study. On 26 March 2018, a severe dust storm arrived in northeast Asia, with sand-blowing and flowing-dust weather appearing in central and eastern Inner Mongolia, northern Shanxi, central and northern Hebei, Beijing, Tianjin, and northeast China. The dust storm covered large regions, appeared in a concentrated time, and caused serious air pollution—visibility in the Beijing area was less than 400 m, accompanied by strong winds.

3.2 Aerosol data assimilation system

NCEP's Gridpoint Statistical Interpolation (GSI) 3DVAR DA system—explained by Wu et al. (2002) and Kleist et al. (2009)—was expanded to assimilate FY-4A and Himawari-8 aerosol observations. The AOD observation operator was described by Liu et al. (2011). In this study, we added a new interface for the AOD observations from FY-4A and Himawari-8 to the GSI system as a follow-up to Liu et al. (2011) and Schwartz et al. (2012). Generally, the 3DVAR algorithm obtains an optimal analysis field by minimizing the deviation between the background and the observations. It constantly adjusts the weight ratio between the background and the observation by minimizing the given cost function so that the analysis field reaches optimal fit. The 3DVAR method is a problem of minimizing the cost function,

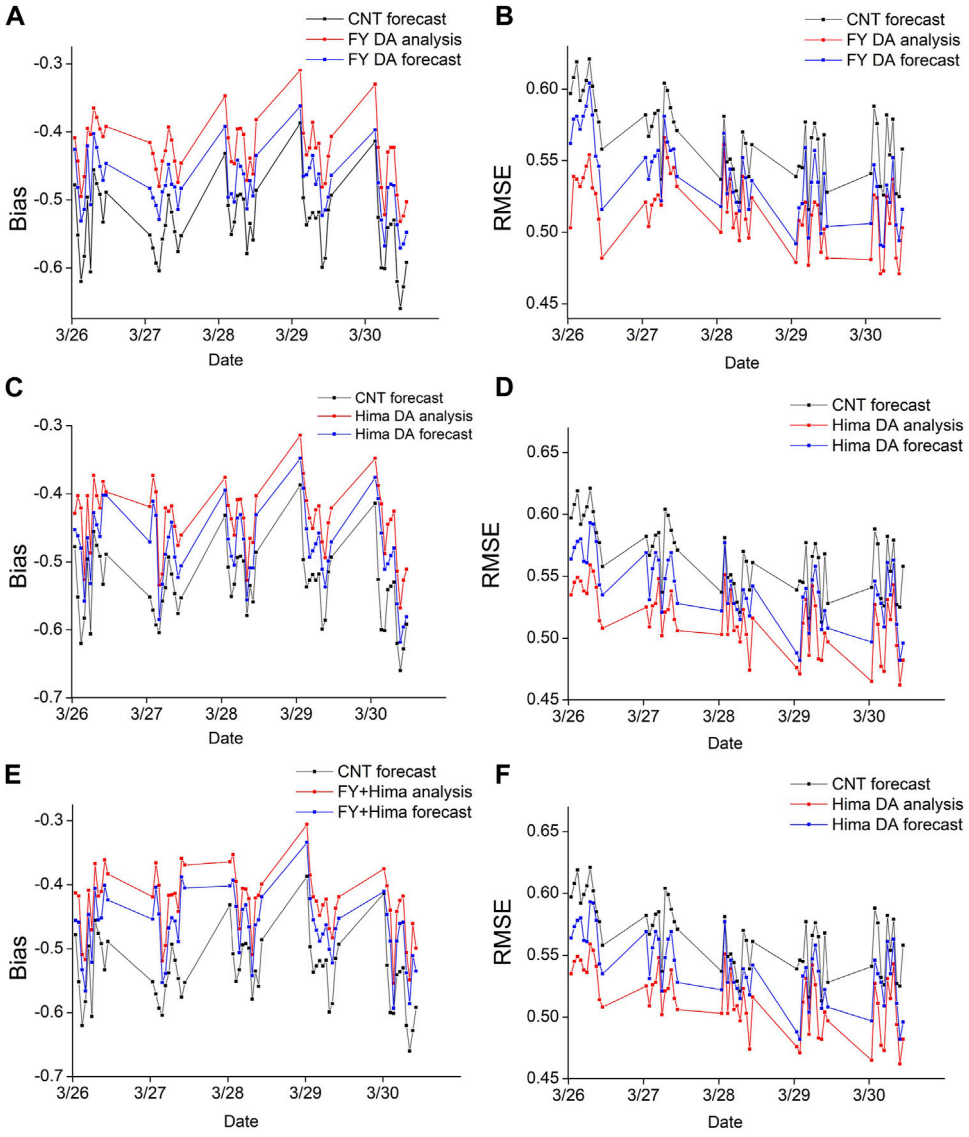

FIGURE 2
Time series of **(A)** bias in the FY DA system; **(B)** RMSE in the FY DA system; **(C)** bias in the Hima DA system; **(D)** RMSE in the Hima DA system; **(E)** bias in the FY + Hima DA system; **(F)** RMSE in the FY + Hima DA system during the period 26–30 March 2018.

and expression of the 3DVAR cost function J(x) could be expressed as follows (Lorenc, 1986; Ide et al., 1997; Chin, et al., 2000; Lorenc et al., 2000):

$$\boldsymbol{J}(\boldsymbol{x}) = \frac{\mathbf{1}}{\mathbf{2}}(\boldsymbol{x}-\boldsymbol{x_b})^T\boldsymbol{B}^{-1}(\boldsymbol{x}-\boldsymbol{x_b}) + \frac{\mathbf{1}}{\mathbf{2}}[\boldsymbol{y}-\boldsymbol{H}(\boldsymbol{x})]^T\boldsymbol{R}^{-1}[\boldsymbol{y}-\boldsymbol{H}(\boldsymbol{x})], \tag{1}$$

where x represents the n-dimensional analysis vector to minimize the cost function J(x), H is the m-dimensional observation operation, x_b denotes the n-dimensional background variable vector, B is the background error covariance matrix of dimensions $n \times n$, and R denotes the observation error covariance matrix of dimensions $m \times m$.

In this study, the WRF-Chem model was selected for aerosol transport prediction. The gaseous chemical mechanism was produced by the Goddard Chemistry Aerosol Radiation and Transport (GOCART) aerosol scheme (Ginoux et al., 2001; Chin et al., 2002), which simulated 14 aerosol types, including sulfate, dust, organic carbon (OC) hydrophobic and hydrophilic, black carbon (BC), and sea salt. The static background error covariance (BEC) matrix of aerosol variables is constructed by using the National Meteorological Center (NMC) method (Parrish and Derber, 2002). At present, this method is widely used for statistical analysis of model background error covariance. We took the differences of 24 and 12 h WRF-Chem forecasts of the aerosol species valid at the common time for 62 pairs valid from 25 February to 25 March 2018.

TABLE 1 Statistical analysis of the simulated and observed AOD in experiments 26 March 2018.

Date	FY DA				Hima DA				FY+Hima DA			
	Bb	Ba	Rb	Ra	Bb	Ba	Rb	Ra	Bb	Ba	Rb	Ra
032,601	−0.426	−0.409	0.562	0.503	−0.453	−0.429	0.564	0.535	−0.456	−0.413	0.576	0.538
032,602	−0.482	−0.443	0.579	0.539	−0.462	−0.403	0.573	0.545	−0.459	−0.418	0.541	0.503
032,603	−0.531	−0.495	0.581	0.537	−0.480	−0.421	0.578	0.549	−0.533	−0.509	0.546	0.504
032,604	−0.466	−0.514	0.532	0.572	−0.558	−0.526	0.580	0.546	−0.566	−0.517	0.512	0.471
032,605	−0.395	−0.421	0.538	0.581	−0.465	−0.403	0.562	0.538	−0.477	−0.409	0.548	0.502
032,606	−0.404	−0.507	0.546	0.588	−0.463	−0.421	0.561	0.536	−0.520	−0.471	0.540	0.501
032,607	−0.365	−0.403	0.554	0.604	−0.402	−0.382	0.593	0.559	−0.406	−0.367	0.578	0.537
032,608	−0.379	−0.423	0.531	0.582	−0.403	−0.397	0.592	0.554	−0.455	−0.418	0.572	0.554
032,609	−0.396	−0.451	0.527	0.553	−0.463	−0.421	0.578	0.541	−0.452	−0.411	0.548	0.501
032,610	−0.407	−0.471	0.509	0.546	−0.402	−0.382	0.543	0.514	−0.401	−0.361	0.523	0.497
032,611	−0.392	−0.447	0.482	0.516	−0.411	−0.398	0.535	0.508	−0.424	−0.381	0.531	0.502

TABLE 2 Statistical analysis of simulated and observed AOD in experiments 27 March 2018.

Date	FY DA				Hima DA				FY+Hima DA			
	Bb	Ba	Rb	Ra	Bb	Ba	Rb	Ra	Bb	Ba	Rb	Ra
032,701	−0.481	−0.416	0.552	0.521	−0.471	−0.419	0.569	0.525	−0.454	−0.419	0.539	0.505
032,702	−0.497	−0.432	0.537	0.504	−0.411	−0.373	0.531	0.509	−0.404	−0.366	0.537	0.494
032,703	−0.508	−0.455	0.549	0.519	−0.433	−0.397	0.556	0.526	−0.446	−0.401	0.535	0.506
032,704	−0.529	−0.480	0.553	0.523	−0.585	−0.534	0.569	0.528	−0.553	−0.519	0.562	0.518
032,705	−0.488	−0.443	0.557	0.526	−0.533	−0.518	0.563	0.548	−0.539	−0.495	0.528	0.495
032,706	−0.479	−0.428	0.522	0.519	−0.489	−0.421	0.521	0.502	−0.468	−0.417	0.523	0.506
032,707	−0.448	−0.393	0.581	0.566	−0.464	−0.426	0.548	0.521	−0.452	−0.416	0.554	0.511
032,708	−0.477	−0.412	0.563	0.552	−0.442	−0.418	0.563	0.523	−0.457	−0.414	0.548	0.512
032,709	−0.481	−0.443	0.557	0.541	−0.493	−0.448	0.569	0.538	−0.489	−0.442	0.563	0.523
032,710	−0.514	−0.474	0.558	0.545	−0.523	−0.476	0.546	0.515	−0.388	−0.359	0.526	0.507
032,711	−0.446	−0.483	0.539	0.532	−0.506	−0.461	0.528	0.506	−0.455	−0.369	0.541	0.493

3.3 Model and experimental design

In this study, the WRF-Chem model was selected for aerosol transport prediction over the domain spanning east Asia (Figure 1) with a 25-km horizontal grid spacing. There were 250 × 160 grid points and 40 vertical levels. The top pressure was 50 hPa. The physical parameterizations were concluded in this study: the rapid radiative transfer model longwave radiation scheme (Mlawer et al., 1997), the Dudhia shortwave radiation scheme (Dudhia, 1989), the Mellor–Yamada–Janjic (MYJ) boundary layer scheme, the Noah land surface model, and the Yonsei University (YSU) planetary boundary layer scheme (Hong and Lim, 2006).

The data assimilation system to assimilate the FY-4A and Himawari-8 aerosol observations was constructed within the GSI. We designed four parallel experiments to assess the performance of the newly developed data assimilation system for this severe dust storm case of 26–30 March 2018 over East Asia. The WRF-Chem settings and physical parameterizations were uniform in all experiments and were the same as those introduced in the previous section. One experiment (CNT) did not employ any DA, while AOD DA was performed in the other three experiments. The other three experiments were all performed based on the GSI using the 3DVAR DA system, but they assimilated different satellite AOD observations: one assimilating FY-4A AOD (FY DA), another assimilating Himawari-8 AOD (Hima DA), and the last assimilating both FY-4A and Himawari-8 AOD (FY + Hima DA). As in Houtekamer et al. (2005), Pagowski et al. (2010), Schwartz et al. (2012), and Pang et al. (2018), the first 5 days' aerosol forecast was

TABLE 3 Statistical analysis of simulated and observed AOD in experiments 28 March 2018.

Date	FY DA				Hima DA				FY+Hima DA			
	Bb	Ba	Rb	Ra	Bb	Ba	Rb	Ra	Bb	Ba	Rb	Ra
032,801	−0.392	−0.347	0.518	0.500	−0.395	−0.376	0.522	0.503	−0.402	−0.364	0.517	0.504
032,802	−0.496	−0.409	0.569	0.561	−0.467	−0.417	0.577	0.551	−0.393	−0.353	0.539	0.523
032,803	−0.491	−0.444	0.527	0.514	−0.492	−0.432	0.528	0.503	−0.434	−0.395	0.525	0.502
032,804	−0.503	−0.447	0.544	0.537	−0.505	−0.461	0.546	0.539	−0.506	−0.469	0.534	0.528
032,805	−0.442	−0.396	0.528	0.503	−0.436	−0.409	0.528	0.506	−0.439	−0.406	0.534	0.505
032,806	−0.451	−0.395	0.521	0.513	−0.431	−0.408	0.523	0.509	−0.432	−0.407	0.523	0.505
032,807	−0.462	−0.404	0.515	0.494	−0.467	−0.436	0.515	0.497	−0.466	−0.422	0.507	0.489
032,808	−0.503	−0.471	0.552	0.539	−0.527	−0.556	0.539	0.523	−0.542	−0.509	0.532	0.508
032,809	−0.472	−0.439	0.538	0.509	−0.466	−0.509	0.532	0.503	−0.463	−0.421	0.519	0.502
032,810	−0.494	−0.462	0.516	0.496	−0.472	−0.509	0.518	0.474	−0.455	−0.417	0.503	0.466
032,811	−0.435	−0.382	0.536	0.524	−0.403	−0.431	0.542	0.516	−0.419	−0.399	0.525	0.489

TABLE 4 Statistical analysis of simulated and observed AOD in experiments 29 March 2018.

Date	FY DA				Hima DA				FY+Hima DA			
	Bb	Ba	Rb	Ra	Bb	Ba	Rb	Ra	Bb	Ba	Rb	Ra
032,901	−0.362	−0.309	0.462	0.457	−0.348	−0.314	0.488	0.476	−0.334	−0.306	0.491	0.473
032,902	−0.465	−0.402	0.517	0.508	−0.392	−0.37	0.482	0.471	−0.422	−0.385	0.497	0.479
032,903	−0.463	−0.434	0.520	0.505	−0.452	−0.41	0.533	0.512	−0.455	−0.419	0.516	0.508
032,904	−0.453	−0.424	0.559	0.521	−0.493	−0.439	0.540	0.531	−0.471	−0.426	0.541	0.526
032,905	−0.435	−0.386	0.496	0.477	−0.484	−0.451	0.504	0.486	−0.488	−0.448	0.498	0.475
032,906	−0.477	−0.424	0.535	0.512	−0.474	−0.424	0.547	0.542	−0.477	−0.432	0.547	0.536
032,907	−0.462	−0.417	0.557	0.521	−0.458	−0.418	0.558	0.526	−0.463	−0.423	0.554	0.513
032,908	−0.523	−0.481	0.535	0.519	−0.511	−0.471	0.537	0.483	−0.501	−0.469	0.538	0.493
032,909	−0.515	−0.476	0.499	0.486	−0.537	−0.494	0.507	0.482	−0.522	−0.483	0.493	0.481
032,910	−0.496	−0.436	0.541	0.502	−0.499	−0.443	0.522	0.504	−0.469	−0.437	0.522	0.503
032,911	−0.464	−0.407	0.504	0.482	−0.471	−0.421	0.508	0.497	−0.453	−0.419	0.502	0.487

used for spin-up, and then, the four experiments began with the same initial fields. In each experiment, a new aerosol forecast simulated by WRF-Chem was initialized at 1-h intervals from 00 UTC on 26 March to 12 UTC on 30 March 2018. For every initialization, the meteorological fields were updated by inserting the final reanalysis data (FNL) analysis into the research domain as a background in all experiments. For the three experiments that employed DA, the observations within each assimilation time window (±0.5) were assimilated. The 1-h prediction initiated by the previous periodic analysis was the background, and the analysis results were then updated hourly. Note that Himawari-8 AODs were only present during the daytime, for 11–12 h data available in East Asia (Yumimoto et al., 2016); therefore, the DA experiments only cycled during daylight hours when the aerosol data were available.

4 Results

In this section, the evaluations of aerosol analysis and prediction of all four experiments by comparing to AOD observations from FY-4, Himawari-8, and independent AERONET are presented.

4.1 Comparison to Himawari AOD and FY-4 AOD

The root-mean-square error (RMSE) and mean bias, as statistical indicators which were calculated from models and observations, were used to evaluate the effectiveness of the assimilation systems. Figure 2 presents the distribution of bias

10.3389/feart.2023.1057299

TABLE 5 Statistical analysis of simulated and observed AOD in experiments 30 March 2018.

Date	FY DA				Hima DA				FY+Hima DA			
	Bb	Ba	Rb	Ra	Bb	Ba	Rb	Ra	Bb	Ba	Rb	Ra
033,001	−0.397	−0.33	0.506	0.461	−0.376	−0.348	0.497	0.465	−0.411	−0.375	0.496	0.472
033,002	−0.475	−0.423	0.547	0.526	−0.407	−0.388	0.546	0.527	−0.447	−0.402	0.568	0.542
033,003	−0.53	−0.482	0.532	0.524	−0.458	−0.415	0.535	0.511	−0.488	−0.440	0.537	0.504
033,004	−0.568	−0.522	0.491	0.471	−0.511	−0.488	0.528	0.477	−0.593	−0.554	0.519	0.481
033,005	−0.482	−0.430	0.490	0.463	−0.503	−0.445	0.509	0.473	−0.488	−0.442	0.502	0.479
033,006	−0.477	−0.423	0.533	0.525	−0.491	−0.438	0.561	0.531	−0.461	−0.425	0.556	0.526
033,007	−0.479	−0.423	0.506	0.521	−0.480	−0.426	0.535	0.515	−0.459	−0.418	0.537	0.518
033,008	−0.537	−0.493	0.552	0.537	−0.562	−0.514	0.563	0.543	−0.538	−0.506	0.559	0.524
033,009	−0.571	−0.532	0.505	0.482	−0.618	−0.568	0.511	0.494	−0.586	−0.549	0.508	0.476
033,010	−0.565	−0.524	0.494	0.471	−0.596	−0.527	0.482	0.462	−0.511	−0.461	0.499	0.458
033,011	−0.548	−0.503	0.516	0.503	−0.581	−0.511	0.496	0.482	−0.535	−0.499	0.502	0.461

Note. Bb and Ba denote the mean bias before and after assimilation, respectively. Rb and Ra denote RMSE, before and after assimilation for the experiments.

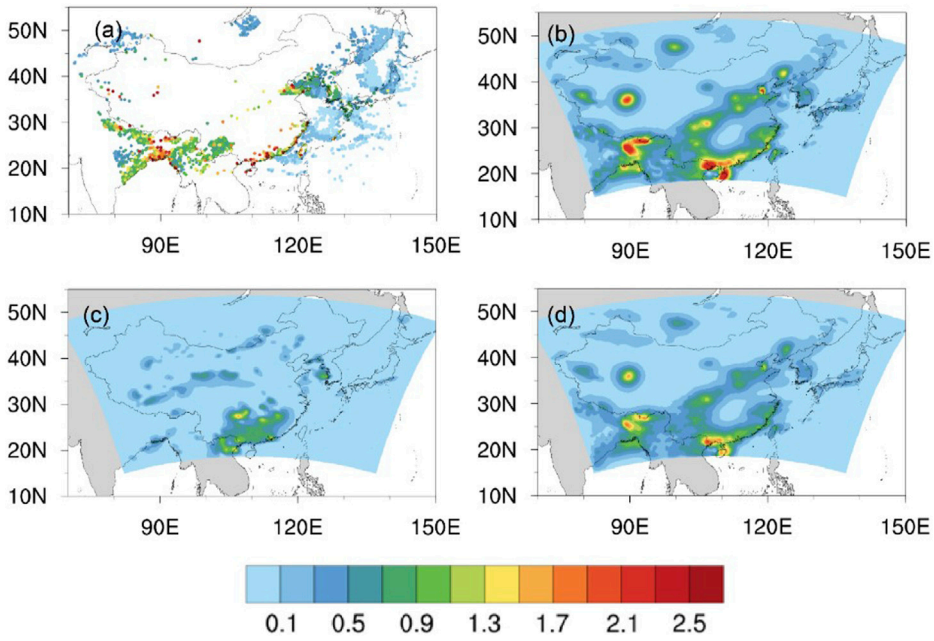

FIGURE 3
(A) Observations of 1-h DA windows from FY4; **(B)** distributions of simulated AOD based on DA background fields; **(C)** analysis fields; **(D)** 1-h forecast fields for the FY DA system, valid at 0600 UTC 26 March 2018.

(Figures 2A, C, E) and RMSE (Figures 2B, D, E) of the simulation of AOD compared to the satellite observations in the FY (Figures 2A, B), Hima (Figures 2C, D), and FY + Hima DA systems (Figures 2E, F) over 26–30 March 2018. These statistics were employed to evaluate the effectiveness of the newly developed aerosol DA system. The X-axis represents the month and day in March 2018, and the Y-axis represents the value of averaged bias and RMSE. We also display the statistical analysis of the comparisons between simulation and observation AOD in the four experiments over 26–30 March 2018 in Tables 1, 2, 3, 4, and 5.

Figure 2 and Tables 1–5 show the results from the four simulations performed. In general, after assimilating AOD, the analysis results are more consistent with the observed AOD than the background; the DA system has good calibration of aerosol

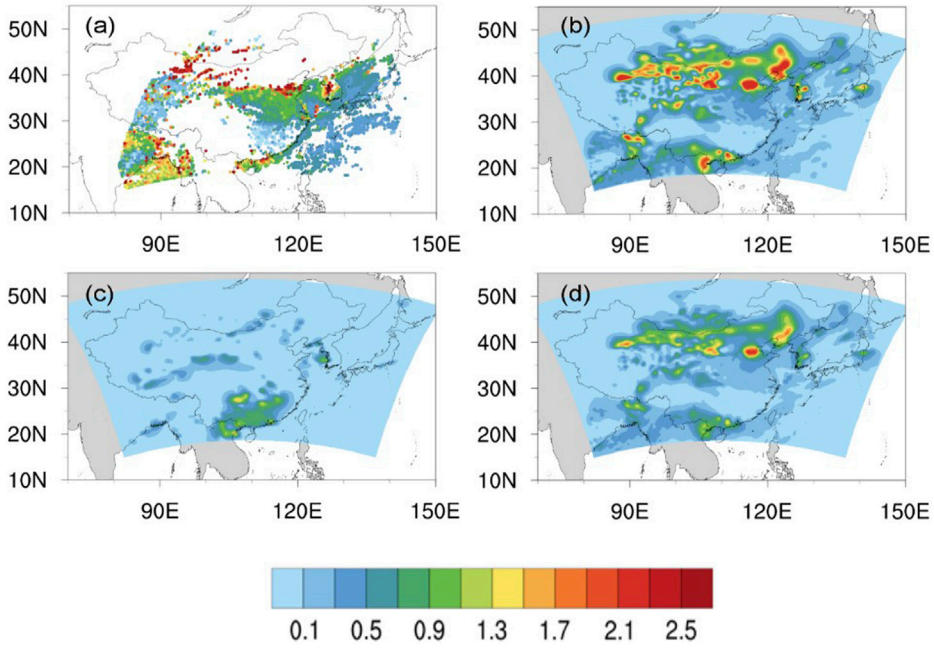

FIGURE 4
(A) Observations of 1-h DA windows from Himawari-8; **(B)** distributions of simulated AOD based on DA background fields; **(C)** analysis fields; **(D)** the 1-h forecast fields for the Hima DA system, valid at 0600 UTC 26 March 2018.

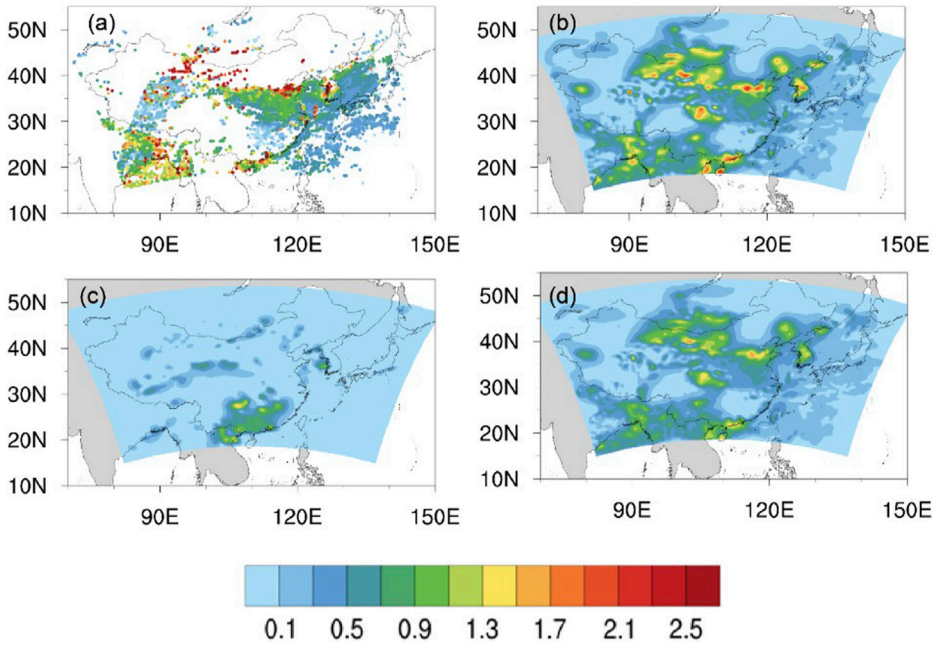

FIGURE 5
(A) Observations of 1-h DA windows; **(B)** distributions of simulated AOD based on DA background fields; **(C)** analysis fields; **(D)** 1-h forecast fields for the FY+Hima DA system, valid at 0600 UTC 26 March 2018.

simulation, with the bias and RMSE reduced by about 20% in all three DA experiments (Hong and Lim, 2006). The CNT experiment did not perform very well, and the AOD was underpredicted (biases of −0.4 to −0.6). After AOD DA, the model low bias and RMSE were dramatically reduced to near −0.1 and 0.2, respectively, indicating that the assimilation of the AOD observations is beneficial for

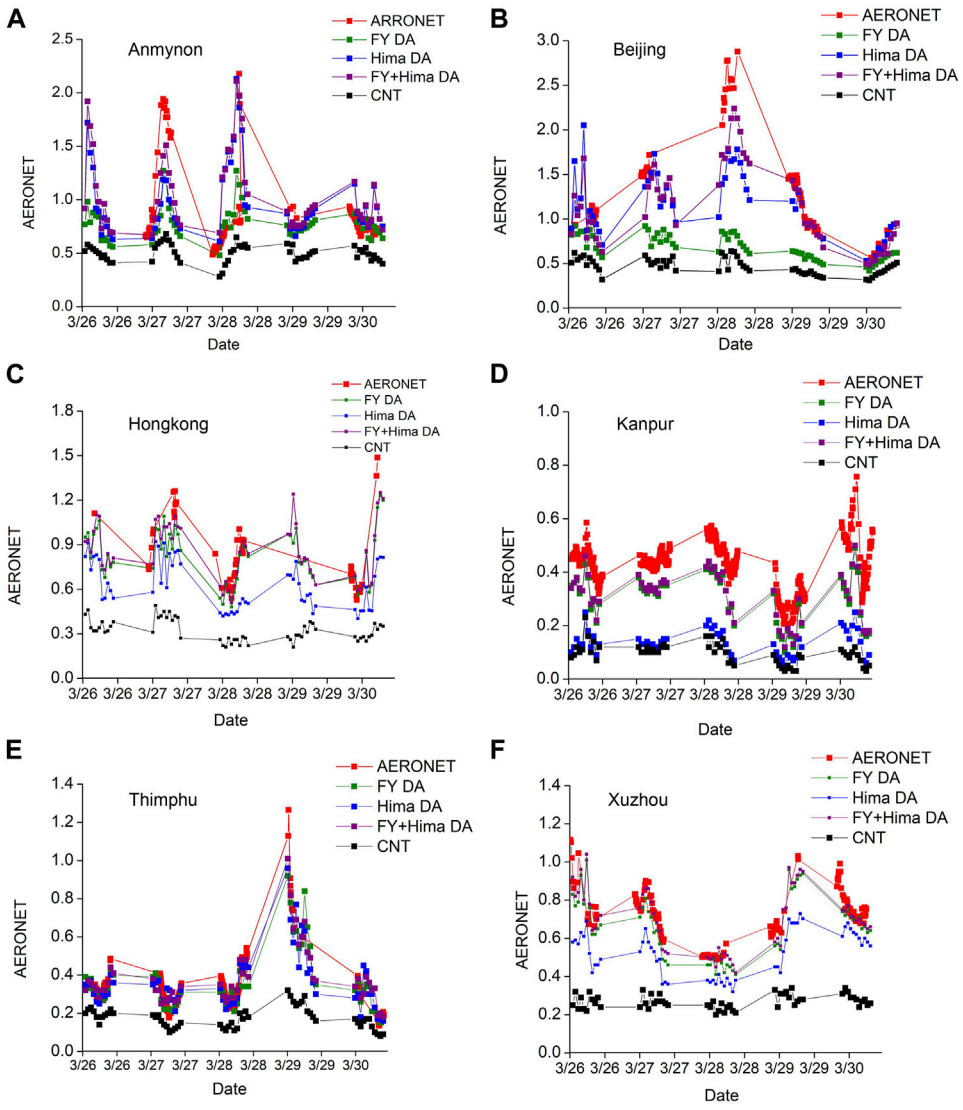

FIGURE 6
Comparisons between AERONET retrievals and modeled results in the four experiments 26–30 March 2018 at the AERONET sites of **(A)** Anmyon, **(B)** Beijing, **(C)** Hong_Kong, **(D)** Kanpur, **(E)** Thimphu, **(F)** Xuzhou, and **(G)** Xitun.

adjusting the background field. It is interesting that the assimilation employing both FY-4 and Himawari-8 reduced more than the other three DA experiments. This may mainly be because more abundant observation information on the dust storm was involved, so the assimilation analysis field was better adjusted to the background field.

The analysis and forecast impacts were then separately compared with the assimilated FY-4 and Himawari-8 AODs, which can directly show the effects of different satellite aerosol data assimilation on model simulation results (Benedetti et al., 2009). In the FY4 DA experiment (Figure 3), the CNT experiment (Figure 3C) failed to simulate the pollution, whereas the DA analysis field successfully presented the pollution over southern China (Figure 3B); however, very few adjustments were provided around Beijing and northeast China—particularly due to a lack of observations. The CNT experiment captured the main features of the dust storm in southeastern China, but the value was greatly underestimated, and then, the DA analysis reduced the underestimation of the aerosol loadings. The results in AOD derived from the Himawari-8 data assimilation system are displayed in Figure 4. Like Figure 3, Himawari-8 AOD data assimilation improved the low bias, and the analysis field was more consistent with the observed AOD distribution than the background field, which also verified the assimilation impact. Furthermore, the analysis fields presented a more abundant dust storm over Inner Mongolia and northeast China. However, little dust information was provided for northwest China due to a lack of observation data. The AOD derived from FY-4 and Himawari-8 were then included in the last aerosol data assimilation. As shown in Figure 5, the simulation of the dust storm in the CNT experiment was inadequate and the

DA simulation improved the AOD values, which were much closer to the satellite observations. The analysis field contained many details of the dust storm system, and the addition of observation data strengthened the distribution of large AOD values in Beijing, Inner Mongolia, and the northeast China region, and especially in northwest China, can make up for the underestimation of CNT.

In general, the results suggest that the newly rapid-update aerosol data assimilation system which assimilates both the FY-4 and Himawari-8 aerosol observations in this study can significantly improve the forecast field, especially in northwest China where Himawari-8 has little data coverage. Data assimilation complemented related aerosol information, which is more conducive to accurately describing the formation and development process of pollution events.

4.2 Comparison with AERONET AOD

AERONET is an aerosol monitoring network of hundreds of solar photometers around the world, organized by the US National Aeronautics and Space Administration (NASA) and France's National Center for Scientific Research (CNRS) (Holben et al., 1998). The ground AOD data obtained from AERONET were used to assess the impact of the assimilation results. This plays an important role in the study of global and regional aerosol optical properties, environmental and radiation effects, validation and evaluation of satellite remote sensing, and numerical model products (Schutgens et al., 2012). In this section, AOD data retrieved by six AERONET sites (See Figure 1) that were affected by the dust storm were selected for comparison with the analysis fields in the four experiments. As shown in Figure 6, the dust storm from 26 March to 30 March 2018 was detected by AERONET at the Anmyon, Beijing, Hong_Kong, Kanpur, Thimphu, and Xuzhou sites. In general, AOD values were underestimated in the control experiment (black line), the data assimilation greatly adjusted the aerosol analysis field, and the intensity is more consistent with AERONET stations. At all sites, the improved effect of the AOD values in the analysis was obvious after assimilating, and the overall variation trend of AOD prediction is more consistent with the ground AERONET data (Figures 6A, C, E, F). However, at the Beijing site (Figure 6B), DA experiments sometimes led to underpredictions, such as on 28 March. Moreover, at the Kanpur site (Figure 6D), where observations were insufficient, all DA experiments always underestimated the AOD values. At the Anmyon and Beijing sites, the Hima DA experiment (blue line) was more prominent, in which the simulated AOD values were closer to AERONET observations than the FY-4 DA experiment (green line). The FY-4 DA experiment performed better than the Hima DA experiment over the Hong Kong and Kanpur sites, likely because of the different coverage of satellite observations. It is interesting to point out that the analysis results in the assimilation experiment involving FY4 and Himawari-8 can better reflect the variation trend of AOD in the dust storm. The AOD values from the FY + Hima DA experiment (purple line) usually performed better than observations in the other three experiments. During the middle of the dust storm period, AOD values at the Beijing and Thimphu sites did not capture the extreme event even with AOD DA, when the air pollution reached a high level and the observed AOD value exceeded 1.0. In general, the assimilation achieved improvements at all six sites and the results showed that aerosol data assimilation could significantly improve the accuracy of forecasting dust storm events.

5 Summary and discussion

This study used a GSI-3DVAR data assimilation system to assimilate the hourly FY-4 and Himawari-8 AOD data. A dust storm in March 2018 was selected as an application to access the impact of the DA system. Three parallel experiments assimilated AOD from FY-4, Himawari-8, both FY-4 and Himawari-8, and a control experiment that did not employ DA. The results of analysis and forecasting were evaluated against AOD observations from FY-4, the Himawari-8 satellite, and the AERONET. In general, the experiment without data assimilation always underestimated the AOD values during the dust storm. All forms of DA experiments improved a low bias, and the RMSE was reduced by approximately 20%. Assimilation of satellite AOD data improved the initial field of the model obviously when compared with the control experiment and had an especially positive effect on the analysis and forecast fields. It is interesting to note that the assimilation employing both FY-4 and Himawari-8 provided the analysis field with more abundant aerosol observation information and a more accurate description of the model's initial field and had much better consistency with satellite observations than the other experiments. The comparison with AOD retrieved from AERONET also proved the ability of the newly developed data assimilation system to improve aerosol prediction.

These results show the potential improvement of air quality prediction systems through the assimilation of FY-4 and Himawari-8 AOD data, which indicates that the new generation geostationary meteorological satellites have the potential to greatly contribute to air quality forecasting. Further improvements could be made in the future by employing more advanced DA techniques and more accurate estimations of emissions. These will be further investigated in our future work.

Data availability statement

The original contributions presented in the study are included in the article/Supplementary material; further inquiries can be directed to the corresponding author.

Author contributions

Conceptualization, XX; Data curation, JM; Formal analysis, XX and JM; Investigation, XX; Methodology, XX; Project administration, JM; Resources, JM; Writing—original draft, XX; Writing—review and editing, SS; Review and Funding acquisition, XC. All authors have read and agreed to the published version of the manuscript.

Funding

This research was primarily funded by Jiangsu Funding Program for Excellent and Postdoctoral Talent and Open Research Fund of Jiangsu Province Key Laboratory of Environmental Engineering (ZZ2020003). Shandong Natural Science Foundation (ZR2021QD154).

Acknowledgments

The authors would like to thank the National Satellite Meteorological Center for sharing FY4A aerosol data. They also thank the reviewers for the constructive comments and suggestions that significantly improved our manuscript.

Conflict of interest

The authors declare that the research was conducted in the absence of any commercial or financial relationships that could be construed as a potential conflict of interest.

Publisher's note

All claims expressed in this article are solely those of the authors and do not necessarily represent those of their affiliated organizations, or those of the publisher, the editors, and the reviewers. Any product that may be evaluated in this article, or claim that may be made by its manufacturer, is not guaranteed or endorsed by the publisher.

References

Benedetti, A., Morcrette, J. J., Boucher, O., Dethof, A., Engelen, R. J., Fisher, M., et al. (2009). Aerosol analysis and forecast in the European centre for medium-range weather forecasts integrated forecast system: 2. Data assimilation. *J. Geophys. Res.* 114, D13205. doi:10.1029/2008jd011115

Bessho, K., Date, K., Hayashi, M., Ikeda, A., Imai, T., Inoue, H., et al. (2016). An introduction to himawari-8/9— Japan’s new-generation geostationary meteorological satellites. *J. Meteorological Soc. Jpn. Ser. II.* 94 (2), 151–183. doi:10.2151/jmsj.2016-009

Chen, L., Shi, M. S., Gao, S., Li, S. H., Mao, J., Zhang, H., et al. (2017). Assessment of population exposure to PM2.5 for mortality in China and its public health benefit based on BenMAP. *Environ. Pollut.* 221, 311–317. doi:10.1016/j.envpol.2016.11.080

Chin, M., Ginoux, P., Kinne, S., Torres, O., Holben, B. N., Duncan, B. N., et al. (2002). Tropospheric aerosol optical thickness from the GOCART model and comparisons with satellite and sun photometer measurements. *J. Atmos. Sci.* 59, 461–483. doi:10.1175/1520-0469(2002)059<0461:taotft>2.0.co;2

Chin, M., Rood, R. B., Lin, S. J., Muller, J. F., and Thompson, A. M. (2000). Atmospheric sulfur cycle simulated in the global model GOCART: Model description and global properties. *J. Geophys. Res.* 105, 24671. doi:10.1029/2000jd900384

Dai, T., Cheng, Y., Suzuki, K., Goto, D., Kikuchi, M., Schutgens, N. A. J., et al. (2019). Hourly aerosol assimilation of himawari-8 AOT using the four-dimensional local ensemble transform kalman filter. *J. Adv. Model. Earth Syst.* 11, 680–711. doi:10.1029/2018ms001475

Dudhia, J. (1989). Numerical study of convection observed during the Winter Monsoon Experiment using a mesoscale two–dimensional model. *J. Atmos. Sci.* 46, 3077–3107. doi:10.1175/1520-0469(1989)046<3077:nsocod>2.0.co;2

Ginoux, P., Chin, M., Tegen, I., Prospero, J., Holben, B., Dubovik, O., et al. (2001). Sources and distributions of dust aerosols simulated with the GOCART model. *J. Geophys. Res.* 106 (225–20), 20255–20273. doi:10.1029/2000jd000053

Goodman, S. J., Gurka, J., DeMaria, M., Schmit, T. J., Mostek, A., Jedlovec, G., et al. (2012). The GOES-R proving ground: Accelerating user readiness for the next-generation geostationary environmental satellite system. *Bull. Am. Meteorological Soc.* 93 (7), 1029–1040. doi:10.1175/bams-d-11-00175.1

Greenwald, T. J., Pierce, R. B., Schaack, T., Otkin, J., Rogal, M., Bah, K., et al. (2016). Real-time simulation of the GOES-R ABI for user readiness and product evaluation. *Bull. Amer. Meteor. Soc.* 97, 245–261. doi:10.1175/bams-d-14-00007.1

Hansen, J., Sato, M., and Ruedy, R. (1997). Radiative forcing and climate response. *J. Geophys. Res. Atmos.* 102, 6831–6864. doi:10.1029/96jd03436

Holben, B. N., Eck, T. F., Slutsker, I., Tanré, D., Buis, J. P., Setzer, A., et al. (1998). AERONET—a federated instrument network and data archive for aerosol characterization. *Remote Sens. Remote Sens. Environ.* 66, 1–16. doi:10.1016/s0034-4257(98)00031-5

Hong, S. Y., and Lim, J. (2006). The WRF single-moment 6-class microphysics scheme (WSM6). *J. Korean Meteor. Soc.*, 42, 129–151.

Houtekamer, P. L., Mitchell, H. L., Pellerin, G., Buehner, M., Charron, M., Spacek, L., et al. (2005). Atmospheric data assimilation with an ensemble kalman filter: Results with real observations. *Mon. Weather Rev.* 133, 604–620. doi:10.1175/mwr-2864.1

Ide, K., Courtier, P., Ghil, M., and Lorenc, A. (1997). Unified notation for data assimilation: Operational, sequential and variational (gtSpecial IssueltData assimilation in meteology and oceanography: Theory and practice). *J. Meteorol. Soc. Jpn.* 75, 181–189. doi:10.2151/jmsj1965.75.1b_181

Kikuchi, M., Murakami, H., Suzuki, K., Nagao, T. M., and Higurashi, A. (2018). Improved hourly estimates of aerosol optical thickness using spatiotemporal variability derived from Himawari-8 geostationary satellite. *IEEE Trans. Geoscience Remote Sens.* 56 (6), 3442–3455. doi:10.1109/tgrs.2018.2800060

Kleist, D. T., Parrish, D. F., Derber, J. C., Treadon, R., Wu, W. S., and Lord, S. (2009). Introduction of the GSI into the NCEP global data assimilation system. *Weather Forecast* 24, 1691–1705. doi:10.1175/2009waf2222201.1

Koren, I., Kaufman, Y. J., Remer, L. A., and Martins, J. V. (2004). Measurement of the effect of Amazon smoke on inhibition of cloud formation. *Science* 303, 1342. doi:10.1126/science.1089424

Lee, S., Song, C. H., Park, R. S., Park, M. E., Han, K. M., Kim, J., et al. (2016). GIST-PM-Asia v1: Development of a numerical system to improve particulate matter forecasts in South Korea using geostationary satellite-retrieved aerosol optical data over Northeast Asia. *Geosci. Model Dev.* 9 (1), 17–39. doi:10.5194/gmd-9-17-2016

Li, X., and Zou, X. (2017). Bias characterization of CrIS radiances at 399 selected channels with respect to NWP model simulations. *Atmos. Res.* 196, 164–181. doi:10.1016/j.atmosres.2017.06.007

Liu, H., Liu, S., Xue, B., Lv, Z. F., Meng, Z. H., Yang, X. F., et al. (2018). Ground-level ozone pollution and its health impacts in China. *Atmos. Environ.* 173, 223–230. doi:10.1016/j.atmosenv.2017.11.014

Liu, Z., Lin, H. C., Schwartz, C. S., Lee, Y. H., and Wang, T. (2011). Three-dimensional variational assimilation of MODIS aerosol optical depth: Implementation and application to a dust storm over East Asia. *J. Geophys. Res.* 116, D23206. doi:10.1029/2011jd016159

Lorenc, A. C. (1986). Analysis methods for numerical weather prediction. *Q. J. R. Meteorol. Soc.* 112, 1177–1194. doi:10.1002/qj.49711247414

Lorenc, A. C., Ballard, S. P., Bell, R. S., Ingleby, N. B., Andrews, P., Barke, D., et al. (2000). The Met. Office global three-dimensional variational data assimilation scheme. *Q. J. R. Meteorol. Soc.* 126, 2991–3012. doi:10.1002/qj.49712657002

Min, M., Wu, C. Q., Li, C., Liu, X., Xu, N., Wu, X., et al. (2017). Developing the science product algorithm testbed for Chinese next-generation geostationary meteorological satellites: Fengyun-4 series. *J. Meteor. Res.* 31, 708–719. doi:10.1007/s13351-017-6161-z

Mlawer, E. J., Taubman, S. J., Brown, P. D., Iacono, M. J., and Clough, S. A. (1997). Radiative transfer for inhomogeneous atmospheres: RRTM, a validated correlated–k model for the longwave. *J. Geophys. Res.* 102, 16663–16682. doi:10.1029/97jd00237

Niu, T., Gong, S. L., Zhu, G. F., Liu, H. L., Hu, X. Q., Zhou, C. H., et al. (2008). Data assimilation of dust aerosol observations for the CUACE/dust forecasting system. *Atmos. Chem. Phys.* 8, 3473–3482. doi:10.5194/acp-8-3473-2008

Pagowski, M., Grell, G. A., McKeen, S. A., Peckham, S. E., and Devenyi, D. (2010). Three-dimensional variational data assimilation of ozone and fine particulate matter observations: Some results using the weather research and forecasting-chemistry model and grid-point statistical interpolation. *Q. J. R. Meteorol. Soc.* 136, 2013–2024. doi:10.1002/qj.700

Pang, J., Liu, Z., Wang, X., Bresch, J., Ban, J., Chen, D., et al. (2018). Assimilating AOD retrievals from GOCI and VIIRS to forecast surface PM2.5 episodes over Eastern China. *Atmos. Environ.* 179, 288–304. doi:10.1016/j.atmosenv.2018.02.011

Parrish, D. F., and Derber, J. C. (1992). The National Meteorological Center's spectral statistical interpolation analysis system. *Mon. Weather Rev.* 120, 1747–1763. doi:10.1175/1520-0493(1992)120<1747:tnmcss>2.0.co;2

Peng, Z., Lei, L., Liu, Z., Sun, J., Ding, A., Ban, J., et al. (2018). The impact of multi-species surface chemical observation assimilation on 552 air quality forecasts in China, *Atmos. Chem. Phys.* 18, 17387. doi:10.5194/acp-18-17387-2018

Rosenfeld, D., Lohmann, U., Raga, G. B., O'Dowd, C. D., Kulmala, M., Fuzzi, S., et al. (2008). Andreae, M.O. Flood or drought: How do aerosols affect precipitation? *Science* 321, 1309–1313. doi:10.1126/science.1160606

Saide, P. E., Kim, J., Song, C. H., Choi, M., Cheng, Y., and Carmichael, G. R. (2014). Assimilation of next generation geostationary aerosol optical depth retrievals to improve air quality simulations. *Geophys. Res. Lett.* 41, 9188–9196. doi:10.1002/2014gl062089

Schmit, T. J., Li, J., Li, J., Feltz, W. F., Gurka, J. J., Goldberg, M. D., et al. (2008). The GOES-R Advanced Baseline Imager and the continuation of current sounder products. *J. Appl. Meteorology Climatol.* 47 (10), 2696–2711. doi:10.1175/2008jamc1858.1

Schutgens, N., Nakata, M., and Nakajima, T. (2012). Estimating aerosol emissions by assimilating remote sensing observations into a global transport model. *Remote Sens.* 4 (11), 3528–3543. doi:10.3390/rs4113528

Schwartz, C. S., Liu, Z., Lin, H. C., and McKeen, S. A. (2012). Simultaneous three-dimensional variational assimilation of surface fine particulate matter and MODIS aerosol optical depth. *J. Geophys. Res.* 117, D13202. doi:10.1029/2011jd017383

Shen, F., and Min, J. (2015). Assimilating AMSU-a radiance data with the WRF hybrid En3DVAR system for track predictions of Typhoon Megi (2010). *Adv. Atmos. Sci.* 32 (9), 1231–1243. doi:10.1007/s00376-014-4239-4

Shen, F., Song, L., Li, H., He, Z., and Xu, D. (2022). Effects of different momentum control variables in radar data assimilation on the analysis and forecast of strong convective systems under the background of northeast cold vortex. *Atmos. Res.* 280, 106415. doi:10.1016/j.atmosres.2022.106415

Sicard, P., Anav, A., Marco, A. D., and Paoletti, E. (2017). Projected global ground-level ozone impacts on vegetation under different emission and climate scenarios. *Atmos. Chem. Phys.* 17, 12177–12196. doi:10.5194/acp-17-12177-2017

Stengel, M., Undén, P., Lindskog, M., Dahlgren, P., Gustafsson, N., and Bennartz, R. (2009). Assimilation of SEVIRI infrared radiances with HIRLAM 4D-Var. *Q. J. R. Meteorological Soc.* 135 (645), 2100–2109. doi:10.1002/qj.501

Stuhlmann, R., Rodriguez, A., Tjemkes, S., Grandell, J., Arriaga, A., Bezy, J. L., et al. (2005). Plans for EUMETSAT's Third Generation Meteosat geostationary satellite programme. *Adv. Space Res.* 36, 975–981. doi:10.1016/j.asr.2005.03.091

Tie, X. X., Wu, D., and Brasseur, G. (2009). Lung cancer mortality and exposure to atmospheric aerosol particles in Guangzhou, China. *Atmos. Environ.* 43 (14), 2375–2377. doi:10.1016/j.atmosenv.2009.01.036

Wang, J., Nair, U. S., and Christopher, S. A. (2004). GOES-8 aerosol optical thickness assimilation in a mesoscale model: Online integration of aerosol radiative effects. *J. Geophys. Res.* 109, D23203. doi:10.1029/2004jd004827

Wang, J., Xu, X., Henze, D. K., Zeng, J., Ji, Q., Tsay, S., et al. (2012). Top-down estimate of dust emissions through integration of MODIS and MISR aerosol retrievals with the GEOS-Chem adjoint model. *Geophys. Res. Lett.* 39 (8), 8802. doi:10.1029/2012gl051136

Wang, J., Xu, Y., Yang, L., Wang, Q., Yuan, J., and Wang, Y. (2020). Data assimilation of high-resolution satellite rainfall product improves rainfall simulation associated with landfalling tropical cyclones in the yangtze river delta. *Remote Sens.* 12, 276. doi:10.3390/rs12020276

Wang, T., Luo, J., Liang, J., Wang, B., Tian, W., and Chen, X. (2019). Comparisons of AGRI/FY-4A cloud fraction and cloud top pressure with MODIS/terra measurements over East Asia. *J. Meteorological Res.* 33 (4), 705–719. doi:10.1007/s13351-019-8160-8

Wang, Y. B., Liu, Z. Q., Yang, S., Min, J. Z., Chen, L. Q., Chen, Y. D., et al. (2018). Added value of assimilating himawari-8 AHI water vapor radiances on analyses and forecasts for "7.19" severe storm over north China. *J. Geophys. Res. Atmos.* 123 (7), 3374–3394. doi:10.1002/2017jd027697

Wilcox, E. M. (2012). Direct and semi-direct radiative forcing of smoke aerosols over clouds. *Atmos. Chem. Phys.* 12, 139–149. doi:10.5194/acp-12-139-2012

Wu, W. S., Parrish, D. F., and Purser, R. J. (2002). Three-dimensional variational analysis with spatially inhomogeneous covariances. *Mon. Weather Rev.* 130, 2905–2916. doi:10.1175/1520-0493(2002)130<2905:tdvaws>2.0.co;2

Xia, X. L., Min, J. Z., Shen, F. F., Wang, Y. B., and Yang, C. (2019a). Aerosol data assimilation using data from Fengyun-3A and MODIS: Application to a dust storm over East Asia in 2011. *Adv. Atmos. Sci.* 36 (1), 1–14. doi:10.1007/s00376-018-8075-9

Xia, X., Min, J., Wang, Y., Shen, F., Yang, C., and Sun, Z. (2019b). Assimilating Himawari-8 AHI aerosol observations with a rapid-update data assimilation system. *Atmos. Environ.* 215, 116866. doi:10.1016/j.atmosenv.2019.116866

Xu, D., Liu, Z., Huang, X., Min, J., and Wang, H. (2013). Impact of assimilating IASI radiance observations on forecasts of two tropical cyclones. *Meteorol. Atmos. Phys.* 122 (1–2), 1–18. doi:10.1007/s00703-013-0276-2

Xu, D., Yang, G., Wu, Z., Shen, F., Li, H., and Zhai, D. (2022). Evaluate radar data assimilation in two momentum control variables and the effect on the forecast of southwest China vortex precipitation. *Remote Sens.* 14 (14), 3460. doi:10.3390/rs14143460

Yang, J., Zhang, Z., Wei, C., Lu, F., and Guo, Q. (2017). Introducing the new generation of Chinese geostationary weather satellites, Fengyun-4. *Bull. Amer. Meteor. Soc.* 98, 1637–1658. doi:10.1175/bams-d-16-0065.1

Yoshida, M., Kikuchi, M., Nagao, T. M., Murakami, H., Nomaki, T., and Higurashi, A. (2018). Common retrieval of aerosol properties for imaging satellite sensors. *J. Meteorological Soc. Jpn.* 96B (0), 193–209. doi:10.2151/jmsj.2018-039

Yu, Y. Y., Tarpley, D., Privette, J. L., Goldberg, M., Rama Varma Raja, M., Vinnikov, K., et al. (2009). Developing algorithm for operational GOES-R land surface temperature product. *IEEE Trans. Geosci. Remote Sens.* 47, 936–951. doi:10.1109/tgrs.2008.2006180

Yumimoto, K. (2013). Impacts of geostationary satellite measurements on CO forecasting: An observing system simulation experiment with GEOS-Chem/LETKF data assimilation system. *Atmos. Environ.* 74, 123–133. doi:10.1016/j.atmosenv.2013.03.032

Yumimoto, K., Kikuchi, N. M., Sekiyama, T. T., Murakami, H., Tanaka, T. Y., Ogi, A., et al. (2016). Aerosol data assimilation using data from Himawari-8, a next-generation geostationary meteorological satellite. *Geophys. Res. Lett.* 43, 5886–5894. doi:10.1002/2016gl069298

Zhang, J. L., Reid, J. S., Westphal, D. L., Baker, N. L., and Hyer, E. J. (2008). A system for operational aerosol optical depth data assimilation over global oceans. *J. Geophys. Res.* 113, D10208. doi:10.1029/2007jd009065

Zhang, J., and Reid, J. S. (2006). MODIS aerosol product analysis for data assimilation: Assessment of over-ocean level 2 aerosol optical thickness retrievals. *J. Geophys. Res.* 111, D22207. doi:10.1029/2005jd006898

Zhang, P., Guo, Q., Chen, B. Y., and Feng, X. (2015). The Chinese next-generation geostationary meteorological satellite FY-4 compared with the Japanese himawari-8/9 satellites. *Adv. Meteorological Sci. Technol.* 6 (1), 1–2016.

Zhao, H., Zheng, Y. F., and Li, C. (2018). Spatiotemporal distribution of $PM_{2.5}$ and O_3 and their interaction during the summer and winter seasons in Beijing, China. *Sustainability* 10 (12), 4519. doi:10.3390/su10124519

Zhao, H., Zheng, Y. F., Zhang, Y. X., and Wang, Z. S. (2020). Spatiotemporal distribution and population exposure of air pollution in Beijing-Tianjin-Hebei region. *Acta Sci. Circumstantiae* 40 (1), 1–12. doi:10.13671/j.hjkxxb.2019.0237

Zhuge, X., Zou, X., and Wang, Y. (2017). A fast cloud detection algorithm applicable to monitoring and nowcasting of daytime cloud systems. *IEEE Trans. Geoscience Remote Sens.* 55 (11), 6111–6119. doi:10.1109/tgrs.2017.2720664

Zou, X., Qin, Z., and Weng, F. (2011). Improved coastal precipitation forecasts with direct assimilation of GOES-11/12 imager radiances. *Mon. Weather Rev.* 139 (12), 3711–3729. doi:10.1175/mwr-d-10-05040.1

frontiers | Frontiers in Earth Science

TYPE Original Research
PUBLISHED 06 April 2023
DOI 10.3389/feart.2023.1148921

OPEN ACCESS

EDITED BY
Feifei Shen,
Nanjing University of Information Science and Technology, China

REVIEWED BY
Jincheng Wang,
CMA Earth System Modelling Center, China
XueXing Qiu,
Anhui Provincial Meteorological Bureau, China

*CORRESPONDENCE
Erliang Lin,
linerliang@foxmail.com
Xiaobin Qiu,
QiuXiaoBin.TJ@outlook.com

SPECIALTY SECTION
This article was submitted to Environmental Informatics and Remote Sensing, a section of the journal Frontiers in Earth Science

RECEIVED 20 January 2023
ACCEPTED 21 March 2023
PUBLISHED 06 April 2023

CITATION
Song W, Lin E, Qiu X and Xue Y (2023), Comparison of different momentum control variables on assimilating radar observations for the forecasts of a dispersive convective event. *Front. Earth Sci.* 11:1148921. doi: 10.3389/feart.2023.1148921

Comparison of different momentum control variables on assimilating radar observations for the forecasts of a dispersive convective event

Wei Song[1,2,3], Erliang Lin[3,4]*, Xiaobin Qiu[1,5]* and Yuting Xue[6]

[1]Tianjin Key Laboratory for Oceanic Meteorology, Tianjin, China, [2]Tianjin Weather Modification Office, Tianjin, China, [3]Key Laboratory of Climate Resource Development and Disaster Prevention of Gansu Province, College of Atmospheric Sciences, Lanzhou University, Lanzhou, China, [4]Taiyuan Satellite Launch Center, Xinzhou, China, [5]Tianjin Institute of Meteorological Science, Tianjin, China, [6]Baotou Meteorological Bureau, Baotou, Inner Mongolia, China

In this study, the effects of background error covariance (BE) using the stream function ψ and unbalanced velocity potential χ_u as momentum control variables (CV5 scheme) and BE using the velocity U and V as momentum control variables (CV7 scheme) on assimilating radar radial velocity and reflectivity data for short-term forecasts of dispersive convection in a weak environmental field are explored based on the weather research and forecasting model (WRF) model and its 3DVAR assimilation system. The 4 km resolution forecast samples are generated to formulate the CV5 and CV7 BE by the National Meteorological Center (NMC) method. The single-observation experiments reveal that the differences between the two BE statistics are mainly reflected on the momentum control variables. The increment of wind field from CV7 shows more small-scale local characteristics. Comparing with control experiment, real radar observation assimilation tests of CV5 and CV7 both improve the reflectivity and precipitation forecasts. But the CV7 scheme improves the forecasting of strong convective systems in weak environmental fields better than CV5. First, the CV7 scheme improves both reflectivity and dispersive precipitation forecasts and significantly suppresses the spurious precipitation forecasts when compared with the CV5 scheme. In addition, CV7 also significantly reduces the forecast errors of surface variables and the wind analysis from CV7 is more local. Further analysis shows that the CV7 improves the water vapor convergence conditions compared to the CV5 scheme, which may be the reason for its better performance in the subsequent forecasts.

KEYWORDS

radar data assimilation, 3DVAR, background error covariance, momentum control variables, dispersive convection

1 Introduction

Hazardous weather induced by mesoscale convective systems such as thunderstorms, gales and rainstorms causes a serious threat to life and property. One of the main reasons why the numerical weather prediction (NWP) model performs the worst in forecasting such intense weather is its sensitivity to initial conditions (Sun, 2005). The data assimilation

technique uses available meteorological observations and NWP products (background) to estimate the optimal state of the atmosphere (Ide et al., 1997), which is the main strategy to reduce the uncertainty of the initial field and improve NWP results at present (Bouttier and Courtier, 2002). Numerous studies have shown that the assimilation of conventional observations, radar and satellite data has a positive impact on initial conditions and forecasts (Sun, 2005; Johnson et al., 2015; Gan et al., 2021; Lin et al., 2021; Eyre et al., 2022). Compared with conventional observations, radar observation has higher temporal resolution (5–10 min) and spatial resolution (250–1000 m), which can better observe meso- and small-scale weather systems and provide valuable information for convective scale data assimilation (Xiao and Sun, 2007; Wang et al., 2013; Tong et al., 2016, *etc.*).

Compared with the more advanced four-dimensional variational method (4DVAR), ensemble method or hybrid method, the three-dimensional variational method (3DVAR) is the most commonly used method for data assimilation due to its practicality in terms of computational efficiency. The 3DVAR approach seeks optimal analysis by minimizing the cost function associated with the control variables (Barker et al., 2004). The calculation of the background cost function requires statistical information on the model prediction error (Buehner, 2010; Brousseau et al., 2011). The background error covariance (BE) matrix is critical to the success of data assimilation systems because it controls the degree of influence of each observation in the analysis and how this influence is propagated spatially and across different analysis variables (Fisher, 2003). However, due to the rather large dimension of the BE matrix ($10^7 \times 10^7$), accurate determination of the BE matrix is very difficult and usually requires simplification through control variable preprocessing (Barker et al., 2012). The selection of control variables changes the entire structure of the BE matrix and thus the assimilation results (Descombes et al., 2015). Therefore, the choice of control variables greatly affects the assimilation effect of variational assimilation systems.

There are two different control variable schemes most commonly used in the variational data assimilation system of the regional NWP model: 1) the stream function (ψ) and velocity potential (χ) as momentum control variables (Wu et al., 2002) and 2) the velocity components (U, V) as momentum control variables (Gao et al., 1999). Scholars have compared two control variable schemes. Xie and MacDonald (2012) analyzed the differences between the two control variable schemes from a mathematical perspective and concluded that background fields and small-scale observations can be better combined when UV is chosen as the momentum control variable, while using $\psi\chi$ as the momentum control variable is more suitable for analyzing large-scale motion. Xu (2019) demonstrated that the choice of different momentum control variables is theoretically equivalent in the case that the error covariance function satisfies the derived relationship. Dong et al. (2022) investigated the role of two control variable schemes for assimilating conventional observation data with a 3 km resolution model. With UV control variables, 0~6-h ground forecast was improved. Sun et al. (2016) compared the effects of two sets of mome of the mesoscale horizontal wind component and reduced the variance, while the use of UV control variables could be closer to the radar wind observations, thus improving the 0–12 h precipitation forecasts. Li et al. (2016) studied the effects of two momentum control variable schemes on radar radial velocity data assimilation using a squall line process as an example and concluded that the UV control variable scheme significantly improves the quality of the initial field and is better for squall line forecasting, while the $\psi\chi$ control variable scheme generates unrealistic convergence/divergence in the analysis field, which leads to a degraded precipitation forecast. Shen et al. (2019) investigated the impacts of different momentum control variables assimilating radar radial velocity data on typhoon forecasts, and the results showed that UV as the control variable could more objectively reflect the observed wind itself. Compared with the vertical structure predicted by the $\psi\chi$ scheme, the vertical structure predicted by the UV scheme is more accurate, and the predicted reflectivity, typhoon track and intensity are improved.

These studies indicate that BE with UV as the momentum control variable is more advantageous than BE with $\psi\chi$ as the momentum control variable when assimilating observations. Nevertheless, among these studies, there are fewer radar data assimilation tests for strong convective cases, and most of them focus on organized convective systems (e.g., squall lines, typhoons). To make better use of radar observation data, it is necessary to carry out radar data assimilation tests for more types of convective cases and compare the effects of different BEs on severe convection forecasts to make the results more applicable. Based on the WRF model and its 3DVAR assimilation system, taking a dispersed convective process in a weak environmental field under the control of a subtropical anticyclone in the Jianghuai region of China on 26 July 2018 as an example, this study further evaluates the impact of the assimilation of radar radial velocity and reflectivity data by the two control variable schemes on the short-term prediction of strong convection to provide a reference for better radar data assimilation.

The remainder of this paper is organized as follows. Section 2 describes the WRF 3DVAR data assimilation method and the specific scheme of control variables in the assimilation system. The severe convective case, Doppler radar observations, model configuration and experimental design are introduced in Section 3. In Section 4, the characteristics of the two BE statistics are compared, and the impact of the two control variable schemes on the short-term prediction of severe convection is assessed. Finally, the summary and discussion are presented in Section 5.

2 Methodology

2.1 WRFDA 3DVAR assimilation method

The basic goal of the WRFDA 3DVAR system is to obtain the optimal estimate of the true atmospheric state at the analysis time by iteratively minimizing a prescribed non-linear cost function (Ide et al., 1997):

$$\begin{aligned} J(x) &= J_b(x) + J_o(x) \\ &= \frac{1}{2}\left(x - x^b\right)^T \mathbf{B}^{-1}\left(x - x^b\right) + \frac{1}{2}\left(y_o - H(x)\right)^T \mathbf{R}^{-1}\left(y_o - H(x)\right) \end{aligned} \tag{1}$$

Where $J(x)$, $J_b(x)$ and $J_o(x)$ represent the cost function, the background term and the observation term, respectively. The analysis states, background states and observation vector are denoted x, x^b and y_o. $\mathbf{B}$ and $\mathbf{R}$ are error covariance matrices for

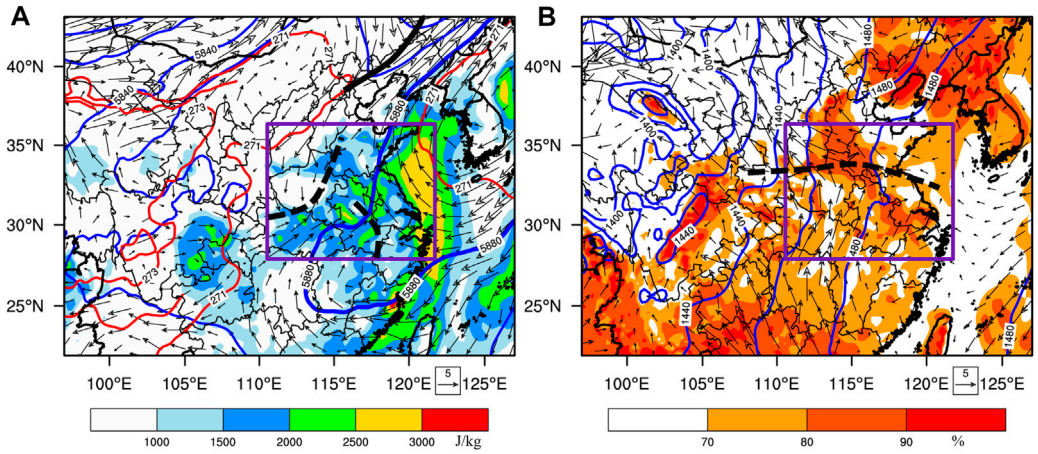

FIGURE 1
(A) Temperature (red contour; units: K), geopotential height (blue contour; units: gpm), CAPE (shaded; units: J kg^{-1}) and wind vector (arrows; units: m s^{-1}) fields at 500 hPa and **(B)** relative humidity (shaded; units: %), wind vectors (arrows; units: m s^{-1}) and geopotential height (blue contour; units: gpm) fields at 850 hPa from the Global Forecast System (GFS) analysis at 1200 UTC on 26 July 2018. The purple rectangle indicates the area of focus for severe convection case. The solid dark line represents a through line and the dashed dark line represents a convergence line. The bolded blue line in the left panel represents the extent of subtropical anticyclone.

background and observation, respectively. H is the observation operator that provides a mapping from the model's grid space to the observation space. In the data assimilation system, it is quite difficult to calculate the inverse of $\mathbf{B}$ directly due to the large dimension of $\mathbf{B}$ ($10^7 \times 10^7$). To reduce the computational cost, the matrix is simplified by using the control variable transformation method. Generally, the $\mathbf{B}$ matrix is decomposed as $\mathbf{B}=\mathbf{U}\mathbf{U}^T$, and the transformation of the control variable $x' = x - x^b = \mathbf{U}\mathbf{v}$ is commonly applied. x' and $\mathbf{v}$ represent the analysis increment vector and control variable vector, respectively. Therefore, Eq. 1 is transformed into Eq. 2:

$$J(\mathbf{v}) = \frac{1}{2}\mathbf{v}^T\mathbf{v} + \frac{1}{2}(\mathbf{d} - H'\mathbf{U}\mathbf{v})^T\mathbf{R}^{-1}(\mathbf{d} - H'\mathbf{U}\mathbf{v}) \quad (2)$$

where H' is the linearization of non-linear observation operator H in Eq. 1, and $\mathbf{d} = y_o - H(x^b)$ is the innovation vector. The transformed $\mathbf{B}$ matrix is given implicitly in the control variable operator and no longer needs to be represented directly.

2.2 Control variable schemes in the WRFDA 3DVAR assimilation system

The following two control variable schemes based on domain specificity are commonly used in the current WRFDA 3DVAR assimilation system, each containing five control variables. One of them uses the stream function (ψ) and unbalanced velocity potential (χ_u) as momentum control variables (CV5 scheme), and the other control variables include the unbalanced temperature (T_u), the unbalanced surface pressure (P_{su}) and the pseudo relative humidity (RH_s). Another option uses the velocity U and V as momentum control variables (CV7 scheme), and other control variables include full temperature (T), full surface pressure (Ps), and pseudo relative humidity (RHs).

The BE matrices for two control variable schemes were generated using the gen_be utility from the WRFDA 3DVAR system by the National Meteorological Center (NMC) method (Parrish and Derber, 1992) in this study. A dataset containing 1 month in summer of cold-start 24-h forecasts over the simulation domain was produced every day starting at 0,000 and 1200 UTC. The domain-averaged BE statistics may then be obtained by averaging these differences between the 24- and 12-h forecasts valid at the same times.

3 Case description and experimental setup

3.1 Overview of the severe convection case

From afternoon to night on 26 July 2018, severe convective weather occurred over the Jianghuai region of China. Sudden strong weather was a dispersed convective process in a weak environmental field under the control of a subtropical anticyclone, mainly caused by the joint action of weak cold air infiltrating from the rear of the Mongolian cold vortex and the stable maintained subtropical anticyclone circulation. The process was of great intensity and serious disaster, with precipitation of more than 100 mm at many stations, thunderstorms and gales more than Grade 8, hail in many districts, severe flooding, traffic jams and damage to people and goods in many cities. Figure 1A shows the temperature, geopotential height, convective available potential energy (CAPE) and wind vector fields at 500 hPa, and Figure 1B shows the relative humidity, wind vector and geopotential height fields at 850 hPa from the National Centers for Environmental Prediction (NCEP) Global Forecast System (GFS) analysis at 1200 UTC on 26 July 2018. The Jianghuai region is controlled by a subtropical anticyclone. At the upper level, there is anticyclonic circulation along its eastern

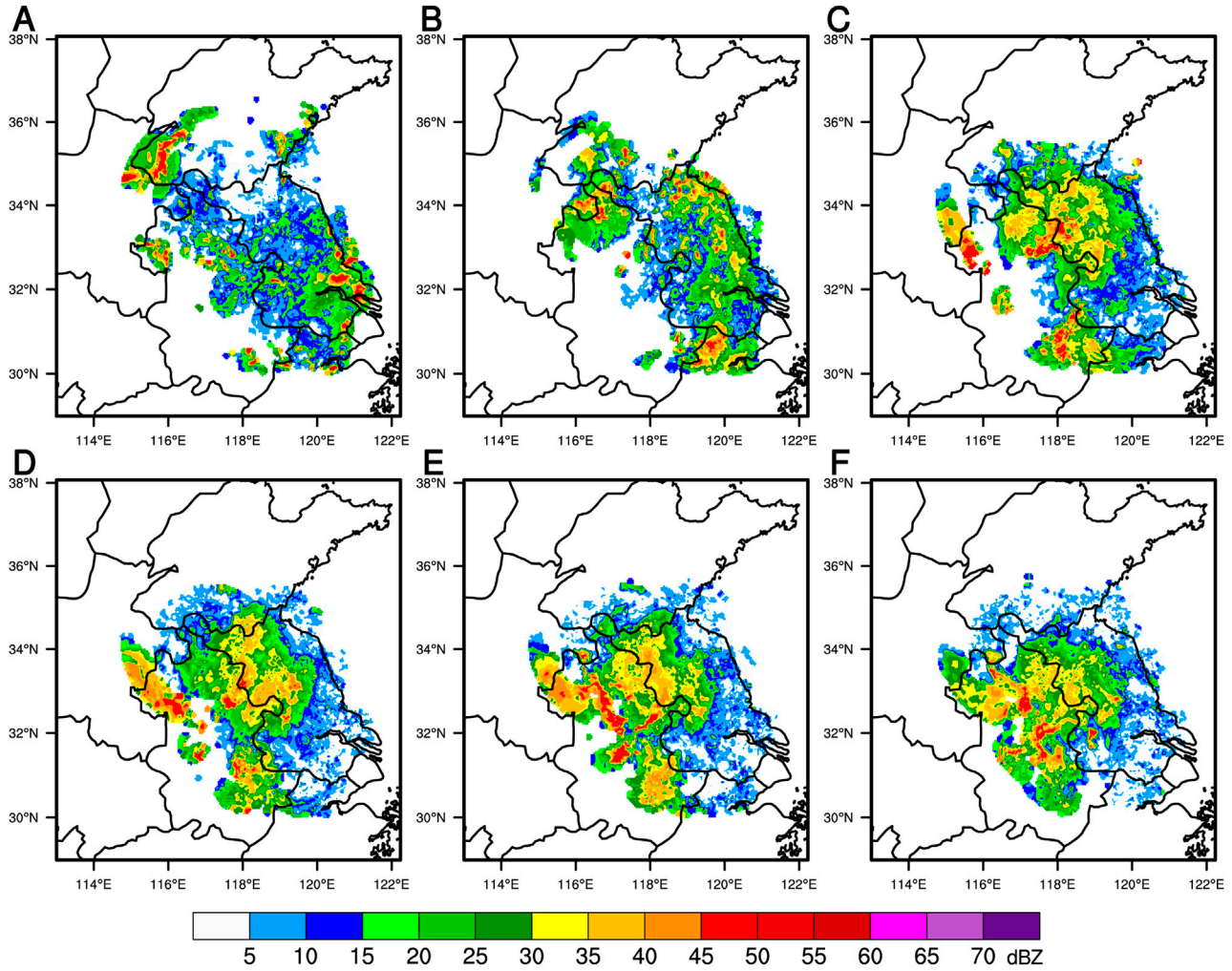

FIGURE 2
Observed radar composite reflectivity (units: dBZ) at **(A)** 0600 UTC, **(B)** 0900 UTC **(C)** 1200 UTC, **(D)** 1300 UTC **(E)** 1400 UTC, and **(F)** 1500 UTC on 26 July 2018.

coast. The cold and dry air from the northeast at the bottom of the northeast trough meets the warm and wet air from the southwest of the subtropical anticyclone in Henan and Anhui provinces. The low-level humidity is very high, with relative humidity exceeding 70%, the southerly winds and easterly southeasterly winds continue to transport water vapor, and wind shear exists in the Jianghuai region. The CAPE value in most parts of the Jianghuai region exceeds 1500 J/kg, and the atmospheric energy is sufficient. Such high- and low-altitude configurations are conducive to the formation and development of convective weather systems and the occurrence of severe convection and even hailstorms.

The radar composite reflectivity observations on 26 July 2018 are shown in Figure 2. At 0600 UTC (Figure 2A), there was dispersed convection over the Jianghuai region and strong convective cores over southeastern Jiangsu Province and southwestern Shandong Province. Then, the severe convective systems in southwestern Shandong Province gradually moved to the southeast, and those in southeastern and eastern Jiangsu Province gradually moved to the west. By 1400 UTC (Figure 2E), the severe convective systems were basically concentrated in Jiangsu and Anhui provinces, causing heavy precipitation and hail. Subsequently, the center of strong convection gradually weakened and largely dissipated by 2000 UTC. Due to the limited coverage of radar observations (8 of the 9 radars used in this study are located in Jiangsu Province, see Figure 3 for the distribution of radar sites), the complete convective weather process cannot be well presented.

3.2 Doppler radar and precipitation observations

The Doppler radar data used in this study are all obtained from nine S-band CINRAD WSR-98D radars in Jiangsu and Zhejiang provinces, the locations of which are shown in Figure 3. All radars use the VCP21 mode during operation, with one volume scan completed in approximately 6 min, consisting of nine scan elevations (0.5°, 1.5°, 2.4°, 3.3°, 4.3°, 6.0°, 9.9°, 14.6° and 19.5°). The azimuth resolution is 1°, and the gate

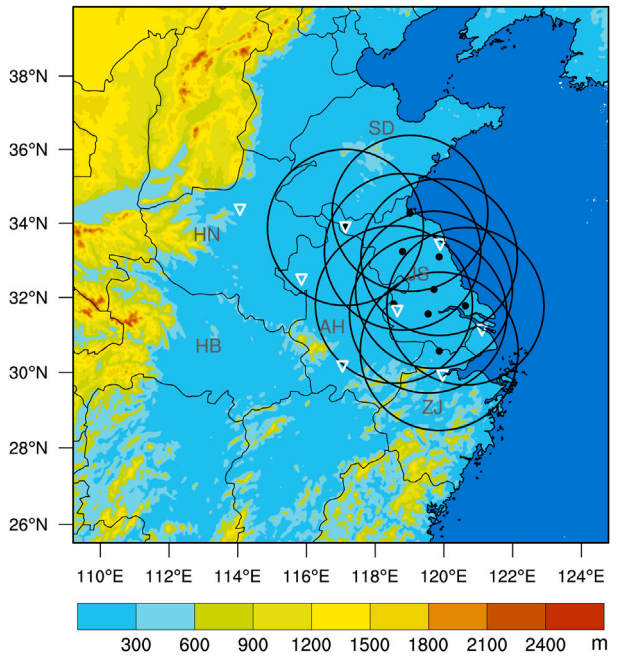

FIGURE 3
Simulation domain superposed with the terrain height (units: m) and the locations of nine radar stations (black dots). The maximum range of every radar is represented by the corresponding circle. The inverted white triangles represent the locations of sounding stations. The abbreviations for Henan, Shandong, Hubei, Anhui, Jiangsu and Zhejiang Provinces are HN, SD, HB, AH, JS and ZJ, respectively.

spacings of radial velocity and reflectivity factor are 250 m and 1,000 m, respectively. Before the radar observations are assimilated, they need to be preprocessed and quality controlled, including velocity dealiasing, removal of isolated points and removal of clutter and noise (Steiner and Smith, 2002; Kessinger et al., 2003; Zhang and Wang, 2006). Figure 4 illustrates the validity of radar data quality control. After the quality control of reflectivity data, non-meteorological echoes such as ground clutter, anomalous propagation signals are greatly suppressed. In addition, the quality controlled data need to be thinned and are spatially mapped from spherical coordinates (distance, azimuth and elevation) onto the model regular grids using a local least square fitting method (Brewster et al., 2005) prior to assimilation. The observation errors of reflectivity and radial velocity are set to 2 dBZ and 1 m s^{-1} in all the radar data assimilation experiments of this study, respectively. The precipitation observation data are obtained from the hourly precipitation grid dataset created by merging data from automatic weather stations in China and CMORPH satellite data with a spatial resolution of 0.1°×0.1°, provided by the Chinese National Meteorological Information Center (NMIC) for the evaluation of precipitation forecasting skills.

3.3 Model configuration and experimental design

The WRF model and its 3DVAR assimilation system WRFDA (version 3.9.1) are adopted in this study, and a single domain (shown in Figure 3) is applied for all simulations. The model domain has horizontal dimensions of 400×400 and grid spacings of 4 km. The integration time step of the simulation is 20 s, and the domain has 50 terrain-following eta layers from the surface to 50 hPa. The initial and boundary conditions are provided by NCEP GFS 0.25°×0.25° analysis and forecast fields at 3-h intervals. The main parameterizations used in WRF simulations include the WRF single-moment 6-class (WSM6) microphysics scheme (Hong and Lim, 2006), the Goddard shortwave radiation scheme (Chou and Suarez, 1999), the Rapid Radiative Transfer Model (RRTM) longwave radiation scheme (Mlawer et al., 1997), the Yonsei University (YSU) planetary boundary layer scheme (Hong et al., 2006) and the Noah land surface model (Ek et al., 2003). The cumulus parameterization scheme is not used due to the fine grid resolution. The two BE matrices (CV5 scheme and CV7 scheme) are calculated by the NMC method using a sample of forecasts of approximately 1 month in summer.

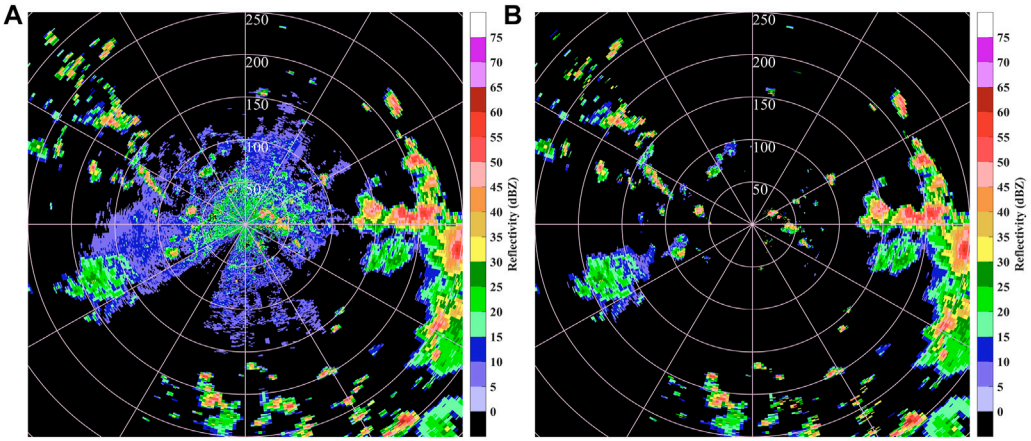

FIGURE 4
(A) Original reflectivity and **(B)** reflectivity after being quality controlled for 0.5° elevation angle at 0600 UTC on 26 July 2018 from the Nanjing radar.

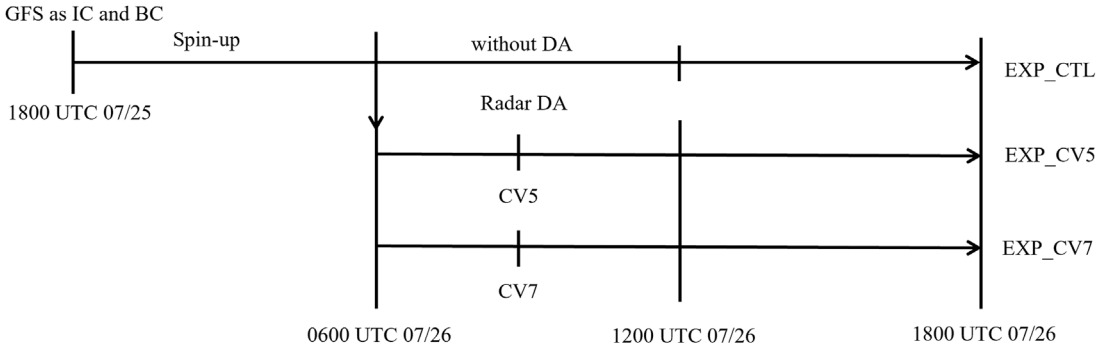

FIGURE 5
Schematic diagram of the experimental design.

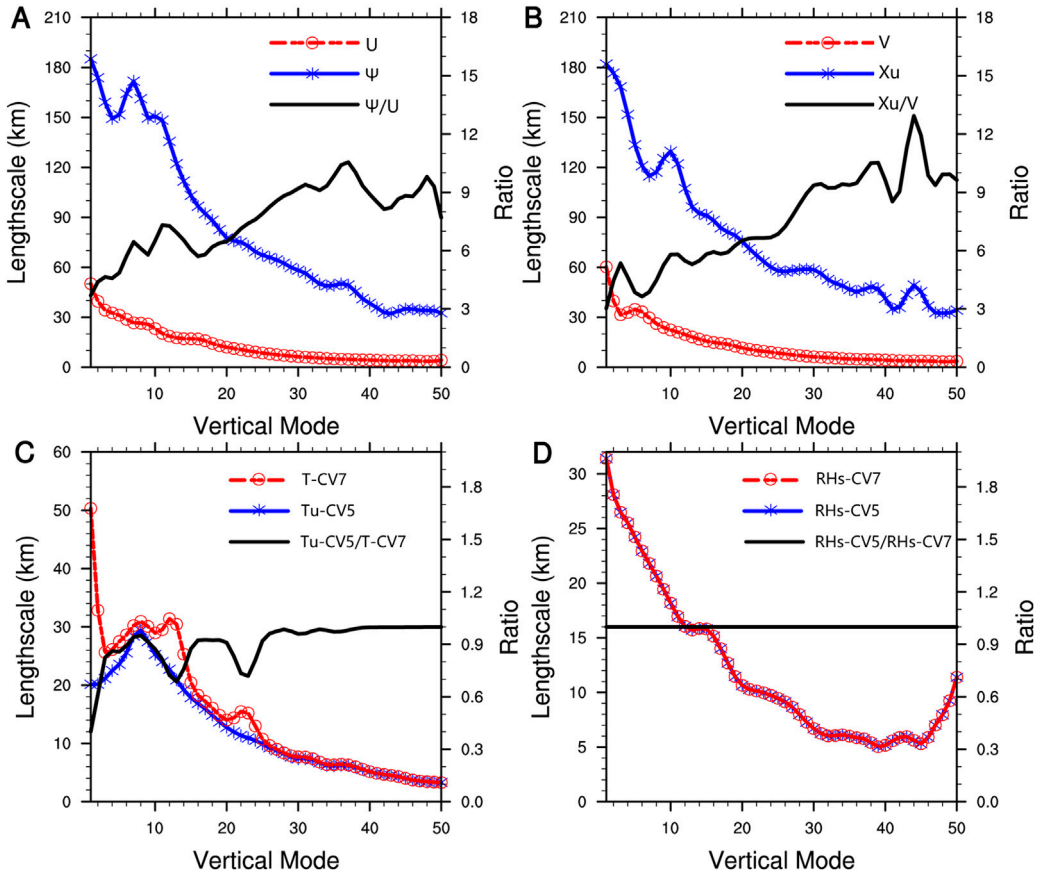

FIGURE 6
Variation of length scale with vertical mode for each variable in the CV5 and CV7 schemes: **(A)** ψ and U **(B)** χ_u and V, **(C)** Tu and T **(D)** RHs-CV5 and RHs-CV7. The blue line represents the control variable of CV5 scheme, and the red line represents the control variable of CV7 scheme. The solid black line represents the ratio of the variable length scales in the two schemes.

To investigate the effects of two BE matrices on radar data assimilation analysis and severe convection forecasting, single observation and real radar observation assimilation experiments are designed in this study. The detailed configuration of the single observation tests is described in the next section. A control experiment and two assimilation experiments are designed for real radar observation experiments (shown in Figure 5). The control experiment EXP_CTL is run 24 h from 1800 UTC 25 July 2018 to 1800 UTC on 26 July, and the initial 12 h represents the "spin-up" period of model integration. EXP_CTL does not assimilate any observations and is used to examine the effect of the assimilation experiments. Both assimilation experiments take the 12-h prediction

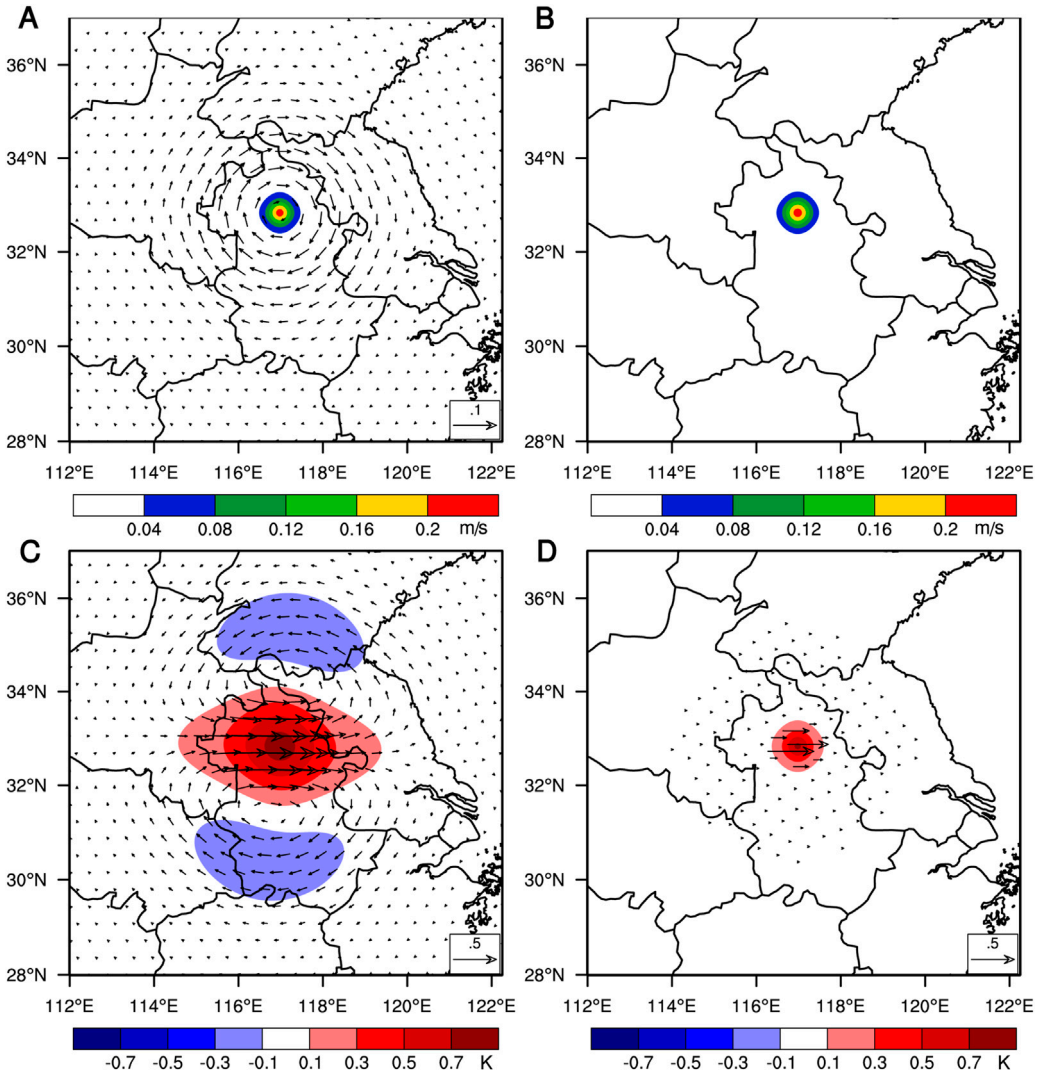

FIGURE 7
The increments of temperature (shaded; units: K) and wind field (vector; units: m s^{-1}) with a single temperature observation at the 11th model level: **(A)** CV5 scheme **(B)** CV7 scheme. The increments of U-wind (shaded; units: m s^{-1}) and wind field (vector; units: m s^{-1}) with a single westward wind observation at the 11th model level: **(C)** CV5 scheme **(D)** CV7 scheme.

field of the control experiment as the background field of the first assimilation. EXP_CV5 and EXP_CV7 assimilate radar observations (both reflectivity and radial velocity) every 3 h from 0600 UTC to 1200 UTC, taking the analysis field assimilated at 1200 UTC as the initial field and integrating forward for 6 h. The difference is that the former uses the BE matrix of the CV5 scheme for assimilation, while the latter uses the BE matrix of the CV7 scheme for assimilation. Current studies generally agree that the BE matrix obtained statistically using the NMC method overestimates the characteristic length scale (Liu et al., 2005; Li et al., 2012; Sun et al., 2016; Stanesic et al., 2019; Thiruvengadam et al., 2020). Therefore, in the two assimilation experiments, the length scales are reduced to half of the default value, which are set to 0.5. The radial velocity observations are assimilated directly using the assimilation scheme described by Xiao et al. (2005). For the reflectivity data, the indirect assimilation scheme introduced by Wang et al. (2013) is used to assimilate retrieved rainwater and water vapor within the cloud estimated from reflectivity. In addition, the snow and graupel mixing ratios retrieved from reflectivity data are assimilated using the relationships presented by Gao and Stensrud (2012).

4 Results

4.1 Comparison of the BE statistics

The characteristic length scale represents the range of influence of background error, and the characteristic length scales of BE in the two control variable schemes are first compared below. Since the control variables are derived based on the assumption of uniformity and isotropy, their length scales vary only with height (Barker et al., 2004). Figure 6 shows the variation of characteristic length scales of

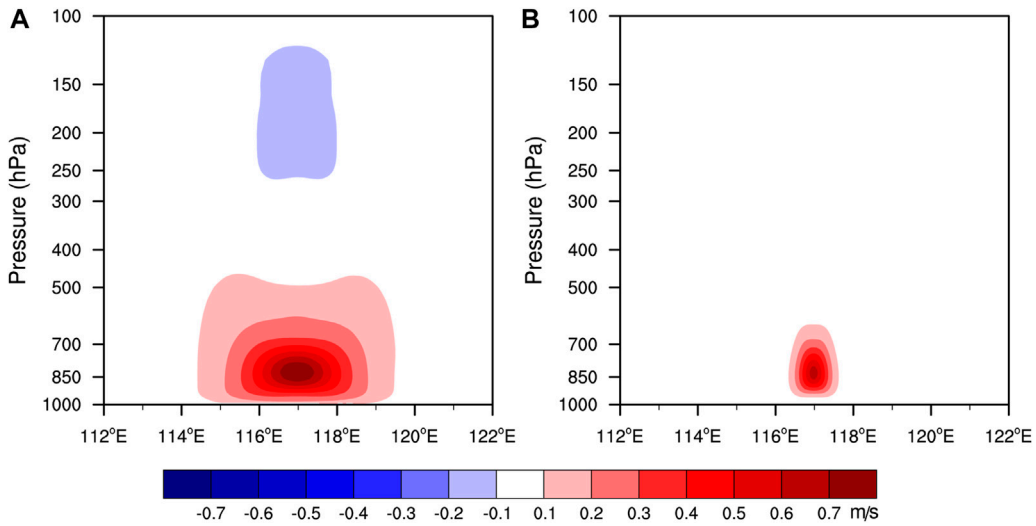

FIGURE 8
Vertical profile of U-wind analysis increments (units: m s^{-1}) along 33°N in the single westward wind observation test: **(A)** CV5 scheme **(B)** CV7 scheme.

two groups of control variables with vertical modes. As seen from Figures 6A,B, the length scales of U and V are significantly smaller than those of ψ and χ_u. The length scales of the first modes of U and V are approximately 60 km, while the corresponding length scales of ψ and χ_u are over 180 km. The solid black line in the figure indicates the ratio of the length scales of the two variables. These two ratios increase gradually with increasing wavenumber, indicating that ψ and χ_u lead to larger length scales for small-scale features of the atmosphere compared to U and V. The characteristic length scale difference of temperature is mainly reflected in the first 25 modes. The length scale of the temperature in the CV7 scheme is slightly larger than that of the unbalanced temperature in the CV5 scheme (Figure 6C). The characteristic length scales of relative humidity are identical in both schemes, with a maximum value of approximately 32 km (Figure 6D). The above comparison shows that the difference in characteristic length scales between the two groups of control variables is mainly reflected in the differences between the variables U and ψ, V and χ_u. The BE generated using the CV7 scheme has a smaller length scale for its momentum control variables, which is consistent with the findings of Sun et al. (2016).

4.2 Single observation tests

To verify the rationality of statistical BEs and more intuitively compare the differences between the two control variable schemes, assimilation tests of single observations are conducted before the assimilation experiments of real radar observations. Using the forecast field of experiment EXP_CTL at 0600 UTC on 26 July 2018 as the background field, a single temperature and westward wind observation are added at the center of the model domain (33°N, 117°E) at the 11th level of the model (approximately 850 hPa). The innovations of the perturbation point (observation-background) are set to 1 K and 1 m/s, and the observation errors are set to 1 K and 1 m/s, respectively.

Figures 7A,B show the analysis increments of temperature and horizontal wind at the 11th model level after assimilating single temperature observations using the CV5 and CV7 schemes, respectively. The temperature increments produced by the two experiments are basically the same, uniform and isotropic. The increment is the largest near the observation location and gradually decreases from the inside out, indicating that there is little difference in the assimilation of temperature between the two BEs. Note that the CV5 scheme generates circular anticyclonic wind field increments near the observation location because the correlation between the variables ψ and temperature is considered in the CV5 scheme, so wind field increments are generated, but the incremental values are very small. The CV7 scheme does not consider the correlation between control variables, so the temperature perturbation will not produce the wind increment.

Figures 7C,D display the analysis increments of U-wind and horizontal wind at the 11th model level after assimilating single westward wind observations using the CV5 and CV7 schemes, respectively. It is easy to find that wind field increments vary greatly between different control variable schemes. The propagation of the positive increment region of the U-wind generated by the CV5 scheme is much larger than that of the CV7 scheme on the horizontal scale because the two have different characteristic length scales. The CV5 scheme generates anticyclonic and cyclonic wind field increments on the north and south sides of the large value area of westerly wind increments, respectively, and produces negative incremental regions of U-wind on both the north and south sides, which has non-physical significance. These negative increments will lead to unrealistic local divergence and convergence if the radial velocity observations are assimilated with the CV5 scheme. In contrast, the CV7 scheme is able to more objectively reflect the observed winds themselves. Since the CV5 scheme considers the correlation of the control variables, the perturbation westward wind variable produces increments of V-wind in the analyzed field, but the

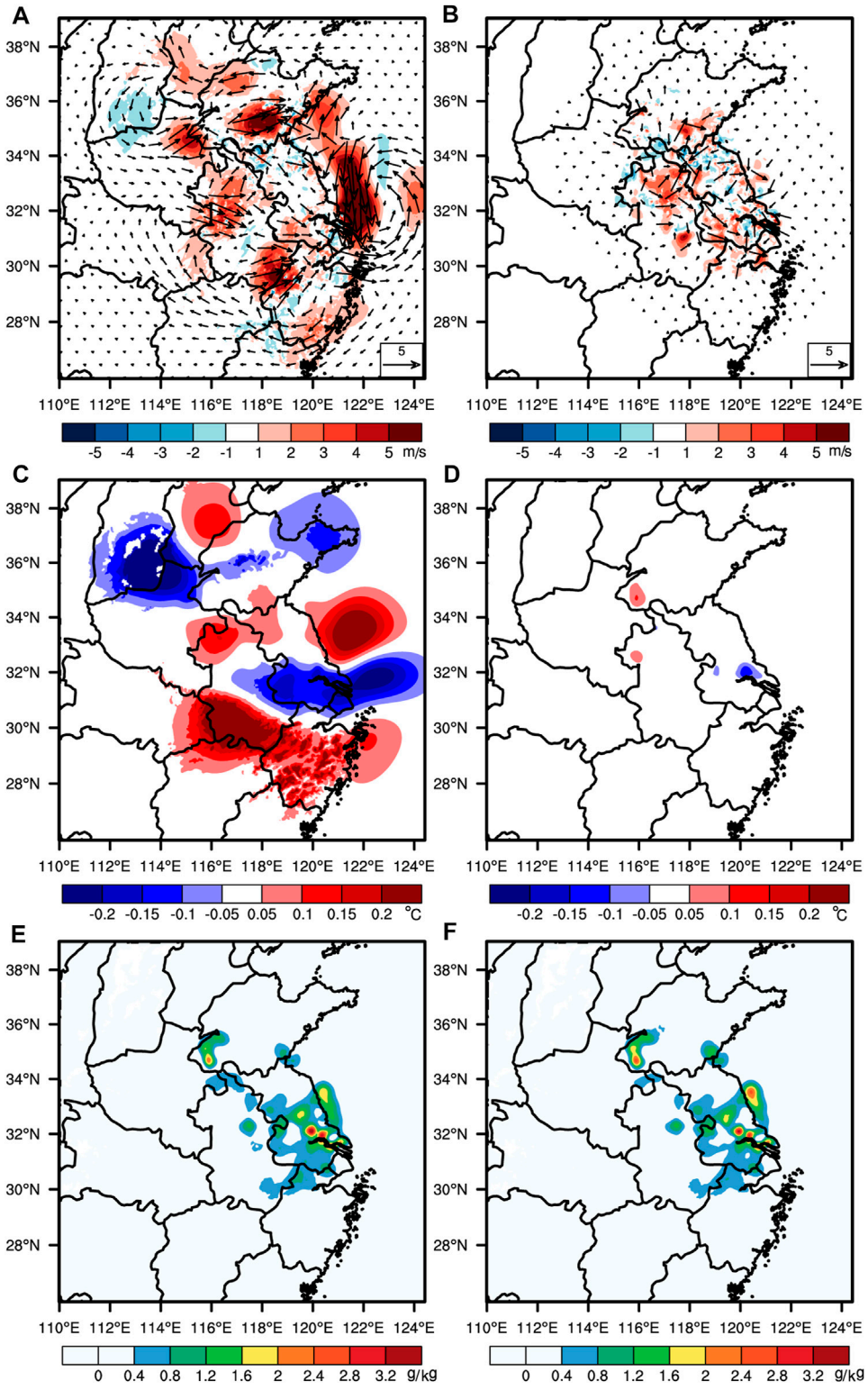

FIGURE 9
Analysis increments of **(A)**, **(B)** wind speed and wind vector (units: m s^{-1}) **(C)** **(D)** temperature (units: °C); and **(E)**, **(F)** water vapor mixing ratio (units: g kg^{-1}) at 850 hPa at 1200 UTC on 26 July 2018 from the real radar observation experiments EXP_CV5 (left column) and EXP_CV7 (right column).

increment value of V-wind is much smaller compared to U-wind. In contrast, U and V are independent control variables that are not correlated with each other, so only westerly wind increments are generated in the CV7 scheme. It is worth noting that humidity is an independent control variable in both schemes, so the assimilation of single observations will not produce humidity increments.

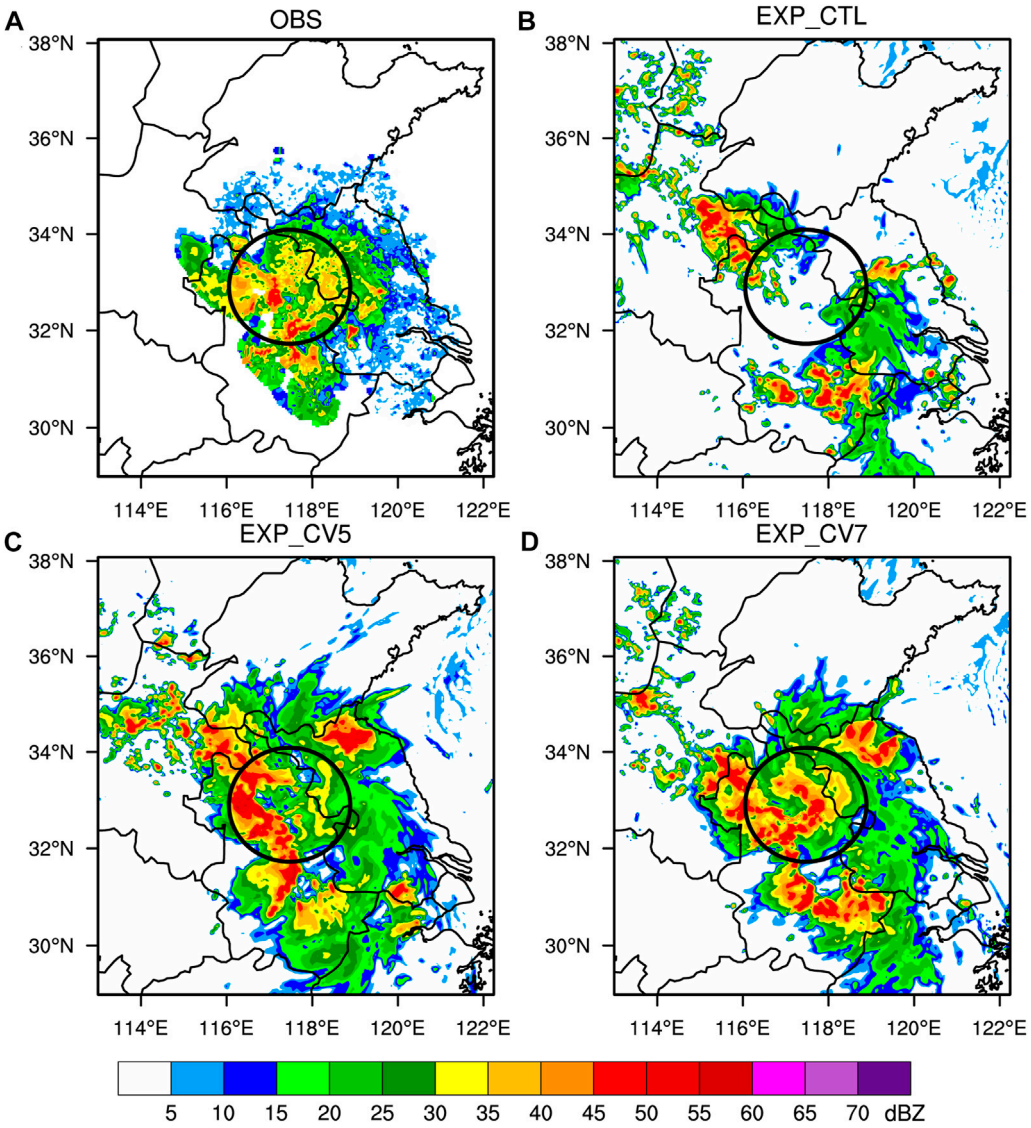

FIGURE 10
Composite reflectivity fields (units: dBZ) at 1500 UTC on 26 July 2018: **(A)** for the observations, the third hour forecast of experiments **(B)** EXP_CTL, **(C)** EXP_CV5, and **(D)** EXP_CV7.

Figures 8A,B show the vertical profile of the increment of U-wind along 33°N in Figures 7C,D, respectively. The increments generated by the CV5 scheme have a much larger propagation in the horizontal direction than those generated by the CV7 scheme. The incremental horizontal propagation range produced by the CV7 scheme is small, and the influence range is relatively concentrated. The single observation tests show that compared with the CV5 scheme, the CV7 scheme contains smaller scale features and is more local.

4.3 Comparison of the increment fields of assimilated radar observations

The effects of the two schemes on the assimilation of real radar observations are investigated next. Figure 9 demonstrates the analysis increments at 850 hPa resulting from the assimilation of the radar observations at 0600 UTC for experiments EXP_CV5 (left column) and EXP_CV7 (right column). EXP_CV5 (Figure 9A) produces a much larger range of wind field increments than EXP_CV7 (Figure 9B). EXP_CV5 produces multiple large value regions of wind speed increments and cyclonic wind field increments in the northern part of Henan Province and the southeastern coastal area of Jiangsu Province. The wind field increments generated by EXP_CV7 contain more small-scale characteristics. EXP_CV7 produces almost no temperature increment (Figure 9D), while EXP_CV5 (Figure 9C) produces a temperature increment of some magnitude (0.1 K), which is due to the correlation between the control variables in the CV5 scheme. There is no significant difference in humidity increment between the two groups of experiments, and both have large humidity increments in the

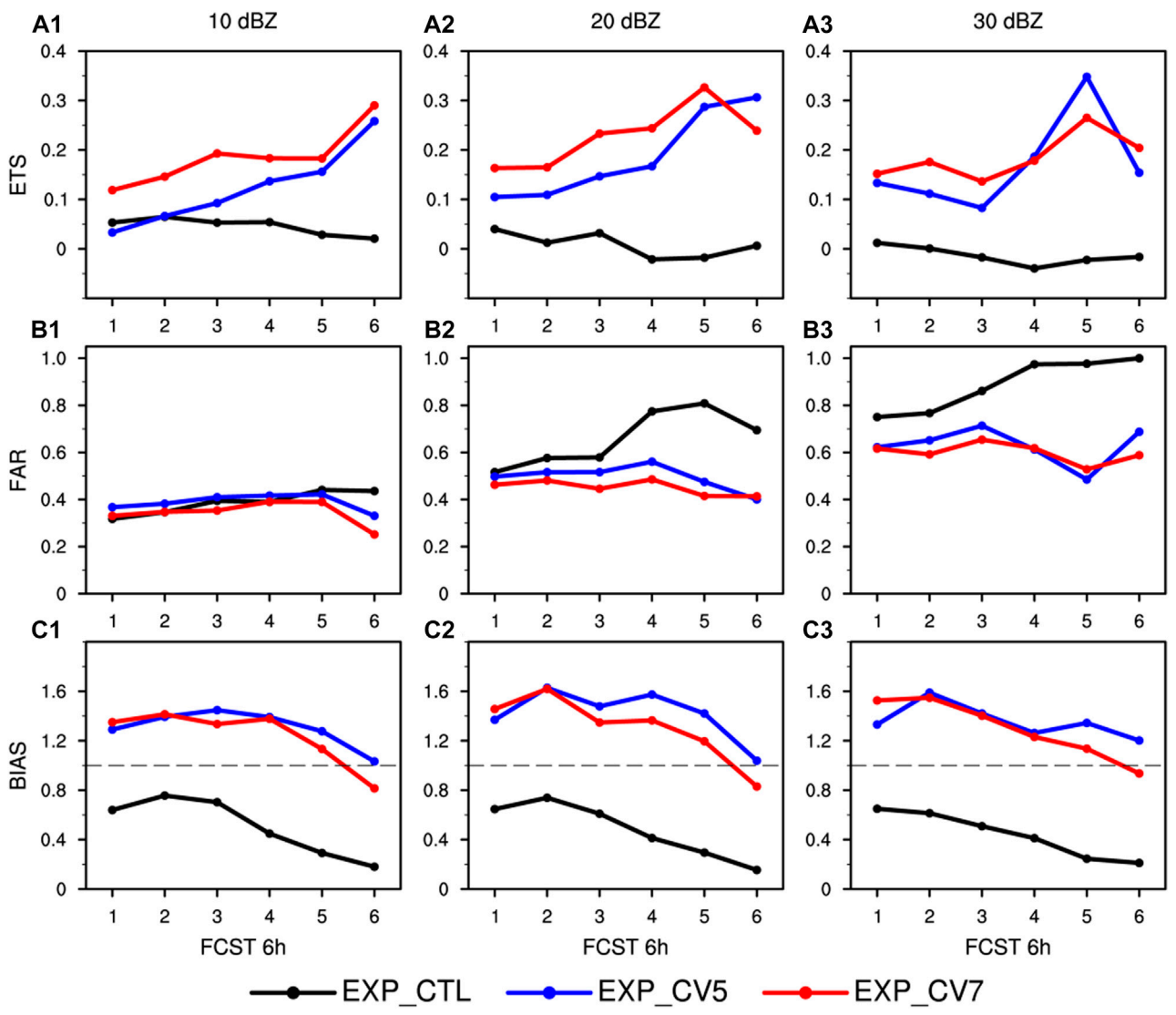

FIGURE 11
ETS **(A1-A3)**, FAR **(B1-B3)** and BIAS **(C1-C3)** scores for the maximum reflectivity predicted by the three experiments. The first, second and third columns are the results of thresholds of 10, 20 and 30 dBZ, respectively.

area with a large value of radar composite reflectivity (see Figure 2A).

4.4 Reflectivity forecasts

To better compare the effects of the two control variable schemes on convective forecasts, the observed composite reflectivity field and the predicted third hour (1500 UTC) composite reflectivity fields calculated from three experiments are presented in Figure 10. At this time, the observed echo areas with large values were mainly located in Anhui Province. The echoes in the high value area are hardly forecasted in EXP_CTL (especially in the area inside the black circle) but instead generate false strong convection in eastern Henan Province and southern Anhui Province. The predicted echoes of EXP_CV5 and EXP_CV7, after cyclic assimilation of radar data, are much improved compared with EXP_CTL. Both assimilation experiments successfully predict strong echoes in north-central Anhui Province, but the predicted echoes from EXP_CV7 are closer to the observations. Although both assimilation experiments produce spurious convection within Henan Province, the false convection predicted by EXP_CV5 is significantly more, which may be due to unrealistic convergence after assimilating radar observations using the CV5 scheme.

In this study, the equitable threat score (ETS), false alarm rate (FAR), BIAS and missing alarm rate (MAR) scores are used to evaluate reflectivity and quantitative precipitation forecasts, and the range of the validation area is shown in Figure 10A. ETS considers the hit number achieved by chance and has the fairness property, which is measured in the range of −1/3 to 1. Larger values indicate better forecasting skill. The measurement range of BIAS is 0 ~ ∞, and the ideal BIAS score is 1. A BIAS higher than 1 indicates

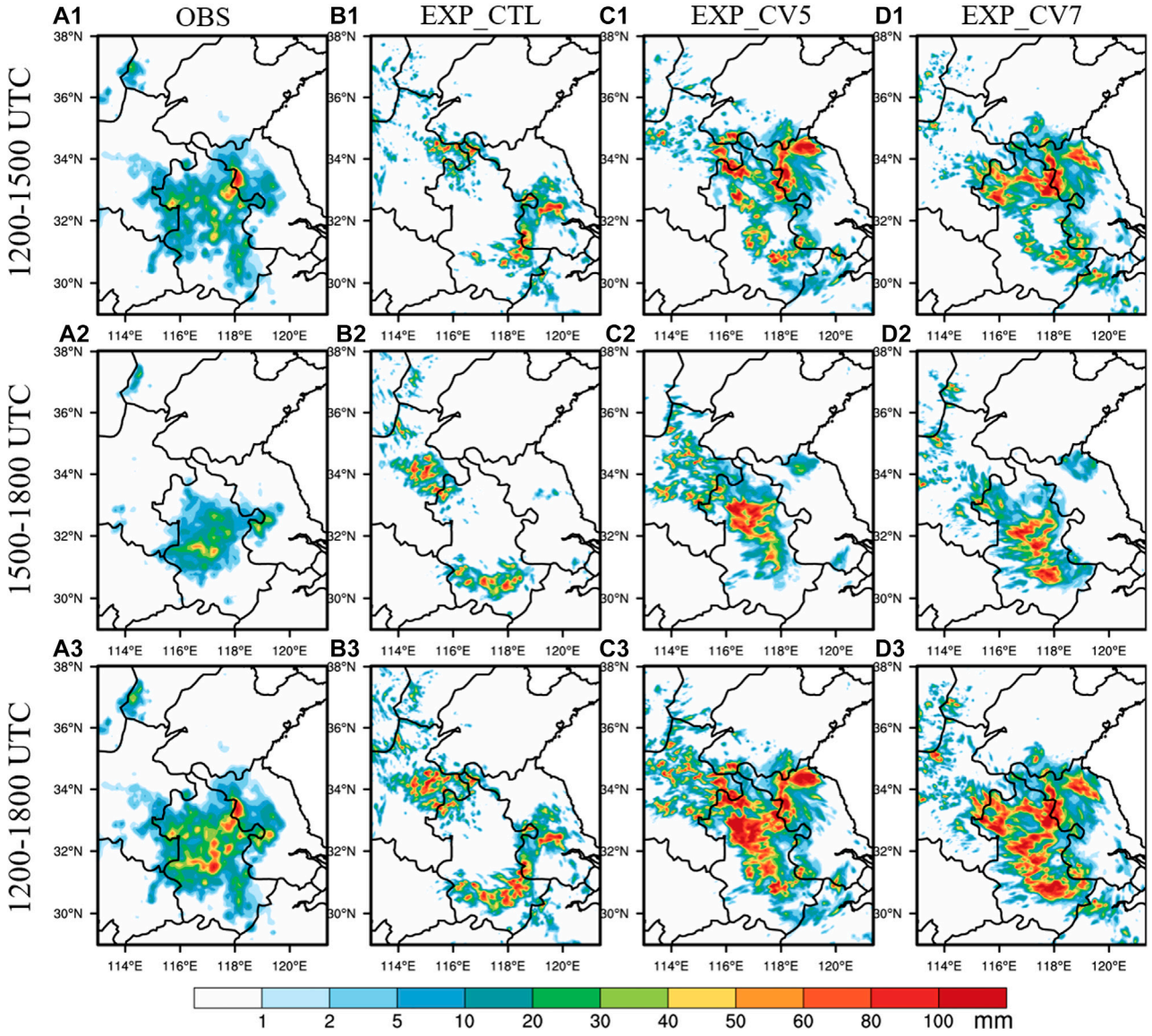

FIGURE 12
Observed and forecasted 3-h and 6-h accumulated precipitation (units: mm). From left to right: observations **(A1, A2, A3)**, EXP_CTL **(B1, B2, B3)**, EXP_CV5 **(C1, C2, C3)** and EXP_CV7 **(D1, D2, D3)**; from top to bottom: 1,200–1500 UTC, 1,500–1800 UTC and 1,200–1800 UTC.

overestimation and less than 1 indicates underestimation (Goines and Kennedy, 2018). The values of MAR and FAR range from 0 to 1, with lower values indicating better forecasting skill.

The ETS, FAR and BIAS scores of the maximum reflectivity predicted by the three experiments against the observations are given in Figure 11 for three thresholds of 10, 20 and 30 dBZ. It can be seen that the two assimilation experiments significantly improve the ETS scores compared to the control experiment. It is obvious that EXP_CV7 has higher ETSs and lower FARs than EXP_CV5, except for the sixth-hour forecast at the 20 dBZ threshold and the fourth- and fifth-hour forecasts at the 30 dBZ threshold. The BIASs of EXP_CTL are below 1 at all thresholds throughout the forecast period, indicating that it underestimates the echoes. In contrast, both assimilation tests overestimate the echoes, and the BIAS values of EXP_CV7 are generally smaller than those of EXP_CV5. Overall, EXP_CV7 performs better in forecasting the echoes.

4.5 Precipitation forecasts

To verify the spatial pattern of precipitation, the simulated precipitation results of the three experiments are compared with the observed precipitation in Figure 12. The first and second rows are the 3-h accumulated precipitation for 1,200–1500 UTC and 1,500–1800 UTC, respectively, and the third row is the 6-h accumulated precipitation for 1,200–1800 UTC. The first column shows the observed precipitation, and the second, third, and fourth columns successively represent the precipitation forecasted by EXP_CTL, EXP_CV5, and EXP_CV7. The observed precipitation is

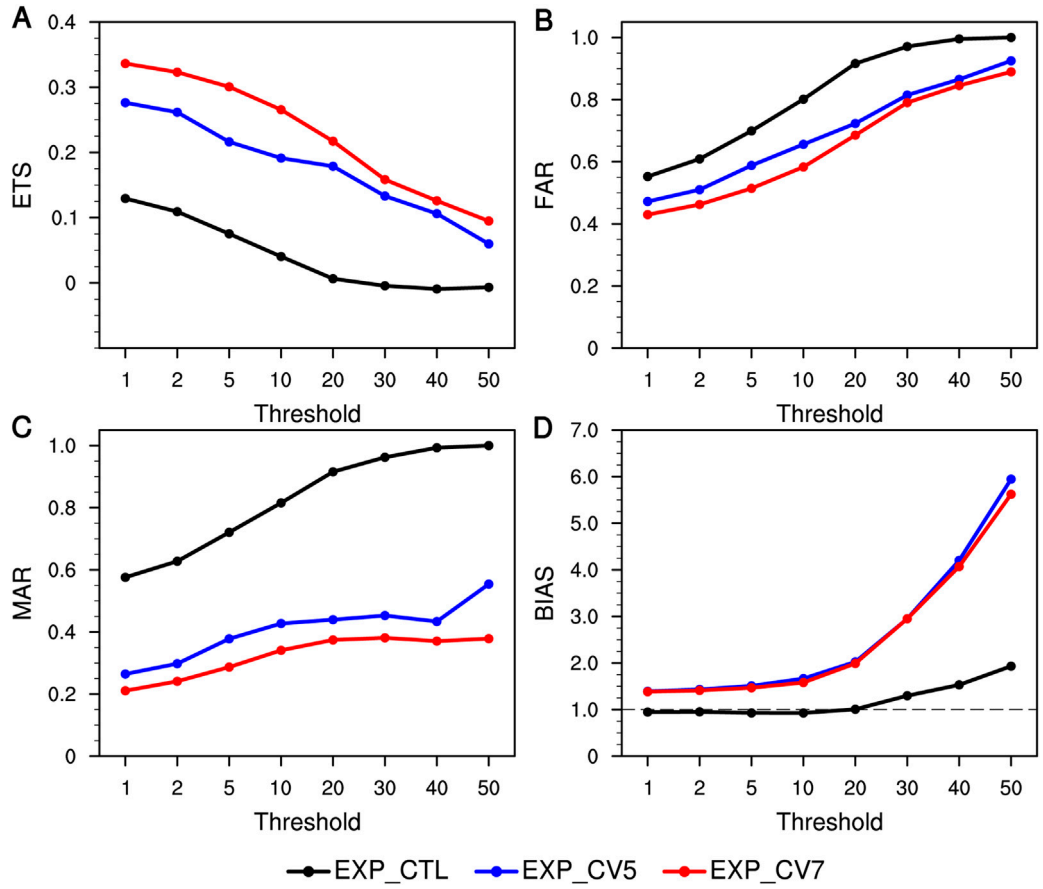

FIGURE 13
(A) ETS, **(B)** FAR **(C)** MAR and **(D)** BIAS scores for forecasted 6-h accumulated precipitation with thresholds of 1, 2, 5, 10, 20, 30, 40 and 50 mm for the three experiments.

mainly located in Anhui Province and western Jiangsu Province, and the area with 6-h accumulated precipitation exceeding 50 mm is mainly located in central Anhui Province. 1,200–1500 UTC, EXP_CTL (Figure 12B1) barely predicts the heavy rainfall band and generates false strong precipitation forecasts in eastern Henan Province and Jiangsu Province. After assimilating the radar data, the intense precipitation forecasts in EXP_CV5 (Figure 12C1) and EXP_CV7 (Figure 12D1) are well improved. Compared with EXP_CV5, EXP_CV7 has better precipitation forecasts in northern Anhui Province, which is closer to the observation, and reduces the false precipitation of EXP_CV5 in Henan Province to some extent. 1,500–1800 UTC, the observed precipitation area shrinks toward central Anhui Province, and EXP_CTL (Figure 12B2) completely misses precipitation and produces false heavy precipitation forecasts in eastern Henan Province and southern Anhui Province. Both experiments EXP_CV5 (Figure 12C2) and EXP_CV7 (Figure 12D2) predicted precipitation in central Anhui Province, but EXP_CV7 forecasted precipitation that was more consistent with observations, and the unrealistic heavy precipitation of EXP_CV5 was significantly reduced in Henan Province. 1,200–1800 UTC, the precipitation in Anhui Province is not predicted by EXP_CTL, while the location of precipitation in EXP_CV5 and EXP_CV7 remains largely consistent with the observation, but the intensity of precipitation is obviously overestimated. EXP_CV7 is better than EXP_CV5 in predicting precipitation in central and southern Anhui Province and Henan Province.

Statistical validation scores are calculated to quantitatively assess the impact of the two control variable schemes on convective precipitation forecasts. The ETS, FAR, MAR, and BIAS scores of the 6-h accumulated precipitation against observed precipitation with different thresholds of 1, 2, 5, 10, 20, 30, 40, and 50 mm are given in Figure 13. The ETSs for both assimilation experiments are consistently higher than EXP_CTL at all thresholds, and the FARs and MARs are consistently lower than EXP_CTL at all thresholds. The FAR and MAR scores of EXP_CTL at the threshold of 50 mm are 1, indicating that heavy precipitation above 50 mm is completely missed, and there are many false heavy precipitations. The ETSs of EXP_CV7 at all thresholds are consistently higher than those of EXP_CV5, and the FARs, MARs and BIASs of EXP_CV7 at all thresholds are consistently lower than those of EXP_CV5. The results show that both assimilation experiments improve precipitation forecasts after assimilating radar observations, but using the CV7 scheme to assimilate radar data has better performance in precipitation forecasting.

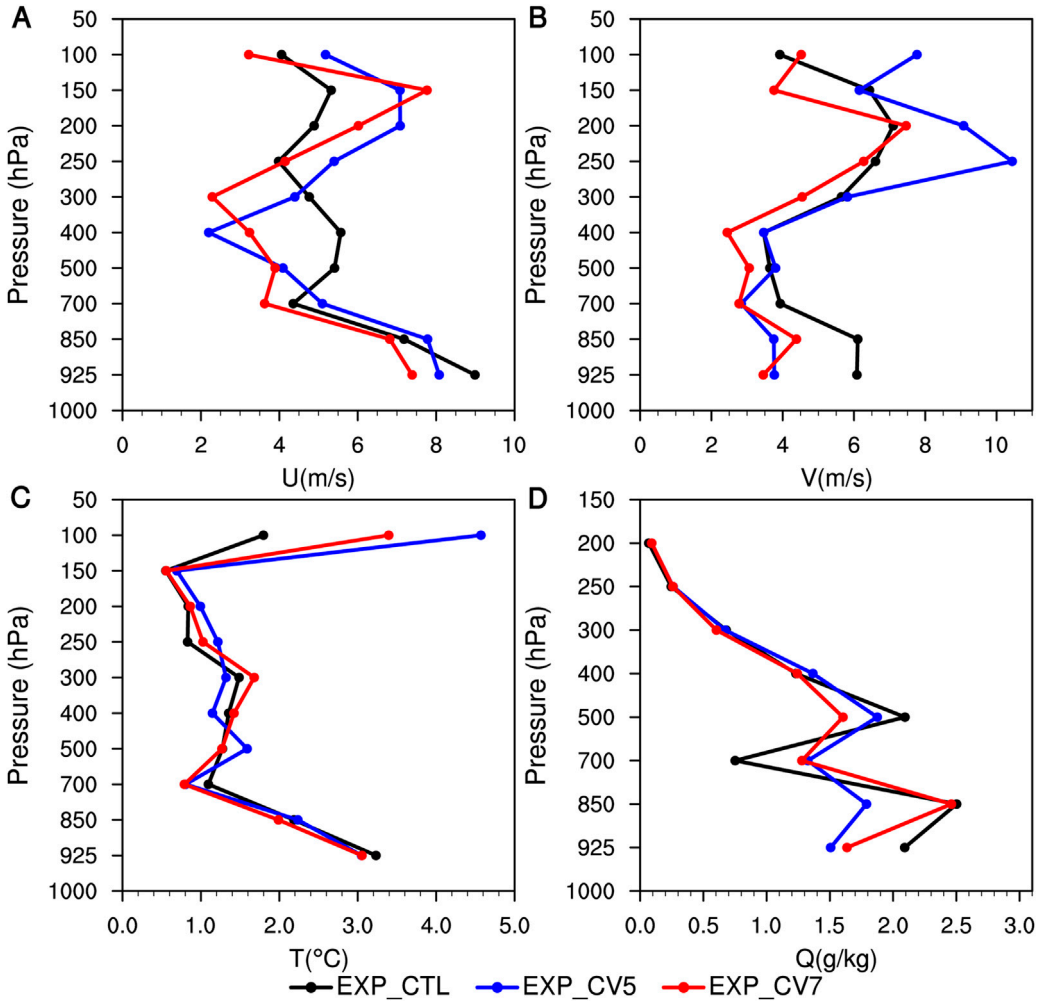

FIGURE 14
Vertical profiles of root-mean-square errors (RMSEs) of analyses against sounding observations at 1200 UTC on 26 July 2018 for **(A)** the U wind component (m s^{-1}), **(B)** the V wind component (m s^{-1}), **(C)** temperature T (°C), and **(D)** water vapor mixing ratio Q (g kg^{-1}).

4.6 Verification against conventional observations

Conventional observations are used to verify the impact of both schemes on analysis and forecasting. Figure 14 shows the vertical profiles of root-mean-square errors (RMSEs) for horizontal wind speed (U and V), temperature T), and water vapor mixing ratio Q) in the initial field (1200 UTC) for each experiment. The RMSEs are calculated against the observations from eight sounding stations in Figure 3. EXP_CV7 greatly improves the wind field compared with EXP_CV5. For the U wind component, the RMSEs of EXP_CV7 are smaller than those of EXP_CTL except for 250–150 hPa and are significantly lower than those of EXP_CV5 except for 400 hPa and 150 hPa. For the V wind component, the RMSEs of EXP_CV7 are significantly smaller than those of EXP_CTL except for 200 hPa and 100 hPa and are significantly lower than those of EXP_CV5 except for 850 hPa. With smaller length-scale, EXP_CV7 could capture more local characteristic and make the analysis increment more consistent with high-density radar observation. For temperature T, the RMSEs of EXP_CV7 are smaller than those of EXP_CV5 except for 400–300 hPa, and its RMSEs are larger than those of EXP_CTL at heights above 500 hPa. For the water vapor mixing ratio Q, EXP_CV7 has lower RMSEs than EXP_CV5 at altitudes above 700 hPa. EXP_CV5 has larger RMSEs than EXP_CTL for multiple height levels for all variables, which may be caused by excessive propagation of variable increments and overestimation of variable subsequent predictions after assimilation of radar observations. Figure 14 shows that the assimilation effect of the CV7 scheme on radar data is better than that of the CV5 scheme, especially for the improvement of the wind field.

Figure 15 describes the time series RMSEs of the 10 m wind speed (WP10 M), 2 m temperature (T2 M), 2 m relative humidity (RH2 M) and surface pressure (Ps) from the forecasts of EXP_CTL, EXP_CV5 and EXP_CV7. The RMSEs are calculated against the SYNOP observations from 319 surface stations. Compared with EXP_CV5, EXP_CV7 seems to have a smaller RMSE for all surface variables, especially for the wind field where the reduction in RMSE

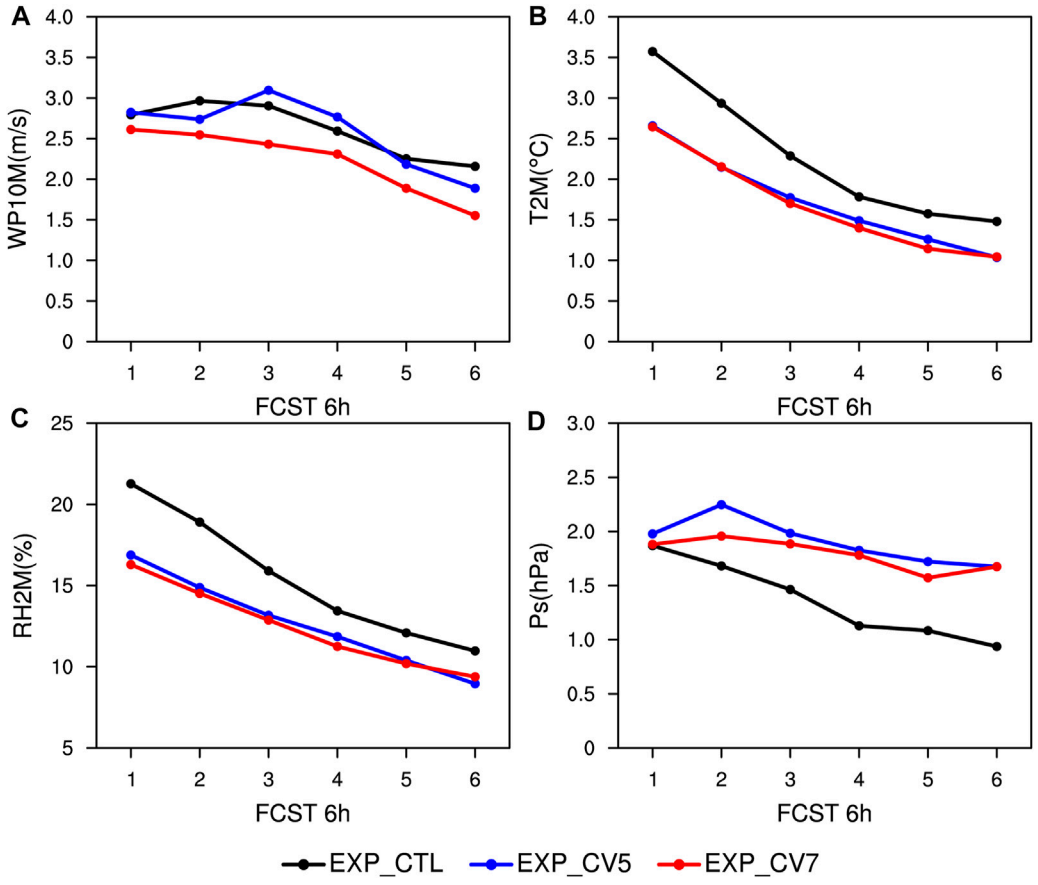

FIGURE 15
Time series of the RMSE of the predicted surface variables against the SYNOP observations for **(A)** wind speed at 10 m, **(B)** temperature at 2 m **(C)** relative humidity at 2 m and **(D)** surface pressure.

is most pronounced. Overall, the assimilation of radar data using the CV7 scheme produces analysis fields fitting observations well and can significantly reduce forecast errors for model surface variables.

4.7 Diagnosis of wind and moisture fields

The wind and moisture fields at 700 hPa provide information on the source and transport mechanism of water vapor. To analyze the reasons for the differences in the forecasts of each experiment, the horizontal wind vector and water vapor flux divergence fields at 700 hPa for the initial fields of the three experiments are presented in Figure 16. The wind speeds in the initial fields of experiments EXP_CV5 and EXP_CV7 are larger than those in EXP_CTL due to the assimilation of high-resolution radar observations, and the enhanced southeasterly wind continuously transports the water vapor from the East China Sea to Jiangsu and Anhui Provinces. The negative large value of water vapor flux divergence in all three experiments is mainly located at the border of Anhui Province and Jiangsu Province. Compared with EXP_CV7, EXP_CV5 has obvious cyclonic wind shear in region A, and there are many scattered water vapor convergence zones, which is also the reason for its spurious heavy precipitation forecast in this region in the subsequent forecast. EXP_CTL has a small range of negative large values of water vapor flux divergence in region B, and water vapor convergence is very weak. EXP_CV5 and EXP_CV7 both significantly enhance the convergence of water vapor in region B. The airflow from all directions gathers in this region, and the range of water vapor convergence increases significantly. However, the latter has a larger range of water vapor convergence than the former (especially in northern Anhui Province) and suppresses the unrealistic convergence of EXP_CV5 in region A, which better matches the observed radar echo region with a large value (Figure 2C), resulting in the improved forecast.

5 Summary and discussion

The choice of control variables is crucial for the assimilation efficiency of variational assimilation systems. In this study, based on the WRF model and its 3DVAR assimilation system, the BE matrix with $\psi\chi_u$ as the momentum control variable (CV5 scheme) and the BE matrix with UV as the momentum control variable (CV7 scheme) are calculated by the NMC method. The characteristic length scales of two BE statistics are compared, and the characteristics of BE of two control variable schemes are

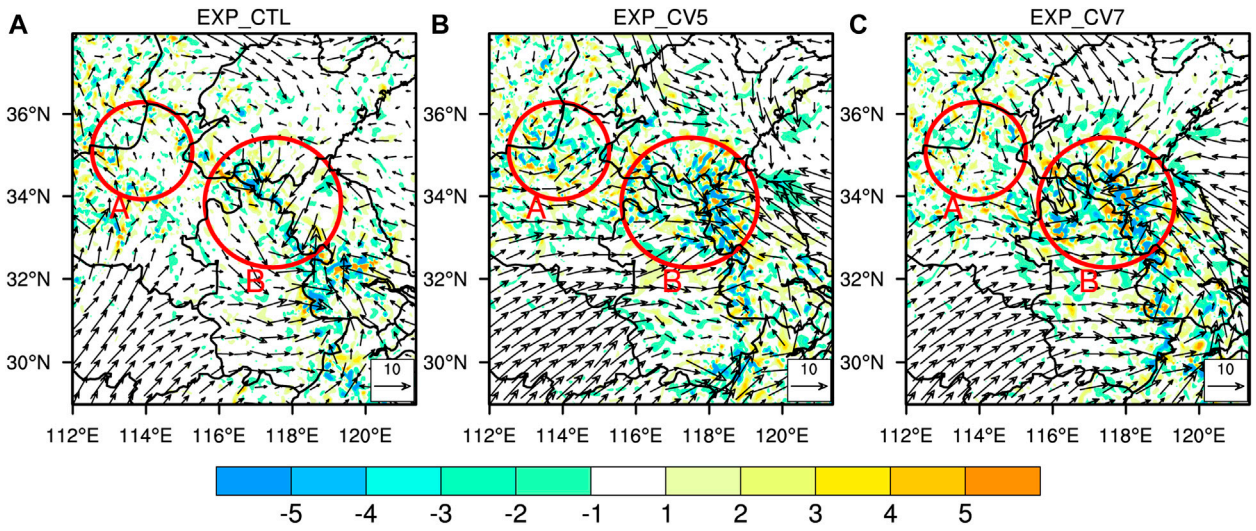

FIGURE 16
Horizontal wind vectors (arrows; units: m s^{-1}) and water vapor flux divergence (shaded; units: g cm^{-2} hPa^{-1} s^{-1}) at 700 hPa from the initial fields of **(A)** EXP_CTL, **(B)** EXP_CV5, and **(C)** EXP_CV7. The valid time is 1200 UTC on 26 July 2018.

analyzed by single temperature and westward wind observation tests. The impact of assimilating radial velocity and reflectivity on short-term forecasts of reflectivity and precipitation using the two control variable schemes is also evaluated by taking a dispersive convective process in a weak environmental field under the control of a subtropical anticyclone in the Jianghuai region of China on 26 July 2018 as an example.

The comparison of the characteristic length scales reveals that the differences between the two BE statistics are mainly reflected in the differences between the momentum control variables. The single observation tests show that the analysis increments of the wind field generated by the two BEs is significantly different. The analysis increments generated by the BE of the CV5 scheme have a larger range of influence, and the negative increments non-physically will lead to unrealistic local divergence and convergence. In contrast, the analysis increments produced by the BE of the CV7 scheme tend to capture small-scale features and are more localized.

The real radar observation assimilation experiments show that the range of the wind field analysis increment generated by EXP_CV5 is much larger than that generated by EXP_CV7, and there is little difference in the temperature analysis increment and almost no difference in the water vapor mixing ratio analysis increment. Compared with EXP_CTL, both assimilation tests improve the reflectivity and precipitation forecasts. However, the distribution of the predicted reflectivity and accumulated precipitation and objective statistical scores show valuable improvements in EXP_CV7 compared with EXP_CV5. EXP_CV7 improves the convective precipitation forecasts and distinctly reduces the spurious precipitation forecasted by EXP_CV5. This is consistent with the results of previous studies for assimilating both radar and other observations (Li et al., 2016; Sun et al., 2016; Thiruvengadam et al., 2019; Wang et al., 2020; Dong et al., 2022). In addition, it also significantly reduces the prediction error of surface variables. Further analysis shows that compared to EXP_CV5, EXP_CV7 improves the wind, temperature and water vapor fields in the initial field and improves the water vapor convergence conditions, which may be the reason for its better performance in the subsequent forecasts.

The results provide strong evidence that the assimilation of radar reflectivity and radial velocity using the CV7 scheme can improve the forecasting of strong convective systems in weak environmental fields. However, in this study, only one dispersed convection process is studied, and more case studies and more long-term experiments are needed to make the results more applicable to make better use of the radar observations.

Data availability statement

The raw data supporting the conclusion of this article will be made available by the authors, without undue reservation.

Author contributions

WS involved throughout the research, analysis, and manuscript process. EL helped to analyze and interpret the results, reviewed and revised the manuscript. XQ developed the concept for the manuscript and provided ongoing manuscript feedback. YX provided insight and feedback in the analysis process.

Funding

This research was mainly supported by the Key Laboratory of Climate Resource Development and Disaster Prevention of Gansu Province (No. 20JR10RA654), Bohai Rim Meteorological Science Collaborative Innovation Fund (No. QYXM201901)

and the Natural Science Foundation of Tianjin (No. 20JCYBJC00780).

Acknowledgments

The authors acknowledge the Mesoscale and Microscale Meteorology Laboratory of National Center for Atmospheric Research (NCAR) for providing the WRF. We also thank the NCEP for providing the 0.25° × 0.25° GFS dataset. We appreciate the China Meteorological Data Service Center for providing 0.1° × 0.1° merged precipitation data from automatic weather stations in China and CMORPH satellite data. This work was supported by the Supercomputing Center of Lanzhou University and the National Supercomputer Center in Tianjin, China.

Conflict of interest

The authors declare that the research was conducted in the absence of any commercial or financial relationships that could be construed as a potential conflict of interest.

Publisher's note

All claims expressed in this article are solely those of the authors and do not necessarily represent those of their affiliated organizations, or those of the publisher, the editors and the reviewers. Any product that may be evaluated in this article, or claim that may be made by its manufacturer, is not guaranteed or endorsed by the publisher.

References

Barker, D. M., Huang, W., Guo, Y. R., Bourgeois, A. J., and Xiao, Q. N. (2004). A three-dimensional variational data assimilation system for MM5: Implementation and initial results. *Mon. Weather Rev.* 132, 897–914. doi:10.1175/1520-0493(2004)132<0897:ATVDAS>2.0.CO;2

Barker, D. M., Huang, X. Y., Liu, Z. Q., Auligné, T., Zhang, X., Rugg, S., et al. (2012). The weather research and forecasting model's community variational/ensemble data assimilation system: WRFDA. *B. Am. Meteorol. Soc.* 93, 831–843. doi:10.1175/BAMS-D-11-00167.1

Bouttier, F., and Courtier, P. (2002). Data assimilation concepts and methods March 1999. Meteorological training course lecture series. *ECMWF* 718, 59.

Brewster, K., Hu, M., Xue, M., and Gao, J. (2005). "Efficient assimilation of radar data at high resolution for short-range numerical weather prediction," in World Weather Research Program Symposium on Nowcasting and Very Short-range Forecasting.

Brousseau, P., Berre, L., Bouttier, F., and Desroziers, G. (2011). Background-error covariances for a convective-scale data-assimilation system: AROME–France 3D-var. *Q.J.R. Meteorol. Soc.* 137, 409–422. doi:10.1002/qj.750

Buehner, M. (2010). *Error statistics in data assimilation: Estimation and modelling. Data assimilation*. Berlin, Heidelberg: Springer, 93–112.

Chou, M. D., and Suarez, M. J. (1999). *A solar radiation parameterization for atmospheric studies*. Available at: https://ntrs.nasa.gov/citations/19990060930.

Descombes, G., Auligné, T., Vandenberghe, F., Barker, D. M., and Barré, J. (2015). Generalized background error covariance matrix model (GEN_BE v2.0). *Geosci. Model Dev.* 8, 669–696. doi:10.5194/gmd-8-669-2015

Dong, Q., Wang, X. L., Fan, S. Y., Li, Y. H., Qiu, X. B., and Liu, L. L. (2022). Comparison of two kinds of momentum control variables in 3DVAR during assimilating low-resolution observations in a convective-scale model: A case study of torrential rainfall in north China. *J. Atmos. Sci.* 58, 697–713. doi:10.1007/s13143-022-00290-5

Ek, M. B., Mitchell, K. E., Lin, Y., Rogers, E., Grunmann, P., Koren, V., et al. (2003). Implementation of Noah land surface model advances in the National Centers for Environmental Prediction operational mesoscale Eta model. *J. Geophys. Res. Atoms.* 108. doi:10.1029/2002JD003296

Eyre, J. R., Bell, W., Cotton, J., English, S. J., Forsythe, M., Healy, S. B., et al. (2022). Assimilation of satellite data in numerical weather prediction. Part II: Recent years. *Q.J.R. Meteorol. Soc.* 148, 521–556. doi:10.1002/qj.4228

Fisher, M. (2003). "Background error covariance modelling," in *Seminar on recent development in data assimilation for atmosphere and ocean*, 45–63.

Gan, R. H., Yang, Y., Qiu, X. B., Wang, R. C., Qiu, X. X., and Zhu, L. J. (2021). Assimilation of the maximum vertical velocity converted from total lightning data through the EnSRF method. *J. Geophys. Res. Atoms.* 126. doi:10.1029/2020JD034300

Gao, J. D., and Stensrud, D. J. (2012). Assimilation of reflectivity data in a convective-scale, cycled 3DVAR framework with hydrometeor classification. *J. Atmos. Sci.* 69, 1054–1065. doi:10.1175/JAS-D-11-0162.1

Gao, J. D., Xue, M., Shapiro, A., and Droegemeier, K. K. (1999). A variational method for the analysis of three-dimensional wind fields from two Doppler radars. *Mon. Weather Rev.* 127, 2128–2142. doi:10.1175/1520-0493(1999)127<2128:AVMFTA>2.0.CO;2

Goines, D. C., and Kennedy, A. D. (2018). Precipitation from a multiyear database of convection-allowing WRF simulations. *J. Geophys. Res. Atoms.* 123, 2424–2453. doi:10.1002/2016JD026068

Hong, S. Y., and Lim, J. O. J. (2006). The WRF single-moment 6-class microphysics scheme (WSM6). *J. Korean Meteor. Soc.* 42, 129–151.

Hong, S. Y., Noh, Y., and Dudhia, J. (2006). A new vertical diffusion package with an explicit treatment of entrainment processes. *Mon. Weather Rev.* 134, 2318–2341. doi:10.1175/MWR3199.1

Ide, K., Courtier, P., Ghil, M., and Lorenc, A. C. (1997). Unified notation for data assimilation: Operational, sequential and variational (gtSpecial IssueltData assimilation in meteology and oceanography: Theory and practice). *J. Meteorol. Soc. Jpn. Ser. II* 75, 181–189. doi:10.2151/jmsj1965.75.1B_181

Johnson, A., Wang, X. G., Carley, J. R., Wicker, L. J., and Karstens, C. (2015). A comparison of multiscale GSI-based EnKF and 3DVar data assimilation using radar and conventional observations for midlatitude convective-scale precipitation forecasts. *Mon. Weather Rev.* 143, 3087–3108. doi:10.1175/MWR-D-14-00345.1

KessingerEllis, S., Vanandel, J., and Yee, J. (2003). "The AP clutter mitigation scheme for the WSR-88D," in 31st Conference on Radar Meteorology, 526–529.

Li, X., Zeng, M. J., Wang, Y., Wang, W. L., Wu, H. Y., and Mei, H. X. (2016). Evaluation of two momentum control variable schemes and their impact on the variational assimilation of radarwind data: Case study of a squall line. *Adv. Atmos. Sci.* 33, 1143–1157. doi:10.1007/s00376-016-5255-3

Li, Y. Z., Wang, X. G., and Xue, M. (2012). Assimilation of radar radial velocity data with the WRF hybrid ensemble–3DVAR system for the prediction of hurricane ike (2008). *Mon. Weather Rev.* 140, 3507–3524. doi:10.1175/MWR-D-12-00043.1

Lin, E. L., Yang, Y., Qiu, X. B., Xie, Q., Gan, R. H., Zhang, B., et al. (2021). Impacts of the radar data assimilation frequency and large-scale constraint on the short-term precipitation forecast of a severe convection case. *Atmos. Res.* 257, 105590. doi:10.1016/j.atmosres.2021.105590

Liu, S., Xue, M., Gao, J. D., and Parrish, D. (2005). "Analysis and impact of super-obbed Doppler radial velocity in the NCEP grid-point statistical interpolation (GSI) analysis system," in Proceedings of the 17th Conference on Numerical Weather Prediction (Washington, DC: American Meteorological Society).

Mlawer, E. J., Taubman, S. J., Brown, P. D., Iacono, M. J., and Clough, S. A. (1997). Radiative transfer for inhomogeneous atmospheres: RRTM, a validated correlated-k model for the longwave. *J. Geophys. Res. Atoms.* 102, 16663–16682. doi:10.1029/97JD00237

Parrish, D. F., and Derber, J. C. (1992). The national meteorological center's spectral statistical-interpolation analysis system. *Mon. Weather Rev.* 120, 1747–1763. doi:10.1175/1520-0493(1992)120<1747:TNMCSS>2.0.CO;2

Shen, F. F., Xu, D. M., and Min, J. Z. (2019). Effect of momentum control variables on assimilating radar observations for the analysis and forecast for Typhoon Chanthu (2010). *Atmos. Res.* 230, 104622. doi:10.1016/j.atmosres.2019.104622

Stanesic, A., Horvath, K., and Keresturi, E. (2019). Comparison of NMC and ensemble-based climatological background-error covariances in an operational limited-area data assimilation system. *Atmosphere* 10, 570. doi:10.3390/atmos10100570

Steiner, M., and Smith, J. A. (2002). Use of three-dimensional reflectivity structure for automated detection and removal of nonprecipitating echoes in radar data. *J. Atmos. Ocean. Technol.* 19, 673–686. doi:10.1175/1520-0426(2002)019<0673:UOTDRS>2.0.CO;2

Sun, J. Z. (2005). Convective-scale assimilation of radar data: Progress and challenges. *Q.J.R. Meteorol. Soc.* 131, 3439–3463. doi:10.1256/qj.05.149

Sun, J. Z., Wang, H. L., Tong, W. X., Zhang, Y., Lin, C. Y., and Xu, D. M. (2016). Comparison of the impacts of momentum control variables on high-resolution variational data assimilation and precipitation forecasting. *Mon. Weather Rev.* 144, 149–169. doi:10.1175/MWR-D-14-00205.1

Thiruvengadam, P., Indu, J., and Ghosh, S. (2019). Assimilation of Doppler Weather Radar data with a regional WRF-3DVAR system: Impact of control variables on forecasts of a heavy rainfall case. *Adv. Water Resour.* 126, 24–39. doi:10.1016/j.advwatres.2019.02.004

Thiruvengadam, P., Indu, J., and Ghosh, S. (2020). Improving convective precipitation forecasts using ensemble-based background error covariance in 3DVAR radar assimilation system. *Earth Space Sci.* 7, e2019EA000667. doi:10.1029/2019EA000667

Tong, W., Li, G., Sun, J., Tang, X., and Zhang, Y. (2016). Design strategies of an hourly update 3DVAR data assimilation system for improved convective forecasting. *Weather Forecast* 31, 1673–1695. doi:10.1175/waf-d-16-0041.1

Wang, C., Chen, Y., Chen, M., and Shen, J. (2020). Data assimilation of a dense wind profiler network and its impact on convective forecasting. *Atmos. Res.* 238, 104880. doi:10.1016/j.atmosres.2020.104880

Wang, H. L., Sun, J. Z., Fan, S. Y., and Huang, X. Y. (2013). Indirect assimilation of radar reflectivity with WRF 3D-var and its impact on prediction of four summertime convective events. *J. Appl. Meteor. Climatol.* 52, 889–902. doi:10.1175/JAMC-D-12-0120.1

Wu, W. S., Purser, R. J., and Parrish, D. F. (2002). Three-dimensional variational analysis with spatially inhomogeneous covariances. *Mon. Weather Rev.* 130, 2905–2916. doi:10.1175/1520-0493(2002)130<2905:TDVAWS>2.0.CO;2

Xiao, Q. N., Kuo, Y. H., Sun, J. Z., Lee, W. C., Lim, E., Guo, Y. R., et al. (2005). Assimilation of Doppler radar observations with a regional 3DVAR system: Impact of Doppler velocities on forecasts of a heavy rainfall case. *J. Appl. Meteor. Climatol.* 44, 768–788. doi:10.1175/JAM2248.1

Xiao, Q., and Sun, J. (2007). Multiple-radar data assimilation and short-range quantitative precipitation forecasting of a squall line observed during IHOP_2002. *Mon. Weather Rev.* 135, 3381–3404. doi:10.1175/mwr3471.1

Xie, Y. F., and MacDonald, A. E. (2012). Selection of momentum variables for a three-dimensional variational analysis. *Pure Appl. Geophys.* 169, 335–351. doi:10.1007/s00024-011-0374-3

Xu, Q. (2019). On the choice of momentum control variables and covariance modeling for mesoscale data assimilation. *J. Atmos. Sci.* 76, 89–111. doi:10.1175/JAS-D-18-0093.1

Zhang, J., and Wang, S. X. (2006). An automated 2D multipass Doppler radar velocity dealiasing scheme. *J. Atmos. Ocean. Technol.* 23, 1239–1248. doi:10.1175/JTECH1910.1

Frontiers in Earth Science

Investigates the processes operating within the major spheres of our planet

Advances our understanding across the earth sciences, providing a theoretical background for better use of our planet's resources and equipping us to face major environmental challenges.

Discover the latest Research Topics

See more →

Frontiers

Avenue du Tribunal-Fédéral 34
1005 Lausanne, Switzerland
frontiersin.org

Contact us

+41 (0)21 510 17 00
frontiersin.org/about/contact